The Neutron-Rich Ejecta of Type Ia Supernovae and Constraints on the Exploding Mass of Their Progenitors

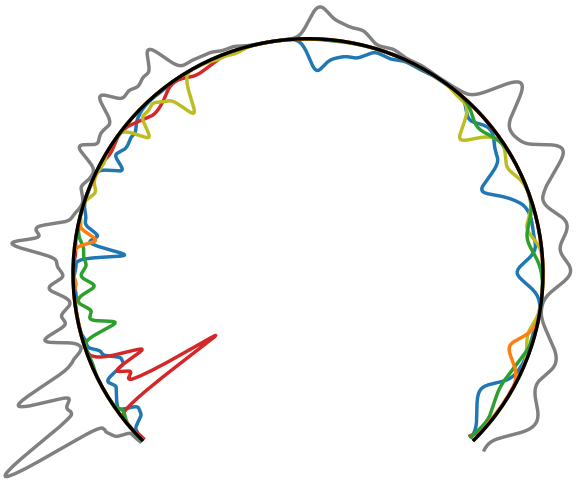

Dissertation

Andreas Flörs

TECHNISCHE UNIVERSITÄT MÜNCHEN

MAX-PLANCK-INSTITUT FÜR ASTROPHYSIK

The Neutron-Rich Ejecta of Type Ia Supernovae and Constraints on the Exploding Mass of Their Progenitors

Andreas Flörs

Vollständiger Abdruck der von der Fakultät für Physik der Technischen Universität München zur Erlangung des akademischen Grades eines

Doktors der Naturwissenschaften (Dr. rer. nat.)

genehmigten Dissertation.

Vorsitzende(r): Prof. Dr. Stephan Paul

Prüfer der Dissertation:

1. Hon.-Prof. Dr. Wolfgang Hillebrandt
2. Prof. Dr. Sherry Suyu

Die Dissertation wurde am 27.07.2020 bei der Technischen Universität München eingereicht und durch die Fakultät für Physik am 17.08.2020 angenommen.

Abstract

Type Ia supernovae (SNe Ia) are the violent stellar deaths of white dwarfs (WDs) in close binary systems, yet the physical mechanism leading to their death remains unclear. Owing to the faintness of WDs, the pre-explosion system of a SN Ia has never been directly detected. Their properties must be inferred from subtle indirect signatures. There are two plausible scenarios for producing SNe Ia. In the Chandrasekhar mass (M_{Ch}) channel, a WD accretes material from the companion star, which can be a main-sequence, giant star or another WD until it explodes near the Chandrasekhar mass limit ($\sim$1.4 $M_{\odot}$). In the sub-Chandrasekhar mass (sub-M_{Ch}) channel the explosion of the WD is triggered significantly below the M_{Ch} through dynamical processes such as mergers, double detonations or head-on collisions.

A distinguishing characteristic of SN Ia progenitor scenarios is the central density and thus the mass of the white dwarf at the time of the explosion. Steadily-accreting M_{Ch} progenitor models predict significantly higher central densities ($\sim 10^9\,\mathrm{g\,cm^{-3}}$) than sub-$M_{Ch}$ progenitor models ($\sim 10^7\,\mathrm{g\,cm^{-3}}$). This has an effect on the neutron excess: only near-M_{Ch} WDs reach the high central densities that are required so that additional neutrons can be produced in electron capture reactions, on top of the neutrons available in both channels if the progenitor already contains neutron-rich material (non-zero metallicity progenitors). An overabundance of neutrons is required to shift the burning from nuclear-statistical-equilibrium (NSE) – which synthesises mainly ^{56}Ni – to neutron-rich NSE (nNSE), producing stable Fe and Ni, among other isotopes.

At late times (> 200 d after explosion), the ejecta become fully transparent to optical and NIR photons and we can see deep into the core to the synthesised iron-rich material. In this thesis we utilise abundances of neutron-rich material derived from nebular phase spectra to constrain the mass of the progenitor system of SNe Ia.

The thesis is structured as follows: the first chapter serves as an introduction to the reader on the observed display of SNe Ia, the current understanding of the explosion mechanism, the explosion nucleosynthesis and progenitor search strategies. Sec. 2.2 presents the physics of the nebular phase and our spectral model which is later applied to observed data. We concentrate on modelling optical and near-IR (NIR) spectra at phases later than 200 days to make sure the residual optical depths are very small in the regions of interest. In Sec. 2.3 we discuss the conditions that lead to different types of line profiles and compare our findings to the commonly assumed Gaussian profile in nebular spectra. In order to determine the abundances of neutron-rich IGEs we first have to identify the respective species in nebular spectra. In Sec. 2.4 we show that optical and NIR nebular phase spectra are dominated by forbidden lines of singly and doubly ionised iron. We demonstrate that the ratio of the NIR to the optical lines serves as a tracer of the degenerate plasma state of the material – the electron density and temperature – which help us to determine abundances. In Sec. 2.5 we identify emission from cobalt, which can either be a decay product of ^{56}Ni or the neutron-rich isotope ^{57}Ni. We utilise the ratio of the Co/Fe mass produced in the explosion to test predictions of explosion models. Finally, in Sec. 2.6, we identify lines of nickel in the optical and, for the first time, in the NIR. Nickel in

the nebular phase has to be due to the neutron-rich isotope ^{58}Ni as all of the ^{56}Ni has long since decayed. We use the mass ratio of Ni/Fe to provide clear and quantitative evidence for the mass of WDs exploding as SNe Ia.

Zusammenfassung

Supernovae vom Typ Ia (SNe Ia) sind die gewaltsamen stellaren Tode von Weißen Zwergen (WDs) in engen binären Systemen, jedoch ist der physikalische Mechanismus, der zu ihrem Tod führt immer noch unklar. Aufgrund der geringen scheinbaren Helligkeit von Weißen Zwergen konnte das Vorgängersystem von SNe Ia nie direkt nachgewiesen werden. Die Eigenschaften des Vorgängersystems müssen aus subtilen indirekten Anzeichen abgeleitet werden. Es gibt zwei plausible Szenarien, die zu SNe Ia führen. Im Chandrasekhar-Kanal (M_{Ch}) akkretiert ein Weißer Zwerg Material von seinem Begleitstern, der ein Hauptreihen- oder Riesenstern oder aber ein anderer Weißer Zwerg sein kann, bis er nahe der Chandrasekhar Grenzmasse ($\sim$1.4 $M_{\odot}$) explodiert. Im Sub-Chandrasekhkar-Kanal (sub-M_{Ch}) wird die Explosion des Weißen Zwergs durch dynamische Prozesse wie Sternverschmelzungen, Doppeldetonationen oder Frontalzusammenstöße deutlich unterhalb der Chandrasekhar-Grenzmasse ausgelöst.

Ein Unterscheidungsmerkmal der SN Ia-Vorläuferszenarien ist die zentrale Dichte und damit Masse des Weißen Zwergs zum Zeitpunkt der Explosion. Kontinuierlich akkretierende M_{Ch}-Vorläufer-Modelle sagen signifikant höhere zentrale Dichten voraus ($\sim 10^9\,\mathrm{g\,cm^{-3}}$) als sub-$M_{Ch}$-Vorläufer-Modelle ($\sim 10^7\,\mathrm{g\,cm^{-3}}$). Dies wirkt sich auf den Neutronenüberschuss aus: nur Weiße Zwerge nahe der Chandrasekhar Grenzmasse erreichen die hohen zentralen Dichten, die erforderlich sind, damit in Elektroneneinfangreaktionen zusätzlich zu den in beiden Kanälen verfügbaren Neutronen, wenn der Vorläufer bereits neutronenreiches Material enthält (Vorläufer mit einer Metallizität ungleich Null), weitere Neutronen erzeugt werden können. Ein Überfluss an Neutronen ist erforderlich, um das Brennen vom Nuklearen Statistischen Gleichgewicht (NSE) – das hauptsächlich ^{56}Ni synthetisiert – auf neutronenreiches NSE (nNSE) zu verlagern, wobei neben anderen Isotopen auch stabiles Fe und Ni erzeugt wird.

Zu späten Zeiten (> 200 d nach der Explosion) wird das ausgestoßene Material für optische und NIR-Photonen vollständig transparent und der eisenhaltige Kern der Explosion wird sichtbar. In dieser Arbeit verwenden wir die Isotopenhäufigkeiten von neutronenreichem Material, das aus Nebelphasenspektren abgeleitet wurde, um die Massen der Vorläufersysteme von SNe Ia einzugrenzen.

Die Doktorarbeit ist wie folgt gegliedert: Das erste Kapitel dient als Einführung in die Beobachtung von SNe Ia, das aktuelle Verständnis des Explosionsmechanismus, die Explosionsnukleosynthese und Vorläufersuchstrategien. Im Abschnitt 2.2 wird die Physik der Nebelphase sowie unser Spektralmodell vorgestellt, das später auf die beobachteten Daten angewendet wird. Wir konzentrieren uns auf die Modellierung von optischen und Nah-IR (NIR)-Spektren zu Phasen jenseits von 200 Tagen, um sicherzustellen, dass die optischen Tiefen sehr klein sind. In Abschnitt 2.3 diskutieren wir die Bedingungen, die zu verschiedenen Arten von Linienprofilen führen, und vergleichen unsere Ergebnisse mit dem allgemein in Nebelspektren angenommenen Gaußprofil. Um die Häufigkeiten von neutronenreichen IGEs zu bestimmen, müssen wir zunächst die entsprechenden Spezies in Nebelspektren identifizieren. In Abschnitt 2.4 zeigen wir, dass optische und NIR-Nebelphasenspektren von verbotenen Linien von einfach und doppelt ionisiertem

Eisen dominiert werden. Wir zeigen, dass das Verhältnis der NIR- zu den optischen Linien als Indikator für den Plasmazustand des Materials dient – die Elektronendichte und die Temperatur – die uns helfen, die Isotopenhäufigkeiten zu bestimmen. In Abschnitt 2.5 identifizieren wir die Emission von Kobalt, die entweder ein Zerfallsprodukt von ^{56}Ni oder des neutronenreichen Isotops ^{57}Ni sein kann. Wir verwenden das Verhältnis der bei der Explosion erzeugten Co/Fe-Masse, um Vorhersagen von Explosionsmodellen zu testen. Im Abschnitt 2.6 schließlich identifizieren wir Linien von Nickel im optischen und zum ersten Mal auch im NIR Bereich. Nickel in der Nebelphase muss auf das neutronenreiche Isotop ^{58}Ni zurückzuführen sein, da das gesamte ^{56}Ni längst zerfallen ist. Wir verwenden das Massenverhältnis von Ni/Fe, um einen klaren und quantitativen Nachweis für die Masse von Weißen Zwergen zu liefern, die als SNe Ia explodieren.

Contents

List of Figures

List of Tables

List of Constants

Physical Constants:[1]

Boltzmann constant	k_{B}	$1.380\,648\,8 \times 10^{-16}\,\mathrm{erg\,K^{-1}}$
elementary charge	e	$4.803\,204\,50 \times 10^{-10}\,\mathrm{statC}$
electron mass	m_e	$9.109\,382\,91 \times 10^{-28}\,\mathrm{g}$
gravitational constant	G	$6.673\,84 \times 10^{-8}\,\mathrm{cm^3\,g^{-1}\,s^{-2}}$
proton mass	m_p	$1.672\,621\,777 \times 10^{-24}\,\mathrm{g}$
Planck constant	h	$6.626\,069\,57 \times 10^{-27}\,\mathrm{erg\,s}$
radiation constant	a_{R}	$7.565\,731 \times 10^{-15}\,\mathrm{erg\,cm^{-3}\,K^{-4}}$
speed of light	c	$2.997\,924\,580 \times 10^{10}\,\mathrm{cm\,s^{-1}}$
Stefan-Boltzmann constant	σ_{R}	$5.670\,373 \times 10^{-5}\,\mathrm{erg\,s^{-1}\,cm^{-2}\,K^{-4}}$
Thomson cross section	σ_{T}	$6.652\,458\,734 \times 10^{-25}\,\mathrm{cm^2}$

Astrophysical Quantities:[2]

solar mass	$M_\odot$	$1.989 \times 10^{33}\,\mathrm{g}$
solar radius	$R_\odot$	$6.955\,08 \times 10^{10}\,\mathrm{cm}$
solar luminosity	$L_\odot$	$3.845 \times 10^{33}\,\mathrm{erg\,s^{-1}}$
solar absolute bolometric magnitude	$m_\odot$	4.74

[1] CODATA 2014 recommended values (Mohr et al., 2012).
[2] Values taken from Allen's Astrophysical Quantities, 4th Edition (Cox, 2000).

1. Introduction

Over the course of many millennia mankind has observed the stars on the fabric of the sky on their nightly progression, foreshadowing the change of seasons and years alike. Year after year, decade after decade, heavenly bodies seemed to be moving at an unchanging pace. Only few generations in the history of mankind were fortunate enough to witness the appearance of a new star on the firmament. These events – often regarded as powerful portents by superstitious people – broke the immutable celestial cycle. Naked-eye transients, such as the supernova that was the source of the Cygnus Loop, a 15,000 year old supernova remnant at a mere distance of 800 pc, surely must have left our ancestors with wonder. The oldest written records of transient events date back nearly two millennia, carefully written down by awestruck observers. However, because of the enormous distances between Earth and even the nearest supernovae, they remained a mystery until the 20th century. Since then, scientists unveiled compelling evidence for the origin of these 'Novae stellae' - latin for 'new stars', considering the overwhelmingly vast dimensions, distances and timescales involved in their study. And yet, there are many more unknowns – secrets of Nature – for us to explore. This thesis addresses one aspect about a specific type of transient: what are the progenitor systems of SNe Ia?

1.1. Historical Supernovae

The first supernova for which written records have been found was SN 185 in the direction of Alpha Centauri, between the Circinus and Centaurus constellations. Hou Hanshu, the book of the Later Han, mentions Chinese astronomers observing a 'guest star', which is believed to be a galactic supernova (Clark & Stephenson 1975, although this is still a matter of debate – see e.g. Dickel et al. 2001; Smith 1997; Vink et al. 2006):

> *In the 2nd year of the epoch Zhongping (中 平), the 10th month, on the day Kwei Hae (癸 亥, December 7, 185 A.D.), a 'guest star' appeared in the middle of the Southern Gate (Nan Mun, asterism containing Alpha Centauri). It seemed to be as large as half a yan (bamboo mat), with scintillating, variegated colours, and it then grew smaller, until in the sixth month of the hou-year (186 A.D.) it disappeared.*
>
> *Hou Hanshu,*
> *book of the Later Han (Clark & Stephenson, 1975)*

Telescope observations in the 20th century finally found a supernova remnant in the direction of Alpha Centauri, subsequently named RCW 86. First discovered in 1961 as the radio source

MSH 1-63 (Mills et al., 1961), it was identified in 1967 as a supernova remnant with a shell-like structure and a diameter of 40 arc seconds. The age and distance to the remnant was estimated to be 2250 yrs (Vink et al., 2006) and 2.5 kpc (Sollerman et al., 2003), respectively.

Two SNe in the years 386 and 393 were also recorded by Chinese astronomers. The symmetric shell remnant with diameter 4 arc minutes G11.2-0.3 was initially associated with SN 386. From the expansion rate of the remnant nebula its age was estimated to be around 1900 years (Borkowski et al., 2016). Radio measurements of the rotational velocities and spin down rate of the pulsar at the centre of G11.2-0.3 had previously indicated a much older age of about 20,000 to 23,000 years (Torii et al., 1999). The remnant of SN 393 – RX J1713.7-3946 – was only discovered in 1996 by the ROSAT All Sky Survey.

SN 1006 was the first supernova with observations recorded from more than one set of observers from China, Japan, the Arabic world and also Europe[1]. It was the brightest SN ever observed at an apparent magnitude of -7 (Stephenson & Green, 2002), meaning it was visible during the day and could be seen on the sky for three years. From the reported sky positions and the positions of the observers on Earth it was possible to reconstruct the probable location of the SN. Coincident with the SN location is a large (∼30 arc seconds diameter) limb-brightened shell of radio emission (Reynoso et al., 2013), which was identified as the remnant of this supernova by Gardner & Milne (1965).

On July 4, 1054, a second SN within 50 years was recorded by astronomers in China, Japan and also briefly in Constantinople (Brecher et al., 1978). Pictographs/petroglyphs from Chaco Canyon in the southwestern USA show a star close to the crescent Moon. It has been suggested that this is a North American observation of SN 1054 (Miller, 1955), as the Moon was close to the supernova on July 5, 1054, waning and had the correct orientation. The remnant of this cataclysmic event was found in the 18th century by Messier (Messier, 1781) and subsequently included as the first object (Messier 1 or M 1) in his catalogue of known nebulae. Only in the 1920s has the remnant – whose name goes back to a crab-like drawing from 1844 by William Parsons, 3rd Earl of Ross – been associated with SN 1054, when Lundmark noted its proximity to the 'guest star' of 1054 (Lundmark, 1921; Hubble, 1928). At the centre of the Crab resides a Pulsar, a fast-rotating magnetised neutron star emitting electromagnetic radiation beamed at Earth (Reifenstein et al., 1969).

The third Galactic SN within two centuries was found in the sky by observers in southern China on August 6, 1181. Unfortunately, due to inaccurate historical records, the location of the SN was not well constrained. It took until 1971 for 3C 58 to be identified as the remnant of SN 1181 (Stephenson, 1971). The centre of the radio-bright remnant appears to be filled (illuminated by a pulsar, Camilo et al., 2002), making it one of the few *plerion* remnants.

Almost 400 years later, a new star which was even brighter than Venus appeared in the constellation of Cassiopeia. First seen on November 6, 1572, by European and Korean observers, this event was attributed to Tycho Brahe (Tycho's SN, thus establishing primacy to the authors

[1] Possibly the SN was also recorded in North American petroglyphs by the Hohokam in White Tank Mountain Regional Park, Arizona.

Table 1.1.: Galactic Supernovae

Supernova	Constellation	App. Magnitude	Distance	Type	Remnant
SN 185	Centaurus	roughly −4	2.8 kpc	Ia	RCW 86
SN 386	Sagittarius	+1.5	4.5 kpc	II	G11.2-0.3
SN 393	Scorpius	−0	1.0 kpc	II	RX J1713.7-3946
SN 1006	Lupus	−7	2.2 kpc	Ia	SNR G327.6+14.6
SN 1054	Taurus	−6	2.0 kpc	II	Crab Nebula
SN 1181	Cassiopeia	−0	2.8 kpc	II?	3C 58
SN 1572	Cassiopeia	−4	2.8 kpc	Ia	3C 10
SN 1604	Ophiuchus	−3	5.0 kpc	Ia	3C 358
Cas A[a]	Cassiopeia	+5	3.4 kpc	IIb	SNR G111.7-02.1
SN G1.9+0.3[b]	Sagittarius	...	7.7 kpc	Ia?	SN G1.9+0.3

[a] Cas A exploded around ∼ 1680
[b] SN G1.9+0.3 exploded around ∼ 1868

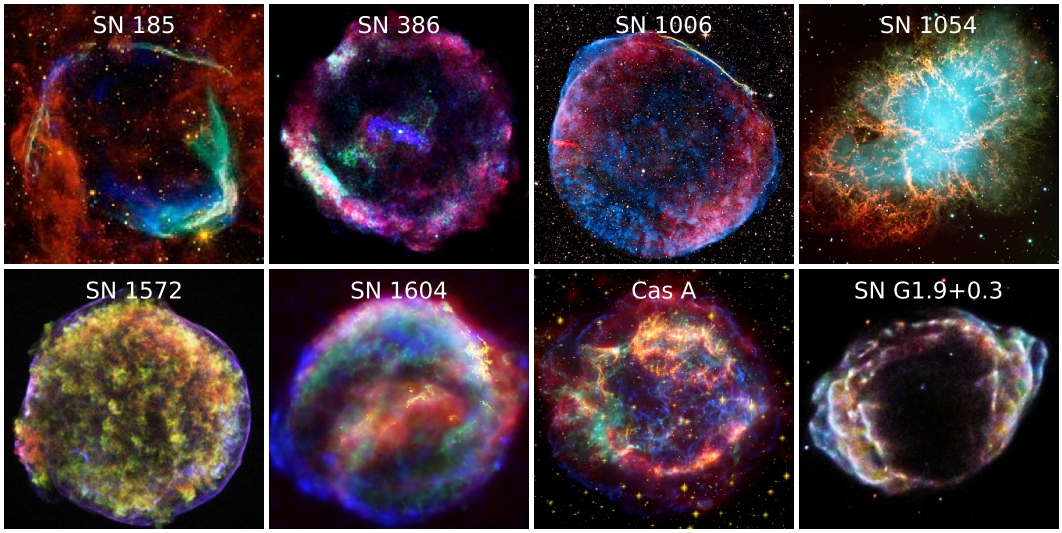

Figure 1.1.: Color-composite images of Galactic SN remnants. Image credit: *SN 185* NASA/JPL-Caltech/UCLA; *SN 386* NASA/NRAO/AUI/NSF/CXC/Eureka Scientific/M. Roberts et al.; *SN 1006* NASA/CXC/NRAO/NOAO/AURA/C&E; *SN 1054* NASA, ESA, J. Hester and A. Loll; *SN 1572* NASA/CXC/Rutgers/J. Warren & J. Hughes et al.; *SN 1604* NASA/ESA/JHU/R. Sankrit & W. Blair; *Cas A* NASA/JPL-Caltech; *SN G1.9+0.3* NASA/CXC/NCSU/K. Borkowski et al.

who publish), who did not see it until November 11, 1572. Over the course of months, Brahe repeatedly measured the brightness and location of SN 1572 relative to nearby stars with unprecedented accuracy. The observations prompted him to write a treatise *Progymnasmata*, in which he discussed SN 1572 in the context of the then accepted view of celestial mechanics (going back to the natural philosopher Aristotle). In this picture, the heavens consist of eight concentric shells. Weather phenomena and atmospheric effects, the moon and the planets all sit on the inner, moving shells. Because SN 1572 was not moving relative to the stars on the sky, Brahe concluded that it must be far beyond the moon – on the most distant eighth shell. This meant that the sky of 'fixed' stars is not constant – a world view believed by many at that time. From Brahe's notes the position of SN 1572 was known to a few arc minutes and its remnant was later identified as the bright radio source 3C 10 by Hanbury Brown & Hazard (1952). Reflections of SN light from interstellar clouds[2] were detected recently and allowed the classification of SN 1572 as a SN Ia (Krause et al., 2008).

SN 1604, also known as Kepler's SN, was first seen in Europe on October 9, 1604, by Ilario Altobelli from Verona and Raffaello Gualterotti from Florence (Shea, 2005). Kepler only noticed the object one week later on October 17, 1604. The SN was not visible by naked eye observations on October 8, 1604, when all interested in astronomy gazed the sky to observe an auspicious conjunction of Mars, Jupiter and Saturn. This places an upper limit on the explosion date when the SN was 9 magnitudes fainter than around maximum brightness ($m_{\rm max} \sim -3$, naked eye limit $m_{\rm eye} \sim 6$) at an epoch of -20 days (Stephenson & Green, 2002). SN 1604 was also observed in China and Korea and light curves from observers around the globe are in good agreement, though they do not reliably distinguish between SN types. From other arguments (mostly the chemical composition of the remnant) it is very likely that Kepler's SN was indeed a SN Ia. Johannes Kepler's name, of all astronomers, is now associated with SN 1604 because of his book *'De Stella Nova in Pede Serpentarii'* (*'On the new star in the foot of the Snake [Ophiuchus]'*), in which he describes his observations of the event. The remnant of SN 1604 – 3C 358 – was discovered by Baade (1943) and subsequently studied in Radio and X-rays.

Kepler's SN was the last observed Galactic SN, though two remnants with an age of a few hundred years have been found recently. Cassiopeia A (or short Cas A), one of the brightest radio sources in the sky, must have exploded at the end of the 17th century, though no known records of such an event exist. It is speculated that circumstellar dust cloaked the star and absorbed most of the optical emission. A light echo observed in 2005 confirmed that the event belongs to the class of SNe IIb (see Sec. 1.3.1). An even younger remnant was found in the Galactic centre (Green & Gull, 1984). Reynolds et al. (2008) estimate its age to about 110 years, suggesting that the SN exploded between 1890 and 1908. Due to strong dust obscuration along the line of sight the SN could not have been observed from Earth. In the Milky Way, nearly 300 SN remnants (SNR) have been found so far. Only for a small number of SN remnants was a light echo observed. For the vast majority of them only crude age estimates from their physical size

[2] this is a 'light echo' from the SN; the reflected light is only now arriving and thus is accessible by modern telescopes.

can be made. Historical SNe and their corresponding optical observations are still useful today as they provide early time data to well-studied remnants that is not accessible through other means.

1.2. Modern Supernovae

In modern times, we watch the night sky not only with our bare eyes, but with ever bigger telescopes, allowing us to find SNe outside our home galaxy. The first observed extragalactic SN occurred in the year 1885 and was subsequently named SN 1885. Nowadays, this event is also known as S Andromedae, as the exploding star happened to reside in the Andromeda galaxy (M31), at a mere distance of 0.77 Mpc. SN 1885 happened to be the brightest observed SN since almost 300 years ago, and with an apparent magnitude of around 6 at peak it would have been observable with the naked eye. Unfortunately, due to its small separation from the centre of M31, it was only observable using telescopes. The observations from the late 19th century have been carefully converted to modern V-band light curves by de Vaucouleurs & Corwin (1985), showing that it was a peculiar SN. The remnant of the SN explosion was only rediscovered by Fesen et al. (1989) in absorption.

From the explosion of S Andromedae to the modern term 'supernova' another 50 years passed until Baade & Zwicky established the distinction between novae and supernovae, with the latter originating from the violent deaths of stars (Baade & Zwicky, 1934). In the following years Zwicky managed to observe 14 SNe in nearby galaxies using the Mt. Palomar 18-inch Schmidt telescope. The spectral similarities between SN 1937C in IC 4182 and SN 1937D in NGC 1003 and the completely different SN 1940C in NGC 4275 may have triggered the idea that there are distinct classes of SNe. These objects were later classified by Minkowski (1941) based on their spectral appearance: objects which did not show hydrogen lines were classified as *Type I*, while objects that did have hydrogen were classified as *Type II*. An extended version of this classification scheme is still being used today (for more details see Sec. 1.3.1).

Photographic plates, as used by Baade, Zwicky and Minkowski, remained the norm until the 1970s and 1980s, when advancements in detector technologies culminated in the development of photoelectric photometers and later charge coupled devices (CCDs). Telescopes, such as the BAIT[3] (Richmond et al., 1993), which employed these new technologies could be controlled automatically. However, difference imaging for finding supernovae was still as labour intensive as it was using the previous generation of telescopes.

At the end of the 1990s observations of SNe at distances of several hundred Mpc – at redshifts which allowed astronomers to probe the expansion of the universe itself – became feasible. As

[3]Berkeley Automatic Imaging Telescope

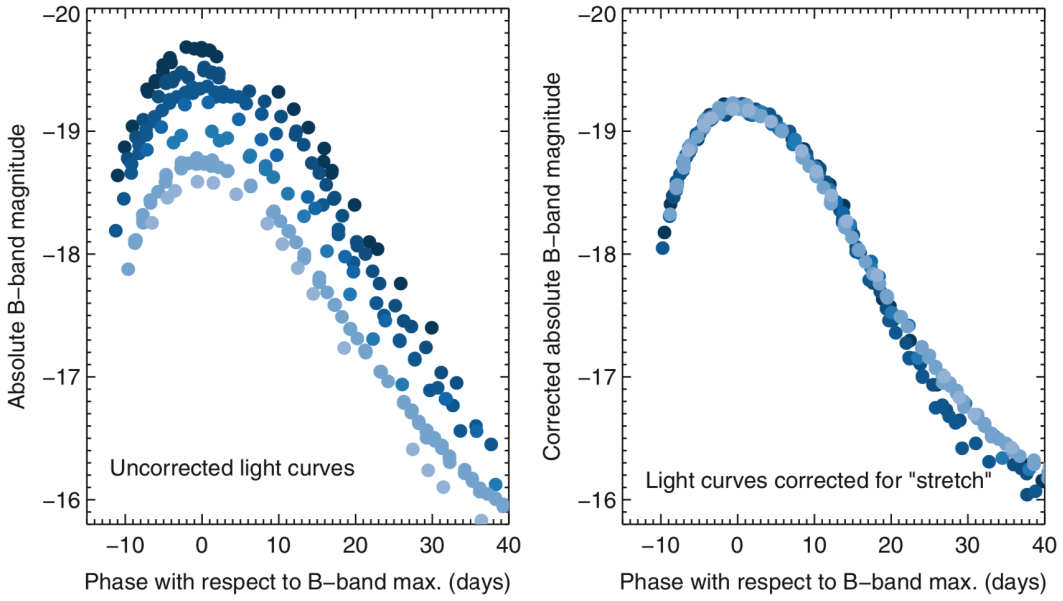

Figure 1.2.: Left: Brighter SNe reach peak luminosity and decline slower than their fainter counter parts. Right: Correcting for light curve stretch produces a 'standardised' light curve. Figure taken from Maguire (2017).

envisioned by Baade (1938), SNe Ia supernovae could finally be used as distance indicators due to their standardisable light curves (see Fig. 1.2, Pskovskii, 1977; Phillips, 1993). Two independent teams (the SCP[4] and the HZSNS[5]) measured the distance to a number of high-redshift SNe and came to the same perplexing conclusion: the expansion of the universe is accelerating (Riess et al., 1998; Perlmutter et al., 1999). In 2011, the leaders of the teams were awarded the Nobel Prize for this groundbreaking discovery.

Many new surveys were launched at the beginning of the 21st century – some of them targeting SNe exclusively, while others observed SNe as a byproduct. It comes with no surprise that the number of detected SNe has been surging exponentially for the past 30 years (see Fig. 1.3). Early surveys were mainly observing galaxies and transients therein (as the SN rate scales with the stellar mass of galaxies), but more recent programmes (ZTF[6]: Kulkarni, 2018; ATLAS[7]: Tonry et al., 2018; Pan-STARRS[8]: Chambers et al., 2016) started to observe the full accessible sky with a cadence of a few days. Upcoming surveys such as the one carried out by the Vera C. Rubin Observatory (formerly known as LSST[9]) will find more supernovae per year than have

[4]Supernova Cosmology Project
[5]High Z Supernova Search
[6]Zwicky Transient Facility
[7]Asteroid Terrestrial-impact Last Alert System
[8]Panoramic Survey Telescope And Rapid Response System
[9]Large Synoptic Survey Telescope

been found during the complete 20th century.

In addition to the unprecedented number of discovered SNe, high-cadence all-sky surveys can also find SNe mere hours after their explosion. A prominent example is SN 2011fe (PTF 11kly) in M101 (Fig. 1.4), found only 11 hours after its estimated explosion (Nugent et al., 2011a). The host galaxy of a recent transient, SN 2018oh, was observed by the K2 (successor of the Kepler mission) Supernova Cosmology Experiment (K2 SCE) starting before explosion, continuing to first light, and through peak brightness (Dimitriadis et al., 2019). To date, the light curve of SN 2018oh with its 30 minute cadence is indisputably the best-sampled pre-maximum light curve of all SNe (see Fig. 1.5). From the light curve, the epoch of first light[10] can be constrained to less than two hours, making it an exquisite probe for the rise time of thermonuclear transients.

Until the end of the 1970s, transients had been observed purely at optical wavelengths. With the advent of space-based telescopes and modern detector technologies, a broad range of the electromagnetic spectrum became accessible. A prime example of multi-wavelength (and even multi-messenger) observations was SN 1987A in the Large Magellanic Cloud (LMC). Discovered by Ian Shelton (Kunkel et al., 1987), it prompted an unprecedented number of observations by photon collecting facilities as well as opening up the field of extra-solar system neutrino astronomy. From the high-energy end of the electromagnetic spectrum (gamma-rays, X-rays, UV) through the visible to the low-energy end (IR, radio) SN 1987A continues to be observed as it evolves. For SNe such as SN 1987A, the explosion energy is carried away by neutrinos, which, on average, deposit about one percent of their energy in the ejecta, which are consecutively blasted away with velocities of up to $20000\,\mathrm{km\,s^{-1}}$. This tiny fraction of the total explosion energy is responsible for the nucleosynthesis taking place in the shock, as well as the complete electromagnetic emission of the supernova (Woosley & Weaver, 1986). The bulk of the explosion energy escapes in the form of neutrinos, of which 25 were detected on Earth (Arnett et al., 1989). Current generation neutrino detectors (Super-Kamiokande, IceCube, ANTARES, KM3NeT, KamLAND, Borexino) will be able to detect thousands of neutrinos from the next galactic core collapse SN within 10 kpc (Müller, 2019).

On 2017 August 17 a binary neutron star coalescence candidate (later designated GW170817) was observed through gravitational waves by the Advanced Laser Interferometer Gravitational Wave Observatory (LIGO) and Advanced Virgo detectors (Abbott et al., 2017). Gravitational waves, as predicted by the general theory of relativity (Einstein, 1918), are produced by objects whose motion involves acceleration and its change, provided that the motion is not perfectly spherically symmetric or rotationally symmetric. So far, gravitational waves have only been directly observed from merging black holes (BHs) or neutron stars (NSs), though they are also

[10] In SNe Ia the time it takes for the shock wave to penetrate the surface is only a few seconds due to the small size of the WD. As a result, the explosion time is essentially the same as the shock breakout or first light time.

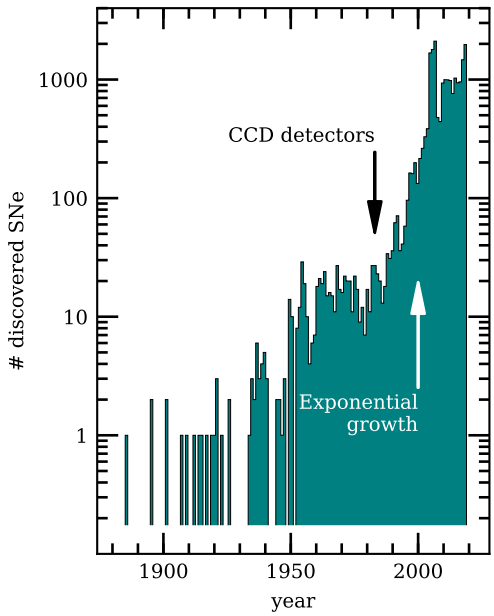

Figure 1.3.: Histogram of discovered SNe from the end of the 19th century until 2020. Data taken from the Transient Name Server (TNS)[12].

Figure 1.4.: SN 2011fe in M101, one of the closest SNe in recent times, outshining an entire galaxy. (B. J. Fulton/LCOGT/PTF)

expected from the inspiral of white dwarfs (WD)[11]. Core collapse SNe will produce a burst of gravitational waves whose shape will depend on the ejecta asymmetries due to hydrodynamical instabilities. Because of the lower frequency of their gravitational wave emission, binary WD systems cannot be detected with ground-based detectors. Future space-based interferometers (e.g. Laser Interferometer Space Antenna (LISA)) will allow us to estimate the rate of in-spiralling WDs, which are potential progenitors of SNe Ia.

1.3. Observed SNe Ia

1.3.1. Supernova Classifications

After the discovery of SN 1940C, which had a spectrum that was 'entirely different from that of any nova or supernova previously observed' (Minkowski, 1940), it became evident that there

[11] The emission of gravitational waves was inferred from the decay of the orbit of the Hulse-Taylor pulsar (Weisberg et al., 1981).
[12] https://wis-tns.weizmann.ac.il/

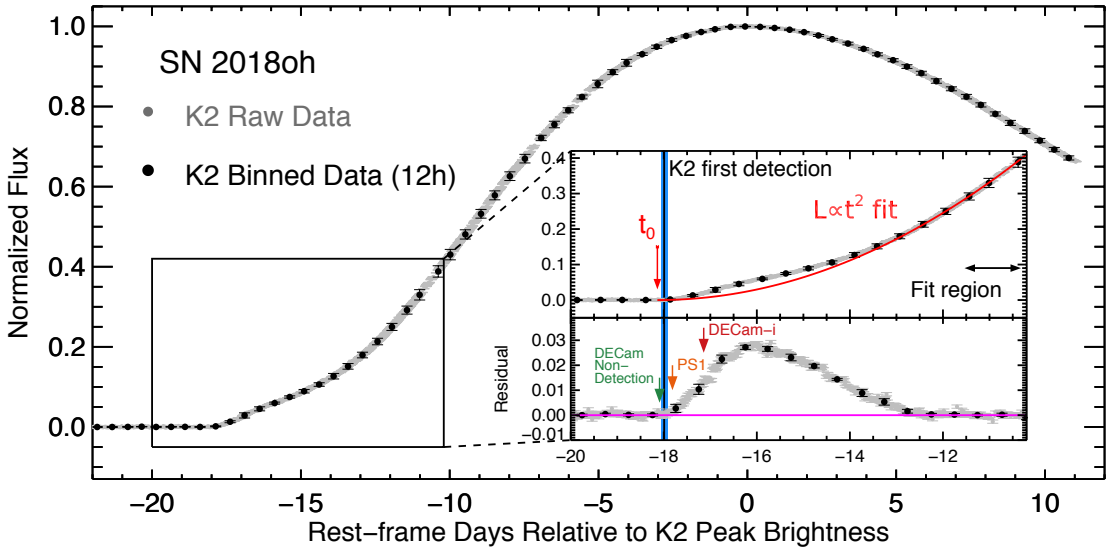

Figure 1.5.: Normalized SN 2018oh K2 light curve with respect to peak brightness. Unbinned K2 photometry and data averaged over 12 hours are shown as grey and black points, respectively. The K2 light curve is pseudo-white light ($\lambda_{\rm eff} = 5982.3$Å, $\lambda_{\rm min} = 4184$Å, $\lambda_{\rm max} = 9050$Å) and thus not sensitive to UV light. In the inset's upper panel, the light curve from 20 to 10 days before peak brightness is shown. Taken from Dimitriadis et al. (2019).

were at least two types of SNe (Minkowski, 1941) which Minkowski classified as type I and type II. The larger and more homogeneous group (9 out of 14 objects) being designated as type I and the remaining objects as type II. Minkowski would possibly be amused to know that this basic classification system is still being used today. SNe whose spectra contain hydrogen lines are now called type II and those without any hydrogen lines in their spectra are called type I. Due to the growth of SNe discovered (see Fig. 1.3) a more diverse/exact scheme was required. Zwicky made an attempt at adding the types III, IV and V, which was based on the light curve shape instead of spectral properties (Zwicky, 1964). Nowadays, these objects fall under the category of type II: supernovae exhibiting a plateau in their light curve are called type IIP, those that show a linear decline in their light curve are of type IIL (e.g. Harkness & Wheeler, 1990). Type IIb supernovae fall between type Ib/c and type II SNe, as their early spectra show strong hydrogen lines but their late time spectra resemble those of type Ib/c. SN IIn show narrow emission lines (predominantly hydrogen) and, in addition, evolve much more slowly than other SNe II.

In the 1980s it was discovered that while almost all SNe I show a broad Si II line at 6150 Å, interestingly, few lacked this line. Silicon-less objects were further divided into groups that show helium – SNe Ib – and those that do not show any helium lines (SNe Ic). Supernovae which contain silicon – the classical SNe I – are classified as SNe Ia. SNe Ia are considered to arise from thermonuclear explosions of WD stars, while all other supernovae (Ib/c, II) are thought to be the result of the collapse of the iron core into a neutron star or black hole in massive stars at the end of their life. Missing H- and He- lines in type Ib/c SNe are attributed to the loss of their

H- (Ib) or H/He-shells (Ic). Thus, these classes would be the result of a core collapse event in Wolf-Rayet stars or in stellar binaries. So far, for ~ 35 core-collapse SNe progenitors have been identified in archival (mostly HST) images of their host galaxies (e.g. Ryder et al., 1993; Van Dyk et al., 1999)[13].

For type Ia SNe, however, no progenitor system has been found to date. In contrast to core-collapse SNe, which are only found in late-type, star forming galaxies, SNe Ia are found in both young and old stellar populations. They occur in a variety of galaxy types, from dwarf irregular galaxies to giant elliptical galaxies and also spiral galaxies. The absence of hydrogen and helium in the ejecta and the composition of the ejecta (mostly intermediate mass elements in the outer layers and iron group elements in the core) require a very particular progenitor system. The standard picture is that SNe Ia are the explosions of WD stars in binary systems.

Properties of SNe Ia seem to depend on metallicity, star-formation rate, age and morphology of their hosts (Hamuy et al., 1996, 2000; Sullivan et al., 2006). Faint SNe Ia occur preferentially in old – probably metal poor – populations, while brighter ones are connected with younger populations and oftentimes even ongoing star formation. Interestingly, star forming galaxies host roughly ten times more thermonuclear SNe than 'dead' galaxies (Mannucci et al., 2005; Sullivan et al., 2006). Some of these properties (stellar age, star formation, metallicity) could influence the environment of the progenitor system, but it remains unclear if this is due to a different delay time distribution or intrinsic effects on the progenitor system such as metallicity, or both. Over the last decade studies have suggested that there are at least two delay time channels: a prompt ($t_{\mathrm{DTD}} < 0.4\,\mathrm{Gyr}$) and a tardy ($t_{\mathrm{DTD}} > 2.4\,\mathrm{Gyr}$) delay time distribution (Maoz et al., 2011; Brandt et al., 2010). The tardy channel might be affected by the changing metallicity with cosmic time (Meng et al., 2011).

WDs are a common result of stellar evolution and therefore an effective parent population for SNe Ia. For every solar mass formed approximately 0.22 WDs are born, with the remaining mass being bound in long-lived low-mass stars. The rate of thermonuclear SNe remained fairly constant over cosmic time at 0.0023 ± 0.0006 per solar mass of stars formed (Mannucci et al., 2005; Maoz et al., 2011). To maintain such a constant rate about one percent of all WDs are expected to end their lives as a SN Ia.

1.3.2. The Zoo of SNe Ia

Even though SNe Ia have been used as cosmological probes, relying on the fact that they are a very homogeneous population (Branch & Tammann, 1992), a number of peculiar events have been recorded. The need for subclasses first became apparent in 1991 when the two peculiar SNe Ia supernovae SN 1991bg and SN 1991T were discovered (Branch et al., 1993). Today, numerous subclasses of SNe Ia have been defined (for a detailed summary see Taubenberger, 2017), and upcoming wide field surveys such as the LSST (Large Synoptic Survey Telescope) are expected to discover even more peculiar events. For the vast majority of subclasses it remains unknown

[13] For a comprehensive list see Van Dyk (2017).

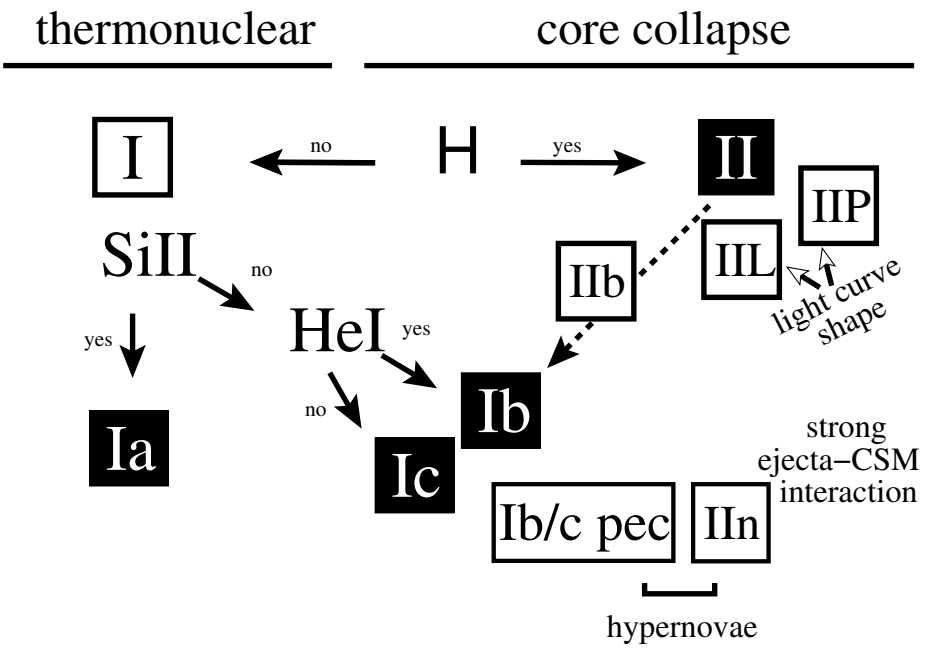

Figure 1.6.: Supernova classification scheme by Turatto (2003).

whether their progenitor systems / explosion mechanisms form a continuum (peculiar SNe Ia being extreme explosions starting from the same initial conditions) or whether the diversity is the result of different populations. It is evident that the classification scheme is currently in philatelic mode and the explosion models are not keeping up. It is possible that there is an over abundance of enthusiasm for new classes on an underlying continuum or that the current suite of explosion scenarios is very incomplete, or both.

This controversy is also depicted in different naming schemes that have been developed over the last three decades. Traditionally, subclasses were named after a prototypical event (e.g 86G-likes, 91T-likes, 91bg-likes). With the detection of an ever increasing number of transients of each subclass, peculiarities and similarities within these subclasses became apparent (see Fig. 1.10 for a comparison of the various subclasses). Gal-Yam (2017), among others, suggested a naming scheme that focuses on observational properties (e.g. the strength of the silicon absorption feature at early times). The focus of this thesis lies on the 'normal' population of SNe Ia. In the rare cases that peculiar SNe Ia are mentioned the traditional prototypical naming scheme is used.

Normal SNe Ia:

In a volume limited sample, the fraction of SNe Ia classified 'normal' is approximately 70% (see Fig. 1.8; Li et al., 2011b). These 'normal' supernovae reach a peak luminosity of $M_{\mathrm{B_{max}}} \approx -19.05 \pm 0.38$ (Hamuy et al., 1996).

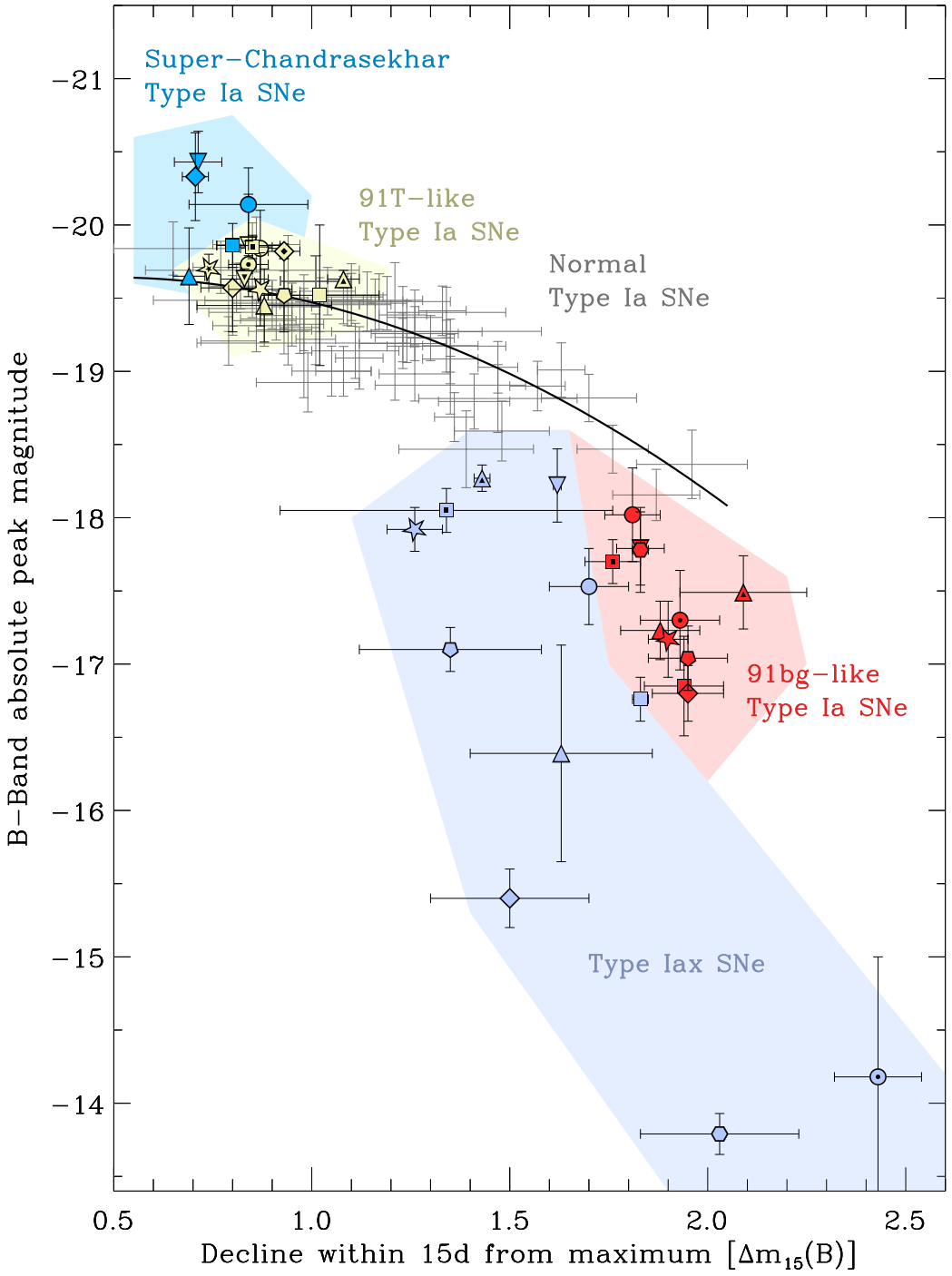

Figure 1.7.: Phase space of potentially thermonuclear transients. The absolute B-band magnitude at peak is plotted against the light-curve decline rate, expressed by the decline within 15 d from peak in the B-band, Δm_{15}(B)(Phillips, 1993). Most of the subclasses are well separated from normal SNe Ia in this space, which shows that they are already peculiar based on light-curve properties alone. The only exception are 91T-like SNe, which overlap with the slow end of the distribution of normal SNe Ia, and whose peculiarities are almost exclusively of spectroscopic nature. Adapted from Taubenberger (2017).

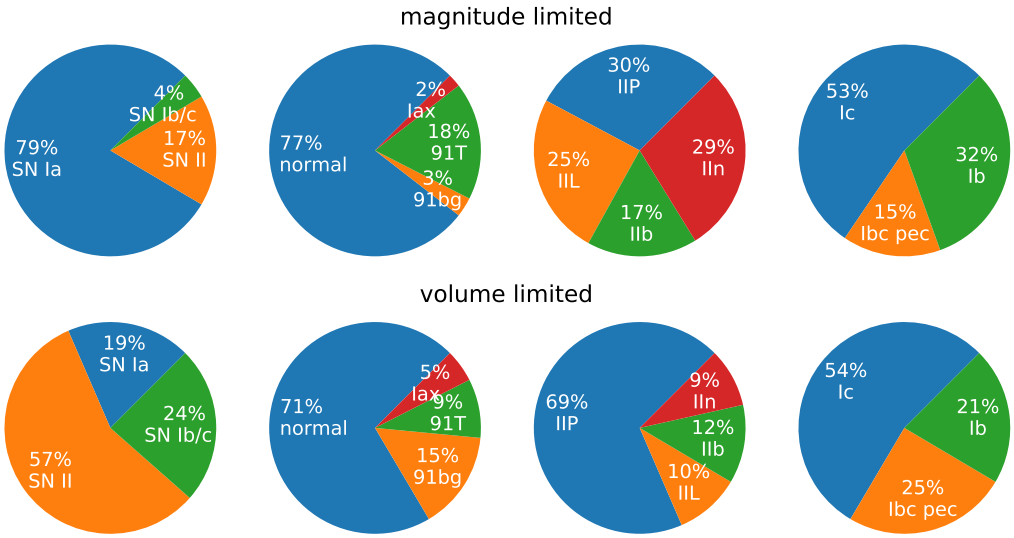

Figure 1.8.: SN subclass fraction for purely magnitude and volume limited searches as determined by LOSS[14](Li et al., 2011b). From left to right: fraction of SNe Ia, SNe Ibc and SNe II; fraction of most common subclasses of SNe Ia; fraction of most common subclasses of SNe II, fraction of subclasses of SNe Ibc.

For the purposes of this introduction a simplified description of the physics of the SN Ia optical display follows: A WD at or a bit below the Chandrasekhar limit may be triggered to explode through a thermonuclear runaway process. The mechanism for the trigger remains a subject of active research. The energy released in the explosion completely disrupts the progenitor resulting in a homologous expansion of the ejecta. The explosion of the WD is powered by the burning of the progenitor to iron group (IGEs) and intermediate mass elements (IMEs). Burning to Nuclear Statistic Equilibrium results in large amounts ($0.3 - 0.9\,\mathrm{M}_\odot$) of radioactive ^{56}Ni being produced. The deposition of the decay products of the ^{56}Ni power the electromagnetic display of the supernova by heating the ejecta with two distinct phases: a diffusion dominated phase early on when the ejecta are optically thick followed by a long exponential tail from the decay of ^{56}Co as the ejecta cool and expand to become optically thin. The red and near-infrared light curves after maximum light exhibit a second peak which is attributed to changes in the ionisation structure of the ejecta. The early spectra are dominated by continuum emission with P-Cygni line profiles superimposed whereas the nebular spectrum is largely continuum free and dominated by Doppler broadened emission by forbidden lines. These effects shall be discussed further in this introduction.

It has been found that more luminous objects have broader light curves, while the faint population of SNe Ia has narrower light curves. Light curve widths are mainly determined by the diffusion time scale, which, in turn, depends on the temperature and the ejecta opacity (most of the opacity is due to IGEs). Objects that produce more IGEs have higher opacities and thus,

longer diffusion timescales, broadening their light curves. The peak brightness is a direct measurement of the ^{56}Ni mass produced in the explosion (Arnett, 1982). The correlation between the peak brightness and the width of the light curve is known as the Phillips relation (Phillips, 1993). It links the maximum B-band brightness with the decline rate of the light curve within 15 days after maximum light. This empirical relation may simply be a property of a homogeneous class of objects ('normal' SNe Ia) or an outcome of the explosion physics.

Since the initial Phillips relation, alternatives for measuring the width of the light curve (x_1, Δ and s) have been proposed, in addition to information from the light curve shape and multiple filter bands (Riess, 1996; Jha et al., 2007; Guy et al., 2005; Conley et al., 2008). In principle, some sort of $\Delta m_{15}(B)$ vs $M_{B,max}$ relation may be obtained for both explosions near the Chandrasekhar mass and significantly below. In the first case, the relation requires more centrally located ^{56}Ni bubbles for less luminous objects. In the second case, the relation is purely driven by the varying mass of the exploding WD.

The light-curve width-luminosity relation (Phillips relation) makes it possible to 'standardise' SNe Ia (see Fig. 1.2), reducing the scatter in B-band from ~ 0.38 to ~ 0.02 mag. This development enabled the use of SNe Ia as probes for precision cosmology.

Subluminous fast-decliners (91bg-like SNe Ia):

91bg-like SNe have a significantly lower luminosity compared to normal SNe Ia. At peak these objects are 1.5–2.5 mag fainter in the optical bands than their normal counterparts. For 91bg-like SNe, ^{56}Ni masses between $\sim$0.05 and $\sim$0.10 $M_\odot$ (Mazzali et al., 1997; Sullivan et al., 2011) are routinely determined using Arnett's rule (see previous section). Their light curves decline rapidly after the peak as characterised by a decline parameter $\Delta m_{15}(B)$ of 1.8–2.1. 91bg-like supernovae are also fainter in the near-infrared than normal SNe Ia supernovae by about 0.5–0.7 mag (Garnavich et al., 2004; Krisciunas et al., 2009). It is noteworthy that normal SNe Ia are very homogeneous in the infrared (Krisciunas et al., 2004; Cormier & Davis, 2011).

Although 91bg-like objects were identified through their spectroscopic peculiarities (Filippenko et al., 1992a; Leibundgut et al., 1993; Mazzali et al., 1997) the spectrum formation and evolution is not that different from the canonical ones. At early phases ($t < t_{max}$) their spectra are shaped by intermediate-mass elements (IME). After peak brightness Fe and Co lines are apparent in the spectrum as the line-forming region recedes into the Fe-rich core of the SN, though the transition from IME to IGE dominated spectra occurs earlier in 91bg-like SNe than in normal SNe Ia. The chemical stratification in both classes seems comparable, though in very early spectra no sign of outward-mixing of IGE can be seen in 91bg-like objects.

91bg-like SNe are typically found in massive elliptical or S0 galaxies, with only few exceptions being located in spiral hosts – though these have spectral features similar to elliptical galaxies (Gallagher et al., 2005). Star-formation rates of 91bg-like host galaxies are extremely low with less than $10^{-9}\,M_\odot\,\mathrm{year}^{-1}$. 91bg-like SNe are relatively common in the local universe with relative

fractions between 6% (Silverman et al., 2012a) and 15% (see Fig. 1.8, Li et al., 2011b) of all SNe Ia. In a purely magnitude limited sample their numbers are much lower due to Malmquist bias.

Nebular spectra of 91bg-like objects exhibit strong emission lines of [Fe II] and [Ca II] $\lambda\lambda$ 7291, 7324, suggestive of a comparatively low degree of ionisation at least in the inner emitting region. Superimposed upon broad ($\sim$ 7000km s^{-1} FWHM) singly ionised forbidden lines of iron are narrower (FWHM = 2000–4000 km s^{-1}) [Fe III] and [Co III] lines whose strength strength gradually increases compared to the singly ionised lines (Turatto et al., 1996b; Mazzali et al., 1997). The narrowness of the doubly ionised lines combined with their near zero systemic velocity indicates that they originate from the very centre of the ejecta.

Transitional Objects (86G-like SNe Ia):

The light curves of 86G-like SNe decline fast (typical Δm_{15}(B) around 1.8), and peak at magnitudes halfway between normal and 91bg-like SNe Ia ($M_{B,max} \sim -18$, corresponding to ^{56}Ni masses of about 0.2 $M_\odot$). In contrast to true 91bg-like objects, 86G-likes do show double-peaked NIR light curves. However, the secondary peaks are weak and appear within days after the first peak. While transitional objects are fainter than normal SNe Ia (but brighter than 91bg-likes), their NIR peak magnitudes are similar to those of normal SNe Ia allowing their use as NIR standard candles (Wood-Vasey et al., 2008; Krisciunas et al., 2009; Kattner et al., 2012).

Not only their light curves but also spectra of 86G-like objects show features half way between normal and 91bg-like SNe. Their maximum-light spectra are driven by a low degree of ionisation as can be seen from the strong Si II λ 5972 but very weak Ti II lines compared to 91bg-like objects. At nebular epochs, transitional objects show singly and doubly ionised IGEs at velocities similar to (or slightly below) those of normal SNe Ia. Especially lines of [Fe III] are in stark contrast to the narrow emission lines seen in 91bg-like objects (Mazzali & Hachinger, 2012). By virtue of sharing properties with both the 91bg-like and the normal SNe Ia, transitional objects may play an important role in determining the progenitor system of thermonuclear explosions. It remains unclear whether they are 'more efficient' 91bg-like objects and thus simply the tail of normal SNe Ia, or an independent class. Due to their similarities, 86G-like SNe are merged with 91bg-like SNe in Fig. 1.7.

Broad and Bright SNe Ia (91T-like SNe Ia):

These supernovae are brighter by about $\sim 0.4 - 0.5$ mag (Jeffery et al., 1992; Mazzali et al., 1995; Sasdelli et al., 2014) compared to normal SNe Ia and their light curves decline more slowly with rates Δm_{15}(B) between 0.8 and 1.0 (Ruiz-Lapuente et al., 1992; Filippenko et al., 1992b). While normal SNe Ia produce on average $\sim 0.5\,M_\odot$ of ^{56}Ni, 91T-like SNe produce between 0.7 and $\leq 1.4\,M_\odot$. Although the class encompasses all bright objects that resemble the prototypical SN 1991T the distribution is skewed towards the lower end of nickel masses around $0.8\,M_\odot$. Aside from the slow decline rates, which are also observed for the bright end of normal SNe Ia, their light curve morphology resembles those of normal SNe Ia. In 91T-like objects, the secondary

maxima in the IR are especially bright compared to normal objects. Due to their brightness they are common in high-redshift samples (Li et al. (2011b) estimate 18% in magnitude limited surveys), and are actually favoured by Malmquist bias. Interestingly, 91T-like SNe are almost exclusively found in late-type star-forming galaxies (Li et al., 2011b) and thus associated with younger stellar populations.

91T-like SNe show a continuum of properties with normal supernovae, especially after maximum light. In contrast to normal SNe Ia IME lines of Si II, S II, Mg II and Ca II only appear around maximum light in 91T-like SNe and are absent at earlier epochs (Branch et al., 1993). Pre-maximum spectra only exhibit a blue continuum with two absorption features of Fe III ($\lambda\lambda\,4250, 4950$) superimposed (Sasdelli et al., 2014). The presence of these lines and the strong absorption in the UV has been argued (Sasdelli et al., 2014) to indicate that 91T-like SNe contain ^{56}Ni in the outer layers.

During the transition into the nebular phase differences between 91T-like and normal SNe begin to diminish. Spectra are dominated by [Fe III] and [Fe II], albeit with slightly broader emission profiles which again indicate a bigger-than-usual emission region.

Bound remnant SNe (02cx-like SNe Ia or SNe Iax):

While most classifications of SNe Ia are based on the presence or timing of the particular spectral features, the 02cx-like objects are identified by their expansion velocity, typically measured in the trough of the Si II P-Cygni profile. Normal SNe Ia exhibit much higher expansion velocities of $> 10,000\,\mathrm{km\,s^{-1}}$ than 02cx-like SNe (between $\sim 2,000$ and $\sim 6,000\,\mathrm{km\,s^{-1}}$). Light curves of 02cx-like SNe can vary significantly between objects, but generally rise faster (10 to 20 days) and decline more slowly ($\Delta \mathrm{m}_{15}(\mathrm{R}) \sim 0.7$) than normal SNe Ia (Magee et al., 2016). They produce only very little ^{56}Ni (few 10^{-3} to $0.3\,\mathrm{M}_{\odot}$) but cover a wide range of luminosities ($M_V \sim -13$ to $M_V \sim -19$).

02cx-like SNe can be found in environments similar to those of 91T-likes: late-type, star forming galaxies (Foley et al., 2009; Perets et al., 2010). The luminosity distribution of 02cx-like SNe is skewed towards the faint end of the distribution, thus making it difficult to find them. The rate of bright 02cx-like SNe is estimated to lie between 2% and 10% of the SNe Ia rate (Li et al., 2011b; Foley et al., 2013; Graur et al., 2017).

In 2012, a potential He-donor star was found in archival data at the location of SN 2012Z (see Fig. 1.9; McCully et al., 2014). If this is indeed the companion of the exploded WD then it would be the first detection of a progenitor system of a thermonuclear SN. Based on this finding and 3D-explosion models Fink et al. (2014) concluded that 02cx-like SNe are likely deflagrations of WDs approaching the Chandrasekhar mass ($\mathrm{M_{Ch}}$). In the simulations the subsonic deflagration results in an explosion which is too weak to unbind the WD (Jordan et al., 2012; Kromer et al., 2013a; Fink et al., 2014) and leaves a remnant behind. The class of 02cx-like SNe has subsequently been named 'failed SNe'.

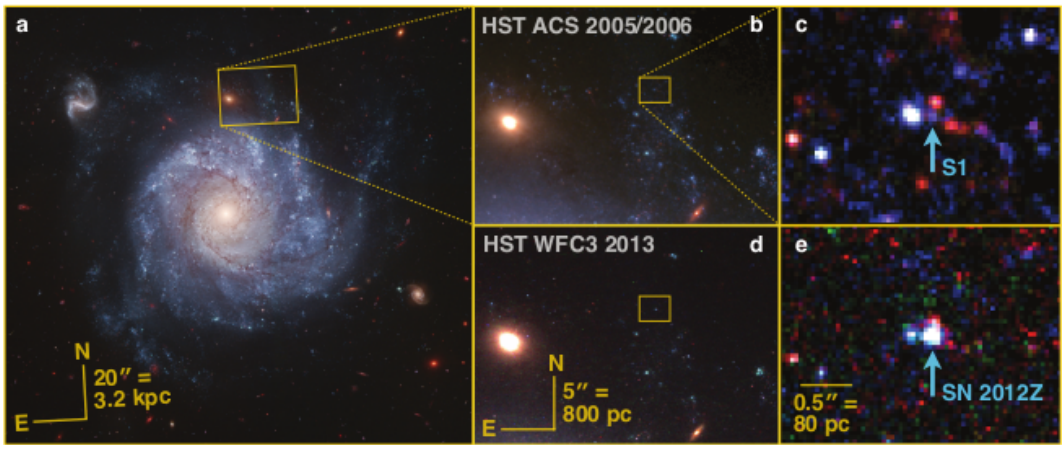

Figure 1.9.: Potential discovery of the progenitor system of the 02cx-like SN 2012Z in NGC 1309 taken in 2005 and 2006 with HST ACS. *Upper panels* b) and c) show a zoom in on the region containing the potential He-star donor to a WD. *Lower panels* d) and e) present the region after the SN explosion. Taken from McCully et al. (2014).

Superchandrasekhar SNe Ia:

For thermonuclear transients, which are believed to originate from exploding WDs, the Chandrasekhar mass limit ($\sim 1.38\,M_\odot$; e.g. Nomoto et al., 1984[15]) determines the threshold when self-gravity exceeds the degeneracy pressure of the relativistic electron gas and a collapse is unavoidable (though rotation might be able to stabilise the WD beyond this limit, see Yoon & Langer, 2005). 'Super-Chandrasekhar' SNe Ia (e.g. 2009dc (Yamanaka et al., 2010) and SN 2012dn (Chakradhari et al., 2014)) seem to show ejecta masses that are much bigger than the Chandrasekhar mass as well as ^{56}Ni masses close to or above the Chandrasekhar mass. 'Super-Chandrasekhar' SNe Ia are thought to be thermonuclear explosions as their light curve shape is quite similar to that of normal SNe Ia as they peak a few weeks after the explosion and over a few months settle on the radioactive tail determined by ^{56}Co decay. Owing to the seemingly higher ejecta masses the evolution is much slower than that of all other subclasses, with rise times between 21 and 25 days (normal SNe Ia have ~ 18.5 days) and $\Delta m_{15}(B)$ between 0.7 and 0.9 (Silverman et al., 2011; Taubenberger et al., 2011). Combining the slow light curve evolution with the fairly bright peak magnitudes would result in ^{56}Ni masses that exceed the Chandrasekhar mass limit (e.g $1.6 - 2.2\,M_\odot$ for SN 2007if; Scalzo et al., 2010).

Spectroscopically, 'super-Chandrasekhar' SNe are dominated by IMEs and unburnt material at early phases. Singly ionised carbon lines, which are only visible for a short period after the explosion in normal SNe Ia, can be seen for about one month (Silverman et al., 2011; Taubenberger et al., 2011; Chakradhari et al., 2014). Spectra are dominated by a high UV flux which

[15]The original idea goes back to Chandrasekhar (1931, 1935). At the time it was believed that WDs are largely comprised of heavy elements (Stoner, 1930) with mean molecular weight $\mu_e \approx 2.5$ (where $\mu_e = 1/Y_e$), resulting in a limiting mass of $0.91\,M_\odot$.

is the result of negligible line-blanketing from IGEs, contrary to normal SNe Ia which emit very little flux in the UV. Low ejecta velocities as inferred from Si II indicate a low kinetic energy per unit mass.

Nebular spectra of 'super-Chandrasekhar' show the same lines of Fe II, Fe III and Co III just as normal SNe Ia do. Owing to the low ejecta velocities some of the usually blended lines are partially resolved. The nebular ionisation is also lower than in normal SNe Ia as measured from the relative strength of [Fe III] and [Fe II] lines (Silverman et al., 2011; Taubenberger et al., 2013).

1.3.3. Spectrum Formation

Light curves give insights into the brightness evolution of a transient, which was used by Pankey (1962) to deduce that SNe Ia are powered by the decay of radioactive ^{56}Ni to ^{56}Co to finally ^{56}Fe. SN spectra are typically classified as photospheric and nebular. The source of the opacity for the photosphere is a mixture of scattering and line blanketing. In SNe Ia line opacity is particularly important enabled by the large Doppler broadening of many lines and a pseudo continuum is emitted. Atoms in the direction of the observer above the photosphere scatter the light out of the line of sight while atoms not in the direction of the observer scatter the light into the line of sight. The spectrum thus exhibits a continuum with P-Cygni profiles superimposed. As time goes by the ejecta expand and become ever more optically thin. In this process, the photosphere recedes inwards to lower velocities. Once the central region of the supernova becomes optically thin the SN evolution enters the nebular phase. The spectrum is no longer dominated by absorption lines superimposed on a continuum but instead emission lines shape the spectrum.

Pre-Maximum Phase

The pre-maximum phase of SNe Ia is defined by very high line velocities (of order 15,000 km s^{-1}), indicating that the photosphere engulfs almost the whole ejecta. As the photosphere recedes deeper into the ejecta the line velocities are decreasing. The spectrum is dominated by P Cygni-profiles, which show an emission peak at the line rest wavelength and an additional blue-shifted absorption feature. P Cygni profiles can be seen for a variety of IMEs and IGEs. IMEs are the burning ashes from the outer layers where burning to NSE is incomplete. Unburnt material from the progenitor, such as carbon, can also be seen during the very early epochs in the evolution of a thermonuclear SN (e.g. Nugent et al., 2011b), providing additional evidence for the explosion of a WD.

Most SNe Ia observed during the pre-maximum phase show high-velocity features of Ca II (and less often Si II). Such features are defined by originating significantly above the photospheric line component of the same element with typical expansion velocities of $> 15,000$ km s^{-1}. The most common occurrence of high-velocity Ca II is in the Ca NIR triplet feature (8498, 8542, 8662 Å). The strong Ca II H&K lines are strongly contaminated by other features and it is thus hard

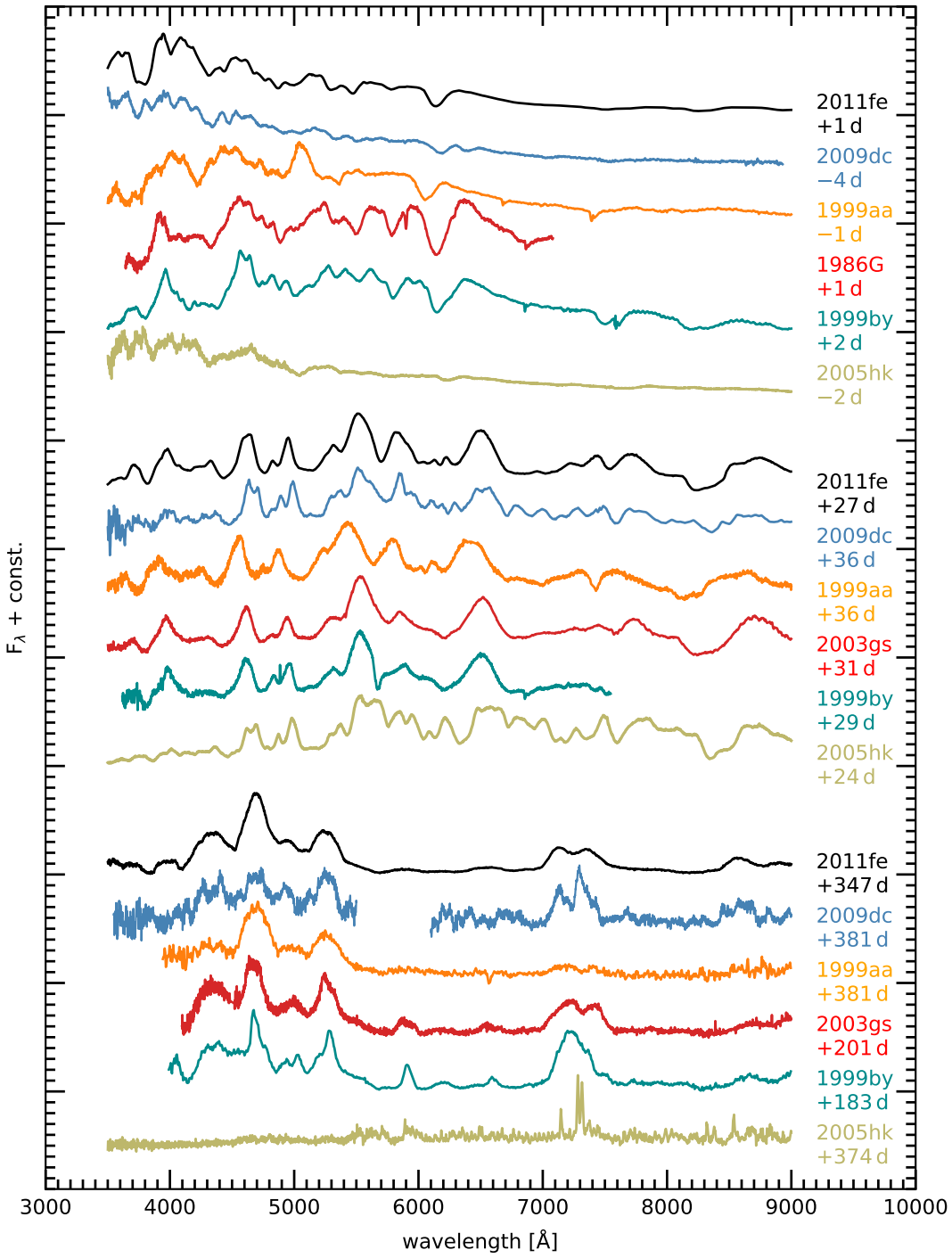

Figure 1.10.: Overview and comparison of the normal SN 2011fe (Mazzali et al., 2014, 2015), 'super-Chandrasekhar' SN 2009dc (Taubenberger et al., 2011, 2013), 91T-like SN 1999aa (Garavini et al., 2004; Silverman et al., 2012a), 86G-like SN 1986G (Cristiani et al., 1992) and SN 2003gs (Silverman et al., 2012a), 91bg-like SN 1999by (Matheson et al., 2008; Silverman et al., 2012a) and Iax SN 2005hk (Silverman et al., 2012a; Blondin et al., 2012) at early (top), post-maximum (centre) and nebular phases (bottom). The strongly extinguished spectrum of SN 1986G has been de-reddened using E(B-V)=0.5 and R_V=3.1 (Phillips et al., 1999).

to unambiguously determine the presence of fast moving material. The origin of high-velocity features is not well understood, though according to several studies (Hatano et al., 2001; Gerardy et al., 2004; Thomas et al., 2004; Mazzali et al., 2005; Quimby et al., 2006; Tanaka et al., 2006; Nugent et al., 2011b) they may either be due to illumination of calcium in the CSM or fast moving clumps of ejecta with intrinsic abundance enhancements.

Maximum Light

Roughly ten days after the explosion the photosphere recedes into a layer containing IGEs, but the spectra are still dominated by IMEs. It is at this epoch that the trademark features of SNe Ia are visible: prominent absorption features from Si II 6355 Å, Si II 5972 Å and Si II 4130 Å. Small amounts ($\sim 10^{-2} M_{\odot}$) of Ca II lead to the formation of strong Ca II lines. Around maximum brightness, the photospheric velocity has decreased to between $8000 - 15000\,\mathrm{km\,s^{-1}}$. In some cases, high-velocity features can still be seen at maximum light, but their velocities are rapidly decreasing with time. Even in the 'normal' population of SNe Ia become spectral differences apparent. Most of them, however, are the result of small variations in temperature and ionisation state. Nugent et al. (1995) discovered that the ratio of Si II 6355 Å compared to Si II 5972 Å serves as a tracer of these physical parameters, with stronger Si II 6355 Å compared to Si II 5972 Å occurring in hotter objects. An overview of the spectral diversity of normal SNe Ia is given in Fig. 1.11.

Post-Maximum Phase

After maximum light the SN spectrum is increasingly shaped by IGEs. Several days after maximum Fe lines begin to emerge, and within two weeks, completely dominate the spectrum. At this point, the photospheric velocity has dropped to less than $8000\,\mathrm{km\,s^{-1}}$. Traces of IMEs can still be seen, although over the course of several weeks, they will fade into oblivion. After maximum the optical bands are dimming. In the NIR a re-brightening (second NIR maximum) is observed (Elias et al., 1981), whose timing was shown to correlate with the intrinsic brightness of the SN (Hamuy et al., 1996; Nobili et al., 2005). Pinto & Eastman (2000) and Kasen (2006) successfully demonstrated that the emissivity of iron and cobalt gas peaks at temperatures of $\sim 7000\,\mathrm{K}$, when recombination from doubly to singly ionised species takes place. The epoch of the secondary NIR maximum is therefore a measure of the time when this critical temperature is reached in the iron-rich ejecta.

Nebular Phase

Roughly half a year after the explosion the outer layers of the SN have become transparent. At this point all of the ejecta can be seen at the same time. The spectrum is now characterised by strong emission lines of mostly IGEs from the very centre of the explosion, with velocities ranging between $6000\,\mathrm{km\,s^{-1}}$ (singly ionised material) to $11000\,\mathrm{km\,s^{-1}}$ (doubly ionised material). During

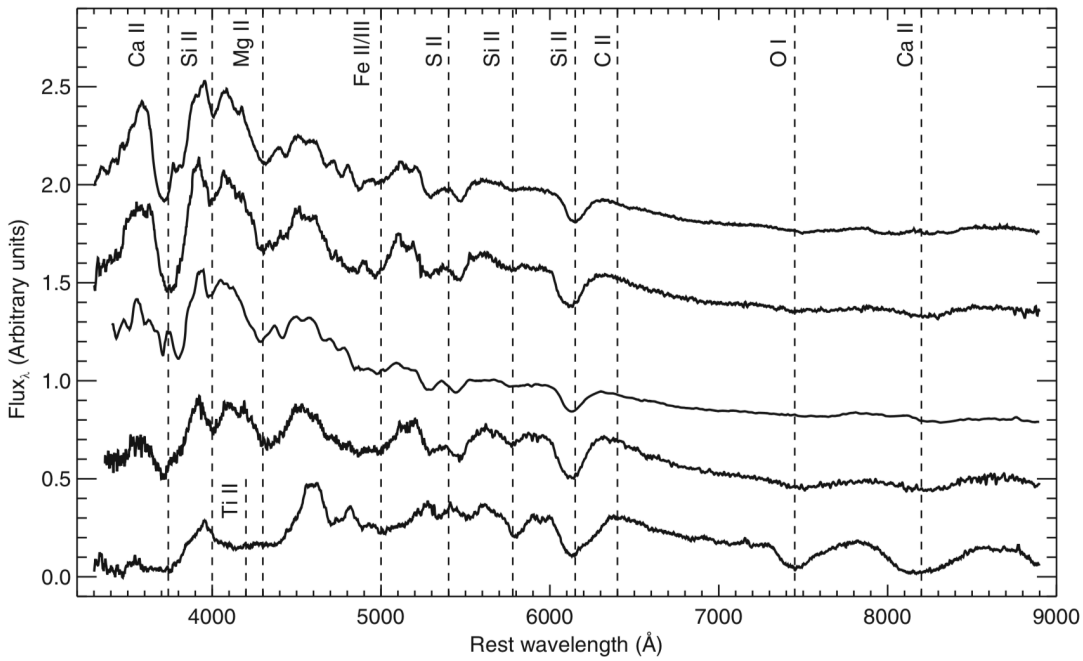

Figure 1.11.: Overview of the spectral diversity of SNe Ia around maximum light with varying intrinsic luminosity. Objects are ordered from most luminous at the top to least luminous at the bottom, corresponding to $\Delta m_{15}(B)$ between 0.86 and 1.72. For clarity, the strongest lines are indicated at their corresponding wavelengths. As described in Sec. 1.3.3, the ratio of two prominent Si II lines (5972 Å and 6355 Å) follows the temperature of the ejecta – cooler object have stronger Si II 5972 Å lines. Taken from (Maguire et al., 2014).

the nebular phase, the gamma-rays and positrons emitted in the radioactive decay of ^{56}Co heat the electron gas which in turn powers the supernova. Energy deposition from gamma-rays and positrons is balanced by forbidden emission line cooling (for more details see Sec. 2.1).

1.4. Explosion Models

SNe Ia are believed to be the violent, luminous deaths of C/O white dwarfs in close binary systems. The thermonuclear disruption of the WD releases enough energy to fully unbind the star. The explosion may be triggered in two separate ways. In the classical Chandrasekhar mass (M_{Ch}) channel the thermonuclear runaway reaction begins as the WD approaches the Chandrasekhar mass limit of $\sim 1.38\,M_\odot$ through accretion from the companion star. In the sub-Chandrasekhar mass (sub-M_{Ch}) channel the explosion of the WD is triggered significantly below the M_{Ch} through dynamical processes involving a companion star, be it a WD, main-sequence or giant star[16].

There are many reasons why evolved and compact WDs are preferred as progenitors of SNe Ia: a rapid rise of the optical light curve (~ 18 d) to maximum brightness, followed by a relatively fast decline over a few weeks points at small ejecta masses. SNe Ia occur in early- (elliptical) and late-type (spiral) galaxies, whether they are still actively star forming or 'red and dead' galaxies which completely stopped star formation. It should be noted though that intrinsically brighter SNe Ia favour late-type galaxies, while the faint end occurs more often in old stellar populations (Hamuy et al., 1996, 2000; Branch et al., 1996). For SNe Ia no progenitor stars have been identified, while for core collapse SNe several dozen progenitors have been found. The early light curve data of SN 2011fe places upper limits on the progenitor radius of a few $10^{-3}\,R_\odot$, consistent with a WD. Spectroscopically, the two most abundant elements in the universe, hydrogen and helium, are not detected in SNe Ia (but see Kollmeier et al., 2019 and Hamuy et al., 2003 for possible detection of hydrogen and Meikle et al., 1996 for possible detection of helium). The signature line of Si II 6355 Å, lines of carbon, oxygen and magnesium at early phases as well as iron at late epochs all hint at C/O WDs undergoing burning to NSE.

While the connection of WDs as progenitors of thermonuclear SNe is undisputed, the chemical composition of the progenitors is less clear. C/O WDs are generally preferred due to their allowed masses ($0.8 - 1.2\,M_\odot$) and accretion rates ($10^{-6} - 10^{-8} M_\odot\,\mathrm{yr}^{-1}$). Helium WDs have by now been excluded as no helium lines were found in SNe observed within days of the explosion. Pristine, unburnt material (helium) should be visible in early spectra if they were the progenitors of SNe Ia (Nomoto & Sugimoto, 1977). Simulations (Nomoto & Kondo, 1991; Gutierrez et al., 1996) suggest that O/Ne/Mg WDs do not reach the Chandrasekhar mass but instead collapse to a neutron star.

The nature of the companion star is probably one of the biggest mysteries in SN Ia research. Despite extensive observational campaigns after the discovery of several nearby SNe Ia in the last

[16] Though a sufficiently massive helium shell can self ignite, requiring no dynamical processes.

decade no trace of a surviving companion star was found (Li et al., 2011a; Kelly et al., 2014). The search for the origin of SNe Ia discriminates between *progenitor star* and *companion star*. The companion can be single-degenerate (SD), double degenerate (DD) or core-degenerate (CD)[17]. In the single-degenerate case the companion is either a main-sequence, subgiant or giant star from which the WD accretes hydrogen- or helium-rich matter (Nomoto, 1982a; Whelan & Iben, 1973). The double degenerate scenario requires two WDs in a close binary system, emitting gravitational waves and progressively getting closer until they merge (Iben & Tutukov, 1984; Webbink, 1984). In the core-degenerate case the WD plunges into the envelope of a giant companion and merges with the core of the giant (Livio & Riess, 2003; Kashi & Soker, 2011; Ilkov & Soker, 2012). The nature of the companion can be studied mostly though spectroscopic observations at early phases, direct searches for surviving companions, radio observations, polarisation signatures and the presence of stripped hydrogen or helium.

We can, on the other hand, focus on the mass of the progenitor at the time of the explosion. A deflagration/detonation thermonuclear runaway can be naturally triggered close to the Chandrasekhar mass limit. In less massive WDs ($0.9 - 1.2\,M_\odot$) ignition can also be achieved through dynamical processes. The mass of the exploding white dwarf mostly affects the explosion nucleosynthesis.

Both Chandrasekhar mass and sub-Chandrasekhar mass explosion scenarios with different initial setups and assumptions have been simulated both in 1-D and more recently 3-D (e.g. deflagrations: Nomoto et al., 1984, Fink et al., 2014; delayed detonations: Khokhlov, 1989, Seitenzahl et al., 2013; sub-Chandrasekhar mass detonations: Woosley et al., 1986, Moll & Woosley, 2013). It remains to be seen whether the simulation of the CD mechanism leads to successful SN Ia explosions as the common-envelope phase leading to the in-spiral and subsequent merger of the WD is extremely challenging to model accurately. In the following, the most promising scenarios of the Chandrasekhar mass and sub-Chandrasekhar mass channels are discussed. It should be noted, however, that for the best observed SNe Ia counter arguments for every proposed explosion model can be made.

1.4.1. Chandrasekhar mass Explosions

Chandrasekhar mass explosion models have long been considered as the most promising candidates for SNe Ia. In the Chandrasekhar mass channel, a WD star in a binary system with a giant, sub-giant, main sequence or symbiotic star accretes material from its companion until it nears the Chandrasekhar mass limit. Close to this mass limit, the density in the centre of the C/O WD becomes high enough that carbon begins to burn, which, after some delay, leads to a thermonuclear explosion which unbinds the WD and imparts a kick on the donor star. In addition to the general WD explosion properties, in this channel the homogeneity of thermonuclear

[17] In principle both the DD and CD scenarios are based off the same idea, except that in the latter the explosion takes place within a hyrdogen-rich envelope. The CD scenario is thus a good candidate for SNe Ia CSM, which are rare objects and not included in normal SNe Ia.

SNe is further explained by the similar mass of the exploding WDs and thus a similarly sized bomb.

In order to reach the Chandrasekhar mass, WDs need to accrete material from the companion. Accretion can be achieved via a powerful stellar wind (e.g. Chen et al., 2011) or through Roche-lobe overflow when part of the donor-star is no longer gravitationally bound. However, the accreted mass needs to be retained so that the WD may grow towards the Chandrasekhar mass. In a number of classical nova systems with accretion rates below $10^{-8}\,\mathrm{M_\odot\,yr^{-1}}$ the mass loss in the nova events exceeds the mass accreted in between outbursts (Livio & Truran, 1992; Yaron et al., 2005). Too high accretion rates ($> 10^{-6}\,\mathrm{M_\odot\,yr^{-1}}$), on the other hand, will cause the WD to expand into a red giant star which engulfs the donor and completely stops any further accretion (see Fig. 1.12). Simulations show that accretion rates need to remain within a narrow parameter range that allows for stable burning of the accreted material to helium (Paczynski & Zytkow, 1978; Nomoto et al., 2007; Shen & Bildsten, 2007; Wolf et al., 2013). Helium flashes in the accumulated helium layer could also expel more mass than was accreted onto the WD, though recent simulations show that this effect is not strong enough to halt the WD growth (Hillman et al., 2016). Observationally, a handful of systems that are hosts to recurrent novae have been observed (Darnley et al., 2015). The WDs in these systems are successfully accreting at high enough rates and are close to the Chandrasekhar mass (Tang et al., 2014).

Having a scenario whereby WDs approach the Chandrasekhar mass does not necessarily make this the channel for the bulk of thermonuclear supernovae. Hydrodynamical simulations have shown that the explosions are sensitive to the mode of the flame propagation which can be subsonic (deflagration), supersonic (detonation) or some mixture (delayed detonation). Arnett (1969) realised that for detonations of C/O WDs at $\mathrm{M_{Ch}}$ in hydrostatical equilibrium NSE burning is achieved across the whole WDs, fully converting it to IGEs. The presence of IME lines – for example the trademark Si II 6355 Å line – fully rules out this scenario. Moreover, pure detonations of WDs not only near the Chandrasekhar mass but with masses above $1.2\,\mathrm{M_\odot}$ are fully ruled out by the same argument. A detonation can only be started through sufficiently high compression by the nuclear burning front and thus requires simultaneous runaway of a region that has small fluctuations in temperature. In accreting WDs, such a scenario cannot be achieved. The more promising Chandrasekhar mass models are described in the following.

Deflagrations

The first promising SNe Ia model proposed to explain the normal population of thermonuclear explosions was the so-called 'W7' (Nomoto et al., 1984), a pure deflagration scenario that uses mixing length theory to describe the enhanced burning rate due to hydrodynamical instabilities. Pure deflagrations have been studied to great detail in the past in numerical simulations (Nomoto et al., 1984; Reinecke et al., 2002; Gamezo et al., 2003; García-Senz & Bravo, 2005; Röpke et al., 2006b,a, 2007a; Jordan et al., 2012; Long et al., 2014; Ma et al., 2013; Fink et al., 2014; Nomoto & Leung, 2018).

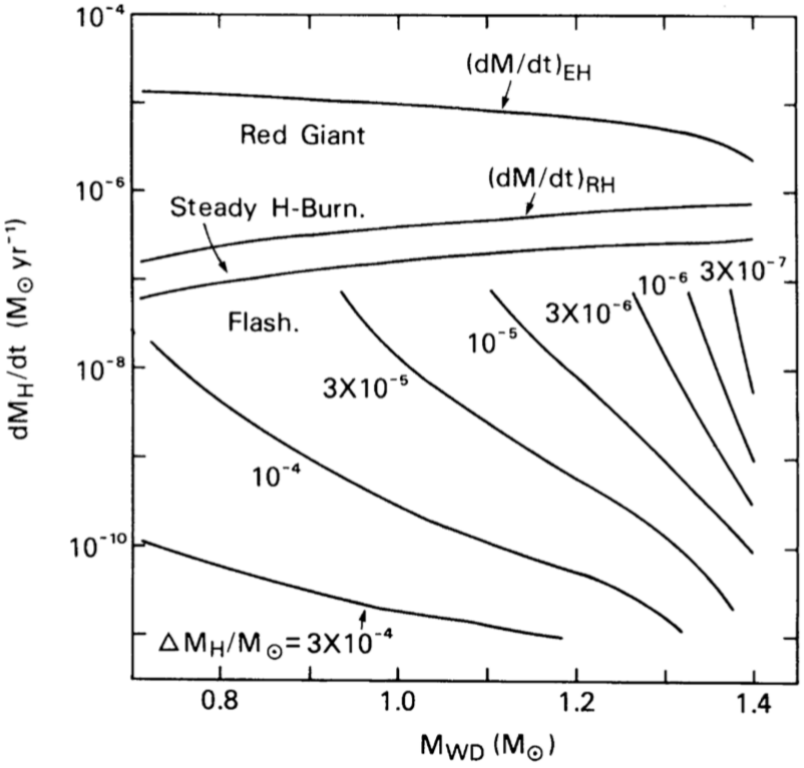

Figure 1.12.: Hydrogen accretion onto a WD as a function of the WD mass (Nomoto, 1982a). In the region indicated by 'Steady H-Burn' hydrogen is steadily burning to helium, leading to an increase in mass of the WD. Below this region, hydrogen shell burning is thermally unstable and the WD experiences helium shell flashes. Above the steady burning region, optically thick winds are accelerated, blowing away the excess mass. Taken from (Nomoto, 1982a).

Due to the high central density of WDs near the Chandrasekhar limit the flame propagation has to start as a sub-sonic deflagration flame. Deflagrations propagate due to micro-physical transport processes and the energy release heats the fuel ahead of the burning front through conduction and diffusion. The flame speed is slow compared to detonations with roughly 1% of the sound speed in the fuel (Ma et al., 2013). This allows the WD to react to the explosive burning with expansion, lowering the density outside of the WD core. In this way, ^{56}Ni can only be produced in the centre where the flame was ignited and the density is high. In the outer layers sufficient amounts of IMEs are produced which are required to match early-phase observations. In more than one spatial dimension is the burning phase of deflagrations dominated by hydrodynamical instabilities (especially Rayleigh-Taylor (RT) instabilities) which mix the IGEs from the core into the outer layers. During the early growth of the reactive RT instability, burning smooths out perturbations. Eventually, the RT modes begin to merge and break down creating a highly creased structure at the smallest scales (Zingale et al., 2005). No strong chemical layering as observed in normal SNe Ia is expected from the turbulent flame propagation (see Fig. 1.13, Gamezo et al., 2003; Townsley et al., 2007; Fink et al., 2014). On the contrary, strong mixing is seen for one particular group of thermonuclear SNe. In SNe Iax iron lines are seen at a wide range of velocities and calcium can be found interior to iron – something that usually does not occur in thermonuclear explosions. At the end of the burning phase turbulence freezes out and the ejected material approaches homologous expansion (Röpke & Hillebrandt, 2005).

Unfortunately, the ignition of the deflagration is difficult to model in state-of-the-art simulations as convective carbon burning begins several hundred years before the thermonuclear runaway (see Sec. 1.5.2; Höflich & Stein, 2002; Kuhlen et al., 2006; Chamulak et al., 2008; Zingale et al., 2009; Nonaka et al., 2012; Martínez-Rodríguez et al., 2016). Numerically, this can be treated in a parametric way through the addition of a number of ignition sparks in the core. The strength and sphericity is mediated by the number of sparks, with spherical explosions being the result of a higher number of sparks (Seitenzahl et al., 2013).

Pure deflagrations have been demonstrated to lead to weak explosions. In modern multidimensional simulations of the turbulent burning front the flame speed and mixing were much lower than in the 'W7' case. As a result, a large fraction of the WD remains unburnt (burning fraction ≤ 0.5) and no clear chemical stratification is obtained. As the burning front never transitions into a detonation and the outer layers of the WD expand significantly, only small amounts of IGEs are produced in the very centre of the explosion (though with large variations in between models). In some simulations, the unburnt material forms remnant WD-like objects with a wide range of masses, dependent on the ignition setup. A bound remnant surviving the explosion would be super-Eddington and drive an optically thick wind into the ejecta. Such a scenario would tie in well with observational evidence that the spectra of SNe Iax do not become fully nebular (McCully et al., 2014).

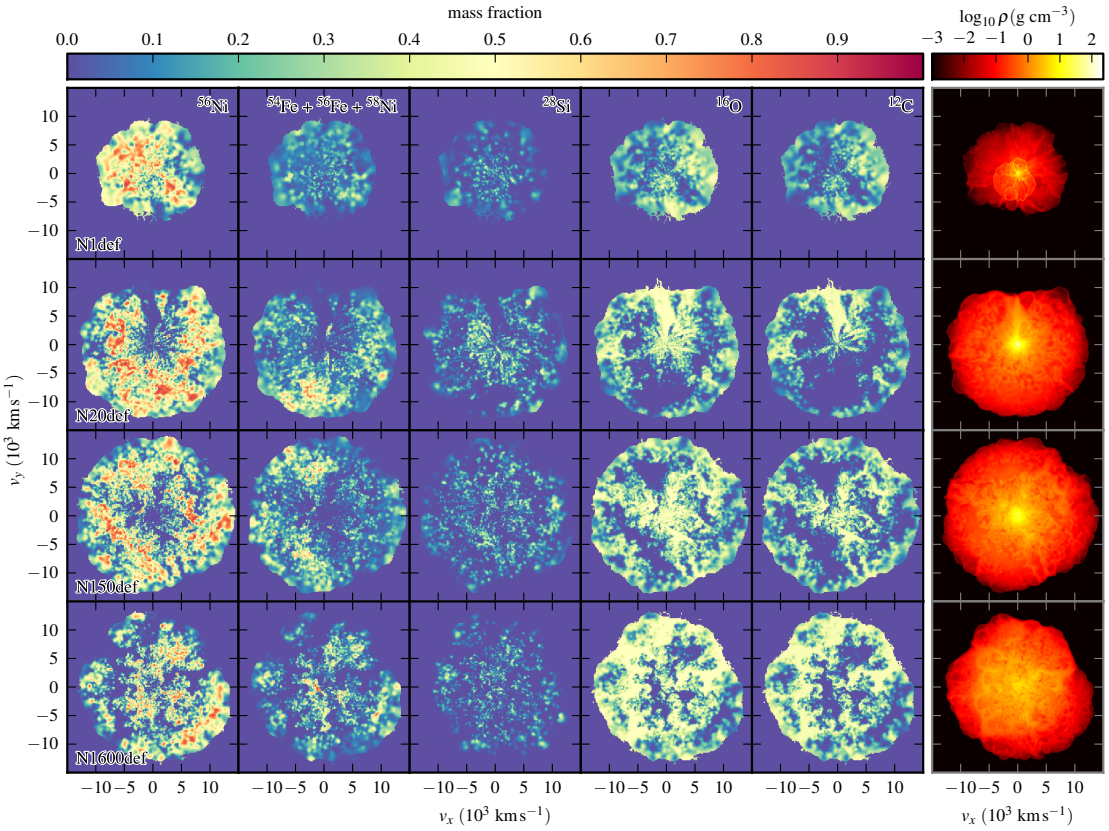

Figure 1.13.: Ejected isotope abundances of four pure deflagration models in the x-y plane of the explosion. Shown are the ^{56}Ni, the stable IGE (^{54}Fe + ^{56}Fe + ^{58}Ni), the IME (^{28}Si), ^{16}O and ^{12}C abundances (from left to right). Taken from Fink et al. (2014).

Delayed Detonations

As detailed above, a pure deflagration cannot explain the observed properties of SNe Ia with the exception of the peculiar SNe Iax, especially the chemical stratification of the ejecta. One possible solution to this is the so-called Delayed Detonation of a near-Chandrasekhar mass WD. Similar to the pure deflagration case, in simulations a deflagration flame is started near the centre of the WD where the density is highest. In the high-density burning regime mainly IGEs are produced. The energy release of the nuclear burning leads to a phase of expansion and mixes burning ashes and nuclear fuel. The expansion of the WD reduces its density causing burning to halt at IMEs. The deflagration eventually transitions to a detonation (supersonic) (see Fig. 1.14). The detonation front permeates the remaining fuel, burning it to IGEs near the centre and mostly to IMEs in the pre-expanded low density zones. Stronger deflagrations before the transition into detonations result in a higher degree of pre-expansion and the production of fewer IGEs in the detonation.

Delayed detonation models of SNe Ia require a spontaneous transition of the flame propagation mode from an initial deflagration to a detonation (Khokhlov, 1989; Khokhlov et al., 1992). Deflagration to detonation transitions (DDT) have been observed in experiments on Earth (Urtiew & Oppenheim, 1966), though they usually emerge from the interaction of the deflagration flame with the confinement. No DDTs have been observed in unconfined media so far. It remains unclear whether a deflagration to detonation transition can occur in WDs.

Since delayed-detonations have been suggested as the explosion mechanism of SNe Ia, many groups have computed explosion models. Especially multidimensional effects (e.g. Rayleigh-Taylor and Kelvin-Helmholtz-instabilities) play a crucial role for the chemical ejecta stratification. 1-D models do not allow any mixing of IGEs and IMEs unless introduced through parametric mixing. In 2-D, the model is axi-symmetric and buoyant bubbles appear as tori. Morphologically, the explosion will be different from 3-D, although angle averaged results might give the impression of minor changes. Major changes are, for example, a very different energy release due to inconsistent bubble volumes (spherical bubbles vs. tori). Most published DDT simulations have been computed in 1-D or 2-D. Only few 3-D DDT simulations have been generated due to their computation cost.

There exist several variants of delayed-detonations. In a gravitationally confined detonation (Plewa et al., 2004) a weak and strongly off-centre deflagration bubble rises to the surface of the WD, transporting IGE-rich ashes to the outer layers. A subsequent detonation can convert most of the WD's interior into ^{56}Ni as the WD expanded only slightly in the deflagration phase. This scenario would result in ^{56}Ni at the surface and in the centre, and a plume of IMEs created in the buoyant bubble (Fisher & Jumper, 2015). However, it is not clear that such a scenario would trigger a detonation (Röpke et al., 2007b).

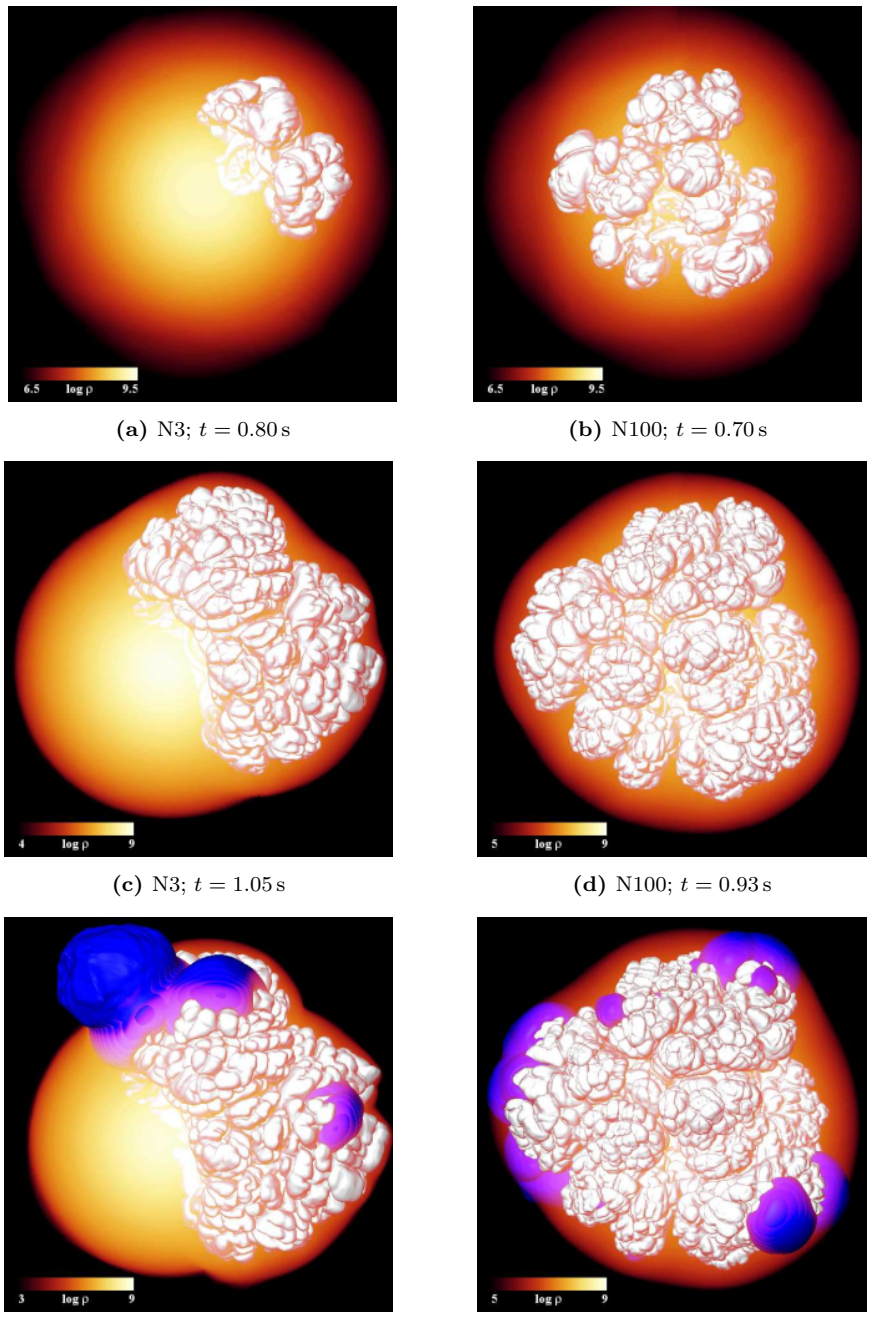

(a) N3; $t = 0.80\,\mathrm{s}$ **(b)** N100; $t = 0.70\,\mathrm{s}$

(c) N3; $t = 1.05\,\mathrm{s}$ **(d)** N100; $t = 0.93\,\mathrm{s}$

(e) N3; $t = 1.15\,\mathrm{s}$ **(f)** N100; $t = 1.00\,\mathrm{s}$

Figure 1.14.: Snapshots of the hydrodynamic evolution of two delayed detonation models (N3, left column and N100, right column). The top panels show the rising deflagration plume during the deflagration phase. The middle row shows the deflagration plume at the time when the detonation transition occurs. The bottom panels show the detonation emerging from the deflagration plumes. Taken from Seitenzahl et al. (2013).

1.4.2. Sub-Chandrasekhar mass Explosions

WDs with masses significantly below the Chandrasekhar limit will not spontaneously initiate a thermonuclear runaway reaction. Instead, explosions have to be triggered through some sort of interaction with the binary companion. In the early 1980s it was discovered that the right conditions – accretion of helium-rich matter at rates of a few times $10^{-8}\,M_\odot/yr$ – could lead to thermonuclear detonations (Taam, 1980a,b; Nomoto, 1980, 1982a,b). Detonations at densities of $\sim 10^7\,g\,cm^{-3}$ (compared to $\sim 10^9\,g\,cm^{-3}$ for M_{Ch}) do not fully convert the star to IGEs, but instead burn to intermediate mass elements in the outer layers. If sub-Chandrasekhar mass WDs do indeed explode, they have to do so via detonations instead of deflagrations.

Sub-Chandrasekhar mass scenarios are – in contrast to M_{Ch} – primarily sensitive to the mode of carbon ignition (double detonation, violent merger, head-on collision etc.). During the last four decades three main scenarios for possible explosions of sub-Chandrasekhar mass WDs have been developed. One is the historical double-detonation scenario, where an accreted helium layer becomes degenerate and detonates, with the subsequent shock wave converging in the core and triggering an obliterating second detonation (Livne, 1990; Woosley & Weaver, 1994; Livne & Arnett, 1995). Another possibility are WD mergers which were among the first proposed scenarios for SNe Ia, though initially not for the sub-Chandrasekhar scenario. In the classical notion, the lower mass secondary WD becomes tidally disrupted and forms a torus around the primary. Over the course of several thousand years, the primary will accrete from the torus and grow in mass until a deflagration is initiated near the Chandrasekhar mass. However, Pakmor et al. (2010, 2013) (but see also van Kerkwijk et al., 2010) found that an explosion is likely triggered much earlier in the accretion process at sub-Chandrasekhar masses. A more exotic scenario is the head-on collisions, where the collision is not a result of spiralling-in due to gravitational wave losses. They are suggested to either occur in extremely dense stellar systems such as globular clusters (e.g. Rosswog et al., 2009), or to be induced by a third body which disturbs the orbit of the binary WD system (Thompson, 2011). In this scenario, ignition is expected to be triggered at the collision interface.

Double-Detonations

Double-detonations have, for a long time, been the default mechanism for the ignition of a sub-Chandrasekhar mass WD. First discussed in the early 1980s, this scenario assumes a WD (most likely in a binary WD system) accreting helium rich material from the donor at fairly low rates ($10^{-8}\,M_\odot/yr$) in order to build up a layer of helium on the surface of the primary WD. In the original works the donors were non-degenerate He stars (Woosley et al., 1986; Nomoto, 1982b), but newer models prefer He or C/O WDs[18] (Bildsten et al., 2007; Fink et al., 2007, 2010; Shen & Bildsten, 2009; Guillochon et al., 2010; Dan et al., 2011, 2015; Raskin et al., 2012; Pakmor et al., 2013; Shen et al., 2018). Sufficiently low accretion rates are capable of growing thick helium

[18] C/O WDs contain significant He layers which can be accreted onto the primary WD

layers of $\sim 0.2\,M_\odot$ on the primary WD. The simulations show that when the base of the helium layer becomes degenerate and finally ignites, a shock wave wraps around the WD and on the opposite side of the ignition is focused towards the centre, where the shock compression triggers a second detonation (thus dubbing this mechanism 'double-detonation', see Fig. 1.15 and 1.16). Unfortunately, it was soon noted that an initial detonation of a thick (of order $0.2\,M_\odot$) helium layer would produce IGEs at high velocities and helium burning products which have not been observed.

More recent models have shown that a much lower helium shell mass ($< 0.05\,M_\odot$) is necessary to trigger a helium shell detonation. Shell helium burning will proceed as a detonation even for very thin shells of $0.0035\,M_\odot$ (Bildsten et al., 2007; Fink et al., 2010) and without exception trigger a detonation of the C/O core (Fink et al., 2010). Thin helium layer detonations will leave no strong spectral imprints and are in good agreement with observations (Bildsten et al., 2007; Shen & Bildsten, 2014; Townsley et al., 2019).

Violent Mergers

WD mergers are a class of models that came up in the 1980s (Webbink, 1984; Iben & Tutukov, 1984), were later discarded as explanations for SNe Ia, but recently got revived after a demonstration of their viability by Pakmor et al. (2010). In classical mergers the secondary WD is disrupted by tidal forces of the primary and subsequently forms a torus. Over several millennia material from the torus is accreted onto the primary WD which is growing in mass until it nears the Chandrasekhar mass limit and is ignited. New studies indicate, however, that unstable mass transfer would cause the primary WD to explode before it can reach the Chandrasekhar mass limit.

In the so-called violent merger scenario ignition of the primary WD is achieved as the accretion stream hits the surface. The strength of the accretion stream depends on the separation of the binary system, growing stronger as the WDs approach each other. At the impact point on the surface of the WD compression of the outer layers is accomplished. However, 'hot spots' are not resolved in numerical simulations making it difficult to determine if ignition conditions have been reached. Carbon ignition conditions depend on the mass ratio of the two WDs. Systems of roughly equal masses between 0.9 and $1.1\,M_\odot$ will consistently lead to a violent merger (Sato et al., 2015) as the secondary is disrupted later during the spiral-in phase, giving rise to a stronger accretion stream (see Fig. 1.17).

If a detonation is successfully triggered in the primary WD it is completely unbound and disrupted. When the expanding burning ashes reach the secondary it is destroyed and forms a torus around the centre of mass of the former binary system (Pakmor, 2017). This introduces asymmetries that depend on the strength of the impact on the secondary: a strong impact might lead to the ignition of the secondary burning to IMEs and filling the innermost ejecta region. In this case, asymmetries are strongest in the centre of the explosion and negligible at the outermost layers. Such a scenario would also lead to oxygen being located in the explosion centre which

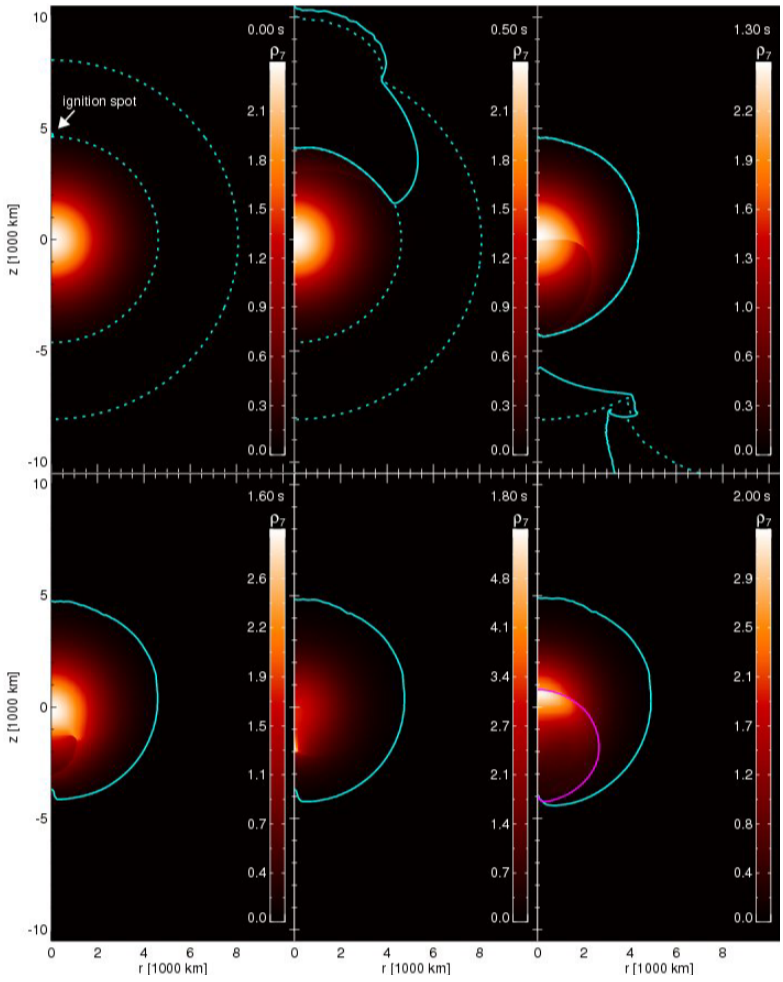

Figure 1.15.: Density evolution of a sub-Chandrasekhar mass double detonation. The border of the He shell is indicated by dashed lines. Solid lines mark the locations of the He (cyan) and C/O detonation. Taken from Fink et al. (2011).

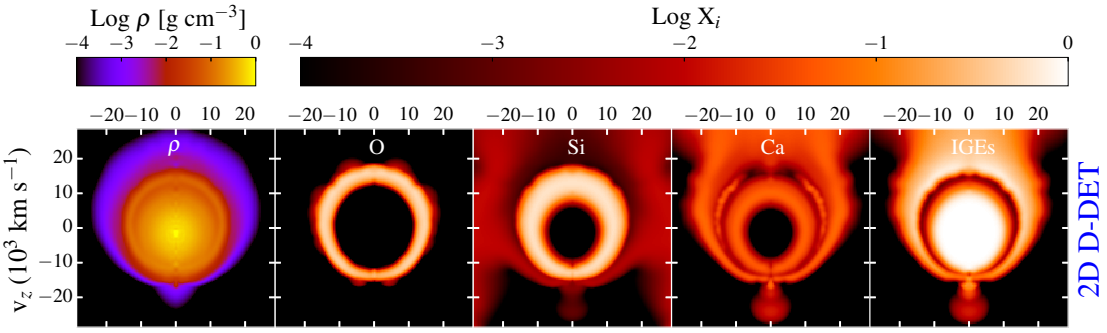

Figure 1.16.: XZ-view of the density and composition of the ejecta 100 s after explosion for a 2D double-detonation model. Taken from Bulla et al. (2016a).

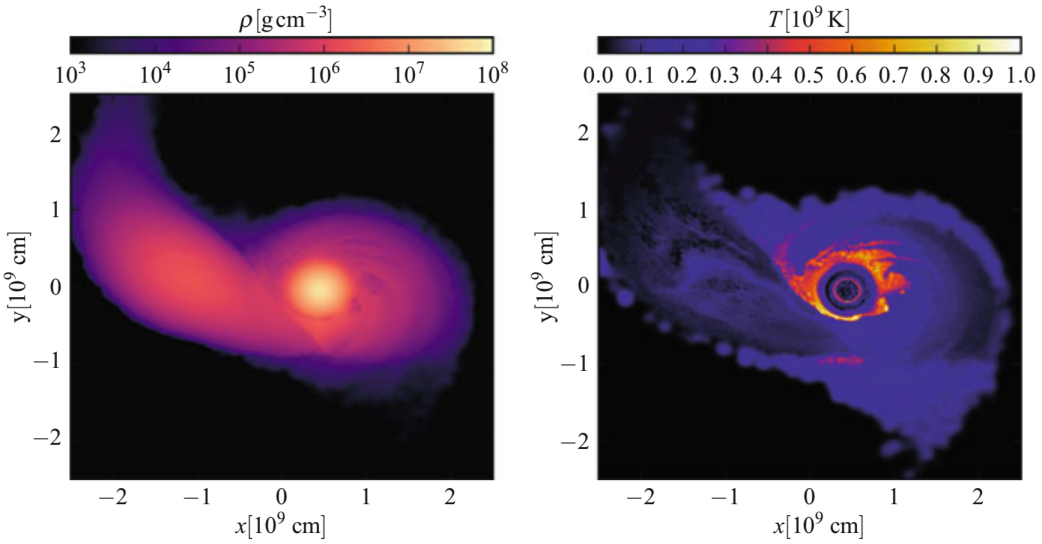

Figure 1.17.: Density and temperature of a 1.1 $M_\odot$ and 0.9 $M_\odot$ CO WD violent merger model (Pakmor et al., 2012). The snapshot shows the final orbit of the secondary WD as it is about to be disrupted by the more massive primary WD and a detonation ensues.

should emit during the nebular phase if it is heated sufficiently (see Fig. 1.18). As only a small number of peculiar objects are known to exhibit nebular [O I] lines, it would appear necessary that the core oxygen either be fully ionised or not heated if such a scenario is to explain the bulk of SNe Ia.

Head-On Collisions

Head-on collisions of WDs are a fairly new class compared to the previously discussed scenarios. Initially it was thought that WD collisions could only occur in very dense stellar environments such as globular clusters and centres of galaxies (Hut & Inagaki, 1985). The expected rate of these collisions, however, is expected to be orders of magnitudes below the observed SN rate (Benz et al., 1989). A second mechanism that could lead to WD collisions was published recently by Thompson (2011) and Antonini & Perets (2012). They demonstrated that in some hierarchical triple systems Kozai-Lidow oscillations (Kozai, 1962; Lidov, 1962) can be induced in the inner binary system, where extreme peri-centre changes can occur on time-scales of single orbits. The inner binary is driven to high eccentricities and ultimately to a collision. If the inner system consists of a WD-WD binary the collision could lead to a SN Ia (Thompson, 2011; Katz & Dong, 2012; Kushnir et al., 2013).

The combustion of the WD is achieved through shock ignition, which is well understood compared to other explosion scenarios. Thermonuclear burning propagates as a carbon detonation and was shown to produce up to 0.5 $M_\odot$ of ^{56}Ni (Kushnir et al., 2013). Due to the nature of

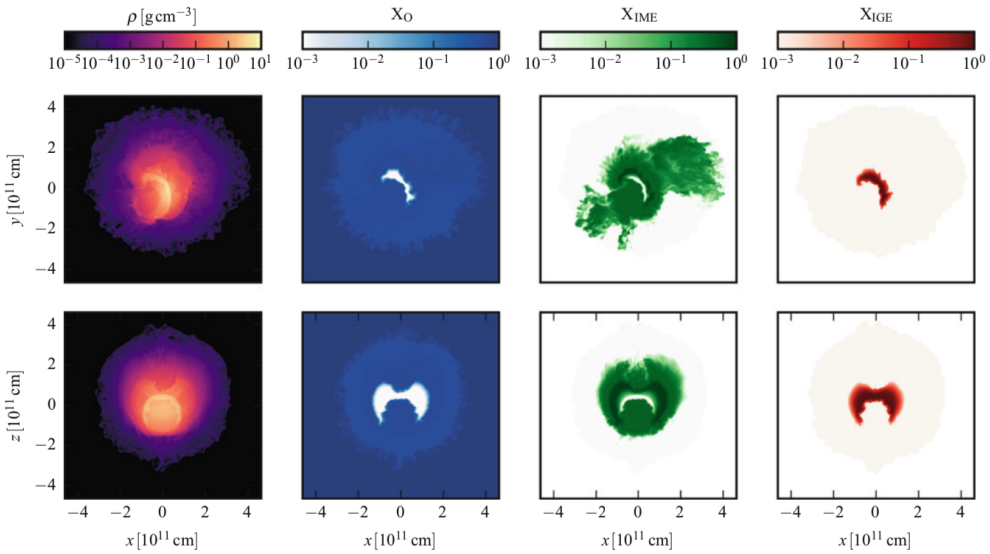

Figure 1.18.: Density and composition of a 1.1 $M_\odot$ and 0.9 $M_\odot$ CO WD violent merger model (Pakmor et al., 2012). The snapshot shows the x-y plane (top panel) and x-z plane (bottom panel) 100 s after the carbon ignition. Columns show the density and the oxygen, IME and IGE mass abundances (from left to right).

this channel, ignition is achieved in both WDs and viewing angle effect are expected in the line profiles. Especially IGE lines during the nebular phase, which originate from the densest regions of the ejecta where burning to NSE is complete, are expected to exhibit double peaked profiles if seen along the line connecting the two WDs on their collision course (Fig. 1.19). From other viewing angles the line profiles may exhibit 'shoulders'. Dong et al. (2015) found a number of objects (three out of ∼twenty) that show a bi-modality of their line profiles. The identified objects belong to the subclass of fast declining transitional objects with Δm_{15}(B) between 1.3 and 1.8. More objects that show such profiles were found by Vallely et al. (2019) and Kollmeier et al. (2019). So far, no bright SNe were identified that exhibit this peculiarity. In fact, Toonen et al. (2018) and Hallakoun & Maoz (2019) argue that the expected collision rate from triple systems can only account for a fraction of the SN rate and is in tension with the delay-time distribution of SNe Ia, indicating that only rare subclasses and not the bulk of normal SNe Ia originate from this channel.

1.5. Explosion Nucleosynthesis

The name 'thermonuclear supernovae' derives from the mechanism that leads to the unbinding and explosion of the WD. Thermonuclear explosions of WDs convert less tightly bound fuel (^{12}C, ^{16}O) into more tightly bound ashes (e.g. ^{28}Si, ^{56}Ni) within fractions of a second (see Fig. 1.22). The liberated binding energy is converted into heat and powers the explosion. Adiabatic expan-

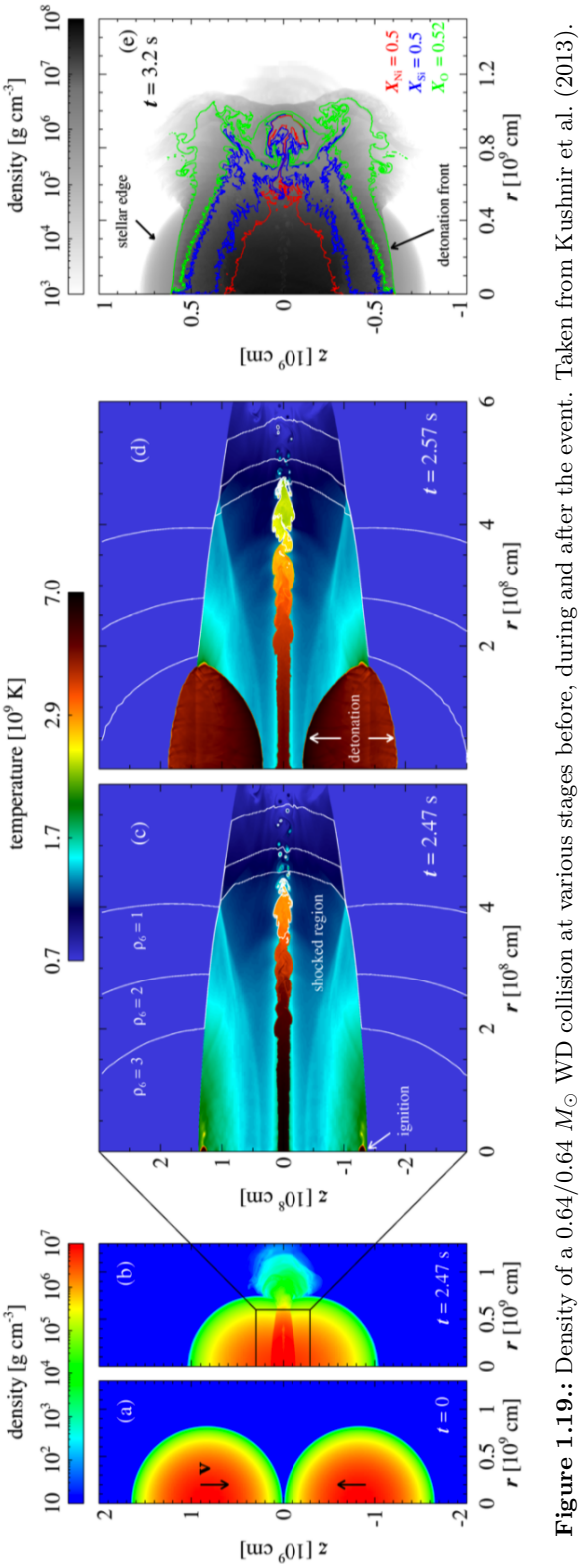

Figure 1.19.: Density of a 0.64/0.64 $M_\odot$ WD collision at various stages before, during and after the event. Taken from Kushnir et al. (2013).

sion of the ejecta leads to extreme cooling within seconds after the explosion as the size of the exploding WD is tiny compared to the ejecta radius (a few s $\times 10000\,\mathrm{km\,s^{-1}} \gg r_{WD}$). There may be a 'dark' phase between the explosion of the WD and rise of the ^{56}Ni powered light curve where no optical or NIR photons are emitted.

The nucleosynthetic yield of exploding WDs depends on the ignition mechanism (detonation vs deflagration) and the density structure of the progenitor (see Fig. 1.20). The most abundant burning product in normal SNe Ia is ^{56}Ni. Spectroscopic observations suggest that in addition to ^{56}Ni neutron-rich isotopes, whose abundance depends on the neutron-excess of the burning fuel, are required to explain observed spectra. Currently, three processes that lead to an excess of neutrons in the NSE burning region of exploding WDs are known: carbon-simmering, electron capture, and progenitor metallicity. In massive WDs nearing the Chandrasekhar limit all of these processes are expected to occur. In sub-Chandrasekhar WDs the density is too low for simmering or electron capture reactions to increase the neutron fraction and therefore progenitor metallicity is considered the sole contributing process. In the following, the processes responsible for a neutron excess in both cases as well as general nucleosynthesis are discussed.

1.5.1. Non-Zero-Metallicity Progenitors

The typical mass of a WD is around $0.6\,M_\odot$. Before shedding their outer layers, the progenitor stars of these WDs had been fusing helium to carbon and oxygen which comprises their cores. Due to gravitational settling only lightweight elements are present at the surface of WDs: most of them have a thin helium ($\sim 10^{-2}\,M_\odot$) and an even thinner hydrogen layer ($\sim 10^{-4}\,M_\odot$) on top. The cores of massive WDs ($> 1.1\,M_\odot$) are assumed to contain oxygen and neon instead. For the evolution of a WD not only its mass but also its chemical composition are important. The main isotope that drives the evolution is ^{22}Ne (García-Berro et al., 2008; Althaus et al., 2010) due to its neutron excess ($Z = 10, A = 22$), which results in it sinking to the core of the WD as it cools. Gravitational binding energy released in this way modifies the cooling time (Deloye & Bildsten, 2002).

In the context of explosion nucleosynthesis the property that determines the fractional production of neutron-rich isotopes is the neutron excess η of the nuclear fuel:

$$\eta = 1 - 2Y_e = \sum_i \frac{(N_i - Z_i)}{A_i} X_i \ . \tag{1.1}$$

During the evolution of the WD leading up to the explosion, as well as in the explosion itself, the value of η can be changed by a number of processes. The starting point of η is determined by the metallicity of the progenitor star of the WD.

Stars with masses above $1.3\,M_\odot$ that undergo H-burning during the CNO cycle (Thielemann et al., 1986) overproduce ^{14}N, as the $^{14}\mathrm{N}(p,\gamma)^{15}\mathrm{O}$ reaction is much slower than the preceding reactions, causing a bottleneck and pileup of ^{14}N. As soon as hydrostatic He burning is started the available ^{14}N is converted to ^{22}Ne through $^{14}\mathrm{N}(\alpha,\gamma)^{18}\mathrm{F}(\beta^+,\nu_e)^{18}\mathrm{O}(\alpha,\gamma)^{22}\mathrm{Ne}$. The resulting

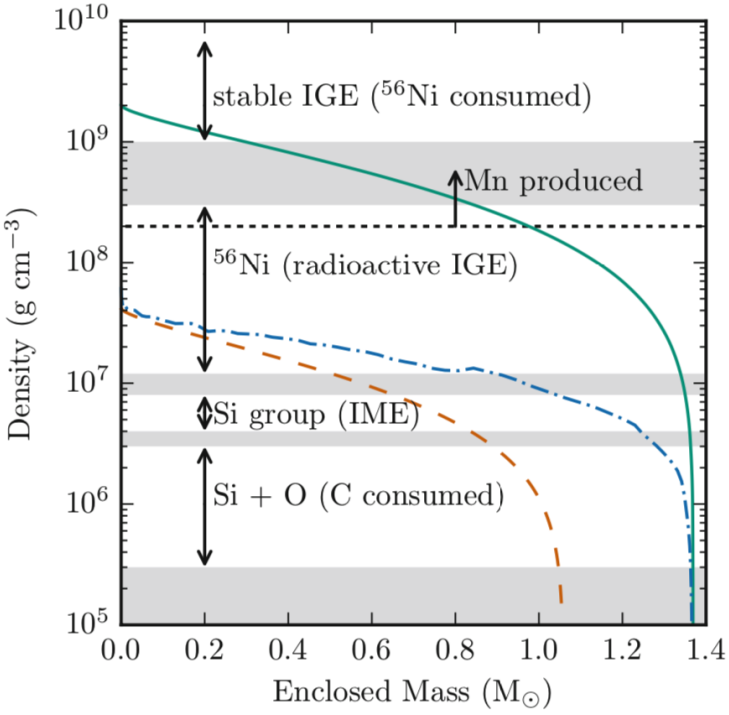

Figure 1.20.: Nucleosynthesis regimes of WDs with varying mass. Higher densities result in more complete burning to NSE, producing IGEs. WDs near the Chandrasekhar mass limit (green solid line) are converted completely into IGEs if no pre-expansion is applied. If the WD expands (see Sec. 1.4.1) a significant fraction of IMEs are produced (blue dot-dashed line). A sub-Chandrasekhar mass WD (1.05 $M_\odot$) without expansion produces similar results as the detonation in a pre-expanded WD (orange dashed line). Only deflagrations in Chandrasekhar mass WDs reach the high densities where neutron-rich material (stable IGEs) can be produced in significant quantities. Taken from Seitenzahl & Townsley (2017).

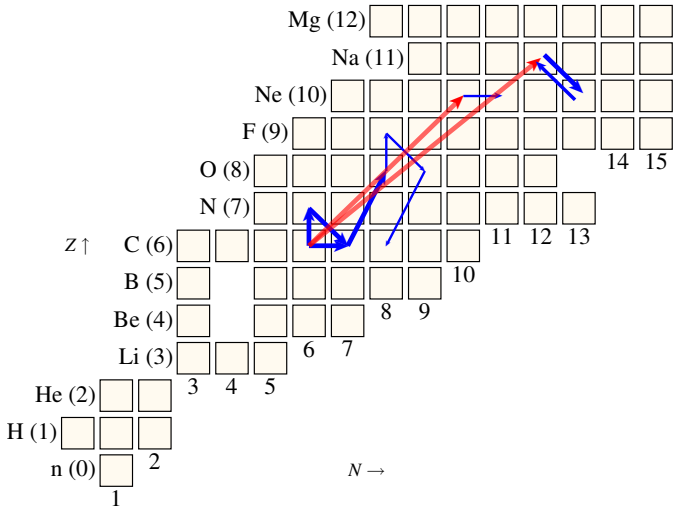

Figure 1.21.: Nuclear reactions during the carbon-simmering phase at $\rho = 3 \times 10^9\,\mathrm{g\,cm^{-3}}$ for a WD with initial composition 30/70 C/O. The widths of the arrows indicate the burning rates of the reactions. The ^{12}C(^{12}C,α)^{20}Ne and ^{12}C(^{12}C,p)^{23}Na reactions are highlighted in red (see text). Taken from Chamulak et al. (2008).

neutron excess from ^{22}Ne is directly linked to the metallicity of the progenitor star (Timmes et al., 2003). It should be noted that this is only true for the *global* and not necessarily for the *local* neutron excess, as dynamical processes could simultaneously lead to an enrichment of the core and depletion of the outer layers with ^{22}Ne.

1.5.2. Carbon-Simmering

Massive WDs near the Chandrasekhar mass limit require no external ignition mechanism. Due to compressional heating from accretion the core temperature rises and carbon fusion is slowly started in the core. For central densities and temperatures exceeding $2\times10^9\,\mathrm{g\,cm^{-3}}$ and $3\times10^8\,\mathrm{K}$, respectively, the ^{12}C+^{12}C reactions (^{12}C(^{12}C,α)^{20}Ne and ^{12}C(^{12}C,p)^{23}Na with branching ratio 0.56/0.44; Caughlan & Fowler, 1988) overwhelm neutrino cooling and core ignition is achieved (see Fig. 1.21). As a result of the rising temperature material begins to ascend and a convective core is formed. It soon grows and encompasses the whole WD. This phase of *carbon simmering* can last for several hundred to a few thousand years during which the core temperature slowly rises. As soon as the core temperature reaches $7 \times 10^8\,\mathrm{K}$ the energy release from nuclear fusion becomes so powerful that it can no longer be quenched by convection: a thermonuclear runaway is going to occur. When the temperature rises to $10^9\,\mathrm{K}$ the burning time scale is shorter than the time scale for sound waves to cross a pressure scale height resulting in a burning front.

The protons liberated in the ^{12}C(^{12}C,p)^{23}Na reaction during the simmering phase are captured by ^{12}C resulting in ^{13}N. Quickly ^{13}N and ^{23}Na decay via electron capture to ^{13}C and ^{23}Ne, respectively, increasing the neutron excess in the process (Chamulak et al., 2008). Carbon-

simmering neutronisation can only occur at high density environments in the cores of near-Chandrasekhar mass WDs. The amount of neutronisation from this process was estimated by Martínez-Rodríguez et al. (2016) to be $\Delta\eta \sim (3-4) \times 10^{-4}$ (corresponding to $\Delta\eta \sim 1/3\eta_{\odot}$, where $\eta_{\odot}$ is the current solar neutron excess). As carbon simmering is expected to occur in all near-Chandrasekhar mass WDs it will lead to a neutron excess floor of $\Delta\eta \sim 1/3\eta_{\odot}$ in the absence of other effects which enhance the neutron excess. If other effects (progenitor metallicity and electron capture in the central region) are contributing then the neutron excess will be even higher. Sub-Chandrasekhar WDs do not reach conditions for carbon simmering and thus their neutron excess at the time of explosion can be lower than the carbon-simmering floor.

1.5.3. Nuclear Statistical Equilibrium Burning

From a nucleosynthesis point of view the temperature profile during combustion is the most important quantity. Nuclear reaction rates are extremely sensitive to changes in temperature and density which are given by the explosion dynamics and ultimately determine the nucleosynthetic products. Several distinct regimes have been identified: complete Si-burning, incomplete Si-burning, O-burning, Ne-burning and C-burning.

Complete silicon burning

In the extreme environment of nuclear combustion (peak temperatures $T > 5 \times 10^9\,\mathrm{K} \approx 0.3\,\mathrm{MeV}$) photons have enough energy to dissociate nuclei into their constituents. On the other hand, there are competing formation reactions of nuclei at densities exceeding $10^6\,\mathrm{g\,cm^{-3}}$. In such cases an equilibrium between strong and electromagnetic reactions which preserves the number of neutrons and protons is reached and abundances follow directly from the Saha equation. Reactions can be assumed to occur instantaneously and the burning outcome only depends on the relative binding energies of the involved species, the density ρ, and the neutron-richness of the composition instead of the individual reaction rates (Clifford & Tayler, 1965; Hartmann et al., 1985; Nadyozhin & Yudin, 2004). Abundances $Y_i = n_i/n$ are then given by

$$Y_i = (\rho N_A)^{A_i - 1} \frac{G_i}{2^{A_i}} A_i^{3/2} \left(\frac{2\pi\hbar^2}{m_u k_B T} \right)^{\frac{3}{2}(A_i - 1)} e^{\frac{B_i}{k_B T}} Y_p^{Z_i} Y_n^{N_i} \tag{1.2}$$

where B_i and G_i are the binding energy $B_i = Z m_p c^2 + (A - Z) m_n c^2 - m_{(Z,A)} c^2$ and nuclear partition function $G_i(T) = \sum_k (2J_k + 1) e^{-E_k/k_B T}$ of species i, respectively (for details see e.g. Arcones et al., 2010). Mass and charge conservation follow from

$$\sum_i Y_i A_i = 1 \tag{1.3}$$

$$\sum_i Y_i Z_i = Y_e \tag{1.4}$$

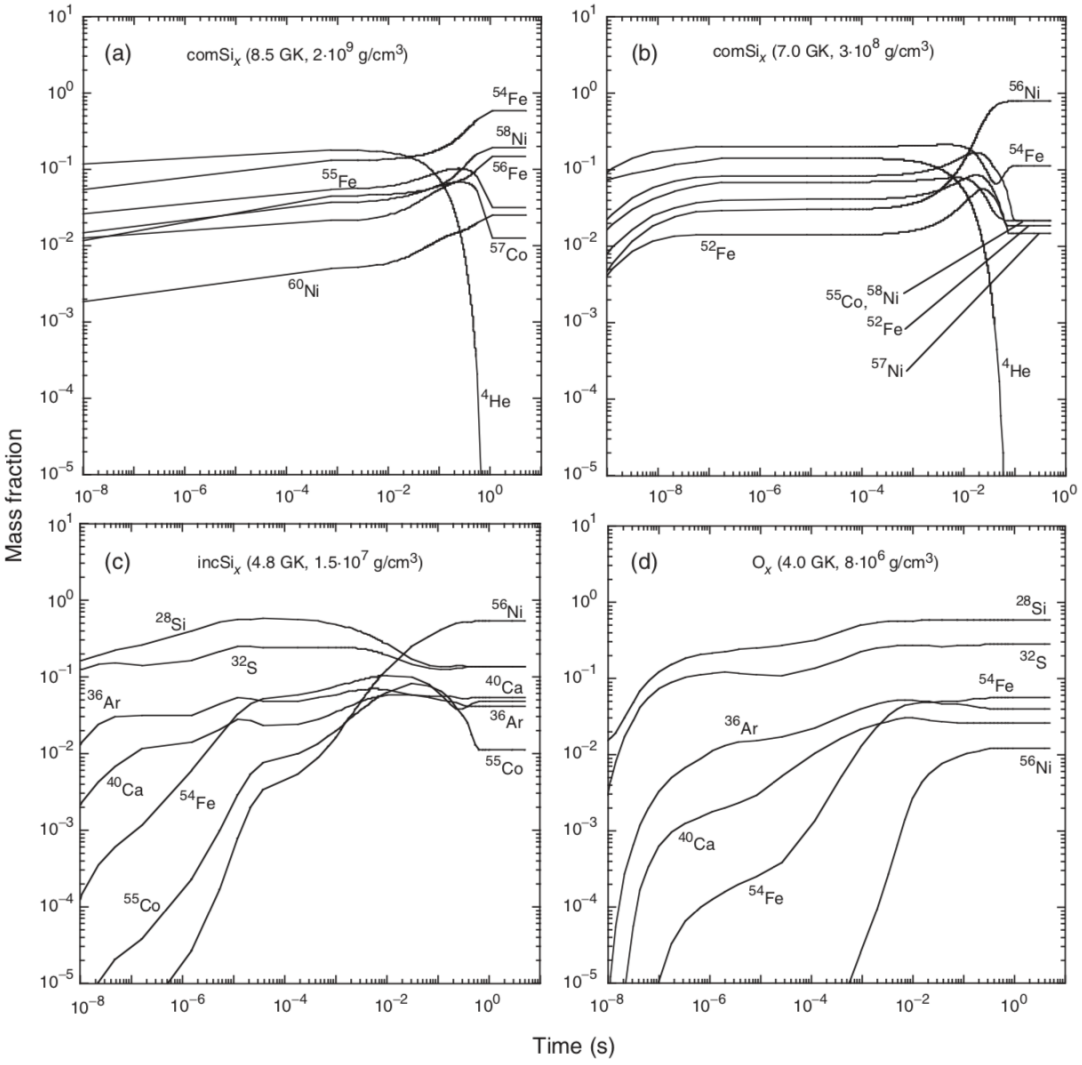

Figure 1.22.: Abundance evolution with time for explosive nucleosynthesis in SNe Ia. Burning conditions are indicated in the panels. Shown from the top left to the bottom right: a) complete silicon burning at high densities b) complete silicon burning at low densities c) incomplete silicon burning d) oxygen burning. The initial composition of the WD is $X_{^{12}\mathrm{C}} = 0.0475$, $X_{^{16}\mathrm{O}} = 0.500$ and $X_{^{22}\mathrm{Ne}} = 0.025$ (neutron excess $\eta = 0.0023$). Taken from Iliadis (2015).

where Y_e is the electron fraction n_{e^-}/n of the nuclear fuel. The electron fraction is typically affected by weak processes which operate on time scales that are much larger than electromagnetic and strong reactions. In NSE, nuclear fuel (^{12}C, ^{16}O, ^{22}Ne) is quickly converted into IGEs with no IMEs (e.g ^{28}Si) remaining. For pure ^{12}C and ^{16}O fuel NSE favours the production of ^{56}Ni as it is the most tightly bound nucleus with $N = Z$. As the ashes are expanding and cooling they are eventually dropping below the freeze-out temperature. At the relatively high densities in exploding WDs, normal freeze-out due to a lack of α-particles occurs on time scales much faster than nuclear rearrangement. As a result, abundances at freeze-out are virtually identical to the final abundances (De et al., 2014).

Incomplete silicon burning

In layers where the burning conditions are less extreme ($4.5 \times 10^9\,\mathrm{K} < T < 5 \times 10^9\,\mathrm{K}$) incomplete silicon burning is still possible. Burning no longer takes place in NSE but instead quasi-NSE conditions are fulfilled. Freeze-out occurs before IMEs are completely converted to IGEs. The exact isotopic distribution depends on the expansion time scale. The most abundant isotope in thermonuclear explosions produced in the incomplete silicon burning regime remains ^{56}Ni, but between 10% and 20% of ^{28}Si, among other IMEs and IGEs, are synthesised.

Oxygen burning

In the outer layers flame temperatures are too low ($3.5 \times 10^9\,\mathrm{K} < T < 4.5 \times 10^9\,\mathrm{K}$) to establish NSE. Only marginal quantities of IGEs are produced while the vast majority of the material is locked in the silicon group. Abundances of isotopes other than those with $N = Z$ depend sensitively on the neutron excess. In this layer, most of the IMEs found in SNe Ia are produced: ^{28}Si, ^{32}S, ^{36}Ar and ^{40}Ca.

Neon-carbon burning

Layers where peak temperatures only reach $2 \times 10^9\,\mathrm{K} < T < 3.5 \times 10^9\,\mathrm{K}$ experience neon-carbon burning (neon at the upper limit, carbon at the lower limit). Below this threshold the nuclear flame is quenched and nucleosynthesis ceases. Both the temperature and expansion time scale during explosive neon-carbon burning are too small to establish quasi-equilibrium. During neon burning, ^{20}Ne is photodisintegrated into ^{16}O and α-particles, which continue to increase the abundances of ^{24}Mg and ^{28}Si. At lower temperatures ^{12}C is burned to mainly ^{20}Ne. The abundances of synthesized species no longer only depend on temperature, density and neutron excess, but are instead dominated by the initial composition and the thermonuclear reaction rates.

1.5.4. Electron Capture

For a pure C/O WD burning to NSE stops at the 'magic number' nucleus ^{56}Ni. In massive WDs above $\sim 1.2\,M_\odot$, the inner core ($\approx 0.2\,M_\odot$) densities are above a few $10^8\,\mathrm{g\,cm^{-3}}$. Under these conditions, the conversion of protons to neutrons through electron capture becomes favourable as the Fermi energy of the degenerate electron gas is high enough. Electron capture reactions then proceed at rates faster than the expansion time scale of the incinerated WD. As a consequence, NSE conditions that otherwise would lead to ^{56}Ni dominated ejecta are adjusted towards more neutron-rich species such as ^{54}Fe and ^{58}Ni. However, only a small part of the WD is affected by electron capture reactions during the nuclear burning phase. For Chandrasekhar mass delayed detonation models that might reproduce normal SNe Ia only 1/3 of the synthesized ^{56}Ni originated in layers where electron capture is relevant. Strong mixing of burning ashes in n-NSE and NSE layers is required as their separation would be in tension with observations.

1.6. The Search for SN Ia Progenitors

The search for solutions to the progenitor and explosion mechanism problem of SNe Ia has been the aim of many studies since their discovery. Even though there is much indirect evidence for one or the other model, alternatingly supporting either single- or double-degenerate as well as Chandrasekhar mass or sub-Chandrasekhar mass scenarios, a smoking gun remains elusive. Up to now, a range of different methods have been applied using observations from before to thousands of years after the explosion and with observations in the radio, IR, optical, UV, x-rays and γ-rays. In the following, a short (and probably incomplete) summary of the chase for thermonuclear progenitors is given.

1.6.1. Companion searches

WD stars are faint and can only be observed in the solar neighbourhood. However, if they explode through accretion from a companion star, the donor may survive and could be found. Companion candidates are expected at velocities of several hundred $\mathrm{km\,s^{-1}}$ – the former orbital velocity – as the binary breaks apart. The impact of the supernova ejecta on the companion could result in the Kelvin-Helmholtz collapse of the extended envelope, increasing its brightness by a factor of $10-10^3$ for up to 10^4 years. Searches for surviving companions have been conducted in historical supernova remnants such as SN 1006 (Kerzendorf et al., 2012, 2018b), SN 1572 (Ruiz-Lapuente, 2004; Kerzendorf et al., 2009, 2013, 2018a; González Hernández et al., 2009) and SN 1604 (Kerzendorf et al., 2014), as well as a number of ancient LMC remnants (Schaefer & Pagnotta, 2012; Edwards et al., 2012). To date, no convincing surviving companions have been found in any of the historical remnants. Non-degenerate puffed-up companions would also be visible at the locations of recent SNe in nearby galaxies, though again, no evidence for surviving

donors has been found neither in archival pre-explosion images nor after the SN has faded (Li et al., 2011a; Bloom et al., 2012; Shappee et al., 2013).

1.6.2. Accretion to the Chandrasekhar mass

In the accreting WD progenitor scenario we can expect some enrichment of the CSM either from the stellar wind or from material that was not accreted and as a result, expelled from the system. On the other hand, coalescing WDs (sub-Chandrasekhar) are not expected to enrich the CSM in any significant way. There are a handful of cases where CSM interaction was observed in SNe Ia: Hamuy et al. (2003) and Deng et al. (2004) for SN 2002ic, Dilday et al. (2012) for PTF 11kx, Harris et al. (2018) and Graham et al. (2019) for SN 2015cp and Vallely et al. (2019) and Kollmeier et al. (2019) for SN 2018fhw (for a summary of 16 SNe Ia CSM see Silverman et al., 2013b). The vast majority of SNe Ia do not show any hint of CSM interaction. After the explosion the SN shock wave ploughs through the CSM, accelerating electrons to relativistic speeds and generating strong magnetic fields. Relativistic electrons moving in a magnetic field radiate via synchrotron emission in radio (Chevalier, 1982a, 1998; Chevalier & Fransson, 2006). Thermal bremsstrahlung from the hot post-shocked gas and inverse Compton scattering of SN light by relativistic electrons can additionally produce x-rays. So far, no radio emission has been detected for any SN Ia (Panagia et al., 2006). Even for the two closest SNe Ia of the last decade (SN 2011fe and SN 2014J) both radio (Pérez-Torres et al., 2014; Horesh et al., 2012) and x-ray (Horesh et al., 2012; Margutti et al., 2014) observations resulted in non-detections for both objects.

1.6.3. Explosion asymmetries

In general, SNe Ia exhibit a relatively high degree of spherical symmetry (see Fig. 1.1), though there seem to be objects that show double-peaked line profiles (Dong et al., 2015). Emission that originates from an expanding sphere or spherical shell will exhibit single-peaked or flat-top line profiles, respectively. Violent mergers and head-on collisions are expected to produce ejecta asymmetries, which result in a viewing angle dependence of the observed light curves and spectra and an overall high polarisation degree. Bulla et al. (2016b) showed that violent mergers would produce a significant polarisation signal. Observations typically exhibit continuum polarisation of order one percent which is incompatible with the results of the models. Only highly polarised objects such as SN 2004dt (Leonard et al., 2005) are in agreement with observations, but only a small fraction of all SNe Ia fall into this category.

1.6.4. Super-soft X-ray sources

Steady accretion and nuclear burning on the surface of WDs was suggested to lead to the emission of super-soft x-rays (van den Heuvel et al., 1992; Kahabka & van den Heuvel, 1997). The emission spectrum peaks between 30 and 100 eV with luminosities between 10^{37} and $10^{38}\,\mathrm{erg\,s^{-1}}$. Gilfanov

& Bogdán (2010) showed that the integrated super-soft x-ray emission in elliptical galaxies provides an upper limit to the number of massive, accreting WDs in binary systems. They conclude that no more than 5% of all SNe Ia in these galaxies originate in the single-degenerate channel. A more recent study by Nielsen et al. (2012) confirmed that none of the nearby objects in their sample were bright super-soft x-ray sources before the explosion, and possibly, none of them were accreting to the Chandrasekhar limit.

1.6.5. Nucleosynthetic yields

A completely different approach to determining the progenitor system of thermonuclear SNe has already been outlined in Sec. 1.5. In contrast to the previously detailed approaches, nucleosynthetic yields are mostly sensitive to the mass of the WD at the time of explosion and not the nature of the companion or the ignition mechanism. In fact, several explosion families (mass range, ignition mechanism and flame propagation) can produce light curves, spectra and absolute brightnesses (in terms of the ^{56}Ni mass) that are in agreement with observations. Large differences between high-density and low-density explosions occur in the neutronisation fraction and the resulting isotopes. This approach has been used extensively over the last decade – though trial studies were conducted much earlier. The neutronisation fraction can be probed in many ways: contributions to the long term evolution of the light curve from longer living isotope decay chains, IME and IGE abundances from x-ray spectra of SN remnants and the iron-rich ejecta composition from nebular spectra.

Contributions to the extremely-late light curve

The optical and NIR light curves of SNe Ia are entirely powered by ^{56}Ni decay chain for the first three years after the explosion (see Fig. 2.1.3). If present in the ejecta, decays of neutron-rich isotopes (^{57}Co, ^{55}Fe) can power the light curve even longer. Massive WDs near the Chandrasekhar limit can produce ^{57}Ni masses between 1.5 and 2.5% of the synthesised ^{56}Ni mass. Sub-Chandrasekhar mass explosions can at most produce 2% unless an unrealistically high progenitor metallicity (several times solar) is invoked (see Fig. 1.23 and Tab. 1.2). For sub-solar to solar metallicity progenitors the fraction of ^{57}Ni / ^{56}Ni remains below 1%.

Supernovae at epochs later than 1000 days are $\sim$ 15 mag fainter than at maximum light - for every one million photons emitted at maximum light only a single photon is emitted when the ^{57}Ni decay chain overtakes the decay chain of ^{56}Ni in the energy deposition rate. Accurate photometric measurements are only possible for nearby, formerly bright, objects which are not contaminated by host galaxy light. The method is among the simplest: filter-band magnitudes are combined to construct a quasi-bolometric (UVB to NIR) light curve, which is then compared with explosion models. Unfortunately, the physical processes that govern the late light curves have long time constants, many of which are poorly constrained by the data. This is especially true for ionisation and recombination, as detailed in Fransson & Jerkstrand (2015).

The prediction made by Axelrod (1980), that roughly one year after explosion the ejecta undergo a so-called *IR catastrophe* (IRC), has not been directly observed in any SN Ia. The IRC is assumed to occur when the temperature drops below the threshold ($\sim 2000\,\mathrm{K}$) where levels responsible for optical and NIR transitions can be easily populated through collisional processes. Below this threshold, cooling proceeds only through low-energy fine-structure transitions in the mid- and far-IR. Cooling through these lines is constant as long as the temperature is higher than the excitation temperature of the levels involved ($\sim 300\,\mathrm{K}$), while the energy input is declining exponentially. As a consequence, the temperature in the ejecta drops to a few hundred Kelvin within a short period. A spectrum of SN 2011fe at an epoch of ~ 1000 days shows lines which have been interpreted to originate from fluorescence, indicating that the IRC has likely occurred (Taubenberger et al., 2015). However, direct evidence for the IRC would require the detection of [Fe II] mid-IR lines.

The fact that SNe Ia at epochs where the IRC should long since have occurred still emit in the optical and NIR adds to the uncertainty of the pseudo bolometric method. It is unclear what fraction of the radioactive decay energy is converted into optical and NIR photons. It comes as no surprise that – even for the same object – conflicting results are obtained (e.g. for SN 2011fe Shappee et al., 2017; Dimitriadis et al., 2017; Kerzendorf et al., 2017). The experiment was repeated for a number of nearby objects: SN 2012cg Graur et al. (2016), SN 2013aa (Jacobson-Galán et al., 2018), SN 2014J (Yang et al., 2018), ASASSN-14lp (Graur et al., 2018a), SN 2015F (Graur et al., 2018b). Kerzendorf et al. (2017) argue that the uncertainty imposed by the energy deposition and emission processes is likely greater than the difference between Chandrasekhar mass and sub-Chandrasekhar mass models. Observations of the [Fe II] $26\,\mu$m fine-structure line would be key in resolving the powering of SN light curves after several years.

X-ray abundances of SN remnants

SNe Ia are classified as remnants when they have swept up their own mass in CSM/ISM and are considerably slowed down. The time it takes to reach this phase depends on the density of the SN environment – from hundreds to a few thousand years. Several decades after the explosion no heating from radioactive decays is in effect any longer. Due to the continued adiabatic expansion of the ejecta they cool to very low temperatures. As the ejecta come in contact with CSM a blast wave forms. The reverse shock reheats the ejecta that run through it, causing them to emit x-rays in the form of continuum emission (hot electron gas with $k_B T \sim 5\,\mathrm{keV}$) and line emission (vacancy of a K or L shell electron filled by an outer shell electron). With the decelerating blast wave the timescale for radiative cooling becomes similar to the remnant age. As cooling becomes more important deceleration decreases and the remnant enter the so-called radiative cooling phase, where low-ionisation stages of abundant material emit UV, optical and IR lines.

X-ray spectra of supernova remnants (SNRs) in the Milky Way and the Large and Small Magellanic Clouds exhibit lines from stable neutron-rich isotopes in the central region of the explosion which was thermalised by the reverse shock. After hundreds of years, no traces of

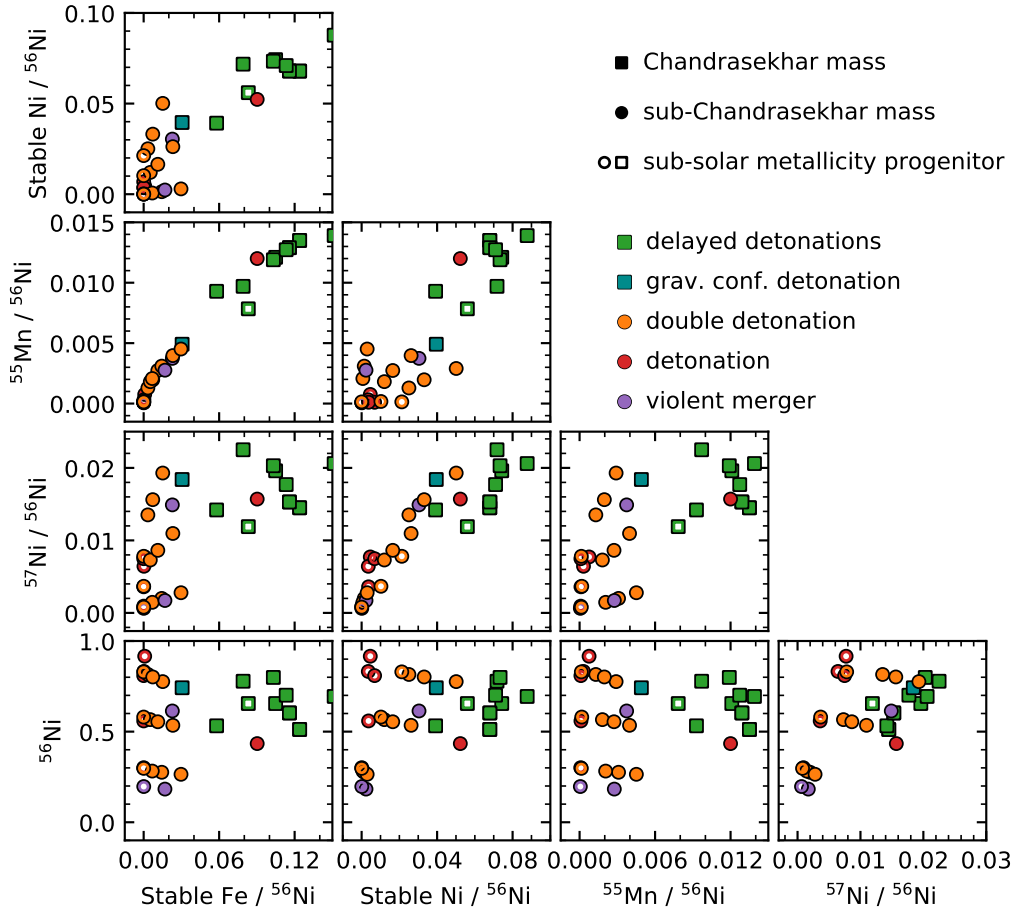

Figure 1.23.: Nucleosynthetic yields of IGE from various explosion models from the literature. Colours denote different explosion mechanisms, symbols distinguish between the WD mass at the time of the explosion and empty symbols indicate sub-solar metallicity progenitors. A clear separation in nucleosynthetic yields of neutron-rich material can be observed between Chandrasekhar mass and sub-Chandrasekhar mass explosions (see text). The red data point within the region defined by Chandrasekhar mass explosion yields stems from a super-solar metallicity detonation ($Z \sim 3Z_{\odot}$). The explosion mechanism only weakly affects the nucleosynthetic yields. 'Stable Fe' includes both ^{54}Fe and ^{56}Fe. 'Stable Ni' includes ^{58}Ni as well as the short lived isotopes ^{60}Zn, ^{61}Zn and ^{62}Zn which decay to stable nickel isotopes of the same atomic mass number. '^{55}Mn' contains all isotopes of the decay chain that will decay to stable manganese. Models are from: delayed detonations (Seitenzahl et al., 2013; Ohlmann et al., 2014), gravitationally confined detonations (Seitenzahl et al., 2016), detonations (Sim et al., 2010; Marquardt et al., 2015), double detonations (Shen et al., 2018) and violent mergers (Pakmor et al., 2012, 2013; Kromer et al., 2016).

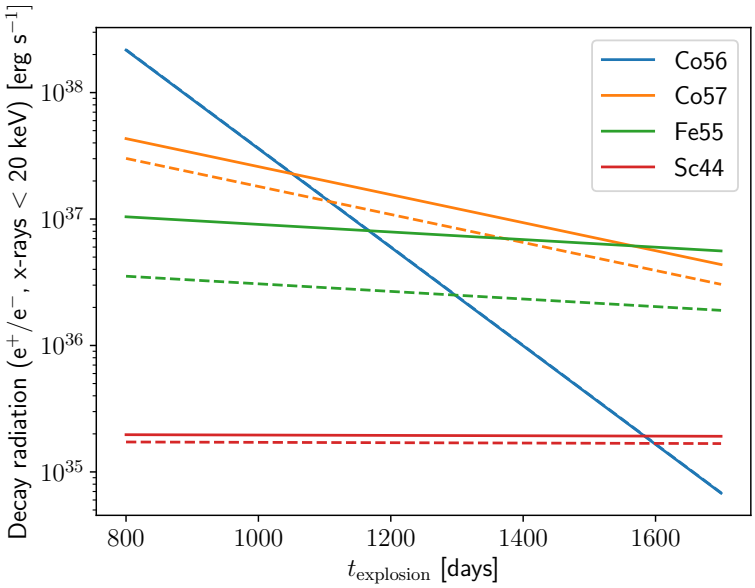

Figure 1.24.: Deposited decay energy for four species as a function of time. Only charged leptons (e^-/e^+ and X-rays up to 20 keV have been considered. Abundances are taken from the Chandrasekhar mass delayed detonation N100 (solid lines) and a sub-Chandrasekhar mass violent merger of a 0.9 and 1.1 $M_\odot$ C/O WD (dashed lines). Adapted from Kerzendorf et al. (2017).

radioactive isotopes of the most common decay chains are left and only stable material is present. X-ray emission can trace both the inner core and the intermediate layers of SNe Ia.

X-ray emission of manganese, iron and nickel serve as tracers of the high-density burning region. Measurements of their relative abundances constrain the properties of the core, where in the Chandrasekhar mass scenario, electron capture neutronisation, progenitor metallicity and carbon simmering contribute (Badenes et al., 2008; Park et al., 2013; Yamaguchi et al., 2015). Substantial variations of the Mn/Fe and Ni/Fe ratio have been found in remnants, though not all SNRs are in the same evolutionary stage. Since the sample is limited and unlikely to increase the possibility that we are observing a peculiar population of SNe Ia in the MW cannot be discounted.

Recently, a different probe was identified by Martínez-Rodríguez et al. (2017) that is based on the Ca/S yield (see Fig. 1.25). Both elements are produced in the intermediate layers and are not affected by electron captures in the inner core. This ratio is very sensitive to the neutronisation in the burning region, with more neutron-rich progenitors having lower Ca/S mass ratios. They find that both LMC and MW SNRs display strong neutronisation that cannot be attributed to progenitor metallicity alone. As electron capture neutronisation does not affect the emitting region and carbon simmering seems to be too weak to explain the observed effect, it remains unclear what causes the observed neutronisation.

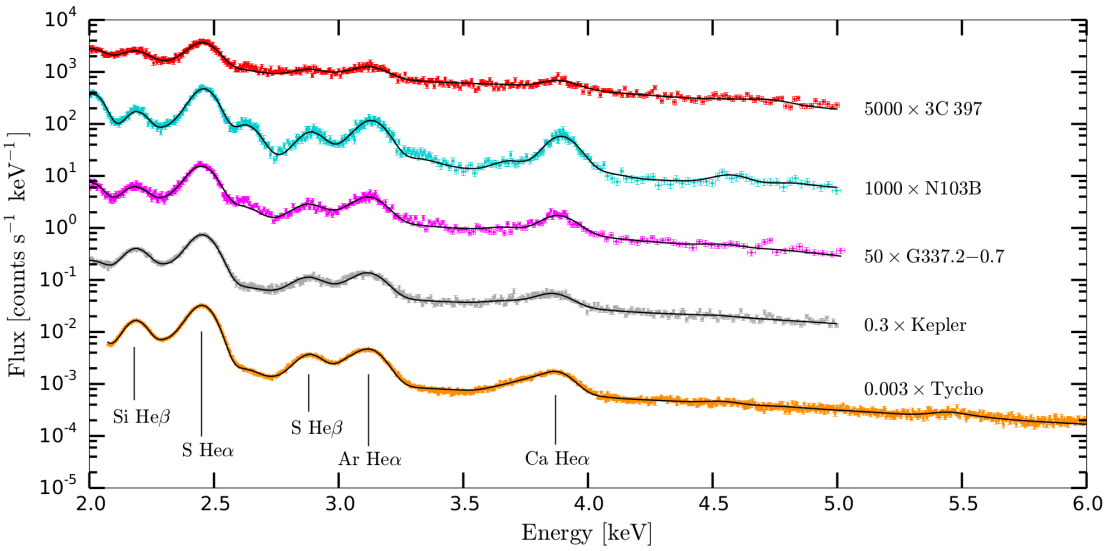

Figure 1.25.: X-ray (Suzaku) observations of five SNRs. The spectra are sorted in decreasing order of Fe ionisation state. *Heα* and *Heβ* indicate spectral lines of two electron ions. Taken from Martínez-Rodríguez et al. (2017).

Nebular phase emission line abundances

Transitioning into the nebular phase, SNe Ia become transparent ($\tau < 1$) to optical and NIR photons. At this stage, the whole ejecta are, in principle, visible, though only the denser inner regions are strong emitters. As a result, emission lines of IGEs are abundant. The intrinsic emission is Doppler broadened reflecting the expansion velocity of the ejecta ($\sim 7000 - 11000\,\mathrm{km\,s^{-1}}$) and consequently the spectral features blend to form broad features. By determining the excitation conditions of the emitting nebula, it is possible to infer ion abundances through spectral modelling. Inferring abundances is a complex inversion process. During the nebular phase, the emitting plasma is a mixture of radioactive and stable material, of a multitude of isotopes and decay products of several decay chains. The aim of the work described herein is to determine the excitation conditions, untangle the contributions of the various ion species and determine the abundances of neutron-rich isotopes for a large population of objects from the local universe.

Table 1.2.: Nucleosynthetic yields of IGE from various explosion models from the literature at 100 seconds after the explosion was started. Masses are given as $A \times 10^B = A(B)$.

Type	Ref.	Z.	Mass	stable Ni	stable Co	stable Fe	^{55}Co	^{55}Fe	^{55}Mn	^{56}Ni	^{56}Co	^{56}Fe	^{57}Ni	^{57}Co	^{57}Fe	^{59}Ni	^{59}Co
		$[Z_\odot]$	$M_\odot$	$M_\odot$	$M_\odot$	$M_\odot$	$M_\odot$	$M_\odot$	$M_\odot$	$M_\odot$	$M_\odot$	$M_\odot$	$M_\odot$	$M_\odot$	$M_\odot$	$M_\odot$	$M_\odot$
DDT N40	(1)	1.00	1.40	7.39(-2)	2.02(-4)	9.00(-2)	1.05(-2)	1.59(-3)	1.00(-5)	6.55(-1)	1.08(-4)	1.49(-2)	1.96(-2)	7.44(-4)	...	3.57(-4)	2.02(-4)
DDT rpc32	(2)	1.00	1.40	6.75(-2)	1.04(-4)	9.90(-2)	1.10(-2)	1.88(-3)	2.00(-5)	6.03(-1)	1.27(-4)	1.69(-2)	1.53(-2)	9.06(-4)	...	4.05(-4)	1.04(-4)
DDT N300C	(1)	1.00	1.40	6.75(-2)	8.00(-5)	1.03(-1)	1.13(-2)	2.12(-3)	8.00(-5)	5.12(-1)	1.19(-4)	2.09(-2)	1.45(-2)	9.92(-4)	1.08(-4)	4.23(-4)	8.00(-5)
DDT N150	(1)	1.00	1.40	6.75(-2)	8.00(-5)	1.03(-1)	1.13(-2)	2.12(-3)	8.00(-5)	5.12(-1)	1.19(-4)	2.09(-2)	1.45(-2)	9.92(-4)	1.08(-4)	4.23(-4)	8.00(-5)
DDT N100H	(1)	1.00	1.40	8.72(-2)	4.29(-4)	9.80(-2)	1.03(-2)	2.94(-3)	6.60(-4)	6.94(-1)	1.22(-4)	5.29(-2)	2.06(-2)	1.36(-3)	5.40(-4)	5.67(-4)	4.29(-4)
DDT N100L	(1)	1.00	1.40	3.91(-2)	9.02(-5)	5.70(-2)	9.01(-3)	2.75(-4)	5.00(-6)	5.32(-1)	5.43(-5)	9.46(-4)	1.42(-2)	6.54(-5)	3.46(-5)	5.78(-5)	9.02(-5)
DDT N100	(1)	0.01	1.40	5.56(-2)	3.39(-4)	6.62(-2)	6.17(-3)	1.66(-3)	1.00(-5)	6.55(-1)	9.66(-5)	1.69(-2)	1.19(-2)	8.25(-4)	7.50(-5)	4.14(-4)	3.39(-4)
DDT N100	(1)	1.00	1.40	6.75(-2)	1.04(-4)	9.90(-2)	1.10(-2)	1.88(-3)	2.00(-5)	6.03(-1)	1.27(-4)	1.69(-2)	1.53(-2)	9.06(-4)	...	4.05(-4)	1.04(-4)
DDT N20	(1)	1.00	1.40	7.15(-2)	3.11(-4)	6.71(-2)	8.48(-3)	1.20(-3)	2.00(-5)	7.78(-1)	8.25(-5)	1.19(-2)	2.25(-2)	5.69(-4)	3.10(-5)	3.01(-4)	3.11(-4)
DDT c50	(2)	1.00	1.40	7.30(-2)	2.30(-4)	8.52(-2)	1.01(-2)	1.76(-3)	4.00(-5)	7.99(-1)	1.13(-4)	1.79(-2)	2.03(-2)	8.58(-4)	...	4.07(-4)	2.30(-4)
DDT rpc40	(2)	1.00	1.40	7.06(-2)	1.58(-4)	9.54(-2)	1.09(-2)	1.83(-3)	...	7.01(-1)	1.23(-4)	1.79(-2)	1.77(-2)	8.88(-4)	1.20(-5)	4.08(-4)	1.58(-4)
Grav. Conf. Det.	(3)	1.00	1.40	3.95(-2)	2.76(-4)	2.96(-2)	4.77(-3)	1.35(-4)	5.00(-6)	7.42(-1)	2.40(-5)	9.76(-4)	1.84(-2)	2.77(-5)	...	6.93(-5)	2.76(-4)
Violent Merger	(4)	1.00	1.10	4.54(-3)	3.02(-4)	8.20(-4)	7.54(-4)	2.87(-7)	...	9.16(-1)	1.36(-5)	...	7.72(-3)	6.59(-7)	...	5.28(-5)	3.02(-4)
Violent Merger	(5)	1.00	0.90	3.49(-3)	2.58(-4)	2.21(-4)	3.10(-4)	9.71(-8)	9.03(-7)	8.32(-1)	1.03(-5)	...	6.43(-3)	5.24(-7)	...	4.79(-5)	2.58(-4)
Violent Merger	(6)	0.01	0.90	5.99(-3)	...	1.65(-5)	1.02(-4)	2.53(-6)	...	8.09(-1)	5.32(-6)	...	7.48(-3)	2.26(-5)	7.40(-6)	8.87(-4)	...
Detonation	(7)	0.00	1.15	5.00(-2)	3.04(-8)	1.51(-2)	2.87(-3)	2.85(-5)	9.51(-9)	7.76(-1)	1.69(-5)	6.76(-5)	1.93(-2)	4.76(-6)	1.14(-8)	6.14(-5)	3.04(-8)
Detonation	(7)	3.00	1.06	2.50(-2)	4.41(-9)	3.33(-3)	1.29(-3)	2.68(-6)	...	8.15(-1)	1.17(-5)	5.33(-6)	1.35(-2)	9.84(-7)	...	2.65(-5)	4.41(-9)
Detonation	(7)	0.00	1.06	3.03(-2)	2.16(-4)	2.28(-2)	3.66(-3)	7.94(-5)	...	6.14(-1)	1.79(-5)	...	1.49(-2)	1.04(-5)	...	8.53(-5)	2.16(-4)
Detonation	(7)	0.00	0.97	2.12(-2)	...	1.87(-6)	1.38(-4)	1.13(-8)	...	8.30(-1)	6.77(-6)	...	7.81(-3)	2.86(-7)	...	8.92(-5)	...
Detonation	(8)	0.00	1.21	3.31(-2)	1.21(-8)	7.20(-3)	1.96(-3)	8.50(-6)	2.07(-9)	8.02(-1)	1.35(-5)	1.69(-5)	1.56(-2)	1.93(-6)	3.07(-9)	4.20(-5)	1.21(-8)
Detonation	(8)	0.00	1.18	5.23(-2)	2.00(-7)	8.73(-2)	1.10(-2)	9.84(-4)	1.60(-5)	4.34(-1)	5.51(-5)	2.94(-3)	1.57(-2)	1.27(-4)	...	3.27(-5)	2.00(-7)
Double Det.	(9)	2.00	1.10	3.08(-3)	...	2.62(-5)	1.06(-4)	1.62(-6)	3.80(-7)	5.59(-1)	3.54(-6)	...	3.60(-3)	9.33(-6)	6.70(-7)	5.94(-4)	...
Double Det.	(9)	0.50	1.10	1.20(-2)	4.39(-8)	5.26(-3)	1.81(-3)	5.23(-6)	1.07(-9)	5.66(-1)	8.78(-6)	1.08(-5)	7.30(-3)	1.05(-6)	3.00(-9)	1.13(-5)	4.39(-8)
Double Det.	(9)	0.00	1.10	2.62(-2)	1.48(-7)	2.31(-2)	3.92(-3)	5.30(-5)	1.64(-8)	5.35(-1)	1.58(-5)	1.34(-4)	1.10(-2)	7.50(-6)	2.21(-8)	2.92(-5)	1.48(-7)
Double Det.	(9)	1.00	1.10	1.65(-2)	7.42(-8)	1.12(-2)	2.72(-3)	1.59(-5)	3.89(-9)	5.54(-1)	1.11(-5)	3.53(-5)	8.63(-3)	2.58(-6)	7.06(-9)	1.89(-5)	7.42(-8)
Double Det.	(9)	0.50	1.00	1.02(-2)	...	1.13(-5)	1.72(-4)	1.31(-8)	...	5.80(-1)	3.68(-6)	...	3.67(-3)	1.12(-7)	...	5.03(-5)	...
Double Det.	(9)	2.00	1.00	7.18(-5)	2.00(-8)	3.27(-5)	8.86(-5)	8.30(-7)	...	3.01(-1)	3.08(-6)	...	9.32(-4)	2.25(-6)	...	5.80(-6)	2.00(-8)
Double Det.	(9)	1.00	1.00	1.38(-3)	3.41(-7)	1.43(-2)	3.07(-3)	2.32(-5)	5.76(-9)	2.76(-1)	9.66(-6)	5.47(-5)	2.00(-3)	3.27(-6)	7.74(-8)	1.28(-6)	3.41(-7)
Double Det.	(9)	0.00	1.00	6.56(-4)	2.74(-7)	6.83(-3)	2.06(-3)	7.62(-6)	1.72(-9)	2.82(-1)	7.24(-6)	1.79(-5)	1.46(-3)	1.20(-6)	4.03(-8)	9.77(-7)	2.74(-7)
Double Det.	(9)	1.00	0.90	2.32(-3)	4.11(-5)	1.59(-2)	2.70(-3)	5.78(-5)	2.20(-6)	1.83(-1)	9.00(-6)	9.91(-4)	1.71(-3)	6.92(-6)	2.31(-5)	7.09(-6)	4.11(-5)
Double Det.	(9)	0.50	0.90	8.53(-5)	7.47(-6)	6.23(-5)	6.08(-5)	1.08(-7)	9.20(-8)	1.97(-1)	2.79(-6)	...	6.30(-4)	8.50(-7)	1.50(-7)	4.23(-6)	7.47(-6)
Double Det.	(9)	2.00	0.90	2.93(-3)	4.64(-7)	2.95(-2)	4.43(-3)	7.80(-5)	2.25(-8)	2.65(-1)	1.50(-5)	2.09(-4)	2.78(-3)	1.01(-5)	5.22(-8)	2.89(-6)	4.64(-7)
Double Det.	(9)	0.00	0.90	2.35(-5)	...	2.43(-5)	1.39(-4)	1.02(-8)	...	2.97(-1)	2.91(-6)	...	7.91(-4)	2.73(-8)	...	4.75(-7)	...

References:
(1) Seitenzahl et al. (2013); (2) Ohlmann et al. (2014); (3) Ohlmann et al. (2014); (4) Pakmor et al. (2012); (5) Pakmor et al. (2013);
(6) Kromer et al. (2016); (7) Sim et al. (2010); (8) Marquardt et al. (2015); (9) Shen et al. (2018)

2. Nebular Phase Spectral Modelling

In this chapter the nebular phase physics is presented and a model to interpret the optical and infrared spectra of SNe Ia shall be developed. Emission spectra of the most common ions will be presented. The spectral model is applied to observed data and serves to extract the salient properties of the lines - flux, rest velocity, and Doppler broadening. These quantities allow us to constrain models of SNe Ia. Results are presented in three published papers and referenced whenever applicable throughout this chapter.

2.1. Nebular Phase Physics

In the nebular phase the ejecta are heated by the products of the radioactive decays of the isotopes made in the explosion. γ-rays, positrons, high-energy electrons or X-rays deposit some fraction of their energy in the ejecta. This energy input determines the plasma state of the ejecta (ionisation and excitation). Excited atomic/ionic states emit radiation, which, due to low opacities, can mostly escape. Fig. 2.1 shows the physical processes during the nebular phase and the associated energies.

2.1.1. Sobolev Approximation

Simulations of SNe Ia have shown that the ejecta are freely expanding (their kinetic energy density is much bigger than their gravitational and internal energy densities) after about one minute after the explosion (Röpke, 2005). Photons emitted inside the ejecta have their co-moving frame frequency redshifted as they propagate through the material. Interactions of photons with spectral lines are only possible where the redshifted photon frequency ν' matches the frequency of the line ν_0. The spatial region where this condition is fulfilled is called the *Sobolev point* (Sobolev, 1957; see also Mihalas, 1978 for a summary). Before this point, the photon encounters no optical depth from this particular line. Upon reaching the Sobolev point the entire optical depth is encountered within a very small volume. As a consequence of the continuous redshifting every Sobolev point can be reached only once.

In bound-bound transitions the opacity is given by

$$\chi_{lu}^{bb} = n_l \frac{B_{lu} h\nu_{lu}}{4\pi} \left(1 - \frac{g_l n_u}{g_u n_l}\right) \frac{1}{\Delta\nu} \tag{2.1}$$

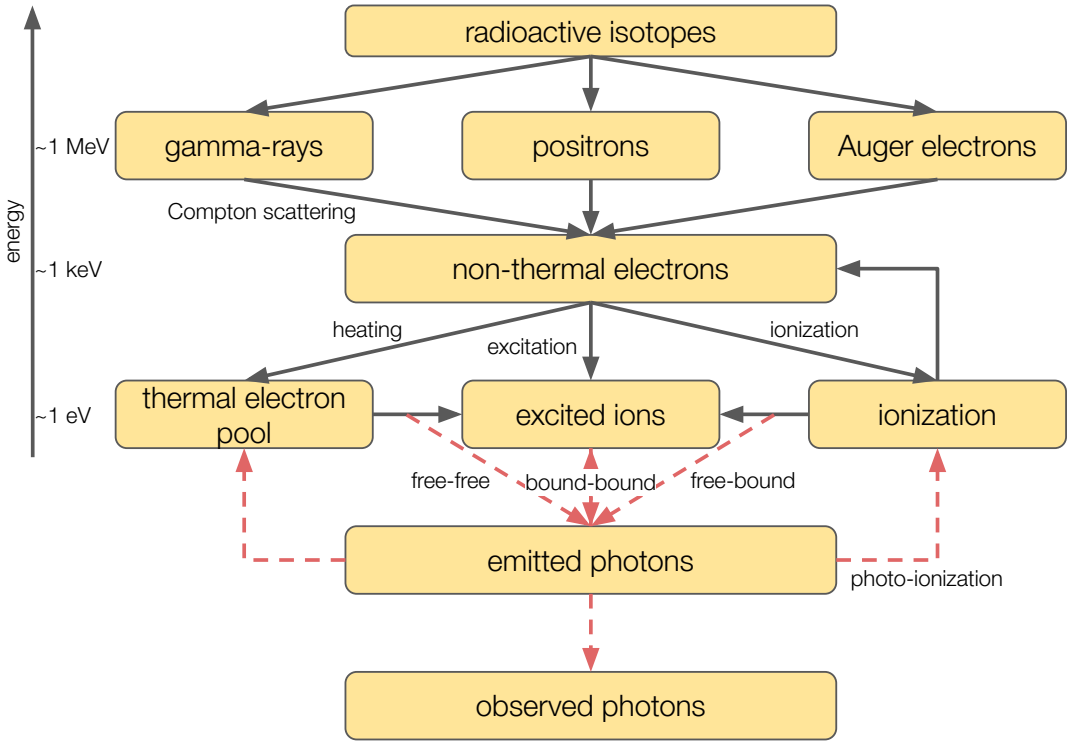

Figure 2.1.: Overview of relevant physical processes during the nebular phase. Changes of the isotopic or plasma state are shown as solid grey lines. Couplings between photons and the plasma state are shown as dashed red lines.

where n_l and n_u are the number densities of the lower and upper level, g_l and g_u are the corresponding statistical weights of the levels, B_{lu} is the Einstein B-coefficient with $A_{ul}/B_{ul} = 2h\nu_{ul}^3/c^2$ and the line profile is assumed to be a box function of width $\Delta\nu$. Enforcing homologous expansion ($dV/ds = 1/t$) in combination with the Doppler formula ($\Delta V_{lu} = \Delta\nu\lambda_{lu}$) leads to

$$s_{lu} = \Delta\nu\lambda_{lu}t \tag{2.2}$$

where s_{lu} is the *Sobolev length*. The Sobolev optical depth $\tau_{lu}^{bb} = \chi_{lu}^{bb}s_{lu}$ is then

$$\tau_{lu}^{bb,S} = \frac{A_{lu}\lambda_{lu}^3 n_l t}{8\pi}\frac{g_u}{g_l}\left(1 - \frac{g_l n_u}{g_u n_l}\right) . \tag{2.3}$$

The photon escape probability is then given by

$$\beta_{\mathrm{esc},lu} = \frac{1 - e^{-\tau_{lu}^{bb,S}}}{\tau_{lu}^{bb,S}} . \tag{2.4}$$

This is the probability that a photon can leave the emitting region instead of being reabsorbed. As the ejecta are expanding ($\rho \propto t^{-3}$) the Sobolev optical depth only decreases as t^{-2}. The Sobolev approximation assumes that lines are isolated and not overlapping, which is well justified for optical and IR lines. The density of strong UV lines in metal-rich ejecta can be so high that the wings of the line profiles begin to overlap and multiple sources of opacity contribute (Baron et al., 1996).

2.1.2. Radioactivity

Shortly after the explosion the main contributor to the deposited energy is ^{56}Ni, but already at maximum brightness the decay of its daughter nucleus ^{56}Co to ^{56}Fe dominates. During the nebular phase until about three years after the explosion will ^{56}Co continue to provide the bulk of the energy to power the SN light curve as it is by far the most abundant radioactive isotope and, assuming that positrons are still trapped, provides the most energetic and easily depositable products. As ^{56}Co fades the contributions of other isotopes can become visible.

Radioactive isotopes which can be produced in significant abundances in thermonuclear explosions are given in Eqs. 2.5–2.8. First steps in the decay chains with half-lives shorter than that of ^{56}Co (77.2 d) do not play a role to the energy deposition during the nebular phase. On the

Table 2.1.: Average radioactive decay energies of the most abundant radioactive isotopes in SNe Ia (keV decay^{-1}) without energy carried away by neutrinos . Positron rest masses are included in the γ-ray column due to annihilation. Data taken from Bé et al. (2004, 2006).

Nucleus	γ-ray		Auger e^-		IC e^-		e^+		X-ray	
	E	%	E	%	E	%	E	%	E	%
^{57}Co	121.54	85.0	7.594	5.3	10.22	7.2	-	-	3.598	2.5
^{56}Co	3329.5	96.5	3.355	0.1	0.374	0.0	115.7	3.4	1.588	0.0
^{55}Fe	-	-	3.973	70.8	-	-	-	-	1.635	29.2
^{44}Ti	138.79	92.4	3.519	2.4	7.064	4.7	-	-	0.768	0.5
^{44}Sc	1172.3	66.3	0.163	0.0	0.074	0.0	595.8	33.7	0.030	0.0

other hand, the decay of ^{44}Sc to ^{44}Ca can be regarded as instantaneous compared to the decay of ^{44}Ti.

$$^{56}\mathrm{Ni} \xrightarrow{t_{1/2}= 6.08d} {}^{56}\mathrm{Co} \xrightarrow{t_{1/2}= 77.2d} {}^{56}\mathrm{Fe} \tag{2.5}$$

$$^{57}\mathrm{Ni} \xrightarrow{t_{1/2}= 35.60h} {}^{57}\mathrm{Co} \xrightarrow{t_{1/2}= 271.79d} {}^{57}\mathrm{Fe} \tag{2.6}$$

$$^{55}\mathrm{Co} \xrightarrow{t_{1/2}= 17.53h} {}^{55}\mathrm{Fe} \xrightarrow{t_{1/2}= 999.67d} {}^{55}\mathrm{Mn} \tag{2.7}$$

$$^{44}\mathrm{Ti} \xrightarrow{t_{1/2}= 58.9y} {}^{44}\mathrm{Sc} \xrightarrow{t_{1/2}= 3.97h} {}^{44}\mathrm{Ca} \tag{2.8}$$

The decay process depends on the decaying isotope. For radioactive nuclei which make significant contributions in the nebular phase only two channels are relevant: electron capture (EC) and beta plus decay (β^+). In the case of EC an electron from the K or L shell is captured, converting a proton in the nucleus to a neutron. Most of the energy released in the conversion is subsequently emitted as an electron neutrino. The missing K or L shell electron is filled by an outer shell electron, emitting X-rays or ejecting other electrons (Auger) in the process. In the β^+ decay, the weak force converts one of the up-quarks in a proton to a down-quark (converting the proton into a neutron), an electron neutrino ν_e and a positron e^+. Right after the conversion, daughter nuclei often end up in excited states, decaying to the ground state by emission of γ-rays and internal conversions (IC), where the energy is used to eject one of the orbiting electrons. If this electron belonged to one of the inner shells the gap in the electron configuration is filled with one of the outer shell electrons which emits the binding energy difference in the form of x-rays. The energies and energy fractions produced in each channel are given in Tab. 2.1. For most of these isotopes a large fraction of the decay energy is emitted in the form of γ-rays. Due to incomplete γ-ray trapping other channels with higher probabilities of thermalisation can still contribute significantly to the energy deposition even if they constitute only a small fraction of the decay energy.

2.1.3. Energy Deposition

Energy deposition is highly dependent on the nature of the energy carrier. In the following, interactions between SN ejecta and each of the channels from Tab. 2.1 are discussed.

γ-rays

γ-rays carry most of the decay energy and interact through Compton scattering. In this process, a photon of energy E collides in-elastically with a free electron. For typical γ-ray energies ($\sim 1\,\mathrm{MeV}$) the difference of the interaction with bound and free electrons becomes negligible. As a result, γ-ray energy deposition is independent of the excitation/ionisation state of the ejecta and similar across for thermonuclear SNe. The Compton opacity κ_C is given by

$$\kappa_\mathrm{C} = \frac{n_\mathrm{e}^\mathrm{tot}}{\rho}\,\sigma \tag{2.9}$$

where n_e is the total electron density (bound and free) of the interacting material and σ is the Compton cross section (see below). Compton scattering leaves the electron with a net energy gain while reducing the photon energy by the same amount. Emergent photons will have an inclination of θ with respect to their initial directions. Considering free electrons at rest the equations of conservation of energy and momentum give us a relation between the energy E_s of the secondary photon and its emission angle relative to the initial direction:

$$E_s = \frac{E}{1+\varepsilon(1-\cos(\theta))} \tag{2.10}$$

Here $\varepsilon = E/(m_e\,c^2)$ is the photon energy in multiples of the electron rest energy. From Eq. 2.10 the minimum and maximum post scattering photon energies become clear:

$$E_\mathrm{s,min} = \frac{E}{1+2\varepsilon} \qquad \text{for backward scattering} \qquad \theta = \pi \tag{2.11}$$

$$E_\mathrm{s,max} = \quad E \qquad\quad \text{for forward scattering} \qquad \theta = 0 \tag{2.12}$$

The angular scattering cross-section is given by Klein-Nishina's formula (Heitler, 1954):

$$\frac{d\sigma_\mathrm{KN}(\theta)}{d\Omega} = \frac{r_e^2}{2}\left[1+\varepsilon\,(1-\cos(\theta))\right]^{-2}\left(1+\cos^2(\theta)+\frac{\varepsilon^2(1-\cos(\theta))^2}{1+\varepsilon(1-\cos(\theta))}\right) \tag{2.13}$$

At the low energy limit the cross section for Compton scattering reduces to the Thomson cross section $\sigma_T = 6.65\times10^{-25}\,\mathrm{cm}^2$. For higher energies of order 1 MeV Compton scattering is less likely ($\sigma \sim \sigma_T/3$) and less efficient, as most photons are forward-scattered and very little energy is transferred to the electron.

Often γ-ray energy deposition is treated as an 'effective opacity' (see Colgate et al., 1980; Axelrod, 1980; Woosley & Weaver, 1980). Swartz et al. (1995) showed that the effective opacity for Compton scattering is between

$$\kappa_{\mathrm{C}}^{\mathrm{eff}} = (0.028 - 0.033)\,\frac{Y_e}{0.5}\,\mathrm{cm}^2\,\mathrm{g}^{-1} \tag{2.14}$$

Jerkstrand (2011) estimate the accuracy of the total energy deposition using an effective opacity to be of order $\sim 10-20\%$, though for highly aspherical ejecta there can be large differences. Additionally, the spatial location of the energy deposition is poorly reproduced (multiple scattering events compared to a single absorption event).

γ-ray energy deposition becomes less effective as the ejecta expand and dilute. Employing an effective γ-ray opacity $\kappa_{\mathrm{C}}^{\mathrm{eff}} = 0.03\,\mathrm{cm}^2\,\mathrm{g}^{-1}$ the time scale when energy deposition is no longer dominated by γ-rays ($P_{\gamma,\mathrm{dep}} < 0.034$, where 0.034 is the fraction of the decay energy given to the positron from Tab. 2.1) is given by

$$t_{\gamma\,\mathrm{to}\,\beta^+} = 240\,\mathrm{d}\,\left(\frac{M}{0.6\,M_\odot}\right)^{1/2}\,\left(\frac{v}{7500\,\mathrm{km\,s^{-1}}}\right)^{-1}\,. \tag{2.15}$$

where M is the mass of radioactive ^{56}Ni and v is the expansion velocity of the IGE-rich ejecta (for a similar derivation for SNe II see Jerkstrand, 2011). While $t < t_{\gamma\,\mathrm{to}\,\beta^+}$ the energy deposition is dominated by γ-rays and thus depends on the density and is spatially inhomogeneous. For $t > t_{\gamma\,\mathrm{to}\,\beta^+}$ the ejecta density is too low for γ-rays to interact and deposit energy. After this time energy deposition is dominated by positrons independently of the density, even though they only carry a small fraction of the decay energy.

Charged leptons

High-energy electrons and positrons lose their energy quickly through interactions (excitations and ionisations). As their energy ($\sim$ 1 MeV) is much higher than excitation ($\sim$ 1 eV) and ionisation ($\sim$ 10 − 50 eV) potentials, of order 10^5 interactions are required until thermalisation is achieved. Using an effective opacity similar as for γ-rays, Colgate et al. (1980) and Axelrod (1980) determined the absorption coefficient to be

$$\kappa_{e^+/e^-}^{\mathrm{eff}} = (7-10)\,\frac{Y_e}{0.5}\,\mathrm{cm}^2\,\mathrm{g}^{-1}\,. \tag{2.16}$$

As the mean free path s scales as $s \propto (\kappa^{\mathrm{eff}})^{1/2}$ charged leptons can only travel 1/17 as far as γ-rays. The time at which the fraction of trapped positrons drops below $\mathrm{f_{trap}}$ is then given by (Jerkstrand, 2011)

$$t_{\mathrm{e^+/e^-}} = 2.1\,\mathrm{yr}\,\left(\frac{M}{0.6\,M_\odot}\right)^{1/2}\,\left(\frac{v}{7500\,\mathrm{km\,s^{-1}}}\right)^{-1}\,(-\log(1-\mathrm{f_{trap}}))^{-1/2}\,. \tag{2.17}$$

As a consequence of their short mean free path nearly all positrons remain trapped in the ejecta during the first year, even if no structured magnetic field is present. In the case of a disordered magnetic field the positron trapping time increases as particles cannot leave the ejecta and instead are locked in Larmor orbits.

X-Rays

Photons can not only interact with the ejecta material through Compton scattering but also by photo-electric absorption. The parameterised cross-sections from Ambwani & Sutherland (1988) (derived from Veigele, 1973) show a simple dependence on the composition of the absorbing material:

$$\chi_\gamma^{\mathrm{bf}}(\nu) = 1.16 \times 10^{-24}\,\mathrm{cm}^2 \left(\frac{h\nu}{100\,\mathrm{keV}}\right)^{-3.13} \frac{\rho}{m_{\mathrm{Si}}}(1 - X_{\mathrm{IGE}}) + 25.7 \times 10^{-24}\,\mathrm{cm}^2 \left(\frac{h\nu}{100\,\mathrm{keV}}\right)^{-3.0} \frac{\rho}{m_{\mathrm{Fe}}} X_{\mathrm{IGE}} \tag{2.18}$$

where the two terms represent cross sections for IMEs and IGEs, respectively, normalised to the mass of silicon m_{Si} or iron m_{Fe}. The mass fractions of IMEs and IGEs are given by X_{IME} and X_{IGE} and the density is ρ. The term corresponding to atoms with $Z < 7$ has been omitted in Eq. 2.18 as the outermost layers containing carbon are not heated by X-rays.

Eq. 2.18 shows that IGEs have a 20 times higher opacity to X-rays than IMEs. The cross-sections from Veigele (1973) are valid for neutral atoms. The inner electrons, which contribute the most to the photo-electric cross-section, are not expected to be missing. Therefore the deviation of the cross-section between neutral and singly/doubly ionised atoms will not be very big. The scaling $E^{-3.13}$ and $E^{-3.0}$ is an excellent approximation in the energy region between 10 and 1000 keV. From this scaling law it becomes clear that photoabsorption is only relevant for very low gamma-photon energies (significantly below 100 keV following multiple Compton interactions) or X-rays (Swartz et al., 1995).

Pair Production

Pair creation is a very weak process for γ-ray energies barely above the energy threshold $E = 2\,m_{\mathrm{e}}\,c^2$. However, the emergent electron and positron deposit their energy much easier than γ-rays (see Sec. 2.1.3). The positron will eventually be slowed down sufficiently and become a positronium atom, decaying after a mere 0.125 ns to two γ-rays with an energy of 511 keV each. Hubbell (1969) and Ambwani & Sutherland (1988) determined parameterised cross-sections for γ-ray energies between $1.022\,\mathrm{MeV} < h\nu < 1.5\,\mathrm{MeV}$

$$\chi_{\gamma\gamma} = \rho \left[\frac{Z_{\mathrm{Si}}^2}{m_{\mathrm{Si}}}(1 - X_{\mathrm{IGE}}) + \frac{Z_{\mathrm{Fe}}^2}{m_{\mathrm{Fe}}} X_{\mathrm{IGE}}\right] \times 1.0063 \left(\frac{h\nu}{1\,\mathrm{MeV}} - 1.022\right) \times 10^{-27}\,\mathrm{cm}^2 \tag{2.19}$$

and for γ-ray energies above 1.5 MeV

$$\chi_{\gamma\gamma} = \rho \left[\frac{Z_{\mathrm{Si}}^2}{m_{\mathrm{Si}}}(1 - X_{\mathrm{IGE}}) + \frac{Z_{\mathrm{Fe}}^2}{m_{\mathrm{Fe}}} X_{\mathrm{IGE}} \right] \times \left[0.0481 + 0.301 \left(\frac{h\nu}{1\,\mathrm{MeV}} - 1.5 \right) \right] \times 10^{-27}\,\mathrm{cm}^2 \quad (2.20)$$

2.1.4. Non-Thermal Electrons

As shown in Sec. 2.1.3 the various channels of energy deposition all lead to a pool of high energy electrons ($E > 1\,\mathrm{keV}$). High-energy electrons passing through the SN ejecta deposit their energy into three channels: excitation, ionisation and heating. Interactions with atoms/ions can lead to ionisations, creating secondary electrons in the process. If the energy exchange is small ($\Delta E < E_{\mathrm{ion}}$) one of the shell electrons can also be *excited* to a higher level. Once electrons reach low enough energies ($E < 1\,\mathrm{keV}$) they can efficiently interact through Coulomb scattering with the thermal electron pool ($E \sim 1\,\mathrm{eV}$). Due to frequent collisions between electrons their motions are well-described by a single temperature. We thus refer to this as the 'thermal electron pool'.

The fractions of energy going into the three channels ionisation, excitation and heating depend on the chemical composition of the ejecta and the electron fraction. They are rather insensitive to the density and the exact distribution of primary high-energy electrons as ionisation, excitation and Coulomb scattering cross sections behave similarly at high energies $\sigma \propto \ln(E)/E$ (Bethe approximation, see Kozma & Fransson, 1992). It is therefore sufficient to inject high-energy electrons at a threshold energy ($\sim 10\,\mathrm{keV}$). Ionisation, excitation and heating rates are obtained by integration of the corresponding cross-sections, which in turn requires knowledge about the distribution of high-energy electrons up to several keV. Fig. 2.2 shows the energy fractions going into the different channels for an Fe I/Fe II plasma (Kozma & Fransson, 1992).

Continuous Slowing Down Approximation

The first self-consistent solution of this problem in the context of SNe was achieved by Axelrod (1980), using the Continuous Slowing Down Approximation, in which the energy loss per interaction of high-energy electrons is assumed to be small and continuous. Using the formalism of Xu & McCray (1991), the fraction of deposition going into the three channels heating (η_{heat}), ionisation ($\eta_{\mathrm{ion},k}$), and excitation ($\eta_{\mathrm{exc},ij}$) follows as

$$\eta_{\mathrm{heat}} = \frac{L_e(E_0) + f \sum_m x_m I_m Q_m(E_0)}{A} \quad (2.21)$$

$$\eta_{\mathrm{ion},m} = \frac{x_m I_m Q_m(E_0)}{A} \quad (2.22)$$

where E_0 is the injection energy of electrons, L_e is the Coulomb loss function, m labels an ion and its ionisation potential I_m, ionisation fraction $x_m = n_m/n$, and collisional ionisation cross section $Q_m(E)$, and $f \sim 0.3$ is the mean energy of a secondary electron, and

$$\eta_{\mathrm{exc},ij,m} = \frac{x_{i,m} E_{ij,m} \sigma_{ij,m}(E_0)}{A} \tag{2.23}$$

where i, j labels a transition with energy $E_{ij,m} = E_{j,m} - E_{i,m} > 0$, the fractional level population of the lower-energy state is $x_{i,m} = n_{i,m}/n$, and the collisional excitation cross section is $\sigma_{ij,m}$, and

$$A = \eta_{\mathrm{heat}} + \eta_{\mathrm{ion},k} + \eta_{\mathrm{exc},ij} \tag{2.24}$$

is the total energy going into the channels and thus a normalisation constant. The Coulomb loss function (Schunk & Hays, 1971; Xu & McCray, 1991) for high-energy electrons is given by

$$L_e(E) = -\frac{1}{n}\left(\frac{dE}{dx}\right)_e = x_e \frac{2\pi e^4}{E} \ln\left(\frac{4E}{\zeta_e}\right) \tag{2.25}$$

where e is the electron charge, E is the electron energy, $x_e = n_e/n$ is the electron fraction, and $\zeta_e = 2\hbar\omega_p$ for the plasma frequency given by

$$\omega_p(n_e) = \sqrt{\frac{4\pi n_e e^2}{m_e}} = 56414.6 \sqrt{\frac{n_e}{\mathrm{cm}^{-3}}}\ \mathrm{s}^{-1} \tag{2.26}$$

Collisional ionisation cross sections (Q_m) can be approximated using the method of Younger (1981). Collisional excitation cross sections of allowed transitions by non-thermal electrons are given by (van Regemorter, 1962)

$$\sigma_{ij,m} = \frac{8\pi}{\sqrt{3}} \frac{1}{k_i^2} \frac{I_H}{\Delta E_{ij}} f_{ij} \bar{g} \pi a_0^2 \tag{2.27}$$

where I_{H} is the ionisation potential of hydrogen, k_i^2 is the initial electron energy scaled to 13.60 eV, f_{ij} is the oscillator strength, a_0 is the Bohr radius, and $\bar{g}$ is given by a quadratic fit to the results of van Regemorter (1962).

Forbidden transitions would yield artificially low cross sections and thus have to be treated separately:

$$\sigma_{ij,m} = \frac{1}{g_{i,m} k_{i,m}^2} \Omega_{ij,m} \bar{g} \pi a_0^2 \tag{2.28}$$

where $g_{i,m}$ is the statistical weight and $\Omega_{ij,m}$ is the collision strength.

Exact Solution

In a more direct way the deposition fractions can be obtained by solving the Boltzmann equation, which in this context was first formulated by Spencer & Fano (1954). The Spencer-Fano equation is a special form of the Boltzmann equation, in which the number of electrons entering and leaving an energy interval dE is balanced (Kozma & Fransson, 1992). The electron flux in the energy interval $(E, E + dE)$ is given by the degradation spectrum $y(E)dE$

$$y(E)\sum_m n_m\left[\sum_{i\neq j}\sigma_{ij,m}(E)+\int_{E_m}^{(E_m+E)/2}Q_m(E,\varepsilon)d\varepsilon\right]-\frac{d}{dE}[y(E)L_e(E)]$$
$$=\sum_m n_m\sum_{i\neq j}y(E+E_{ij})\sigma_{ij,m}(E+E_{ij,m})+\sum_m n_m\int_{E_m}^{\lambda}y(E+\varepsilon)Q_m(E+\varepsilon,\varepsilon)d\varepsilon$$
$$+\sum_m n_m\int_{2E+E_m}^{E_{\max}}y(E')Q_m(E',E+E_m)dE'+S(E) \tag{2.29}$$

where $\lambda=\min(E_{\max}-E,E+E_m)$ and symbols from Sec. 2.1.4 apply. Knowledge of the degradation spectrum $y(E)dy$ allows for the computation of the fractions going into heating, excitation and ionisation

$$\eta_{\rm heat}=\frac{1}{E_{\rm init}}\int_{E_0}^{E_{\max}}y(E')L_e(E')dE'+\frac{1}{E_{\rm init}}E_0y(E_0)L_e(E_0)$$
$$+\frac{1}{E_{\rm init}}\int_0^{E_0}N(E')E'dE' \tag{2.30}$$
$$\eta_{{\rm exc},ij,m}=\frac{n_{ij,m}E_{ij,m}}{E_{\rm init}}\int_{E_{ij,m}}^{E_{\max}}y(E')\sigma_{ij,m}(E')dE' \tag{2.31}$$
$$\eta_{{\rm ion},m}=\frac{n_{ij,m}E_m}{E_{\rm init}}\int_{E_m}^{E_{\max}}y(E')Q_m(E')dE' \tag{2.32}$$

with $E_{\rm init}$ being the mean energy of the initial electrons, E_0 the lowest excitation or ionisation energy, and for $E\leq E_0$

$$N(E)=\sum_m n_m\Bigg[\sum_{ij}y(E+E_{ij,m})\sigma_{ij,m}(E+E_{ij,m})$$
$$+\int_{E_m}^{\lambda_m}y(E+E')Q_m(E+E',E')dE'$$
$$+\int_{2E+E_m}^{E_{\max}}y(E')Q_m(E',E+E_m)dE'\Bigg]+S(E)\ . \tag{2.33}$$

2.1.5. Ionisation and Recombination

For SNe in the nebular phase ionisations are caused by non-thermal electrons, photo-ionisations and charge transfer. Collisional ionisation from thermal electrons are not possible as the thermal electron energy ($\sim 1\,$eV) is much smaller than typical ionisation energies of IGE ($\sim 30\,$eV).

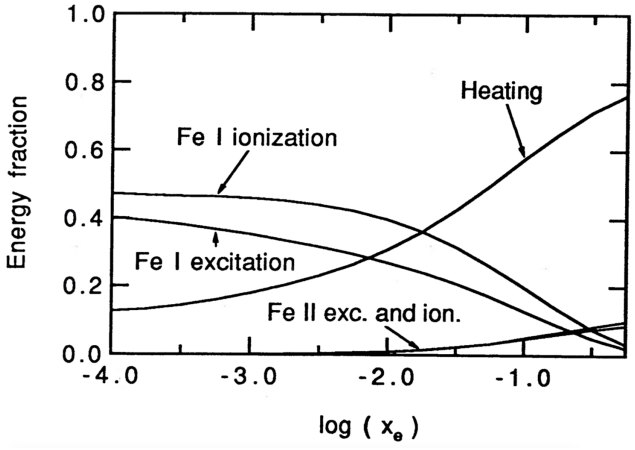

Figure 2.2.: Energy deposition fraction going into the different channels heating, excitation and ionisation as a function of the electron fraction x_e for a pure iron plasma. Taken from Kozma & Fransson (1992).

Assuming the ionisation equilibrium approximation ($\frac{dx_m}{dt} = 0$) the ionisation balance equation becomes

$$\Gamma_{i-1} x_{i-1} = n_e \alpha_i x_i \tag{2.34}$$

where Γ_i is the ionisation rate from ionisation state i to $i+1$, x_i is the ionisation fraction $x_i = N_i / \sum_i N_i$, n_e is the electron density and α_i is the recombination rate from ionisation state i to $i-1$. The degeneracy in this equation system ($N_{\rm ele} \times N_{\rm ion\ states}$) can be broken by introducing number conservation

$$\sum_i x_i = 1 \tag{2.35}$$

and charge conservation

$$\sum_i i x_i = n_e \ . \tag{2.36}$$

These sums extend over all elements and all ionisation states.

The ionisation rate is given by

$$\Gamma_i = \Gamma_i^{\rm nt} + \Gamma_i^{\rm photo} + \Gamma_i^{\rm ce} \tag{2.37}$$

as the sum of non-thermal (nt), photoionisation (photo) and charge-exchange (ce) ionisations. For a given non-thermal energy deposition fraction $\eta_{{\rm ion},m}$ into ionisations of an element with ionisation level m, the effective ionisation potential becomes

$$\chi_{{\rm eff},m}(x_e) = \frac{E_m X_m}{\eta_{{\rm ion},m}(x_e)} \tag{2.38}$$

where X_m is the number fraction of that element (Kozma & Fransson, 1992). The rate of non-thermal ionisations per unit volume follows from the effective ionisation potential

$$\Gamma_i^{\rm nt} n_m = \frac{4\pi J_\gamma \sigma_{\gamma,m}}{\chi_{{\rm eff},m}(x_e)} n_m \tag{2.39}$$

with the γ-ray mean intensity J_γ and the energy averaged cross section for absorption by the ion $\sigma_{\gamma,m} = 0.06 Z_m m_p {\rm cm}^2$ (Fransson & Chevalier, 1989).

The photoionisation rate is determined by the mean intensity of the radiation field J_ν

$$\Gamma_i^{\rm photo} = \sum_j y_j \int_{\nu_{0,j}}^{\infty} \sigma_{j,\nu} \frac{4\pi J_\nu}{h\nu} d\nu \tag{2.40}$$

where y_j is the fraction of ionisation state i in the excited level j, $\sigma_{j,\nu}$ is the photoionisation cross section and $\nu_{0,j}$ is the lower threshold energy for photoionisation (Jerkstrand, 2011).

Charge-exchange $\Gamma_i^{\rm ce}$ denotes reactions where electrons are transferred between ions. Charge-exchange depends on the ion density and thus scales as t^{-3} as opposed to non-thermal and photoionisation, which scale mainly with the energy deposition rate in the ejecta and thus with the half-live of the radioactive material and only to a lesser degree with the density. For ^{56}Co decays ($\tau = 111\,{\rm d}$) the minimum effect of charge transfer is expected at an epoch of $3\,\tau$, which is roughly one year after the explosion (Jerkstrand, 2011):

$$\frac{\Gamma_{j,i}^{\rm ct}}{\Gamma_{j,i}^{\rm photo} + \Gamma_{j,i}^{\rm nt}} \propto e^{t/2\tau} t^{-3/2} \tag{2.41}$$

After this time, charge transfer becomes increasingly important as the repulsive Coulomb force in the low-ionised ejecta weakens.

Recombination can also occur through different processes. The total recombination rate is given as the sum of radiative, dielectronic, charge-exchange and stimulated recombination rates:

$$\alpha_i = \alpha_i^{\rm rad} + \alpha_i^{\rm diel} + \alpha_i^{\rm ce} + \alpha_i^{\rm sr} \ . \tag{2.42}$$

In radiative recombination processes an electron is captured by an ion, reducing the ionisation state from i to $i-1$ resulting in the emission of a photon carrying the energy difference. The captured electron can also remain in a highly excited state, which depopulates through a cascade of transitions to the ground state. The rate of radiative recombination scales approximately with $T^{-1/2}$. Dielectronic recombinations transfer the released energy onto a shell electron. It is possible that the excited electrons de-excite to the ground state or are re-ejected from the ion (autoionisation). Charge-exchange recombinations go hand-in-hand with charge-exchange ionisations and are only relevant at sufficiently late epochs. Stimulated recombination can be considered as the opposite of photo-ionisation, where the presence of a photon triggers the recombination event with a free electron and is also transferred the released energy.

2.1.6. Ion Excitations

Ions can be excited and de-excited through collisions with non-thermal electrons, the thermal electron pool, ionisations and recombinations, and interactions with photons. All of these processes can be combined in a set of equations named *Statistical Equilibrium Equations*:

$$\frac{dn_{m,i}}{dt} = \sum_j n_{m-1,j}\Gamma_{m-1,j\to m,i} + \sum_j n_{m+1,j}\alpha_{m+1,j\to m,i}n_e + \sum_{j\neq i} n_{m,j}T_{j,i} - n_{m,i}\left(\sum_{j\neq i} T_{i,j} + \sum_j \Gamma_{m,i\to m+1,j} + \sum_j \alpha_{m,i\to m-1,j}\right) . \tag{2.43}$$

Here $n_{m,i}$ denotes the level population of an element with ionisation state m. The first three terms on the right hand side represent processes which populate $n_{m,i}$ through ionisations ($\Gamma_{m-1,j\to m,i}$), recombinations ($\alpha_{m+1,j\to m,i}$) and radiative and collisional transitions ($T_{j,i}$). The last three terms describe processes which depopulate out of $n_{m,i}$ through ionisations ($\Gamma_{m,i\to m+1,j}$), recombinations ($\alpha_{m,i\to m-1,j}$) and radiative and collisional transitions ($T_{i,j}$).

Stationarity ($\frac{dn_{m,i}}{dt} = 0$) can be assumed if the excitation timescale is short compared to the ejecta expansion and radioactive decay timescales. Even forbidden rates are $\sim 10^{-3}\,\mathrm{s}^{-1}$ and thus much smaller than the radioactive timescale (hundreds of days), consequently validating the *excitation equilibrium approximation* (stationarity) at all times. The system of equations is linear as long as the lines are optically thin. ionisation and recombination rates connect levels of adjacent ionisation states. Transition rates ($T_{i,j}$) only connect levels of a single ionisation state. The contributions to T depend on whether $i > j$ or $j > i$ (hereafter l, u and u, l, respectively).

$$T_{u,l} = C_{u,l}^{\mathrm{thermal}} + C_{u,l}^{\mathrm{non-thermal}} + T_{u,l}^{\mathrm{spont}} + T_{u,l}^{\mathrm{stim}} \tag{2.44}$$

$$T_{l,u} = C_{l,u}^{\mathrm{thermal}} + C_{l,u}^{\mathrm{non-thermal}} + T_{l,u}^{\mathrm{abs}} \tag{2.45}$$

Collisions with thermal and non-thermal electrons can both excite and de-excite ionic levels while spontaneous and stimulated emission can only de-excite. Absorptive transitions only excite ions.

Spontaneous emission

Spontaneous emission allows shell electrons to de-excite to a lower lying energy level resulting in the emission of a photon carrying the energy difference. The rate of this transition is given by

$$T_{u,l}^{\mathrm{spont}} = A_{u,l}\beta_{\mathrm{esc},u,l} \tag{2.46}$$

where $A_{u,l}$ is the Einstein A-value and $\beta_{\mathrm{esc},u,l}$ is the Sobolev escape probability from Eq. 2.4:

$$\beta_{\mathrm{esc},u,l} = \frac{1 - e^{-\tau_{u,l}}}{\tau_{u,l}} \tag{2.47}$$

Table 2.2.: Selection rules for discrete transitions. Adopted from the National Institute of Standards and Technology (NIST).

	#	electric dipole E1 allowed	magnetic dipole M1 forbidden	electric quadrupole E2 forbidden
rigorous rules	1	$\Delta J = 0, \pm 1$ except $0 \not\leftrightarrow 0$	$\Delta J = 0, \pm 1$ except $0 \not\leftrightarrow 0$	$\Delta J = 0, \pm 1, \pm 2$ except $0 \not\leftrightarrow 0$, $1/2 \not\leftrightarrow 1/2$, $0 \not\leftrightarrow 1$
	2	$\Delta M = 0, \pm 1$ except $0 \not\leftrightarrow 0$ when $J = 0$	$\Delta M = 0, \pm 1$ except $0 \not\leftrightarrow 0$ when $J = 0$	$\Delta M = 0, \pm 1, \pm 2$
	3	parity change	no parity change	no parity change
with negligible configuration interaction	4	one electron jumping, with $\Delta l = \pm 1$, Δn arbitrary	no change in electron configuration: $\Delta l = 0$, $\Delta n = 0$	no change in electron configuration; or one electron jumping with $\Delta l = 0, \pm 2$, Δn arbitrary
for LS coupling only	5	$\Delta S = 0$	$\Delta S = 0$	$\Delta S = 0$
	6	$\Delta L = 0, \pm 1$ except $0 \not\leftrightarrow 0$	$\Delta L = 0$ $\Delta J = \pm 1$	$\Delta L = 0, \pm 1, \pm 2$ except $0 \not\leftrightarrow 0$, $0 \not\leftrightarrow 1$

There are two types of spontaneous radiative emission processes: allowed transitions and forbidden transitions. Allowed transitions obey the selection rules of quantum mechanics while forbidden transitions do not. According to some approximations (e.g. electric dipole approximation) forbidden transitions cannot happen, but for a higher order approximation (e.g. magnetic dipole and electric quadrupole) the transition can occur (see Tab. 2.2). Forbidden transitions have drastically reduced transition coefficients ($A \sim 10^{-2}$) compared to allowed transitions ($A \sim 10^{5}$).

Radiative Absorption

Radiative absorption is given by

$$T^{\mathrm{abs}}_{l,u} = B_{l,u} J^{b}_{\nu} \beta_{\mathrm{esc},u,l} \tag{2.48}$$

with the Einstein-B coefficient

$$B_{l,u} = \frac{A_{l,u}\lambda^3}{2hc^2} \ . \tag{2.49}$$

Stimulated Emission

The rate of stimulated emission in a line depends on the rate of radiative absorption in the same line:

$$T^{\mathrm{stim}}_{u,l} = \frac{g_l}{g_u} T^{\mathrm{abs}}_{l,u} \tag{2.50}$$

Non-Thermal Collisions

Non-thermal processes, including excitation of ionic levels, are described in detail in Sec. 2.1.4. The rate of non-thermal excitations into and out of level i are given by Eq. 2.31. As long as the temperature of the emitting material is high compared to the fine-structure energy splitting of the involved multiplets they are assumed to be populated according to their statistical weights g_i.

Thermal Collisions

Collisions of particles in the ejecta of SNe are common at early phases, but because of the t^{-3} dependency of the density they decline rapidly. Collisions can occur between electrons and ions, though the collision speed and energy transfer render the latter negligible

$$\frac{C_{l,u}^{\text{thermal,ion}}}{C_{l,u}^{\text{thermal,electron}}} \sim \frac{v_{\text{ion}}}{v_{\text{electron}}} \frac{n_{\text{ion}}}{n_e} = \left(\frac{m_e}{m_{\text{ion}}}\right)^{1/2} \frac{n_{\text{ion}}}{n_e} \ . \tag{2.51}$$

For an IGE dominated plasma $m_{\text{ion}} \sim 10^5 m_e$ while the number ratio of ions and electrons is between 1 and 2.

Electron collisions do not obey selection rules and thus connect every level i to every other level j. Collisions between thermal electrons are frequent and fast enough that their distribution never significantly deviates from Maxwell-Boltzmann. The thermal collision rates for excitation and de-excitation follow as

$$C_{u,l}^{\text{thermal}}(T) = \frac{8.63 \times 10^{-6}}{g_u \sqrt{T}} n_e e^{-E_{u,l}/k_B T} \Upsilon_{u,l} \tag{2.52}$$

$$C_{l,u}^{\text{thermal}}(T) = \frac{g_u}{g_l} e^{E_{u,l}/k_B T} C_{u,l}^{\text{thermal}} \tag{2.53}$$

where $\Upsilon_{u,l}$ are the 'effective' or 'Maxwellian-averaged' collisional strengths. They are obtained from

$$\Upsilon_{u,l} = \int_0^\infty \Omega_{u,l} e^{-\epsilon_l/kT} d(\epsilon_l/kT) \tag{2.54}$$

where $\Omega_{u,l}$ is the collisional cross section for an electron to excite transition between the levels u and l. $\Upsilon_{u,l}$ are slowly varying with the electron temperature. Sometimes higher levels can, in contrast to LTE excitation, be more easily populated by collisions than lower levels. Unfortunately, effective collision strengths are not available for all ions. There have been attempts (e.g. van Regemorter, 1962; Jefferies, 1968) to approximate effective collision strengths for neutral atoms and positive ions, respectively,

Table 2.3.: Collision strength approximations similar to Axelrod (1980) (for Fe III) and Graham et al. (1987) (for Fe II) using state-of-the-art atomic data.

$\Omega_{u,l} = \omega_{\mathrm{opt/IR}}\, g_u\, g_l$				
	In this thesis		Approximation	
Ion	ω_{opt}	ω_{IR}	ω_{opt}	ω_{IR}
Fe III	0.0066	0.0244	0.00375	0.0225
Fe II	0.0040	0.0132	...	0.02
Co III	0.0090	0.0252	...	...
Co II	0.0312	0.0717	...	...

$$C_{u,l}(T) = \begin{cases} 3.9 f_{u,l} n_e \left[\dfrac{E_{u,l}}{kT}\right]^{-1} T^{-3/2} e^{-E_{u,l}/kT} & \text{(positive ions)} \\ 2.16 f_{u,l} n_e \left[\dfrac{E_{u,l}}{kT}\right]^{-1.68} T^{-3/2} e^{-E_{u,l}/kT} & \text{(neutral atoms)} \end{cases} \tag{2.55}$$

where $f_{u,l}$ is the oscillator strength, T is the electron temperature, $E_{u,l}$ is the transition energy, and n_e is the electron density.

Forbidden transitions without collisional data need to be treated separately, as oscillator strengths for these transitions result in artificially low collisional rates. An approximation for optical and IR forbidden transitions (defined as $f_{u,l} \leq 0.001$) has been formulated by Axelrod (1980):

$$\Omega_{u,l,forb} = \begin{cases} 0.00375\ g_u g_l, & \lambda \leq 10\mu\mathrm{m} \\ 0.0225\ g_u g_l, & \lambda > 10\mu\mathrm{m} \end{cases} \tag{2.56}$$

However, a comparison of this approximation with recently published effective collision strengths shows large discrepancies of about one order of magnitude in the bulk of the transitions. Eq. 2.56 was only derived for Fe III – other ions need to be treated differently, though the dependency on the statistical weights should be similar (see Fig. 2.3 and Fig. 2.4). An overview of 'revised' collision strength approximations is given in Tab. 2.3.

2.2. Spectral Model

In the limit of zero optical depth, the line flux is fully determined by the distribution of the upper-level populations throughout the ejecta. If emitting material is found near the explosion centre, the emission profile peaks at the rest wavelength. If the emitting material is located in a thin shell surrounding the innermost region, the emission profile is flat near the rest wavelength. This method allows probing the radial distribution of IGEs in the deepest layers, where explosive nuclear burning is thought to be most efficient.

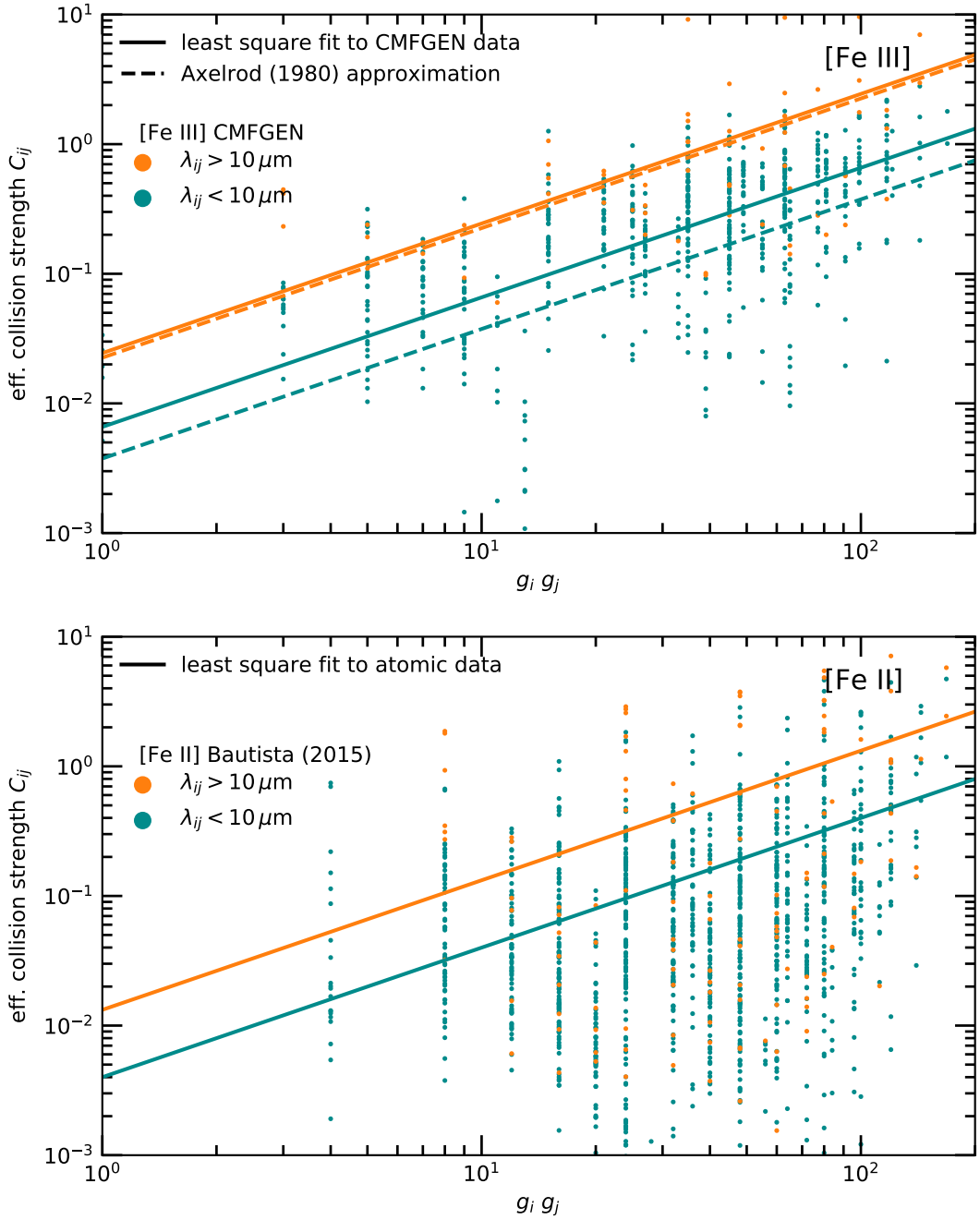

Figure 2.3.: Effective collision strengths of Fe III and Fe II against the product of the statistical weights of the involved levels. Orange data points indicate IR transitions while teal data points are higher energy transitions. Linear fits similar to Axelrod (1980) are shown for both ions as solid lines. The original approximation from Axelrod (1980) in the case of Fe III is included as a dashed line.

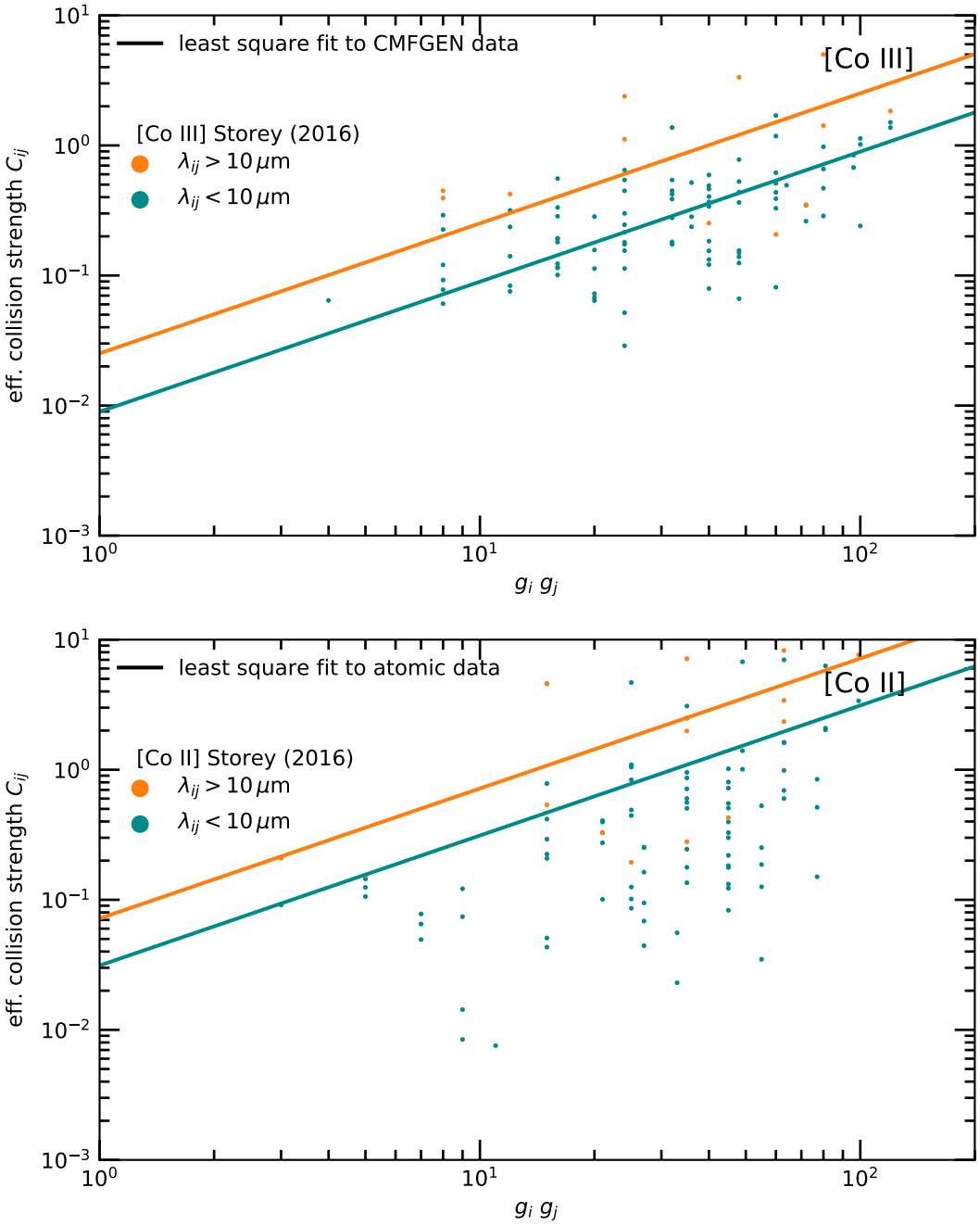

Figure 2.4.: Comparison of the Axelrod (1980) approximation with quantum mechanical computations of the effective collision strength. Same as Fig. 2.3 but for Co III and Co II.

Table 2.4.: Atomic data used in this thesis.

ion	levels[a]	ref. A_{ij} [b]	ref. Υ_{ij} [c]
Fe II	52	Bautista et al. (2015)	Bautista et al. (2015)
Fe III	39	Quinet (1996)	Zhang (1996)
Co II	15	Storey et al. (2016)	Storey et al. (2016)
Co III	15	Storey & Sochi (2016)	Storey & Sochi (2016)
Ni II	18	Cassidy et al. (2016a)	Cassidy et al. (2010a)
Ni III	9	Fivet et al. (2016)	Watts & Burke (1998)

[a] Energy levels and statistical weights are taken from NIST (Kramida et al., 2018).
[b] Einstein A coefficient between levels i and j.
[c] Maxwellian averaged collisional strength between levels i and j.

Nebular phase spectral models build on the early work of Axelrod (1980) and many authors over the years (Ruiz-Lapuente & Lucy, 1992; Spyromilio et al., 1992; Kozma & Fransson, 1992; Kuchner et al., 1994; Kozma et al., 2005; Mazzali et al., 2007; Fransson & Jerkstrand, 2015; Botyánszki & Kasen, 2017; Maguire et al., 2018a; Diamond et al., 2018; Shingles et al., 2020) with spectral synthesis codes of varying complexity (see Sec. 2.1 for an overview of the relevant processes).

In this thesis a one zone model is used which includes the singly and doubly ionised states of Fe, Co and Ni. Such a model has been used in many studies (e.g. Axelrod, 1980; Ruiz-Lapuente & Lucy, 1992; Mazzali et al., 1997; Spyromilio et al., 2004; Mazzali et al., 2010) as, despite the simplicity of the model, the resulting spectra yield good fits to observed data. By definition, the one zone model does not allow density or composition gradients across the ejecta. While this simplification will likely introduce systematic differences compared to multi zone models, our findings, which are mostly based on the line fluxes, are not significantly affected by this limitation. Additionally, SN Ia explosion simulations – irrespective of the specific progenitor system and explosion mechanism – do not show a very steep decline of the density profile in the IGE-rich ejecta (see Sec. 2.3). Outside of the iron-rich core, the density profiles exhibit a much faster decline. The steep density decline in layers dominated by IMEs would lead to a significantly reduced γ-ray optical depth and subsequently reduced energy deposition, resulting in a thermal electron pool which might be unable to collisionally excite even the lowest-lying levels of IMEs. In fact, observed nebular phase spectra do not show IMEs (except possibly sulphur between 8500 and 10000 Å, see e.g. Botyánszki & Kasen, 2017; Shingles et al., 2020). However, we want to emphasise that peculiar objects (91bg-likes, 86G-likes) have been found which are suspected to show nebular lines of IMEs such as calcium.

For the set of ions given in Tab. 2.4, the electron density and temperature in addition to the population of the ionic levels are simultaneously determined from the statistical equilibrium equations (2.43). We treat collisional excitation and de-excitation by collisional and radiative processes. Stimulated excitation and de-excitation do not play a role in the low photon density regimes considered in this thesis. The solution of Eq. 2.43 determines the level populations of

the ion species in our model. Eq. 2.46 allows us to compute line emissivities for which we take into account the Sobolev escape probability (see Sec. 2.1.1). Other radiative transfer effects are not included as the optical depths of the lines in our region of interest are low ($\tau \ll 1$) and self-absorption of line flux is negligible. The electron gas is characterised by a Boltzmann distribution of temperature T and an electron density n_e. Non-thermal effects are ignored as they should be limited in strength for the relatively high densities ($\sim 10^6\,\mathrm{cm}^{-3}$) typical for the first 1.5 years after the explosion. No charge-exchange or time-dependent effects are included as we solve the statistical equilibrium equations in steady-state. Finally, we do not directly solve for the ionisation balance but instead treat the relative number of emitting ions as a free parameter which allows us to probe a large parameter space.

2.3. Line Profiles and the one zone model

SNe Ia shortly after the explosion enter a homologous expansion phase that can last for tens to hundreds of years, depending on the density of the ISM (Reynolds, 2017)[1]. During the nebular phase iron-rich material emits from within a volume expanding at $\sim 11000\,\mathrm{km\,s}^{-1}$. The thermal motion of the ions is ~ 1000 times lower than the expansion velocity and thus negligible. Expansion along the line of sight leads to Doppler broadening of the emission lines. Each thin sheet of material with surface area dA and line of sight velocity offset from the explosion centre Δv contributes to the line profile at $\nu = (1 + \Delta v/c)\nu_0$, where ν_0 is the frequency of an emission line (see Fig. 2.5 for an illustration). The exact profile shape is given by the convolution of the emitting mass distribution and the emissivity per unit mass. The emission profile of the nebula is therefore strongly dependent on the ejecta velocity structure, including the chemical composition.

In the case of a uniform emissivity per unit volume the line profile becomes parabolic. When determining emission line properties (shift, flux) Gaussian (and to a lesser extent parabolic) line profiles are often assumed. There is no particular obvious reason why the line profiles of SNe Ia should be Gaussian, and the density structure can certainly not be assumed to adhere to a uniform distribution. In the following, we will demonstrate how a profile that can be approximated by a Gaussian naturally arises from an exponential density profile.

We examine the emergent line profiles of four explosion models: a detonation with primary mass $M = 0.97\,M_\odot$ (Sim et al., 2010), a detonation with primary mass $M = 1.18\,M_\odot$ (Marquardt et al., 2015), a violent merger with primary mass $M = 1.1\,M_\odot$ and secondary mass $M = 0.9\,M_\odot$ (Pakmor et al., 2012), and a delayed detonation with 100 ignition kernels (N100, Seitenzahl et al., 2013). For this simplified problem the ionisation state and electron temperature are not solved in a self-consistent way. Instead, the electron density is assumed to follow the density profile with the material being on average doubly ionised. Observed SNe exhibit a multitude of emission lines

[1] In reality, the ejecta are never in 'perfect' homologous expansion, though deviations are relatively small for the given time range. As soon as the blast wave encounters the ISM, deceleration of the ejecta begins.

from singly and doubly ionised material, and some fraction of the material is also expected to be triply ionised. On average, the electron density should not deviate too much (much less than a factor of two) from our assumption. The electron temperature is assumed to increase linearly from the centre of the explosion to the radial coordinate where the density of ^{56}Ni is highest (though the result is not particularly sensitive to the temperature profile). From this point it is assumed to linearly decrease to the outermost radial coordinate where ^{56}Ni is present. Given the plasma conditions we can compute the line emissivities of [Fe II], [Co II] and [Ni II]. The radial emission profile for each line follows as the convolution of the emissivity per ion and the enclosed IGE mass at each radial coordinate. The emission profile is mainly determined by the enclosed mass and thus the density profile (see bottom left panel in Fig. 2.5). The line profile follows from the radial emission profile through integration of the emitting slices with velocities in the interval $[v, v + \Delta v]$ along the line of sight of an observer (see Fig. 2.5).

We find that the emission line profile for three out of four simplified cases closely resembles a Gaussian. For all practical purposes the uncertainty of the spectroscopic observations is likely bigger than the difference between the commonly assumed Gaussian profile and the simulated profile shape, considering that features in the nebular phase are comprised of several lines. The only exception is the violent merger scenario with its flat-top profiles.

A flat-top profile can be caused by several effects in the very centre of the ejecta: a lack of IGEs, too low ($< 3000\,\mathrm{K}$) electron temperatures or too high/low ionisation. The apparent Gaussian profile seen in all normal SNe Ia indicates that the core contains IGEs, is heated to more than 3000 K even at late phases (450 days after the explosion) and that singly ionised iron is abundant up to $\sim 8000\,\mathrm{km\,s^{-1}}$ throughout the nebular phase. In the violent merger model, however, the innermost region ($< 2000\,\mathrm{km\,s^{-1}}$) does not contain IGEs but unburnt material of the tidally disrupted companion. The emission originates from a thick shell ($2000 - 8000\,\mathrm{km\,s^{-1}}$) leading to flat-top profiles in the emission lines.

We further notice that no strong differences between the emission profiles of the strongest lines of [Fe II], [Co II] and [Ni II] are found, despite the fact that optical and NIR emission peaks at slightly different velocities from the explosion centre (see Figs. 2.6 – 2.9). In principle, every emission line has a unique emission profile which depends on the energetics of the excited level and the plasma state across the ejecta. The emission region in radial direction suggests that employing a one zone model results in only small differences compared to multi-zone models as long as the electron density and electron temperature gradients across this region remain moderate. Due to the low mass contained in the inner core ($v < 3000\,\mathrm{km\,s^{-1}}$) it does not contribute significantly to the total emission. Only the complete absence of emitting IGEs will be noticeable in the line profiles.

Here we have shown that a Gaussian line profile arises naturally in the expanding ejecta of SNe Ia, and that no strong differences of the FWHM are expected for lines of singly ionised IGEs. In our model, we broaden the lines using a Gaussian profile of variable width. We assume the

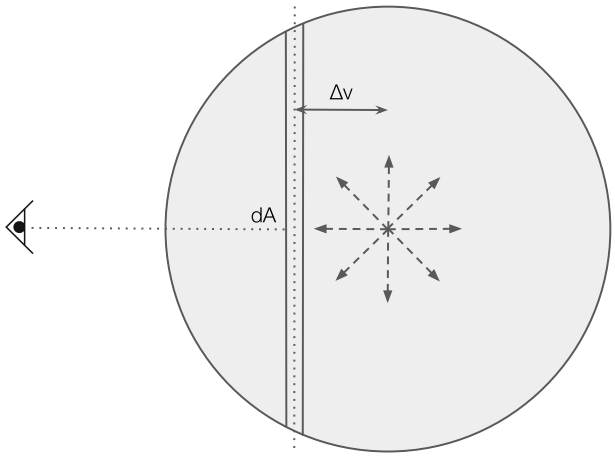

Figure 2.5.: Line broadening schematic. Along the line of sight of the observer emission from each thin slice is shifted by the velocity offset of the slice Δv with respect to the explosion centre.

same Gaussian profile for all lines of an ion, though the Gaussian FWHM is allowed to vary between ions.

2.4. The Presence of Iron in Nebular spectra

The most abundant iron-group isotope in SNe Ia is ^{56}Ni. The decay of its daughter nucleus ^{56}Co powers the light curves from a few days to several years after the explosion. During the nebular phase ($t \sim 150$ d, corresponding to $\sim 2 \times T_{1/2}$) a significant fraction of the synthesised ^{56}Ni has already fully decayed to ^{56}Fe (see Fig. 2.10). It comes as no surprise that nebular phase spectra are dominated by emission from iron. In explosions of WDs nearing the Chandrasekhar limit stable iron isotopes (mainly ^{54}Fe) can be synthesised directly with mass fractions $M_{^{54}Fe}/M_{^{56}Ni}$ between 5 and 15%. Sub-M_{Ch} explosions are unable to produce large quantities of stable iron ($M_{^{54}Fe}/M_{^{56}Ni} < 5\%$).

An open question in the field of SNe Ia is the ionisation state of iron. It remains unclear how much neutral iron is present in the ejecta of SNe Ia as no strong lines have been identified in the spectra so far. An additional complication is the fact that the currently available atomic data for neutral iron is lacking as the electronic configuration of this ion imposes considerable difficulties. Triply ionised iron, unfortunately, does not have any strong lines in the optical and NIR which could be used to infer its abundance. Radiative transfer simulations which include Fe IV predict its mass fraction to be of order 30%. Observed emission lines originate from the singly and doubly ionised states exclusively. This chapter will describe the process of identifying and measuring iron lines throughout the nebular phase of normal SNe Ia.

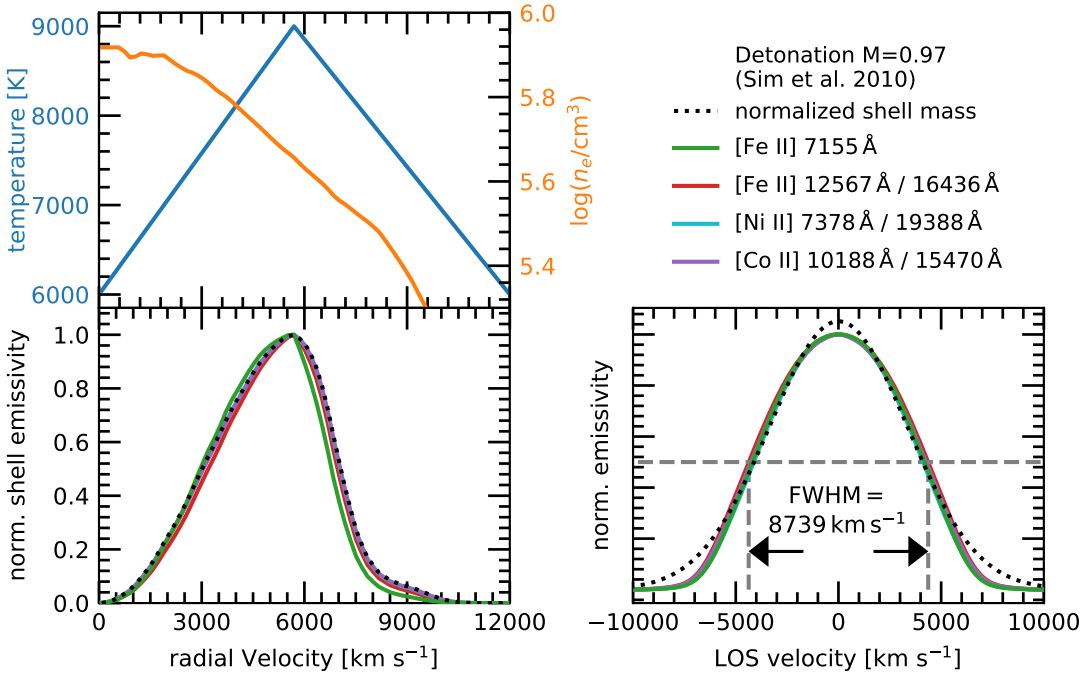

Figure 2.6.: Multi-zone emission profiles of the strongest Fe, Co and Ni lines for a detonation model with primary mass $M = 0.97\,M_\odot$ at 300 days after the explosion. The top left panel shows the electron density and temperature in the inner ejecta. We assumed doubly ionised material ($2\,e^-$ per ion) and the shown temperature profile. The normalised line emissivities per shell mass as a function of radial velocity are shown in the lower left panel. The line profile of the various lines are shown in the lower right. Coloured curves indicate different emission lines and the dotted curve is a Gaussian fit to the [Fe II] 12567 Å line profile.

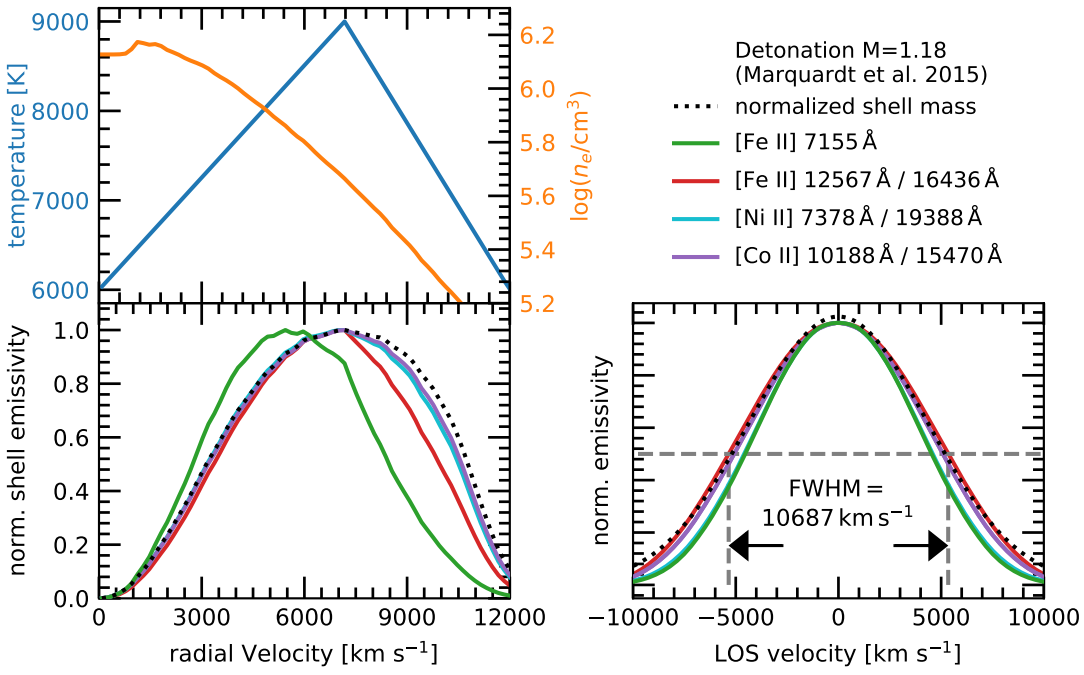

Figure 2.7.: Same as Fig. 2.6 but for a detonation model with primary mass $M = 1.18\,M_\odot$.

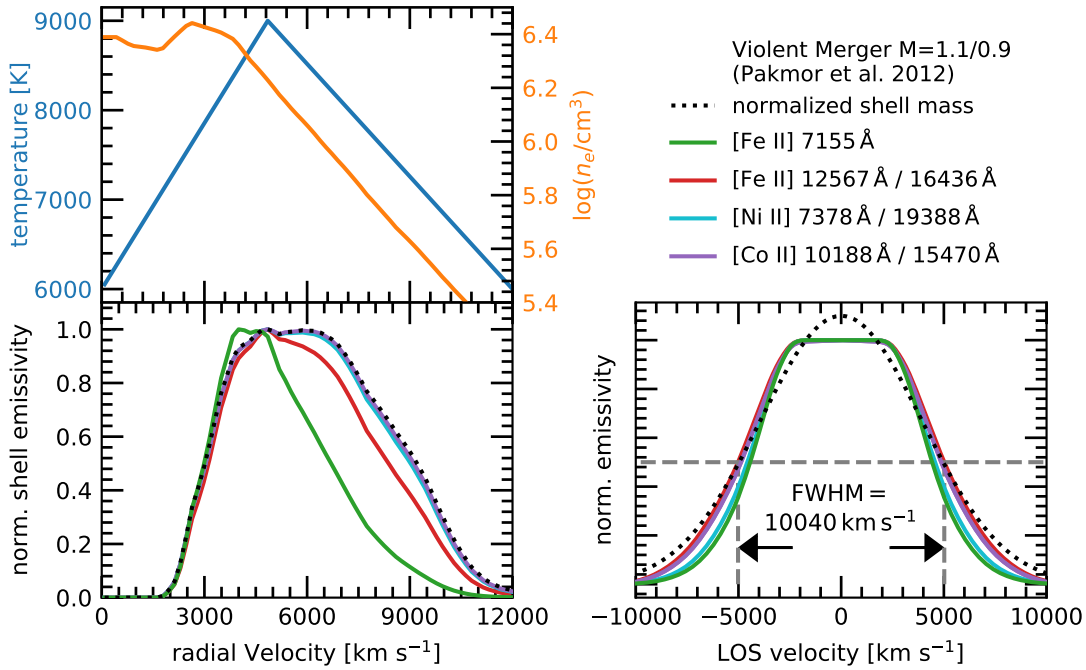

Figure 2.8.: Same as Fig. 2.6 but for a violent merger model with primary mass $M = 1.1\,M_\odot$.

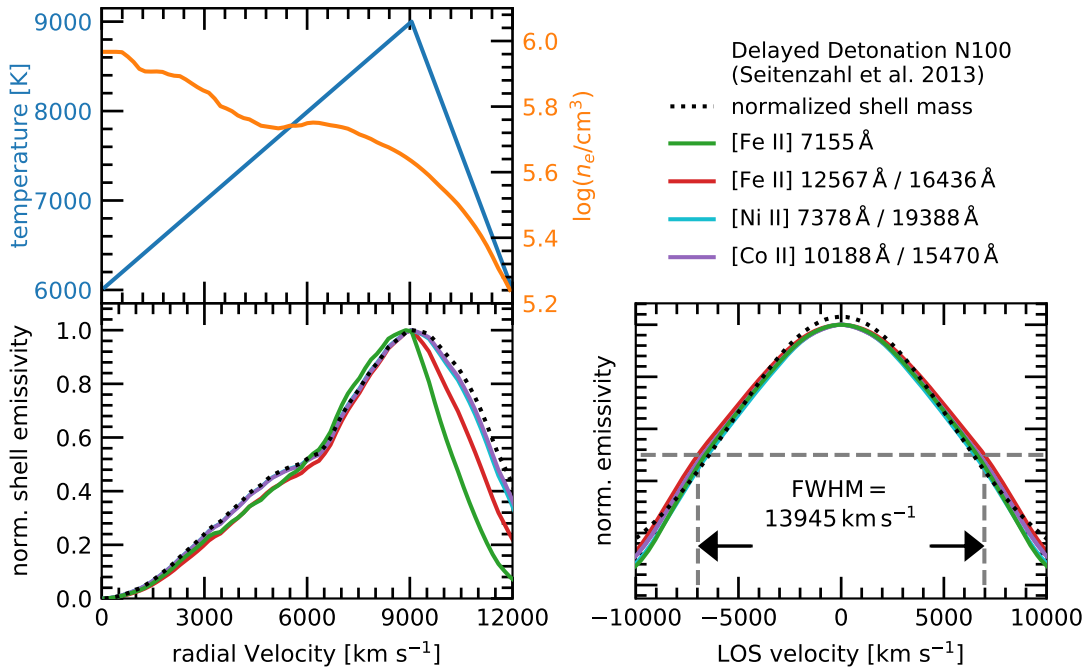

Figure 2.9.: Same as Fig. 2.6 but for a delayed detonation model with 100 ignition kernels.

Table 2.5.: Selected forbidden lines of singly and doubly ionised iron in the optical, NIR and MIR.

Ion	$\lambda_{\mathrm{rest,vac}}$ [Å]	A_{ij} [s^{-1}]	E_i [cm^{-1}]	Term	J_i	E_j [cm^{-1}]	Term	J_j	Exc. Temp [10^3 K]
Fe II	4245.2	8.51e-01	1872.6	a^4F	9/2	25429.0	a^4G	11/2	36.596
Fe II	4288.5	1.50e+0	0.0	a^6D	9/2	23318.0	a^6S	5/2	33.558
Fe II	4417.5	4.52e-01	0.0	a^6D	9/2	22637.0	b^4F	9/2	32.574
Fe III	4659.4	4.50e-01	0.0	^5D	4	21462.2	$^3F2$	4	30.886
Fe III	4702.9	2.50e-01	436.2	^5D	3	21699.9	$^3F2$	3	31.226
Fe III	4735.2	9.80e-02	738.9	^5D	2	21857.2	$^3F2$	2	31.448
Fe III	4756.0	8.40e-02	436.2	^5D	3	21462.2	$^3F2$	4	30.882
Fe III	4770.8	8.50e-02	738.9	^5D	2	21699.9	$^3F2$	3	31.226
Fe II	4815.9	4.71e-01	1872.6	a^4F	9/2	22637.0	b^4F	9/2	32.572
Fe II	4890.9	3.45e-01	384.8	a^6D	7/2	20831.0	a^2H	5/2	29.974
Fe III	4931.9	7.00e-01	932.4	^5D	1	21208.5	$^3P2$	0	30.514
Fe III	5012.7	5.40e-01	738.9	^5D	2	20688.4	$^3F2$	1	29.768
Fe II	5160.1	4.06e-01	1872.6	a^4F	9/2	21252.0	a^4H	13/2	30.575
Fe II	5263.2	3.95e-01	2430.1	a^4F	7/2	21430.0	a^4H	11/2	30.837
Fe III	5271.9	4.20e-01	436.2	^5D	3	19404.8	$^3P2$	2	27.925
Fe II	5274.7	5.23e-01	1872.6	a^4F	9/2	20831.0	a^2H	5/2	29.978
Fe II	5335.0	3.23e-01	2837.9	a^4F	5/2	21582.0	a^4H	9/2	31.057
Fe II	5377.9	3.13e-01	3117.5	a^4F	3/2	21712.0	a^4H	7/2	31.244
Fe II	5528.9	3.33e-01	2430.1	a^4F	7/2	20517.0	a^2D2	5/2	29.522
Fe II	7157.0	1.56e-01	1872.6	a^4F	9/2	15845.0	a^2G	9/2	22.794
Fe II	7174.2	5.96e-02	2430.1	a^4F	7/2	16369.0	a^2G	7/2	23.557
Fe II	7390.4	4.56e-02	2837.9	a^4F	5/2	16369.0	a^2G	7/2	23.552
Fe II	7454.4	5.13e-02	2430.1	a^4F	7/2	15845.0	a^2G	9/2	22.790
Fe II	8619.6	3.18e-02	1872.6	a^4F	9/2	13474.0	a^4P	5/2	19.382
Fe III	9703.9	8.50e-02	20051.1	^3H	6	30356.2	^1I	6	43.677
Fe III	10611.4	2.00e-01	21462.2	$^3F2$	4	30886.0	^3D	4	44.440
Fe II	12570.2	5.16e-03	0.0	a^6D	9/2	7955.3	a^4D	7/2	11.447
Fe II	12706.9	4.22e-03	977.1	a^6D	1/2	8846.8	a^4D	1/2	12.723
Fe II	12791.2	2.91e-03	862.6	a^6D	3/2	8680.5	a^4D	3/2	12.489
Fe II	12946.3	2.29e-03	667.7	a^6D	5/2	8391.9	a^4D	5/2	12.072
Fe II	13209.1	1.52e-03	384.8	a^6D	7/2	7955.3	a^4D	7/2	11.441
Fe II	13281.5	1.30e-03	862.6	a^6D	3/2	8391.9	a^4D	5/2	12.078
Fe II	15339.1	2.87e-03	1872.6	a^4F	9/2	8391.9	a^4D	5/2	12.072
Fe II	15999.0	3.88e-03	2430.1	a^4F	7/2	8680.5	a^4D	3/2	12.485
Fe II	16440.1	5.77e-03	1872.6	a^4F	9/2	7955.3	a^4D	7/2	11.444
Fe II	16642.0	4.68e-03	2837.9	a^4F	5/2	8846.8	a^4D	1/2	12.720
Fe II	16773.5	2.30e-03	2430.1	a^4F	7/2	8391.9	a^4D	5/2	12.079
Fe II	18098.9	1.27e-03	2430.1	a^4F	7/2	7955.3	a^4D	7/2	11.447
Fe II	20072.3	1.00e-01	13905.0	a^4P	1/2	18887.0	a^2P	1/2	27.171
Fe II	20462.5	7.41e-02	13474.0	a^4P	5/2	18361.0	a^2P	3/2	26.412
Fe III	21456.9	3.71e-02	20481.9	^3H	4	25142.4	^3G	3	36.178
Fe III	22184.3	3.41e-02	20051.1	^3H	6	24558.8	^3G	5	35.331
Fe III	22426.6	2.20e-02	20481.9	^3H	4	24940.9	^3G	4	35.881
Fe III	23485.2	2.40e-02	20300.8	^3H	5	24558.8	^3G	5	35.339
Fe II	179372.2	5.84e-03	1872.6	a^4F	9/2	2430.1	a^4F	7/2	3.496
Fe III	229252.6	2.80e-03	0.0	^5D	4	436.2	^5D	3	0.626
Fe II	245218.2	3.95e-03	2430.1	a^4F	7/2	2837.9	a^4F	5/2	4.080
Fe II	259882.0	2.12e-03	0.0	a^6D	9/2	384.8	a^6D	7/2	0.555
Fe III	330360.1	1.80e-03	436.2	^5D	3	738.9	^5D	2	1.063

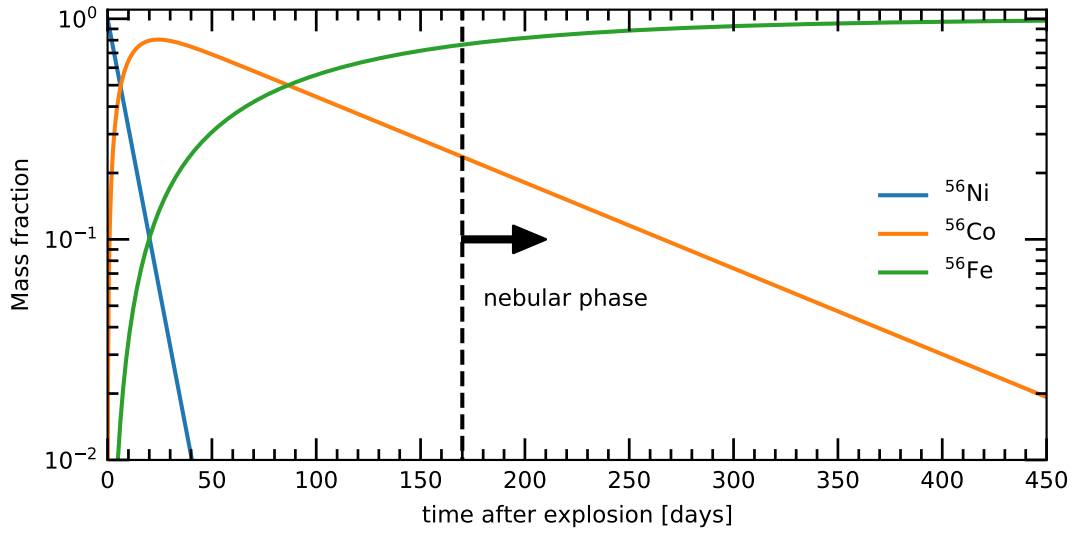

Figure 2.10.: Mass fractions of ^{56}Ni, ^{56}Co and ^{56}Fe as a function of time after explosion. The initial composition is assumed to be purely ^{56}Ni. During the nebular phase ^{56}Ni has completely decayed and less than 20% of ^{56}Co is left.

2.4.1. Iron in the NIR

The NIR emission of SNe Ia in the nebular phase is dominated by lines of [Fe II] originating from the a^{4}D multiplet (see Fig. 2.11). This multiplet with an excitation temperature between 7955 and 8856 cm^{-1} (0.986 and 1.098 eV) lies halfway between the ground state a^{6}D (including the lowest excited multiplet a^{4}F) and the a^{4}P multiplet (see Tab. 2.5 and Fig. 2.11)[2]. It serves as a stepping stone between the ground state and the higher energy multiplets ($T_{\rm exc} > 15000$ K), leading to efficient excitation of the ion. If thermal electron collisions are responsible for the majority of ion excitations then the a^{4}D multiplet can be populated even at low electron temperatures.

In doubly ionised iron no such multiplet is present (Fig. 2.12). The first excited multiplet above the ground state of Fe III has an energy of ~ 20000 cm^{-1} (2.48 eV), making it much harder to excite the ion. As a result, only few weak lines (e.g. $\lambda\lambda$ 9701.3, 10608.5, 21451.1, 22178.2, 22420.5, 23478.8) of doubly ionised iron emission contribute to the NIR display. In general, it is much more difficult to excite Fe III compared to Fe II.

[2]In this Chapter, wavelengths are given in air unless indicated otherwise. The refractive index of air is between 1.000282 and 1.000274 for optical and NIR lines, respectively. Lines are given in Ångstrom throughout the text. Emission line features are given in Ångstrom in the optical and in μm in the infrared. Energy levels use the classical spectroscopic unit 'wave number' (cm^{-1}), which is proportional to the frequency, and thus, the photon energy. For simplicity, the corresponding value in eV is given whenever wave numbers are mentioned in the text.

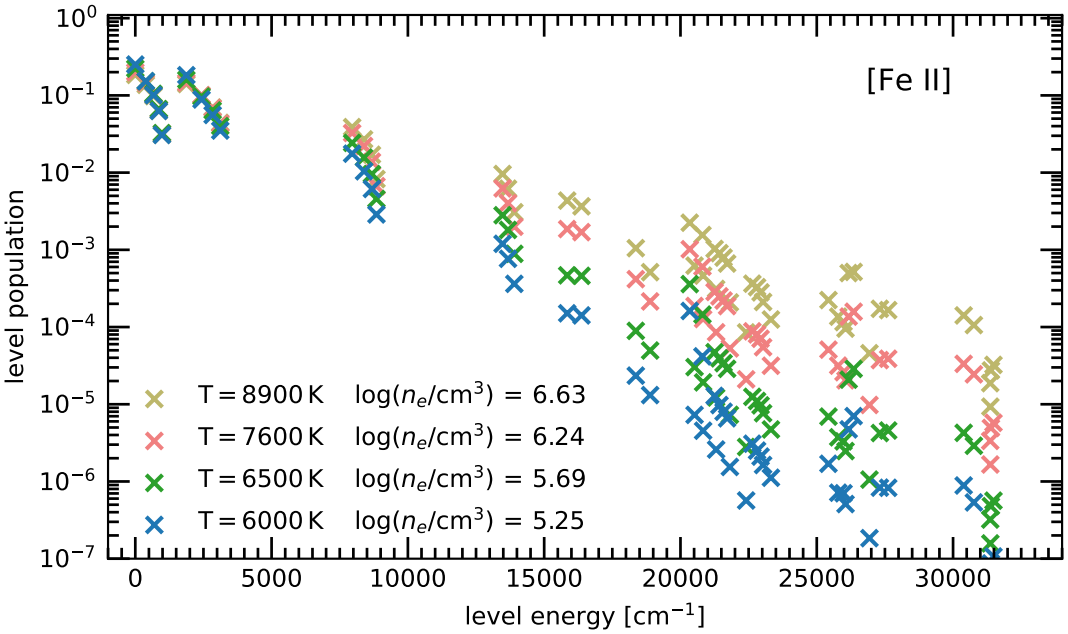

Figure 2.11.: Level populations as function of level energy for [Fe II]. The level populations are shown for four combinations of temperature and density which are typical for the nebular phase between 200 and 400 days.

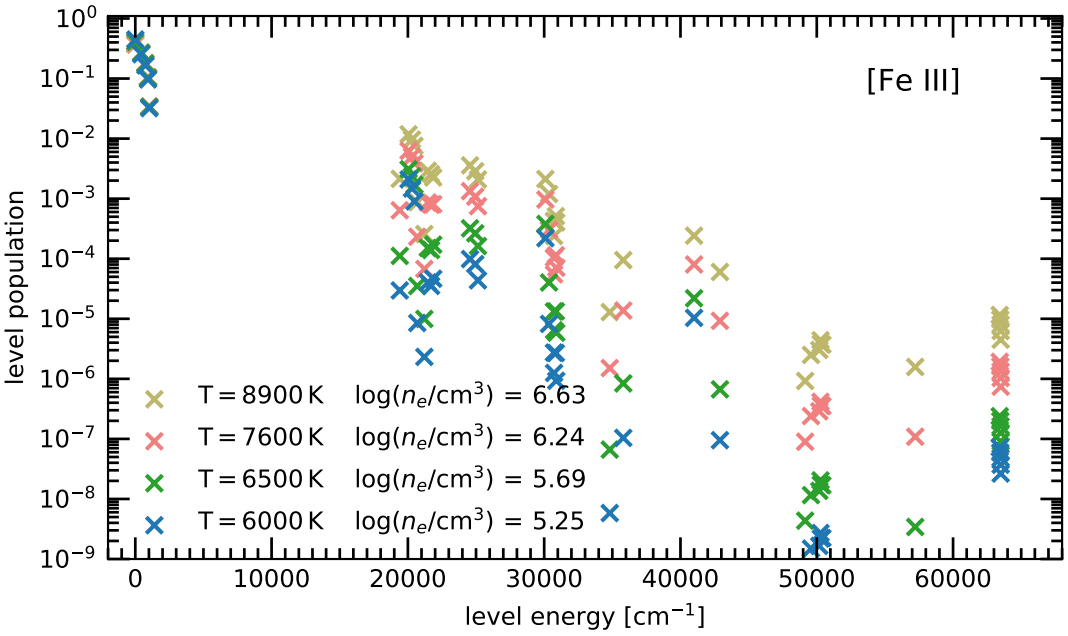

Figure 2.12.: Level populations as function of level energy for [Fe III]. The level populations are shown for four combinations of temperature and density which are typical for the nebular phase between 200 and 400 days.

The strongest NIR [Fe II] lines are the 12567 Å and 16436 Å transitions originating from the same upper level $a^4D_{7/2}$. Their relative strength is given by

$$\frac{F_{12567\,\text{Å}}}{F_{16436\,\text{Å}}} = \frac{A_{a^6D_{9/2}-a^4D_{7/2}}(E_{a^4D_{7/2}} - E_{a^6D_{9/2}})}{A_{a^4F_{9/2}-a^4D_{7/2}}(E_{a^4D_{7/2}} - E_{a^4F_{9/2}})} = 1.17 \tag{2.57}$$

and is fixed, in the supernova (zero optical depth) case. As both lines are relatively isolated from other [Fe II] lines we can test, whether in the absence of dust extinction and optical depth effects other ions contribute to the features at these wavelengths. However, as can be seen from Fig. 2.13, the expected line ratio of the [Fe II] NIR lines matches the observed features very well and differences are only due to [Co III] (see Fig. 2.14 for the [Co III] emission contribution to the 16436 Å feature). We can exclude non-IGEs contributing to the 1.25 μm and 1.6 μm features in objects which have NIR spectra during the nebular phase.

The 1.26 μm feature can be be attributed to lines of singly ionised iron. None of the other species present in the ejecta have significant lines in this range. The strongest contribution to this feature comes from [Fe II] 12567 Å. The second strongest line at 13206 Å shares the same upper level as the 12567 Å line leading to temperature independent relative strengths (see above). Other, weaker lines only contribute marginally with less than 25% of the strength of the 12567 Å line. Electron temperature and density induced changes of the line strengths are limited to less than 10%. Modelling this feature provides excellent constraints on the emitting region of [Fe II].

NIR lines of [Fe II] emerging from the a^4D multiplet remain in LTE until late in the nebular phase. Optical lines, on the other hand, decouple much earlier when the ejecta are not fully transparent. It is therefore much easier to model the NIR than it is to model the optical regime.

2.4.2. Iron in the Optical

In the optical, strong lines of both [Fe II] and [Fe III] are visible. Iron lines are dominant in three distinct regions: between 4200 Å and 5400 Å, near 7200 Å and at 8500 Å. However, unlike in the NIR, the features contain lines of singly and doubly ionised material and of several elements (iron, nickel and cobalt). Optical lines from singly ionised iron originate from a multitude of levels with energies between $\sim$ 13000 and 25000 cm^{-1} (1.61 and 3.10 eV), much higher than those of the [Fe II] NIR lines ($\sim$ 8000 cm^{-1}, corresponding to 0.992 eV). Optical [Fe III] lines require even higher excitation energies between $\sim$ 20000 and 30000 cm^{-1} (2.48 and 3.72 eV). As a result, cooling occurs mainly through the optical lines as long as the emitting material remains hot and dense. As the ejecta cool over the course of months an ever increasing fraction of energy is emitted through NIR lines instead.

The strongest optical and NIR feature visible in SNe Ia is seen between 4600 and 4800 Å and has subsequently been dubbed the '4700 Å' feature. It is seen in normal and also a number of peculiar SNe Ia. The origin of this feature is commonly attributed to a blend of [Fe III] lines

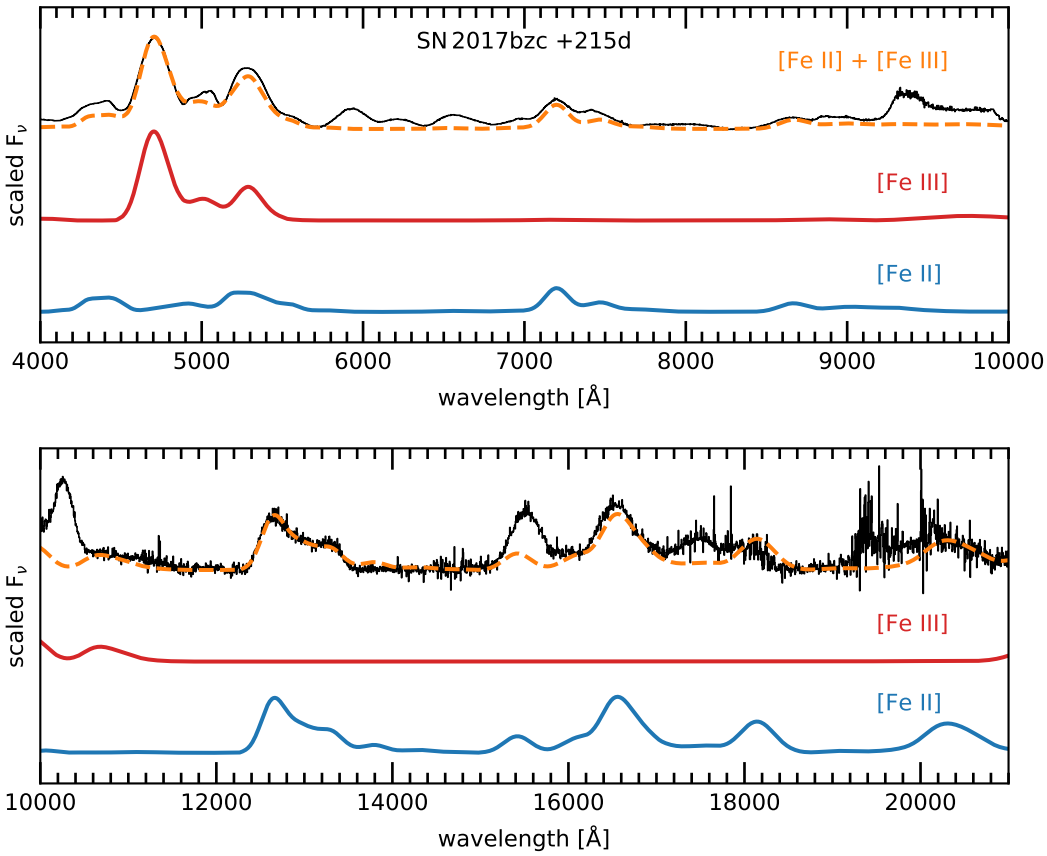

Figure 2.13.: Synthetic nebular spectrum of singly and doubly ionised iron. At the top of each panel the combined emission of [Fe II] and [Fe III] and a spectrum of SN 2017bzc is shown.

at 4658, 4702 and 4734 Å(e.g. Axelrod, 1980; Kuchner et al., 1994; Bowers et al., 1997; Mazzali et al., 2015, and references therein). As shown in Fig. 2.13, emission from [Fe II] is expected to contribute to this feature, albeit it is much weaker than that of [Fe III]. However, the changing properties of the plasma state of the emitting material over the course of several hundred days make it difficult to estimate what fraction of the flux originated in singly and doubly ionised iron, respectively.

At the onset of the nebular phase (6 months after the explosion) the 4700 Å feature is always seen blueshifted by several 10^3 km s^{-1} compared to the rest wavelength of the pure [Fe III] blend. Over the course of the subsequent year the feature appears to gradually shift towards their rest wavelength. It is currently unknown what causes this effect. Possible explanations are time variable contributions from other unidentified ions, changes of the emitting region with time, or changes in the relative contribution of singly and doubly ionised iron. On the other hand, [Fe II] lines are seen both blue- and redshifted compared to its rest wavelength.

From the width of the strong emission lines it becomes clear that the emitting region of doubly ionised iron is different from that of singly ionised iron. Whereas the former extends to roughly $\sim$ 11000 km s^{-1} in FWHM, the latter is confined to the inner 7000 km s^{-1}. The width of the 4700 Å feature has been suggested to anti-correlate with the SN decline rate, measured in Δm_{15} (Mazzali et al., 1998). Such a relation would imply that a more efficient explosion (higher ^{56}Ni mass, brighter at maximum and thus more slowly declining) would lead to higher kinetic energies of the iron-rich ejecta, resulting in broader line profiles. The initial correlation found by Mazzali et al. (1998) has not been confirmed in larger samples (Mazzali & Hachinger, 2012; Silverman et al., 2013a; Black et al., 2016).

A strong emission feature of [Fe II] emerges from the a^4F–a^4P multiplet near 8600 Å. While it is clear that singly ionised iron contributes to this feature, it remains to be seen whether it is the sole contributor. The feature is best reproduced at late phases ($>$ 350 d) with just [Fe II]. The wavelength of the strongest [Fe II] line at 8617.2 Å in this feature coincides with the central wavelength of the Ca II IR-triplet (8495.7, 8539.7 and 8659.8 Å), making the identification less certain at early times.

The 7200 Å feature in SNe Ia has been attributed to the a^4F-a^2G multiplet of [Fe II] and the strongest line therein at 7155 Å. However, the region is difficult to model due to a broad blend of [Co III] and nearby lines of [Ni II] (see Sec. 2.5 and 2.6). It was found that the NIR and optical lines of [Fe II] exhibit similar widths and shifts, indicative for a common emitting region (Maguire et al., 2018a, see also Sec. 2.3). The ratio of 12567 Å and 7155 Ålines can be used to determine the plasma conditions of the material. From the onset of the nebular phase around 150 days, the electron density and temperature of the ejecta decrease resulting in a shift of the emission from higher excitation optical lines to infrared lines arising from lower lying energy levels. This can be expressed in terms of the ratio of the 12567 Å and 7155 Å lines, which is an increasing function of the time since explosion. However, there is a degeneracy in the allowed temperatures and densities which cannot be broken with the ratio of only two lines. Each line ratio therefore

corresponds to a curve in the parameter space. While knowledge of the exact plasma conditions is relatively inconsequential for converting NIR line ratios into mass ratios due to their departures from Boltzmann populations being small, is is paramount when attempting to do the same with optical lines. In **Paper III** the [Fe II] NIR to optical line ratio relation is determined.

2.5. The Presence of Cobalt in Nebular spectra

Similarly to iron, the emission lines of Co arise predominantly from the ^{56}Ni decay chain. ^{56}Co is the decay product of ^{56}Ni and has a half-life of 77.2 days. The only other significant source of cobalt is the neutron-rich isotope ^{57}Ni, which decays in a matter of days to ^{57}Co. Compared to ^{56}Co, ^{57}Co has much longer half-life of 271.79 days, though the neutron-rich variant of nickel is produced in low abundances ($< 3\%$) and thus the number of ^{57}Co nuclei overtakes the number of leftover ^{56}Co nuclei only after > 400 days. In sub-M_{Ch} explosions this timescale is even longer as the lack of available neutrons severely limits the amount of ^{57}Ni that can be synthesised.

The atomic structure of singly and doubly ionised cobalt is very similar to that of iron (compare Fig. 2.15 and 2.11 for [Co II] and Fig. 2.16 and 2.12 for [Co III]). The a^5F multiplet of Co II, at an energy of $\sim 5000\,\mathrm{cm}^{-1}$ (0.62 eV), serves the same purpose as the a^4D multiplet in Fe II by making it easier to excite higher levels. Co III, again, does not have such a multiplet. Its first excited multiplet above the ground state already has an energy of $\sim 15000\,\mathrm{cm}^{-1}$ (1.86 eV), which is slightly lower than that of Fe III but considerably harder to excite than Co II. An overview of the dominant lines of singly and doubly ionised cobalt is given in Tab. 2.6.

Similarly to Fe II, Co II has a number of low lying NIR transitions arising between the a^3F–b^3F and a^5F–b^3F multiplets with excitation energies of $\sim 10000\,\mathrm{cm}^{-1}$ (1.24 eV). The two strongest NIR lines are from the a^3F–b^3F transition at 10188 Å and the a^5F–b^3F transition at 15470 Å(see Fig. 2.14). As they depopulate the same upper level their ratio is fixed (see Sec. 2.4):

$$\frac{F_{10188\,\text{Å}}}{F_{15470\,\text{Å}}} = \frac{A_{a^3F_4-b^3F_4}(E_{b^3F_4} - E_{a^3F_4})}{A_{a^5F_5-b^3F_4}(E_{b^3F_4} - E_{a^5F_5})} = 1.76 \tag{2.58}$$

The 10188 Å[Co II] line is bordered on both sides by the [Fe III] $^3H_6$–$^1I_6$ and $^3F2_4$–$^3D_4$ lines at 9701 and 10608 Å, respectively. Having excitation energies of $\sim 30000\,\mathrm{cm}^{-1}$ (3.72 eV) these transitions do not contribute in the advanced nebular phase, but their contribution at earlier epochs is significant. Naïve modelling of the feature with just [Co II] would lead to much broader lines, where [Co II] is emerging from a 'pseudo-continuum'. At early epochs (< 200 days) the [Co II] a^5F_5–b^3F_4 and [Co III] $a^2G_{9/2}$–$a^2H_{9/2}$ lines at 15470 Å and 15485 Å are responsible for most of the emission in the 1.55 μm feature. As the ejecta are expanding and cooling, the contribution from [Co III] begins to wane first.

The excitation energy of the [Co III] $a^2H_{9/2}$ level is more than twice as high as that of [Co II] b^3F_4 and can only be sustained while the ejecta are hot and dense.

Similar to the NIR [Fe II] transitions arising from the a^4D multiplet, [Co II] emission from the b^3F multiplet remains in LTE until late in the nebular phase ($\sim$ 500 days). Additionally, the [Co II] b^3F_4 and [Fe II] $a^4D_{5/2}$ levels have comparable excitation energies (9812 cm^{-1} and 8391 cm^{-1}; corresponding to 1.217 and 1.040 eV). This means that their line ratio can easily be converted into a mass ratio of the involved species, as has been demonstrated for SN 1987A (Varani et al., 1990). The assumption of LTE coupled with the similar excitation energies only leads to errors of order $\sim 10\%$ (see right panel in Fig. 2.17) in the determined mass ratio.

Knowledge about the cobalt to iron mass ratio is important in order to distinguish between the Chandrasekhar mass and sub-Chandrasekhar mass channels. A mass ratio close to the value expected from pure ^{56}Co decay to ^{56}Fe would indicate that the explosion took place at low densities typical for sub-Chandrasekhar mass WDs. Deviations from ^{56}Co decay would point towards Chandrasekhar mass explosions as the source of SNe Ia. In **Paper II** this method is applied to a sample of well studied SNe Ia to determine the most likely Co/Fe mass ratio.

The only strong [Co III] NIR lines are blends with singly ionised states of Fe and Co: the aforementioned 1.55 μm feature and the 1.75 μm feature. The latter is composed of singly and doubly ionised cobalt, but the moderately strong telluric absorption in this region imposes great difficulties on observations.

The optical display of cobalt is dominated by the doubly ionised state. There are no strong lines of [Co II] except a^3F_3–a^1D_2 at 9342 Å, which is likely blended with the [S III] transitions $^3P_1$–$^1D_2$ and $^3P_2$–$^1D_2$ at 9066 Å and 9528 Å, respectively (see e.g. Botyánszki & Kasen, 2017; Shingles et al., 2020). [Co III] has a number of transitions from the a^2G and a^4P multiplets between 5888 Å and 6961 Å, which yield good agreement with observed spectra (see Fig. 2.14). The ratio of its strongest line at 5888 Å ($a^4F_{9/2}$–$a^2G_{9/2}$) to the 4658 Å [Fe III] trademark line of nebular spectra has been used to infer that the nebular phase of SNe Ia is powered by radioactive decay of ^{56}Co (Kuchner et al., 1994). In principle, these lines can be used to infer a mass ratio of the doubly ionised species of cobalt and iron, yielding complementary results to the method presented in **Paper II**. However, it turns out that the energy separation of the upper levels of [Fe III] – $^3F2_4$ – and [Co III] – $^1D_2$ – leads to a mass ratio that is highly sensitive to the excitation conditions ($\Delta E = 4484\,cm^{-1}$). For typical temperatures in the nebular phase between 3000 K and 10000 K the mass ratio cannot be inferred to less than a factor of two using this method. While this certainly allows the confirmation of the powering mechanism of SNe Ia, a $< 10\%$ effect such as the ^{57}Co abundance is probably out of reach.

2.6. The Presence of Nickel in Nebular spectra

In contrast to iron and cobalt no substantial amount of ^{56}Ni is expected to survive until the nebular phase ($> 25\times T_{1/2}$; see Fig. 2.10). However, as detailed in Sec. 1.5, the neutron-rich isotope ^{58}Ni is stable and a few $10^{-2}\,M_\odot$ can be produced in the explosion, depending on the neutron excess of the fuel (see also Fig. 1.23 for an overview of nucleosynthetic yields of various

Table 2.6.: Selected forbidden lines of singly and doubly ionised cobalt in the optical, NIR and MIR.

Ion	$\lambda_{\mathrm{rest,vac}}$ [Å]	A_{ij} [s^{-1}]	E_i [cm^{-1}]	Term	J_i	E_j [cm^{-1}]	Term	J_j	Exc. Temp [10^3 K]
Co III	4 500.9	0.73400	841.0	a^4F	7/2	23 059.0	a^2D2	5/2	33.178
Co III	5 890.0	0.37100	0.0	a^4F	9/2	16 978.0	a^2G	9/2	24.428
Co III	5 908.4	0.14000	841.0	a^4F	7/2	17 766.0	a^2G	7/2	25.562
Co III	6 129.3	0.10400	1 451.0	a^4F	5/2	17 766.0	a^2G	7/2	25.562
Co III	6 196.9	0.11700	841.0	a^4F	7/2	16 978.0	a^2G	9/2	24.428
Co III	6 578.1	0.05550	0.0	a^4F	9/2	15 202.0	a^4P	5/2	21.873
Co III	6 855.4	0.03140	841.0	a^4F	7/2	15 428.0	a^4P	3/2	22.198
Co III	6 963.3	0.01510	841.0	a^4F	7/2	15 202.0	a^4P	5/2	21.873
Co II	8 123.2	0.06980	950.3	a^3F	3	13 260.8	a^3P	2	19.080
Co II	9 344.8	0.16700	950.3	a^3F	3	11 651.5	a^1D	2	16.764
Co II	9 641.8	0.02730	950.3	a^3F	3	11 321.9	b^3F	2	16.290
Co II	9 946.0	0.07990	1 597.2	a^3F	2	11 651.5	a^1D	2	16.764
Co II	10 190.7	0.03360	0.0	a^3F	4	9 812.9	b^3F	4	14.119
Co II	10 248.0	0.02220	950.3	a^3F	3	10 708.3	b^3F	3	15.407
Co II	10 283.1	0.02810	1 597.2	a^3F	2	11 321.9	b^3F	2	16.290
Co II	15 474.2	0.02900	3 350.5	a^5F	5	9 812.9	b^3F	4	14.119
Co III	15 489.5	0.12300	16 978.0	a^2G	9/2	23 434.0	a^2H	9/2	33.717
Co II	16 266.7	0.00495	4 560.8	a^5F	3	10 708.3	b^3F	3	15.407
Co II	16 347.5	0.01410	5 204.7	a^5F	1	11 321.9	b^3F	2	16.290
Co II	17 366.3	0.01040	4 950.1	a^5F	2	10 708.3	b^3F	3	15.407
Co III	17 415.5	0.03940	16 978.0	a^2G	9/2	22 720.0	a^2H	1/2	32.690
Co III	17 642.9	0.03700	17 766.0	a^2G	7/2	23 434.0	a^2H	9/2	33.717
Co II	19 040.1	0.00521	4 560.8	a^5F	3	9 812.9	b^3F	4	14.119
Co III	19 577.1	0.17700	15 811.0	a^4P	1/2	20 919.0	a^2P	1/2	30.099
Co III	20 028.0	0.14100	15 202.0	a^4P	5/2	20 195.0	a^2P	3/2	29.057
Co II	105 227.3	0.02230	0.0	a^3F	4	950.3	a^3F	3	1.367
Co III	118 906.1	0.02000	0.0	a^4F	9/2	841.0	a^4F	7/2	1.210
Co II	147 385.2	0.01240	3 350.5	a^5F	5	4 029.0	a^5F	4	5.797
Co II	154 589.8	0.00971	950.3	a^3F	3	1 597.2	a^3F	2	2.298
Co III	163 934.4	0.01310	841.0	a^4F	7/2	1 451.0	a^4F	5/2	2.087
Co II	188 040.3	0.01080	4 029.0	a^5F	4	4 560.8	a^5F	3	6.562
Co III	240 384.6	0.00463	1 451.0	a^4F	5/2	1 867.0	a^4F	3/2	2.686
Co II	256 889.1	0.00572	4 560.8	a^5F	3	4 950.1	a^5F	2	7.122

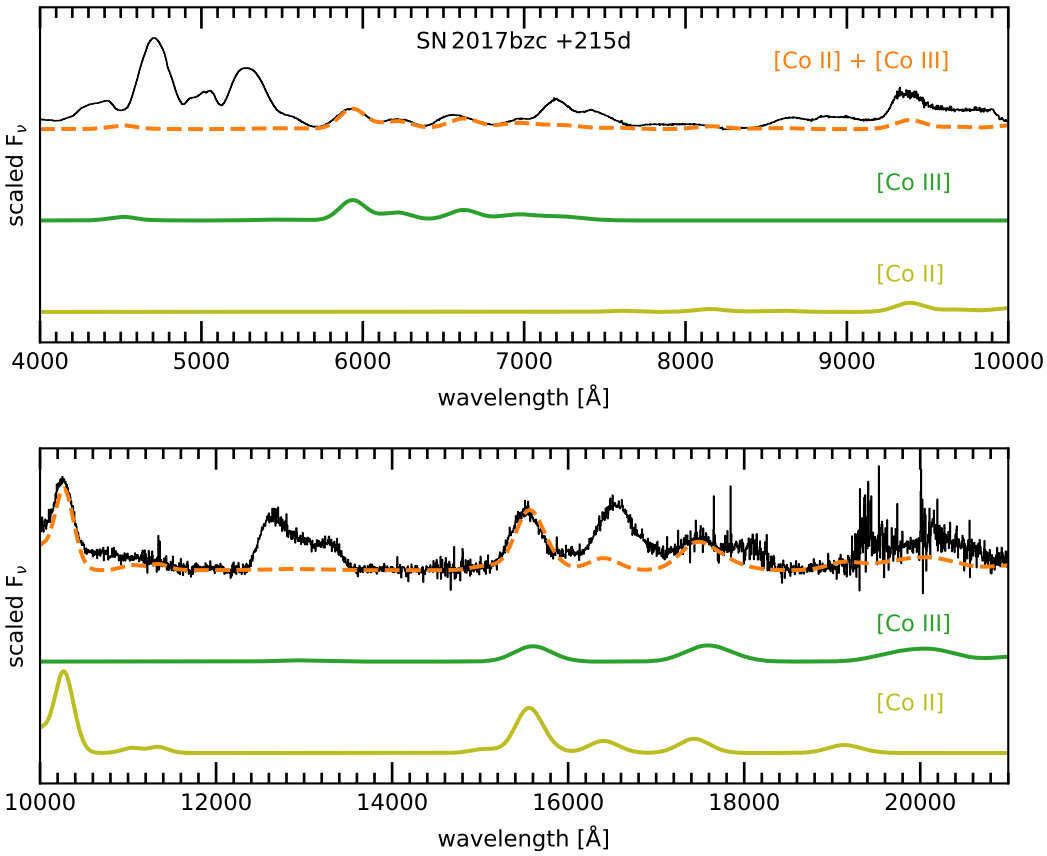

Figure 2.14.: Synthetic nebular spectrum of singly and doubly ionised cobalt. At the top of each panel the combined emission of [Co II] and [Co III] and a spectrum of SN 2017bzc is shown.

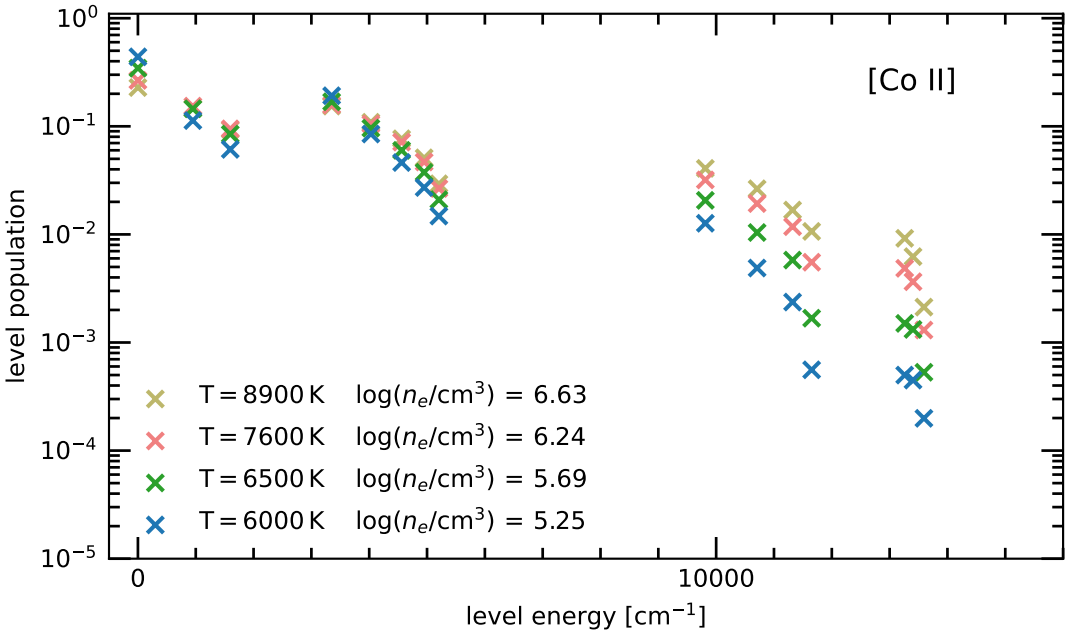

Figure 2.15.: Level populations as function of level energy for [Co II]. The level populations are shown for four combinations of temperature and density which are typical for the nebular phase between 200 and 400 days.

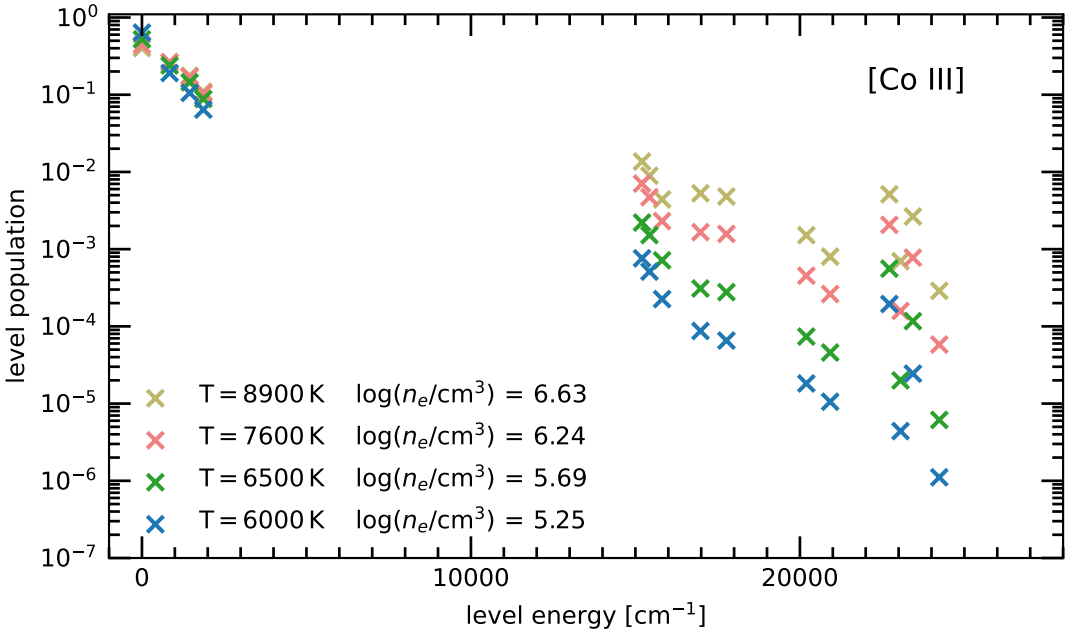

Figure 2.16.: Level populations as function of level energy for [Co III]. The level populations are shown for four combinations of temperature and density which are typical for the nebular phase between 200 and 400 days.

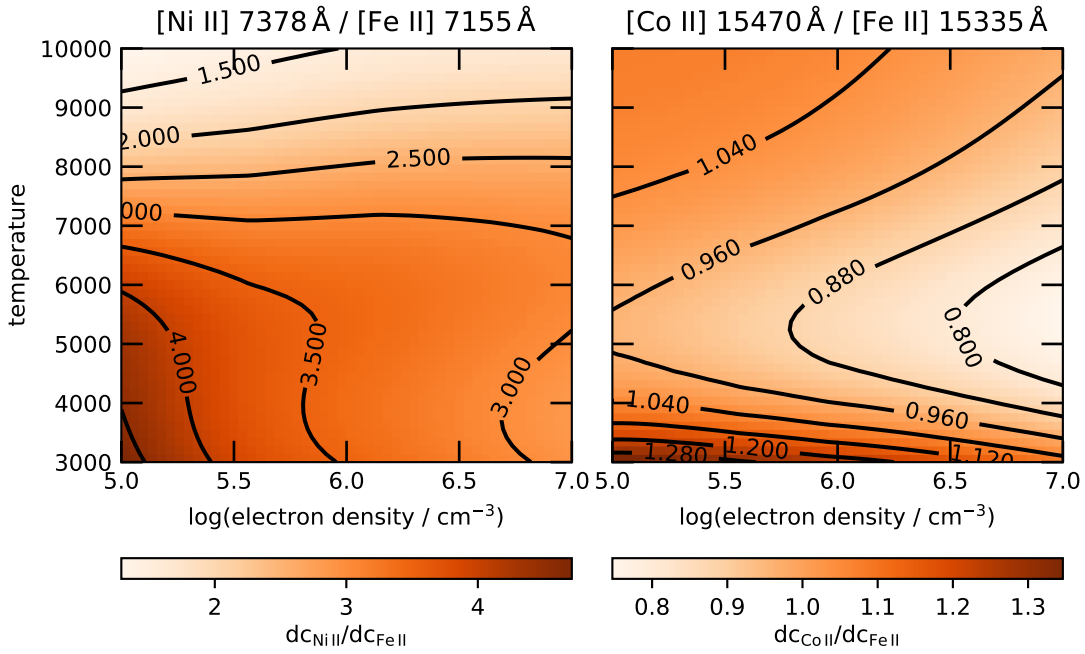

Figure 2.17.: Departure coefficients for optical lines of [Ni II] and [Fe II] (left panel) and NIR lines of [Co II] and [Fe II] (right panel). Colours and contours indicate the ratio of the departure coefficients for the respective transitions.

Table 2.7.: Selected forbidden lines of singly ionised nickel in the optical, NIR and MIR.

Ion	$\lambda_{\mathrm{rest,vac}}$ [Å]	A_{ij} [s^{-1}]	E_i [cm^{-1}]	Term	J_i	E_j [cm^{-1}]	Term	J_j	Exc. Temp [10^3 K]
Ni II	3 077.0	3.8000	0.0	^{2}D	5/2	32 499.5	^{2}G	9/2	46.761
Ni II	3 224.1	2.8900	1 506.9	^{2}D	3/2	32 523.5	^{2}G	7/2	46.796
Ni II	3 439.9	4.5300	0.0	^{2}D	5/2	29 070.9	^{2}P	3/2	41.828
Ni II	3 994.2	0.4230	0.0	^{2}D	5/2	25 036.4	^{2}D	5/2	36.023
Ni II	4 202.4	0.4890	0.0	^{2}D	5/2	23 796.2	^{2}D	3/2	34.239
Ni II	4 327.5	0.2670	0.0	^{2}D	5/2	23 108.3	^{4}P	5/2	33.249
Ni II	6 668.6	0.0767	0.0	^{2}D	5/2	14 995.6	^{2}F	5/2	21.576
Ni II	7 379.9	0.1730	0.0	^{2}D	5/2	13 550.4	^{2}F	7/2	19.496
Ni II	7 413.7	0.1410	1 506.9	^{2}D	3/2	14 995.6	^{2}F	5/2	21.576
Ni II	8 303.3	0.0098	1 506.9	^{2}D	3/2	13 550.4	^{2}F	7/2	19.496
Ni II	19 393.0	0.0918	8 393.9	^{4}F	9/2	13 550.4	^{2}F	7/2	19.496
Ni II	23 085.7	0.0302	10 663.9	^{4}F	3/2	14 995.6	^{2}F	5/2	21.576
Ni II	29 114.4	0.0151	10 115.7	^{4}F	5/2	13 550.4	^{2}F	7/2	19.496
Ni II	66 359.6	0.0557	0.0	^{2}D	5/2	1 506.9	^{2}D	3/2	2.168

explosion models). If any nebular nickel lines are seen in observed spectra they are evidence for at least some neutron excess during the NSE burning phase of the explosion. This is a huge advantage over iron and cobalt, for which it is difficult to disentangle the abundances of their neutron-rich isotopes from the overwhelming fraction of daughter products of radioactive ^{56}Ni.

Despite having a similar level structure as singly ionised iron and cobalt, Ni II only has few lines at optical and NIR wavelengths. The Ni II ^{4}F multiplet at energies of $\sim 10000\,\mathrm{cm}^{-1}$ (1.24 eV) is hardly connected to the ground state – there are only two transitions at 66 μm and 107 μm, which are both fully saturated at temperatures of several 10^3 K (see Fig. 2.18 and Tab. 2.7). In Fe II and Co II, the corresponding multiplets at these energies – a^{4}D and b^{3}F – give rise to a copious number of NIR transitions.

The ^{2}F multiplet at energies of $\sim 14000\,\mathrm{cm}^{-1}$ (1.74 eV) is strongly connected to the ground state ^{2}D and the first excited multiplet ^{4}F. Most of these transitions are rather weak ($\mathrm{A}_{ij} < 10^{-3}$), which, coupled with the low expected abundance of ^{58}Ni in SNe Ia, renders them almost impossible to detect. Five transitions from the ^{2}F multiplet have transition probabilities higher than 10^{-2} (6667 Å, 7378 Å, 7412 Å, 8301 Å and 19388 Å). Only these lines have a chance of being identified in observed data (see Fig. 2.19).

Higher energy multiplets such as ^{4}P, ^{2}D, ^{2}P and ^{2}G suffer from too high excitation energies and too low abundances of ^{58}Ni to be observable, even though their A-values are quite high (see Fig. 2.18 for typical level populations). For the same reason we do not include doubly ionised nickel in our model, as the expected lines are too weak to detect and heavily blended with lines from other ions.

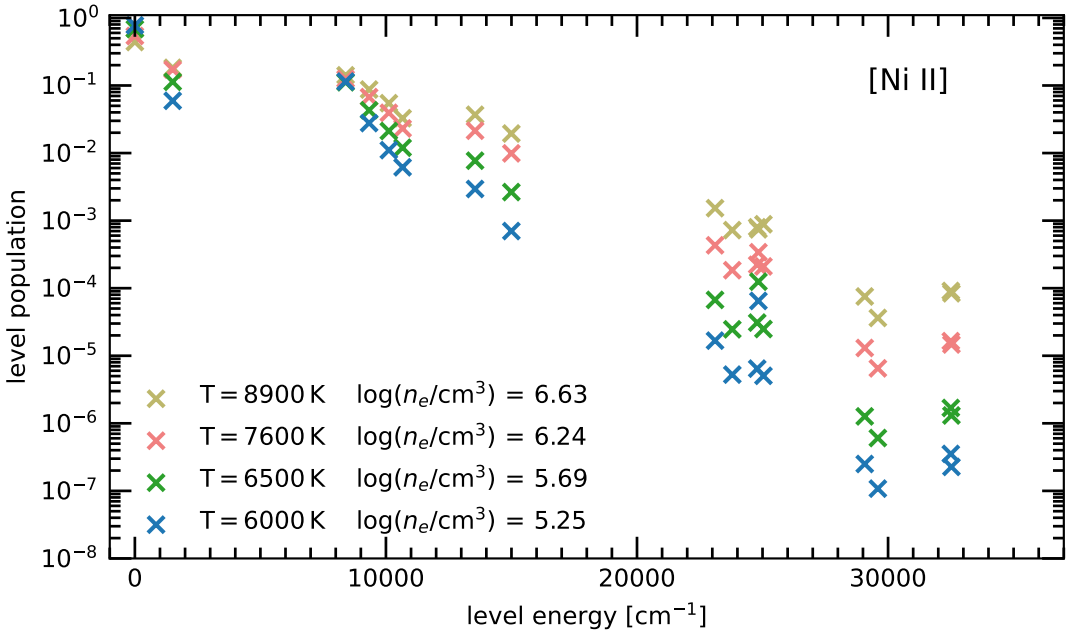

Figure 2.18.: Level populations as function of level energy for [Ni II]. The level populations are shown for four combinations of temperature and density which are typical for the nebular phase between 200 and 400 days.

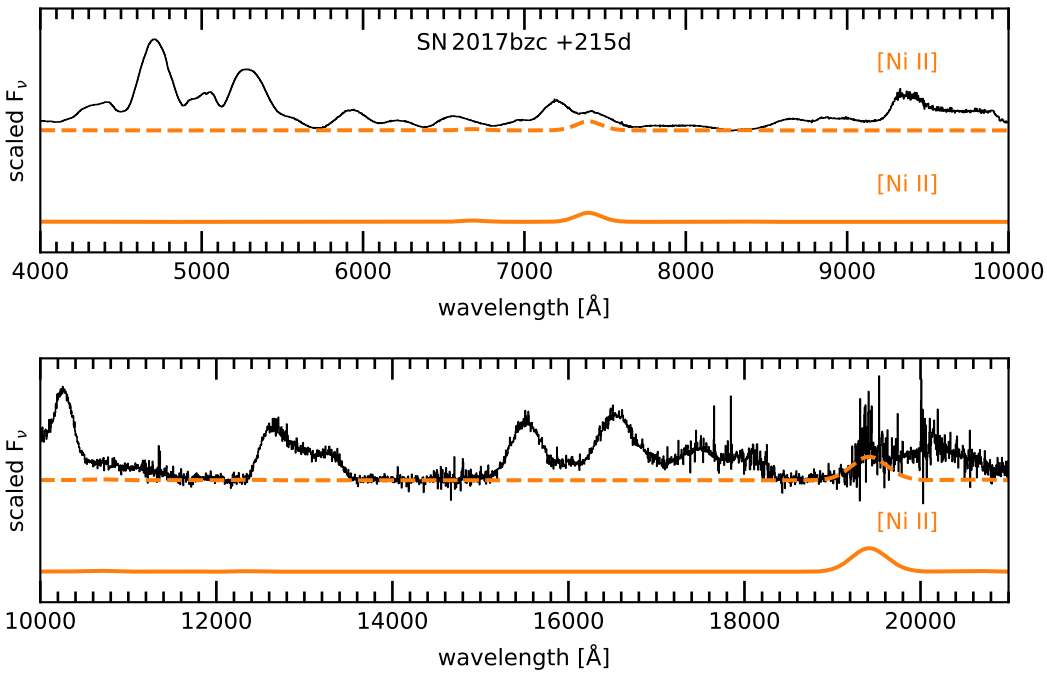

Figure 2.19.: Synthetic nebular spectrum of singly ionised nickel. At the top of each panel the emission of [Ni II] and a spectrum of SN 2017bzc is shown.

2.6.1. NIR Nickel emission at 1.93 μm

There is only a single strong [Ni II] line in the NIR: the transition $^4F_{9/2}$–$^2F_{7/2}$ near 19388 Å. Weak lines of [Fe II] (18954 Å from $a^4F_{3/2}$–$a^4D_{5/2}$ and 19670 Å from $a^4D_{5/2}$–$a^4P_{5/2}$), [Co II] (19035 Å from a^5F_3–b^3F_4) and [Co III] (19572 Å from $a^4P_{1/2}$–$a^2P_{1/2}$) form a pseudo-continuum that affects the feature. Assuming stable nickel abundances as predicted by explosions models, the line with an excitation energy of 13550.4 cm^{-1} (1.68 eV) should be observable in nearby SNe. However, it is in a difficult region of the NIR which is affected by poor atmospheric transmission.

NLTE radiative transfer simulations predict this line to be of comparable strength to the [Fe II] 12567 Å and 16436 Å lines, at least in Chandrasekhar mass explosions (Wilk et al., 2018; Blondin et al., 2018). Such a line would be clearly visible in all but the faintest objects. Sub-Chandrasekhar SNe Ia are expected to produce no to very little stable nickel and the 19388 Å line should be at least one order of magnitude weaker than in the Chandrasekhar mass channel. Transitional spectra (when the spectra are not fully transparent yet) show a feature near 1.98 μm (Friesen et al., 2014), but it remains unclear whether this is due to [Ni II] or the aforementioned [Co III] 19572 Å line (Blondin et al., 2018).

The nearby SN 2014J provided a rare opportunity to test whether the [Ni II] 19388 Å line is present, and if so, whether the predicted strength agrees with Chandrasekhar mass models. In **Paper I** we report the first unambiguous detection of this line which proves that SNe Ia indeed produce neutron-rich material.

In **Paper III** a number of additional nebular spectra are analysed. Two of the objects clearly show the [Ni II] 19388 Å line with widths and shifts similar to those of [Fe II] and [Co II]. Unfortunately, the remaining objects do not have the required S/N to detect the line if it was there. In all objects for which the [Ni II] NIR line can be found it is much weaker than predicted by any Chandrasekhar mass radiative transfer simulation.

2.6.2. Optical Nickel emission

Of the four optical [Ni II] lines only two are strong and secluded enough to be detectable. The 6667 Å line is weak and buried underneath relatively strong [Co III] emission, and the 8301 Å line is even weaker. The remaining two lines at 7378 Å and 7412 Å lie atop a complex of [Fe II] lines at 7155, 7172, 7388, 7453 Å. The two strongest [Fe II] lines share the same upper level and their relative strength is known. In principle, the feature could contain [Ca II] emission at 7291 Å and 7324 Å which do not necessarily have to exhibit Gaussian profiles. As such, the degree of their contribution is difficult to assess. On the other hand, the same argument can be brought forward for the contribution of the [Ni II] lines to the feature. Ni II lines contributing to this feature do not necessarily have to exhibit Gaussian profiles if the stable nickel is spatially separated from the ^{56}Ni decay products.

Fortunately, the 7378 Å and the 19388 Å lines both originate from the $^2\mathrm{F}_{7/2}$ level at 13550.4 cm^{-1} (1.68 eV). Their line ratio is

$$\frac{F_{7378\,\text{Å}}}{F_{19388\,\text{Å}}} = \frac{A_{^2D_{5/2}-^2F_{7/2}}(E_{^2D_{5/2}} - E_{^2F_{7/2}})}{A_{^4F_{9/2}-^2F_{7/2}}(E_{^4F_{9/2}} - E_{^2F_{7/2}})} = 4.95 \tag{2.59}$$

and independent of the electron temperature. For objects where the 19388 Å line has been detected, the contribution of [Ni II] to the optical 7300 Å emission complex can be tested. In **Paper III** we show that no additional lines are required to simultaneously obtain good matches between observations and models in the two regions.

Using this result, the strongest lines of [Fe II] and [Ni II] at 7155 Å and 7378 Å can be exploited to infer the Ni/Fe mass ratio and thus determine whether the normal population of SNe Ia originates from Chandrasekhar mass or sub-Chandrasekhar mass WDs. The multiplets responsible for these lines decouple from LTE before the ejecta become transparent, in contrast to the NIR lines of cobalt and iron (see Sec. 2.5). Departure coefficients, which characterise whether or not the excitation conditions are close to LTE, are shown in Fig. 2.17. For the phase range of interest their ratio varies between 2 and 4, dependent on the electron density and temperature of the emitting ejecta. Smaller values apply at earlier epochs when the conditions are closer to LTE.

There is a significant advantage in using the Ni/Fe mass ratio compared to other tracers such as the Co/Fe mass ratio, as optical nebular phase observations are abundant compared to rare cases of NIR spectra. Also, no leftover ^{56}Ni and limited contributions of stable iron to the total iron budget make it much easier to draw conclusions from the determined ratio. In **Paper III** we determine the Ni/Fe mass ratio for a large sample of observations.

3. Summary of Publications

Large parts of Chapter 2 have already been published in three peer-reviewed articles in Astronomy & Astrophysics (Dhawan et al., 2018; Flörs et al., 2018, reproduced with permission ©ESO) and Monthly Notices of the Royal Astronomical Society (Flörs et al., 2020, reproduced with permission ©Royal Astronomical Society). In order to submit a coherent thesis, I adapted some of the published contents to the style and narrative of the thesis. References to the corresponding article have been given in Chapter 2. A summary of the publications is presented in the following.

I **Nebular spectroscopy of SN 2014J: Detection of stable nickel in near-infrared spectra**
Dhawan S., **Flörs A.**, Leibundgut B., Maguire K., Kerzendorf W., Taubenberger S., Van Kerkwijk M. H., Spyromilio J., A&A, 619, A102, 2018

II **Limits on stable iron in Type Ia supernovae from near-infrared spectroscopy**
Flörs A., Spyromilio J., Maguire K., Taubenberger S., Kerzendorf W. E., Dhawan, S., A&A, 620, A200, 2018

III **Sub-Chandrasekhar progenitors favoured for Type Ia supernovae: evidence from late-time spectroscopy**
Flörs A., Spyromilio J., Taubenberger S., Blondin S., Cartier R., Leibundgut B., Dessart L., Dhawan S., Hillebrandt W., MNRAS, 491, 2902, 2020

3.1. Paper I: Nebular spectroscopy of SN 2014J: detection of stable nickel in near infrared spectra

As shown in Sec. 1.6, the nature of the progenitor system and the explosion mechanism are still unknown. A potential tracer of the density at the time of explosion and therefore a way to distinguish between explosion channels is the neutron-rich isotope ^{58}Ni. The relative ratios of ^{58}Ni compared to ^{56}Ni depends on the neutron excess of the progenitor WD, which, in turn, provides constraints on the mass of the exploding system. Only WDs near the Chandrasekhar-mass limit can synthesise high (> 0.05) fractions of ^{58}Ni/^{56}Ni.

Stable ^{58}Ni produced in the explosion is expected to be located in the central part of the ejecta which is blocked from view by the outer layers at early times. Only about 180 days after the explosion the ejecta become sufficiently transparent to optical and NIR photons that the iron-rich core can be seen. Detailed radiative transfer simulations predict a clear emission line of [Ni II] at 1.939 μm. The strength of this line is expected to scale with the fraction of nickel over iron. Chandrasekhar-mass explosions are expected to exhibit a line comparable in strength with the strongest iron lines in the NIR.

So far, no secure detection of the 19388 Å line of [Ni II] has been made. This is mainly due to the faintness of SNe Ia during the nebular phase ($5 - 8$ mag fainter than at maximum), and the general faintness of the NIR compared to the optical bands. Additionally, the 19388 Å line is in a region which is strongly affected by absorption in the atmosphere, which further decreases the number of collected photons. In this paper we present NIR spectroscopy of SN 2014J at a distance of 3.5 Mpc, the closest SN Ia since SN 1972E. We obtained three NIR spectra at epochs $+408, +450$ and $+478$ days with GNIRS on Gemini-North. In addition to emission lines of iron and cobalt, which have already been seen in other objects, the spectra of SN 2014J exhibit a clear feature near the expected wavelength of [Ni II] at 19388 Å.

My primary contribution to the paper was to model and analyse the obtained spectra to determine the strength of the 19388 Å line of [Ni II]. The model includes singly ionised iron, nickel and cobalt and is in good agreement with observed spectra. The presence of [Ni II] emission provides confirmation for the nucleosynthesis of neutron-rich material in SNe Ia. However, the strength of the [Ni II] line turned out to be much weaker than predicted by many Chandrasekhar-mass and even sub-Chandrasekhar-mass models. The weakness of the line means that it can only be detected in few nearby SNe. The estimated temperature and electron density of the emitting material allows us to exclude the occurrence of an IR-catastrophe. From the ratios of the strong iron lines the extinction to the SN can be estimated. Our findings for the extinction are compatible with earlier studies near maximum light.

Author contributions: I was responsible for the modelling and the analysis of the spectra. I have performed the involved computations, developed the spectral model and conducted the spectral analysis of the NIR spectra of SN 2014J. I provided two of the figures included in the work. All authors contributed to the manuscript equally.

3.2. Paper II: Limits on stable iron in type Ia supernovae from NIR spectroscopy

We have shown that the neutron-rich isotope ^{58}Ni was synthesised in SN 2014J (see **Paper I**). This finding naturally leads to the question whether other SNe also produce neutron-rich material. Unfortunately, no NIR observations with sufficiently high S/N late enough in the nebular phase were available at the time of the writing of this paper. However, ^{58}Ni is not the only neutron-rich isotope that is expected to be produced in SNe Ia. In this work we examine the effect of the decay chain of ^{57}Ni (particularly ^{57}Co) as well as stable isotopes of iron (^{54}Fe, ^{56}Fe) synthesised during the explosion on the nebular spectrum. Similarly to stable iron, the amount of ^{57}Ni and ^{54,56}Fe depends on the mass of the exploding WD. Chandrasekhar-mass WDs produce significant amounts of these isotopes while zero-metallicity sub-Chandrasekhar-mass WDs are unable to produce noteworthy amounts of neutron-rich material. Explosions of solar metallicity sub-Chandrasekhar-mass WDs produce ^{57}Ni and ^{54,56}Fe at quantities between those of Chandrasekhar-mass WDs and zero-metallicity sub-Chandrasekhar-mass WDs. Quantifying the ratio of ^{54,56}Fe/^{56}Ni and ^{57}Ni/^{56}Ni therefore serves as a tracer of the mass of the WD at the time of the explosion.

We obtained optical and NIR spectra of eight objects. An additional three objects only have NIR spectra available. We identify emission lines from forbidden transitions of singly ionised iron and cobalt as the origin of the features in the NIR. We develop an emission line model which can reproduce the spectra of normal SNe Ia in the nebular phase. We account for significant departures from local thermodynamic equilibrium (LTE) due to low densities of the ejecta through a non-LTE (NLTE) excitation treatment.

In order to make extracted properties of the lines (line shifts, widths and fluxes) comparable across studies we develop a Bayesian nebular spectrum fitter which requires a noise model for the data. The use of the spectrum fitter allows us to probe a large parameter space and automatically model nebular spectra without input from the user. These significant improvements allow us to quantify uncertainties of the extracted parameters – which was not possible in earlier studies.

We use the ratio of two lines in the NIR: an [Fe II] line at 15335 Å and a [Co II] line at 15470 Å. The levels responsible for these lines remain in LTE until late in the nebular phase due to their low excitation energies. NLTE effects on these lines are limited to $\sim 10\%$. The fluxes of the two lines can be converted into a mass ratio of the involved ions.

A comparison of the measured line widths and shifts of singly ionised iron and cobalt suggest a shared emitting region. As a result, the plasma properties (electron density and temperature) are expected to be similar for [Fe II] and [Co II].

We compare the inferred mass ratios of Co/Fe to theoretical predictions of a number of SN Ia explosion models. The models include, in addition to ^{56}Ni, different amounts of ^{57}Ni and stable ^{54}Fe and ^{56}Fe. We compute Bayes factors between the models and exclude models that produce only ^{54,56}Fe or only ^{57}Ni in addition to ^{56}Ni. Of the remaining two models (no neutron-rich

contributions as in zero-metallicity sub-Chandrasekhar-mass WDs vs. both ^{57}Ni and ^{54,56}Fe as in $\sim$ solar metallicity sub-Chandrasekhar-mass WDs and Chandrasekhar-mass WDs) we find a higher evidence for the model including both ^{57}Ni and ^{54,56}Fe. For such a model our data imply that the ratios ^{54,56}Fe/^{56}Ni=0.272$\pm$0.086 and ^{57}Ni/^{56}Ni= 0.032 $\pm$ 0.011.

Author contributions: I developed the numerical NLTE model and devised the Bayesian fitting code used in the analysis of the data. I performed the model comparison in the Bayesian framework. I took the lead in writing the manuscript and I made all figures presented therein. All authors provided critical feedback for the final manuscript.

3.3. Paper III: Sub-Chandrasekhar progenitors favoured for type Ia supernovae: evidence from late-time spectroscopy

In **Paper I** we have shown that the explosive nucleosynthesis in SN 2014J led to the production of the neutron-rich stable isotope ^{58}Ni. During the nebular phase all radioactive nickel will have decayed, meaning that if nickel lines are seen they must be due to stable ^{58}Ni. The strength of nickel emission lines in the nebular phase compared to those of iron can provide a way to distinguish between burning at high or low densities and thus the mass of the primary WD. It is currently unclear whether WDs explode as they approach the Chandrasekhar-mass limit or significantly below.

Singly ionised nickel does not only emit in the NIR but also at optical wavelengths. Unlike the relatively unblended line in the NIR, the optical lines are found in a feature near 7300 Å containing emission from several species. It is not trivial to determine the contributions of individual components based on the optical spectrum alone. The detection of the NIR 19388 Å [Ni II] line fully determines the parameters (line shift, Doppler broadening and strength) of the optical lines and thus provides clarity on the composition of the optical features containing [Ni II]. We present two additional objects that exhibit the NIR [Ni II] line and find that the optical feature containing nickel can be fully explained by a model containing [Fe II], [Ni II] and [Co III]. In particular, we do not require emission from [Ca II].

Knowledge of the line fluxes is not enough to determine the mass ratio of Ni/Fe as the emitting levels are far from LTE during the nebular phase (in contrast to the lines used in **Paper II**). For levels mainly populated by NLTE excitation the conditions (electron density and temperature) of the emitting plasma are important. We found that the ratio of the strongest lines of [Fe II] in the NIR and optical evolves in a systematic fashion with SN epoch, and that it is a direct measurement of the plasma state of the emitting material – the temperature and electron density. Knowledge of the evolution of this ratio for a large enough sample of objects enables us to use the SN epoch as a proxy for the temperature and electron density.

For the modelling of the data we use the Bayesian fitter developed in **Paper II**. The treatment of optical lines requires us to include doubly ionised species of iron and cobalt. This in turn allows us to model archival SNe Ia for which only optical spectra are available, extract the abundance of

stable nickel produced during the explosion and discriminate between the two explosion channels (Chandrasekhar-mass or sub-Chandrasekhar-mass). The inclusion of objects that have only optical spectra increases the sample size by about one order of magnitude. The analysis of the optical 7300 Å feature consisting of mainly [Fe II] and [Ni II] yields Ni/Fe abundances that are in agreement with predictions of sub-Chandrasekhar-mass explosion simulations. The distribution peaks at abundances characteristic of $\sim Z_{\odot}$ sub-Chandrasekhar-mass progenitors. The mode of the distribution is at a Ni/Fe mass ratio of 0.034 ± 0.019. We find that only few objects (11%) have a Ni/Fe abundance in agreement with Chandrasekhar-mass explosion models.

Author contributions: I conceived the presented idea and developed the numerical NLTE model and the Bayesian fitting code used in the analysis of the data. I reduced the new data presented in the study. I took the lead in writing the manuscript and I made all figures presented therein. All authors provided critical feedback for the final manuscript.

3.4. Additional Publications

I **Multi-messenger Observations of a Binary Neutron Star Merger**
Abbott B. P, [2601 authors], **Flörs A.**, [1073 authors], 2017, Phys. Rev. Lett., 119, 161101

II **A kilonova as the electromagnetic counterpart to a gravitational-wave source**
Smartt S. J., [44 authors], **Flörs A.**, [75 authors], 2017, Nature, 551, 75

III **Light Curves of Hydrogen-poor Superluminous Supernovae from the Palomar Transient Factory**
De Cia, A., [8 authors], **Flörs A.**, [17 authors], 2018, ApJ, 860, 100

IV **The evolution of luminous red nova AT 2017jfs in NGC 4470**
Pastorello, A., [18 authors], **Flörs A.**, [26 authors], 2019, A&A, 625, L8

V **SN 2012dn from early to late times: 09dc-like supernovae reassessed**
Taubenberger, S., **Flörs A.**, [41 authors], 2019, MNRAS, 488, 5473

VI **SN2018kzr: A Rapidly Declining Transient from the Destruction of a White Dwarf**
McBrien O. R., [11 authors], **Flörs A.**, [21 authors], 2019, ApJL, 885, L23

VII **The rise and fall of an extraordinary Ca-rich transient. The discovery of ATLAS19dqr/SN 2019bkc**
Prentice S. J., Maguire K., **Flörs A.**, [25 authors], 2020, A&A, 635, A186

4. Conclusions and Outlook

4.1. Summary

A challenging problem in SN Ia research is the determination of the progenitor system and the explosion mechanism. Over the years, many indirect probes in support of either single- or double-degenerate as well as Chandrasekhar-mass or sub-Chandrasekhar-mass scenarios have been found (Sec. 1.6). However, a smoking gun still remains elusive.

Many other probes try to find *the* particular configuration of the progenitor system *in conjunction* with the exact explosion model (Sec. 1.6). The continuous development of new ideas for the progenitor system and explosion mechanism question whether the current parameter space is complete. Additionally, the combination of progenitor system and explosion mechanism (e.g. accretion from a main-sequence companion to the Chandrasekhar-mass-limit with subsequent deflagration) makes it difficult to disentangle effects. It remains unclear whether the combination of progenitor system and explosion mechanism is unique or whether several progenitor systems lead to the same explosion mechanism (e.g. single- or double-degenerate double detonation) (Sec. 1.4).

In this thesis we *do not* want to answer which binary system ends its life as a SN Ia. Instead, we focus on the exploding mass of the primary WD which can either be significantly below the Chandrasekhar-mass limit (sub-Chandrasekhar-mass, see Sec. 1.4.2) or close to it (Chandrasekhar-mass, see Sec. 1.4.1). Furthermore, each of the two explosion mass regimes corresponds to exactly one allowed mode of the flame propagation: Chandrasekhar-mass explosions require some sort of deflagration-detonation-transition, while sub-Chandrasekhar-mass WDs have to explode in a detonation.

The outer layers of SNe Ia are strongly influenced by the explosion mechanism and the nature of the companion. The composition and structure of the inner core mainly follows from the mode of the flame propagation and the central density of the WD at the onset of the explosion. Both the burning mode and the central density are determined by the mass of the exploding WD (Sec. 1.5). Simulations indicate that it is possible to produce ^{56}Ni in agreement with observations in both Chandrasekhar-mass and sub-Chandrasekhar-mass explosions, leading to similarly luminous events. However, the two classes differ in the amount of neutron-rich material which can be synthesised: only near-Chandrasekhar-mass WDs reach the high central densities that are required so that additional neutrons can be produced through carbon simmering and

electron capture reactions, on top of the neutrons available in both channels if the progenitor already contains neutron-rich material (Sec. 1.5).

At late times (> 200 d after explosion), the ejecta become fully transparent to optical and NIR photons and we can see deep into the core to the synthesised iron-rich material. Most of the mass in the iron-rich core is expected to originate from the decay chain of ^{56}Ni – ^{56}Co and ^{56}Fe. Radioactive decay of the residual ^{56}Co heats the electron gas, which, in turn, collisionally excites metastable energy levels of the IGEs. Radiative de-excitations result in an emission spectrum dominated by forbidden lines (Sec. 2.1).

In this thesis we have developed a non-LTE level population model of the first and second ionisation stages of iron, nickel and cobalt. From the level populations of the included ions line emissivities can be derived. Taking into account the Doppler broadening of the emission lines in the expanding ejecta, our model reproduces observed optical and NIR spectra in good agreement. In contrast to previous studies that modelled nebular phase spectra of SNe Ia, we do not fit the spectra by hand. Instead, we have created a probabilistic model for the observed and synthetic spectrum that takes sources of uncertainties of the observed data as well as some of the simplifications of our NLTE model into account. This novel approach not only allows us to determine the parameters of our model, but also to assess the involved parameter uncertainties.

We apply our NLTE model to multi-zone toy cases of spherically symmetric Chandrasekhar-mass and sub-Chandrasekhar-mass explosions in order to compare the emergent line profiles of IGEs (Sec. 2.3). We find that as long as the singly ionised material follows the elemental abundances and the temperature gradient across the iron-rich core remains moderate the emergent line profiles are reminiscent of Gaussian profiles. At the edges of the line profiles the deviations become strongest, but considering the overlap of lines in nebular spectra such an effect will be difficult to prove observationally. We further notice that the total emissivities of optical and NIR lines peak at different radii, depending on the temperature gradient. However, the FWHM of the emergent line profiles do not appear to be affected significantly.

In Sec. 3.1 we applied our probabilistic NLTE model to NIR spectra of SN 2014J obtained with GNIRS on Gemini-North. We showed that SN 2014J, the closest SN Ia since SN 1972E, exhibits lines of [Ni II]. Owing to its short half life, radioactive ^{56}Ni cannot be present at nebular epochs. The detected nickel has to be entirely in the form of the neutron-rich stable isotopes ^{58}Ni and ^{60}Ni. The expected amount of stable ^{58}Ni depends on the mass of the primary WD: Chandrasekhar-mass explosion models predict a Ni/Fe mass ratio of $0.07 - 0.12$, while the Ni/Fe ratio is < 0.06 for sub-Chandrasekhar-mass models. We detect [Ni II] emission at $1.939\,\mu$m in all three spectra of SN 2014J. This result establishes that at least some amount of neutron-rich material is present in the iron-rich core, and that it is heated. However, we also noticed a considerable discrepancy in the [Ni II] line strength between our observations and predictions from mainly Chandrasekhar-mass explosion models.

In Sec. 3.2 further applied our model to a sample of optical+NIR spectra, most of which have been obtained with XShooter at ESO's Very Large Telescope. We followed the approach laid out

by Varani et al. (1990) and Spyromilio et al. (2004) of exploiting [Fe II] and [Co II] lines in the NIR in order to extract the mass ratio of these ions. As both iron and cobalt are the result of the ^{56}Ni decay chain, the mere presence of these ions is unsurprising. However, deviations of the Co/Fe mass ratio from the decay of ^{56}Co would imply additional stable isotopes of iron (^{54,56}Fe) or cobalt (^{57}Co from the decay of ^{57}Ni) which were produced in the explosion. We tested the significance of our inferred Co/Fe mass ratio through Bayes factors between a number of hierarchical models. We can reject models which include only stable iron or only ^{57}Ni. When having to decide between a model that neither has stable iron nor ^{57}Ni and a model which includes both, we strongly favour the latter with the preferred abundances being $^{54,56}\mathrm{Fe}\,/\,^{56}\mathrm{Ni} = 0.272 \pm 0.086$ and $^{57}\mathrm{Ni}\,/\,^{56}\mathrm{Ni} = 0.032 \pm 0.011$. This result disfavours zero-metallicity sub-Chandrasekhar-mass progenitors as the dominant channel of normal SNe Ia.

The inference of the Co/Fe mass ratio has a number of limitations: only few objects have high quality NIR spectra during the nebular phase and the mass ratio is evolving with time, largely following the radioactive decay of ^{56}Co. Additionally, the contributions to the Co/Fe mass ratio from stable iron compensate ^{57}Co around one year after the explosion. Spectra at these epochs have hardly any diagnostic power as the Co/Fe mass ratio becomes indistinguishable from pure ^{56}Co decay (Sec. 3.2).

Determining nickel abundances from optical lines does not suffer from the same limitations as the nickel abundance remains constant at the epochs considered in this thesis. However, the application of our NLTE model to optical spectra requires a more precise knowledge of the generally unknown plasma state as optical iron and nickel lines decouple from LTE early in the nebular phase – unlike NIR lines, for which the assumption of LTE only yields differences of $\sim 10\%$. In Sec. 3.3 we demonstrate that the ratio of the strongest lines of [Fe II] at optical wavelengths and in the NIR evolves in a systematic way with SN epoch, and that it is a direct measurement of the temperature and electron density of the emitting material. This result enables us to use the SN epoch as a proxy for the temperature and electron density and allows us to model archival SNe Ia of the past 30 years for which only optical spectra are available, extract the abundance of stable nickel produced during the explosion and discriminate between the two explosion channels. We show that the use of the optical and NIR [Fe II] lines as a proxy of the plasma state does not change our inferred abundances significantly.

We apply this method to a large sample of 130 optical spectra of 58 SNe Ia (Sec. 3.3). We conclude that the majority (85%) of normal SNe Ia have a Ni/Fe abundance that is in agreement with predictions of sub-Chandrasekhar-mass simulations of $\sim Z_\odot$ progenitors. Only a small fraction (11%) of objects in the sample have a Ni/Fe abundance in agreement with Chandrasekhar-mass explosion models.

4.2. Outlook

The main focus of this work was to establish a method which is sensitive to the mass of WDs exploding as normal SNe Ia. While the results of both methods presented in this thesis are convincing, certain aspects of the presented analysis deserve additional studies.

In Sec. 2.3 toy models have been used to examine the emergent line profiles of IGEs both at optical and NIR wavelengths. It seems that the explosion symmetry combined with an exponentially decreasing density profile and mixing of IGEs naturally leads to line profiles which are similar to those observed in the nebular phase. We suggest that a large grid of models could help identify which ejecta structures lead to pseudo-Gaussian line profiles. Radial temperature gradients would cause optical and NIR lines of [Fe II] to be emitted at different radii. While deviations from Gaussian line profiles are expected to be too small to detect, little differences in the FWHM of the lines originating from levels with varying energies might arise. In particular, it could be possible that parts of the ejecta become too cool to excite optical [Fe II] lines, while, at the same time, being warm enough to excite levels responsible for the NIR emission. In this case, the FWHM of the optical and NIR lines is no longer identical. Precise measurements of the FWHM of [Fe II] lines in the optical and NIR might lead to constraints on the temperature gradient in SNe Ia.

We have investigated the ratio of [Fe II] optical and NIR lines, which can be exploited to establish strong priors for the temperature and electron density of the emitting material. The evolution of the line ratio with time should be obtainable in more sophisticated radiative transfer models which are based on the output of explosion simulations. However, additional optical and, particularly, NIR observations are also warranted as the inferred relation is based on few objects. One could also imagine that the evolution of the line ratio correlates with other SN parameters, but due to the small sample size we were unable to examine such an idea in this thesis.

Due to the scarcity of NIR data we restricted our analysis to the 'normal' population of SNe Ia as it is by far the most abundant subclass. However, as described in Sec. 1.3.2, many outliers have been detected so far. It is currently unknown whether any of our results apply to these objects as many of them occur rarely and at great distances where nebular phase spectroscopy becomes unfeasible. It might be that these objects hold the key to understanding the origin of SNe Ia.

Several of these points may be solved with the upcoming *James Webb Space Telescope* (JWST). Using its unprecedented sensitivity and the opportunity of MIR observations, the emitting region of nebular lines can be constrained. Storey et al. (2016) presented an idea to use the [Co II] MIR lines as tracers of the temperature and electron density. Compared to the method presented in this thesis, the observation of the [Co II] MIR lines fully determines the plasma state of the emitting material. The expected evolution of the [Co II] MIR line ratio is shown in Fig. 4.1. JWST is capable of determining the plasma conditions at epochs later than ~ 250 days after the explosion.

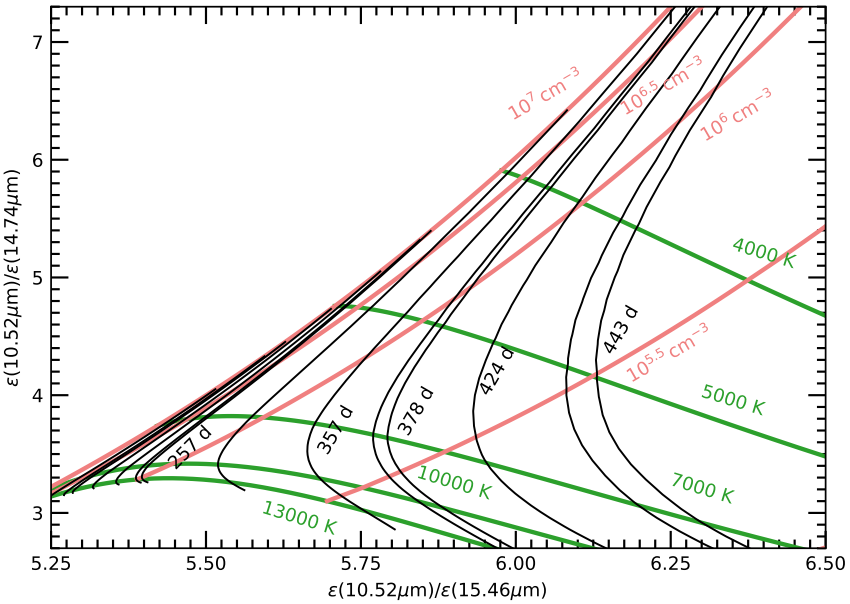

Figure 4.1.: Density and temperature from [Co II] MIR lines. Coloured lines show the [Co II] MIR line ratio for constant temperatures (green) and constant density (red). Observations of the three [Co II] MIR lines can fully determine the temperature and density without degeneracies, in contrast to the optical and NIR [Fe II] lines. Black lines indicate the expected [Co II] MIR line ratio evolution between 200 and 450 days after the explosion using the plasma conditions as inferred from the 7155 and 12567 Å [Fe II] lines. Their time evolution suggests that this method is capable of determining the plasma conditions at epochs $>$ 250 days after the explosion.

A. Paper I: Nebular spectroscopy of SN 2014J: Detection of stable nickel in near infrared spectra

S. Dhawan, **A. Flörs**, B. Leibundgut, K. Maguire, W. Kerzendorf, S. Taubenberger, M. Van Kerkwijk, J. Spyromilio

ABSTRACT
We present near infrared (NIR) spectroscopy of the nearby supernova 2014J obtained ∼450 d after explosion. We detect the [Ni II] 1.939 μm line in the spectra indicating the presence of stable ^{58}Ni in the ejecta. The stable nickel is not centrally concentrated but rather distributed as the iron. The spectra are dominated by forbidden [Fe II] and [Co II] lines. We use lines, in the NIR spectra, arising from the same upper energy levels to place constraints on the extinction from host galaxy dust. We find that that our data are in agreement with the high A_V and low R_V found in earlier studies from data near maximum light. Using a ^{56}Ni mass prior from near maximum light γ-ray observations, we find ∼0.05 $M_\odot$ of stable nickel to be present in the ejecta. We find that the iron group features are redshifted from the host galaxy rest frame by ∼600 km s^{-1}.

Introduction

Type Ia supernovae (SNe Ia) have long been identified as thermonuclear explosions of C/O white dwarfs (WD; Hoyle & Fowler, 1960). Following a simple calibration (Phillips, 1993) they are excellent distance indicators used extensively in cosmology (Riess et al., 1998; Perlmutter et al., 1999). There remain several open questions regarding the physics of SNe Ia, e.g. progenitor channel, mass of the progenitor, explosion mechanism, (see Hillebrandt & Niemeyer (2000); Leibundgut (2001); Hillebrandt et al. (2013); Maoz et al. (2014); Livio & Mazzali (2018) for reviews). Many attempts to address these issues have concentrated on photometric and spectroscopic observations of SNe Ia near maximum light (i.e. the photospheric phase). However, at late times, as the ejecta thin and the core of the ejecta is revealed, additional diagnostics of the explosion mechanism become accessible. The elegance of SNe Ia lies in the fact that both the energy of the explosion and the electromagnetic display are due to the burning of the core to ^{56}Ni and its subsequent decay. Direct or indirect measurements of the mass and topology of ^{56}Ni provide

some of the best probes of the explosion physics. The decay of ^{56}Ni to ^{56}Co and on to stable ^{56}Fe proceeds through the emission of γ-rays and positrons which power the electromagnetic display.

Nebular phase spectroscopy enables a direct view into the core of the ejecta and provides key insights into the progenitor and explosion properties of SNe Ia, complementary to the early time observations which contain information about the outer layers of the ejecta. The evolution of the cobalt to iron line ratios in nebular spectra have been used to demonstrate radioactive decay as the mechanism powering SNe Ia (Kuchner et al., 1994) and a combination of optical and NIR spectra have provided constraints on the iron mass in the ejecta (Spyromilio et al., 1992, 2004). Moreover, correlations of nebular-phase line velocities with photospheric-phase velocity gradients have indicated asymmetries in the explosion mechanism (Maeda et al., 2010a,b; Maguire et al., 2018b). Most nebular-phase studies of SNe Ia (e.g. Silverman et al., 2013a; Graham et al., 2017) have concentrated on optical wavelengths. Since the iron and cobalt features in the NIR are relatively unblended compared to the optical, it is an interesting wavelength region to study the line profiles. Some studies have used the [Fe II] 1.644 μm feature to probe the kinematic distribution of the radioactive ejecta (Höflich et al., 2004; Motohara et al., 2006) and have also tried to constrain the central density and magnetic field of the progenitor WD (Penney & Hoeflich, 2014; Diamond et al., 2015). Gerardy et al. (2007) have used mid-IR nebular spectra to explore the explosion mechanism and electron capture elements.

The presence of large amounts of stable isotopes of nickel (e.g. ^{58}Ni and ^{60}Ni) has been suggested as an indicator of burning at high central densities and therefore would favour higher progenitor masses, contributing to evidence for a Chandrasekhar-mass progenitor scenario for some supernovae (Höflich et al., 2004).

SN 2014J in M82 is one of the nearest SN Ia in decades and has been extensively studied (e.g. Kelly et al., 2014; Diehl et al., 2014; Foley et al., 2014; Ashall et al., 2014; Vacca et al., 2015; Galbany et al., 2016; Vallely et al., 2016). It is heavily reddened by host galaxy dust, but shows spectral features of a normal SN Ia (Amanullah et al., 2014). The extinction law and properties of the dust along the line of sight have been extensively discussed by a number of authors (Kawabata et al. (2014), Foley et al. (2014), Goobar et al. (2014)). Imaging of the supernova reveals the presence of clear echoes (Yang et al., 2017). Estimates of the ^{56}Ni mass using the timing of the NIR second maximum (Dhawan et al., 2016) and γ-ray observations (Churazov et al., 2015) infer masses of $0.64 \pm 0.13\,M_{\odot}$ and $0.62 \pm 0.13\ M_{\odot}$, respectively, consistent with the estimate for a normal SN Ia (Stritzinger et al., 2006; Scalzo et al., 2014). Optical spectra of SN 2014J in the nebular phase are remarkably similar to the 'normal' SNe 2011fe and 2012cg (Amanullah et al., 2015).

In this work we present the first detection of a spectral line at 1.939 μm in an SN Ia, a forbidden [Ni II] transition ($^4\mathrm{F}_{9/2}$–$^2\mathrm{F}_{7/2}$), indicating the presence of stable nickel isotopes (e.g., see Wilk et al., 2018). We use the ratios of the [Fe II] lines to measure the parameters describing the host galaxy extinction and evaluate the line shifts and profiles for the spectra. We present the data in

Table A.1.: Observing log of spectra obtained with GNIRS on the Gemini-North telescope.

MJD	UT Date	Phase	Wavelength coverage (μm)	Exposure Time (s)
57096.085	Mar 15, 2015	+408	0.825 - 2.5	2400
57137.864	Apr 26, 2015	+450	0.825 - 2.5	2400
57166.263	May 24, 2015	+478	0.825 - 2.5	2400

Section *Observations and Data Reduction*, analyse them in Section *Analysis*, discuss our results in Section *Discussion* and conclude in Section *Conclusions*.

Observations and data reduction

SN 2014J was discovered in M82 at the University of London Observatory on Jan 21st 2014 (Fossey et al., 2014). We adopt MJD56671.7 as the epoch of explosion (Goobar et al., 2014). We present NIR spectra of SN 2014J, obtained using GNIRS on Gemini-North. The dates and phases are shown in Table A.1. The observations were made using the Gemini fast turnaround program (Mason et al., 2014) under proposal GN-2015A-FT-3. The spectra were obtained in cross-dispersed (XD) mode with a central wavelength of 1.65 μm and have a wavelength coverage from 0.825 to 2.5 μm.

The spectra were reduced using the standard Gemini IRAF[1] package. The final spectra were extracted using the IRAF task apall which extracts one-dimensional sums across the apertures. For the first epoch (March) we used the A0 star HIP 32549 from the Gemini archive (not observed on the same night) for telluric correction corrections but we are unable to colour correct our data since no suitable standard on the same night was observed. The March spectrum is therefore only used for measurements of line shifts and profiles but not for line ratios. For the second (April) and third (May) epochs, we use the A7 star HIP 50685 obtained on the same nights as the observations of the supernova for both telluric and spectrophotometric calibration. Given that the features we are studying lie in regions of variable atmospheric transmission, we have checked our standard star observations against atmospheric transmission models of the atmosphere. We find that the transmission of the standard star is compatible with the Mauna Kea atmospheric models from the Gemini web site[2] for 50 mm of water vapour and an airmass of 2.0. The individual features of the atmosphere are reproduced well by the spectrum at the appropriate instrumental resolution.

No discernible continuum is present in the J and H bands in any of our data. In the K band we cannot exclude the presence of an underlying continuum although this may have an instrumental contibution as well as an astronomical one. The spectra are shown in Figure A.1.

[1] IRAF is distributed by the National Optical Astronomy Observatories, which are operated by the Association of Universities for Research in Astronomy, Inc., under cooperative agreement with the National Science Foundation

[2] http://www.gemini.edu/sciops/telescopes-and-sites/observing-condition-constraints/ir-transmission-spectra

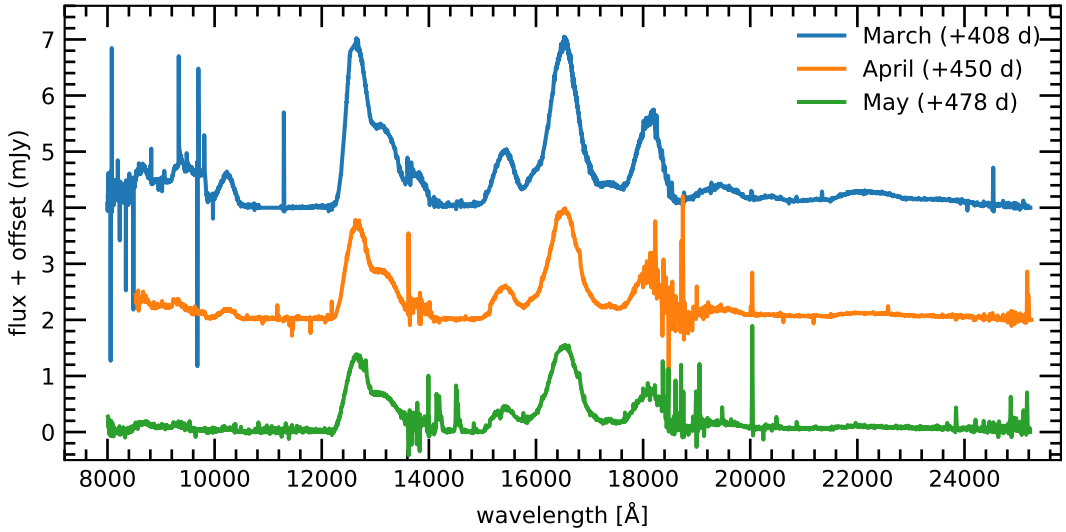

Figure A.1.: NIR spectra of SN 2014J (for the three nights it was observed). The spectra are plotted in mJy for visibility and each spectrum is incrementally displaced vertically by 2 mJy. The March data are at top and the May data at the bottom. The regions of poor atmospheric transmission around 1.4 and 1.9 μm are clearly identifiable due to the increased noise. The inset shows the region between 1.85 and 2.03 μm (the expected region for the [Ni II] feature) in the March spectrum.

Analysis

Nickel detection

In our data (see Figure A.1), we note the presence of a weak line at a wavelength coincident with the central wavelength of a [Ni II] transition. In Figure A.2 we fit the feature and present the first clear detection of the $^4F_{9/2}$–$^2F_{7/2}$ [Ni II] 1.939 μm line in the spectra of a Type Ia supernova. Since the e-folding timescale of radioactive nickel is 8.8 d (Nadyozhin, 1994) and the spectra are taken at $\sim$ 450 d, this would indicate that the detection of the [Ni II] line indicates the presence of a stable nickel isotope.

In our spectra there is no evidence for the $^2D_{5/2}$–$^4F_{7/2}$ line of [Ni II] at 1.0718 μm, which has an A value two orders of magnitude lower than the 1.939 μm line. Our modelling of the atmospheric transmission and the standard star spectra suggest that, if the line were strong, we should observe the centre of the line and the blue wing. Given the extinction and our assumed excitation conditions (see Section *Fitting the Spectrum*) we cannot use the absence of a strong line at 1.0718 μm to challenge the identification of the 1.939 μm line.

Fitting the spectrum

The NIR spectrum of SN 2014J is dominated by forbidden lines of singly ionised iron and singly ionised cobalt. In particular the prominent features at the long end of the J window (around

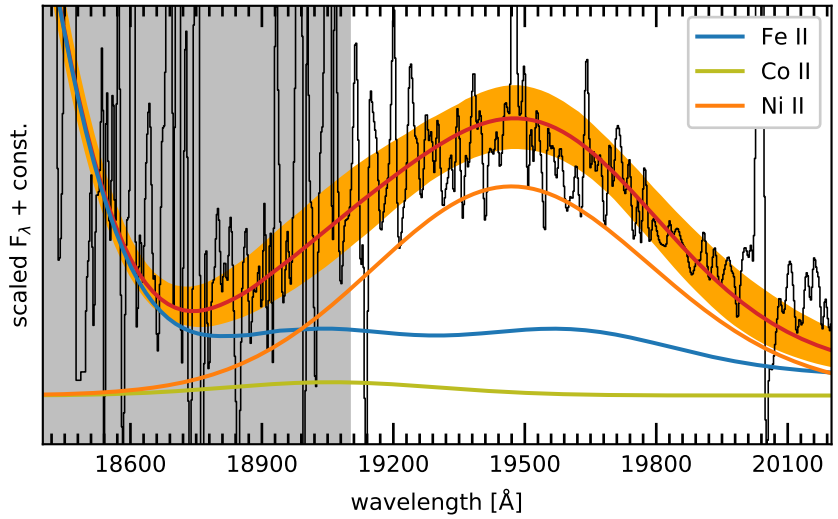

Figure A.2.: The May spectrum and a model using an [Ni II] NLTE atom (orange) with a line width of 11 000 km s^{-1} redshifted by 800 km s^{-1} from the laboratory rest frame. In the 1.8–2 μm region weak [Fe II] lines (blue) and [Co II] lines (olive) are also present. Shortwards of the central wavelength of this line the transmission is low and the noise in the spectrum increases (grey shaded region). This region has not been used in the fitting algorithm.

1.26 μm) and most of the H-band emission arise from multiplets a^{6}D–a^{4}D and a^{4}F–a^{4}D of [Fe II], respectively, while the feature around 0.86 μm has contributions from the [Fe II] a^{4}F–a^{4}P multiplet and from [Co II] a^{3}F–b^{3}F. Additional contributions from [Co II] a^{5}F–b^{3}F are present in the H band (at 1.547 μm). The line identification is provided in Table A.2.

Fitting the J and H band spectra is relatively straightforward. The K band is very faint but the transitions in the K band are not expected to be strong. The model we use (Flörs et al. in preparation) uses NLTE excitation of singly and doubly ionised iron group elements. For the purposes of fitting only the NIR data, the only contributing features are from the singly ionised

Table A.2.: Dominant line identifications for SN 2014J

λ μm	Species	transition	flux 450 d erg/s/cm^2	flux 478 d erg/s/cm^2
0.8617	[Fe II]	$a^4F_{9/2}$–$a^4P_{5/2}$	$(4.26\pm0.74)\times10^{-14}$	$(2.45\pm0.25)\times10^{-14}$
1.019	[Co II]	a^3F_4–b^3F_4	$(1.40\pm0.12)\times10^{-14}$	$(4.24\pm0.35)\times10^{-15}$
1.257	[Fe II]	$a^6D_{9/2}$–$a^4D_{7/2}$	$(1.20\ \pm0.07)\times10^{-13}$	$(9.89\pm0.16)\times10^{-14}$
1.547	[Co II]	a^5F_5–b^3F_4	$(9.35\pm0.32)\times10^{-15}$	$(2.83\pm0.23)\times10^{-15}$
1.644	[Fe II]	$a^4F_{9/2}$–$a^4D_{7/2}$	$(9.62\pm0.21)\times10^{-14}$	$(7.91\pm0.13)\times10^{-14}$
1.939	[Ni II]	$a^2F_{7/2}$–$a^4F_{9/2}$	$(1.03\pm0.11)\times10^{-14}$	$(9.68\pm0.87)\times10^{-15}$

species and a one zone model, convolved with a Gaussian line profile, suffices to provide an excellent fit. The atomic data for our NLTE models are from Storey et al. (2016), Nussbaumer & Storey (1988), Nussbaumer & Storey (1980), Cassidy et al. (2010b). The free parameters are the electron density and temperature of the gas, the ratio of iron to cobalt to nickel, the line width, the offset from the systemic velocity of the supernova that the singly ionised transitions of the iron group elements may exhibit and the extinction. We explore the parameter space with the nested-sampling algorithm Nestle (https://github.com/kbarbary/nestle) and a χ^2 likelihood. Uniform priors are used for all parameters except the electron density. For this we assume a lower bound of $10^5\,\mathrm{cm}^{-3}$. As has also been observed for other SN Ia at this epoch, our spectrum shows no evidence for neutral iron lines. The strong lines of the [Fe I] a^5D–a^5F multiplet at $1.4\,\mu$m are in a poor transmission region but still remain undetected. The lowest-excitation and therefore presumably strongest [Fe I] line in the $2\,\mu$m region at $1.9804\,\mu$m from multiplet a^5F–a^3F is also not seen. The infrared spectrum provides some evidence in the K band for doubly ionised iron but it is well known from combined optical and infrared spectra (e.g. Spyromilio et al., 1992) that strong transitions of [Fe III] and [Co III] are present in the 4000 to 6000 Å region. As discussed in the introduction, from earlier work (Churazov et al., 2015; Dhawan et al., 2016) it has been determined that SN 2014J made $\approx 0.6\,\mathrm{M}_\odot$ of ^{56}Ni. A simple distribution of this mass of Nickel and its daughter elements in singly ionised state in a volume expanding for the age of the supernova at $8000\,\mathrm{km\,s}^{-1}$ sets the electron density to be at least $10^5\,\mathrm{cm}^{-3}$.

The fits are shown in Figure A.3. Additional constraints arise from a few higher excitation lines in the 8600 Å region but these are extremely sensitive to the choice of atomic data. For the purposes of this work we note that we can fit these lines and that the fits are consistent with our derived properties but we do not draw conclusions based on this aspect of our data.

Extinction

The two strongest lines in the spectrum are the [Fe II] $1.257\,\mu$m $a^6D_{9/2}$–$a^4D_{7/2}$ and the $1.644\,\mu$m [Fe II] $a^4F_{9/2}$–$a^4D_{7/2}$ which arise from the same upper level. In the absence of additional contributions to the features at these wavelengths and optical depth effects the observed line ratio and can be used to determine the extinction between the J and H bands as it depends solely on the Einstein A-values these transitions. Additional constraints, independent of the excitation conditions come from the [Co II] lines at $1.547\,\mu$m (a^5F_4–b^3F_4) and $1.0191\,\mu$m (a^3F_4–b^3F_4) which also come from the same upper level. From our model fits of these features we can ensure that blending is taken consistently into account. We constrain the Cardelli et al. (1989) prescription for the extinction in the range shown in Figure A.4. The NIR data are compatible with both high and low values of R_V. The degeneracy between A_V and R_V arises from the short wavelength lever arm between the J and H windows.

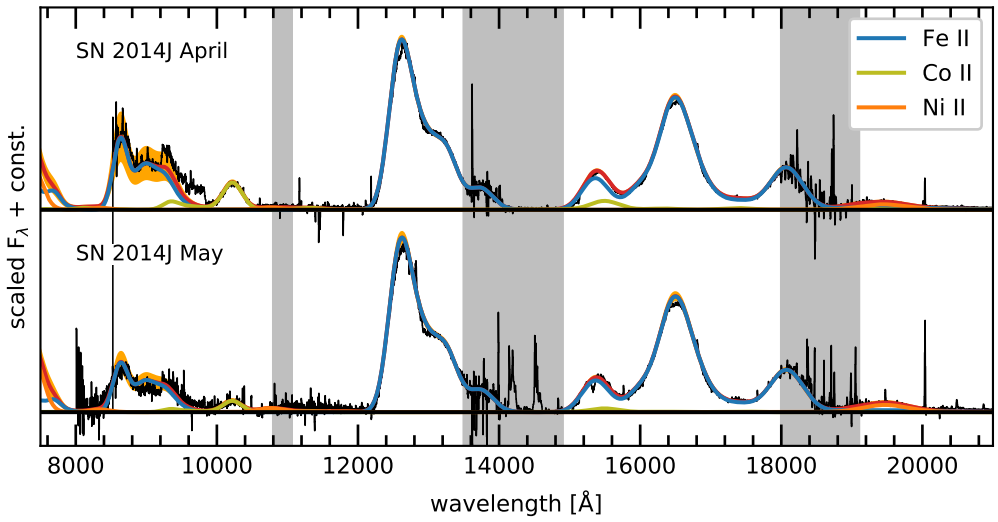

Figure A.3.: Fits to the observations using a NLTE one zone emission code. (Top): April and (Bottom): May spectra. The red lines indicate the mean model. The orange shaded band shows the 95% credibility region. Ion contributions are shown in blue ([Fe II]), olive ([Co II]) and orange ([Ni II]). The atmospheric absorption bands shortwards of 1.12, 1.48 and 1.915 μm are shaded grey. The resulting values for the temperature and electron density for April spectrum are 3700 $\pm$ 400 K and 2.18 ($\pm$ 0.56) $\times$ 10^5 cm^{-3} and 3300 $\pm$ 200 K and 1.69 ($\pm$ 0.59) $\times$ 10^5 cm^{-3}

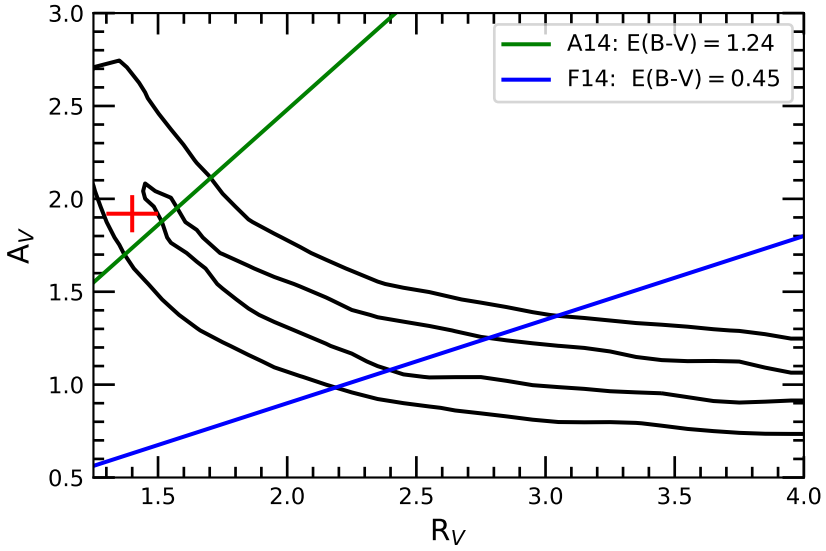

Figure A.4.: The distribution for R_V and A_V values by fitting the [Fe II] lines (the contours shown here are for the April spectrum, the results for the May spectrum are consistent with the contours displayed here). The values measured by Amanullah et al. (2014) are marked in red and agree with our April spectrum. The contours mark the 1 and 2 σ credible regions of the MCMC samples. The lines show a constant $E(B-V)$ of 1.37 as derived by Amanullah et al. (2014) and a constant $E(B-V)$ of 0.45 as derived by Foley et al. (2014).

Line shifts and widths

As noted by Maeda et al. (2010b) some type Ia supernovae exhibit a shift of the line centres of the singly ionised iron group lines relative to the systemic velocity of the supernova and also with respect to the doubly ionised features. In the absence of doubly ionised features in our data we cannot identify a differential velocity shift. However, the lines in our data exhibit a $\sim$800 km s^{-1} redshift which is $\sim$600 km s^{-1} in excess of the M82 recession velocity. The [Ni II], [Co II] and [Fe II] lines exhibit the same shifts within the errors, although the constraint on the [Ni II] is weak and degenerate with the width.

The profiles of the iron and cobalt lines are well fit by a simple Gaussian line shape for each individual component of the multiplets. We find that a Full Width Half Maximum of 8 600$\pm$150 km s^{-1} fits the [Fe II] and [Co II] data.

The [Ni II] line width is $\sim$11 000 km s^{-1}, somewhat higher than that needed to fit the iron and cobalt lines. It is thus clear that the stable iron group elements are not at the lowest velocities, unlike the predictions from 1-D M_{ch} models. However, we find that the model predictions from 3-D delayed detonation explosions of Seitenzahl et al. (2013) which predict stable isotopes at intermediate velocities are consistent with our observations. The somewhat higher velocity of the Nickel may be an artefact of our continuum placement which has been conservatively assumed to be non-existent. A small residual continuum, possibly from incomplete background subtraction, would result in the [Ni II] velocity being consistent with the other lines (see Section *Fitting the Spectrum*).

Discussion

Wilk et al. (2018) argued that the [Ni II] 1.939 μm line is relatively unblended compared to the strong [Ni II] feature at 7378 Å in the optical and therefore a more suitable test for the presence of large amounts of stable Nickel. Wilk et al. (2018) used models of Blondin et al. (2013) and Blondin et al. (2017) to model the optical and NIR spectra in the nebular regime.

That study (see Wilk et al. (2018) figure 13) shows a dramatic variation in the strength of the 1.939 μm line for their models, however, we note that their synthetic spectra are at epochs $\sim$ 200 d before the spectra presented here. The mass of stable nickel, however, in the models of Wilk et al. (2018) only varies by a factor of 3 between the different models used ($\sim$0.011 to 0.03 M$_\odot$). Compared to their yields, the M_{ch} models of Seitenzahl et al. (2013) are slightly higher in the range between 0.03 and 0.07 $M_\odot$. The appearance of the spectrum is particularly sensitive to the ionisation conditions in the models and therefore the derivation of masses from lines arising from a single ionisation stage, such as we have attempted here, is challenging. Our confirmation of the presence of the 1.939 μm line, which arises from the same upper level as the 7378 Å line confirms the identification of [Ni II] by Maguire et al. (2018b).

Ionisation and masses of Fe^+ and Ni^+

From our fitting we determine an un-blended flux for 1.644 μm line and infer the mass of the emitting iron. For a distance to M82 of 3.5 Mpc (Karachentsev & Kashibadze, 2006) and our measured flux for the 1.644 μm line we determine a mass of $\sim$0.18 $M_\odot$ for Fe^+ at the epoch of the SN spectrum. We note that without the high density prior from the ^{56}Ni mass, our spectra allow for low densities and high excitation conditions which can give Fe^+ yields as low as 0.01 $M_\odot$ (the masses reported here are the weighted mean for the +450 and +478 d spectra).

We note the strength of the 1.533 μm $a^4F_{9/2}$–$a^4D_{5/2}$ line and the presence of a blue shoulder at the 1.644 μm feature (at 1.6 μm) due to the $a^4F_{7/2}$–$a^4D_{3/2}$ [Fe II] line at 1.599 μm. The ratios of these lines to the 1.644 μm line are sensitive to the electron density, and the 1.54 μm feature as well as the shoulder drop for electron densities below 10^5 cm^{-3} (see also Nussbaumer & Storey (1988)). Here again we have avoided placing a disproportionate weight on a particular feature in our likelihood function. We only note that this presents corroborating evidence for high electron densities, consistent with the inference on the density from the ^{56}Ni mass prior, hence increasing our confidence in the Fe^+ mass determination.

Using the derived mass of Fe^+, the total iron mass prior and assuming the only the singly and doubly ionised species are present, we get an ionisation fraction of $\approx$1.7. This value is consistent with calculations from theory ($\sim$ 1.6) in the literature Axelrod (e.g. 1980).

We can now proceed to derive a value of 0.016$\pm$0.005 $M_\odot$ for the Ni^+ mass based on the emissivity of the 1.939 μm line and the other derived parameters from our fits. Similarly, assuming that all the Ni exists in singly and doubly ionised state and that ionisation fractions for nickel as for iron (see Wilk et al., 2018, for caveats) then we estimate that approximately 0.053$\pm$0.018 $M_\odot$ of stable nickel is present in SN 2014J. While this is higher than the predictions for the different models, it is within 3 σ of the predicted range of estimates.

We observed a complex of weak [Fe III] lines in the K-band. Using the Fe^{++} mass derived above (0.42 $M_\odot$), the distance to M82 (3.5 Mpc) and the observed flux in the region between 21000 and 24000 Å ($0.75 \pm 0.2 \times 10^{-14}$ ergs^{-1}cm^{-2}) we derive an emissivity of $\sim 2 \cdot 10^{-18}$ erg s^{-1}atom^{-1}. This is consistent with the derived line emissivity from the NLTE calculations with a temperature of 4000 K and N_e of 10^5 cm^{-3}. However, these estimates are highly sensitive to the temperature and N_e values, placement of the continuum and hence, only offer a consistency check.

Extinction by host galaxy dust

Measurements from maximum light photometry would point to a high $E(B-V)$ (1.37 mag, see Amanullah et al., 2014). The authors find a non-standard reddening law describing the colour excesses at maximum light. Fitting a Cardelli et al. (1989) reddening law the authors also find a preference for $R_V \sim 1.4$, significantly smaller than the typical Milky Way value of 3.1. This is confirmed by spectro-polarimetry data in Patat et al. (2015), who also demonstrate the preference

for low R_V in other highly reddened SNe Ia, a trend that has been observed with multi-band observations of large samples of nearby SNe (Nobili & Goobar, 2008; Phillips et al., 2013; Burns et al., 2014). The low R_V would indicate smaller dust grains in the host of SN 2014J than in the Milky Way. UV spectrophotometry (Brown et al., 2015), the wavelength independence of the polarisation angle (Patat et al., 2015) and modelling the optical light curves (Bulla et al., 2018) point towards an interstellar origin of the dust. We note however, that Foley et al. (2014) find that a mixture of typical dust in a combination of interstellar reddening and circumstellar scattering provides good fits to the early multi-wavelength data. For this case an R_V of 2.6 is derived by Foley et al. (2014). We find that the extinction derived from our NIR spectra using the [Fe II] and [Co II] line ratios is compatible with maximum light estimates for the reddening.

Conclusions

In this study we have presented NIR spectra of SN 2014J in the nebular phase. The dominant component of these spectra are [Fe II] and [Co II] lines. We detect, for the first time, a [Ni II] line at 1.939 μm, confirming the presence of stable nickel isotopes. The [Fe II] and [Co II] lines are Gaussian with a width of $8\,600\,\mathrm{km\,s^{-1}}$ whereas the [Ni II] lines at at least as wide and possibly wider at $11\,000\,\mathrm{km\,s^{-1}}$. This indicates that the stable nickel is likely not at low velocities but rather at intermediate velocities, as predicted by multi-D M_{ch} models. Our line profiles show no evidence for flat-tops. The host galaxy extinction has been estimated from the NIR [Fe II] line ratios and is seen to be consistent with the inference from near-maximum photometry and polarimetry. Combining our spectral modelling with a prior on the ^{56}Ni mass from maximum light and γ-ray observations, we obtain a mass of stable nickel of $0.053\,\mathrm{M_\odot}$.

B. Paper II: Limits on stable iron in Type Ia supernovae from NIR spectroscopy

A. Flörs, J. Spyromilio, K. Maguire, S. Taubenberger, W. E. Kerzendorf, S. Dhawan

ABSTRACT
We obtained optical and near-infrared spectra of Type Ia supernovae (SNe Ia) at epochs ranging from 224 to 496 days after the explosion. The spectra show emission lines from forbidden transitions of singly ionised iron and cobalt atoms. We used non-local thermodynamic equilibrium (NLTE) modelling of the first and second ionisation stages of iron, nickel, and cobalt to fit the spectra using a sampling algorithm allowing us to probe a broad parameter space. We derive velocity shifts, line widths, and abundance ratios for iron and cobalt. The measured line widths and velocity shifts of the singly ionised ions suggest a shared emitting region. Our data are fully compatible with radioactive ^{56}Ni decay as the origin for cobalt and iron. We compare the measured abundance ratios of iron and cobalt to theoretical predictions of various SN Ia explosion models. These models include, in addition to ^{56}Ni, different amounts of ^{57}Ni and stable ^{54,56}Fe. We can exclude models that produced only ^{54,56}Fe or only ^{57}Ni in addition to ^{56}Ni. If we consider a model that has ^{56}Ni, ^{57}Ni, and ^{54,56}Fe then our data imply that these ratios are $^{54,56}\mathrm{Fe}\,/\,^{56}\mathrm{Ni} = 0.272 \pm 0.086$ and $^{57}\mathrm{Ni}\,/\,^{56}\mathrm{Ni} = 0.032 \pm 0.011$.

Introduction

Type Ia supernovae (SNe Ia) are a remarkably uniform class of objects. Exceptions such as overly bright (e.g. SN 1991T Filippenko et al., 1992b; Phillips et al., 1992; Ruiz-Lapuente et al., 1992) or overly faint (e.g. SN 1991bg Filippenko et al., 1992a; Leibundgut et al., 1993; Turatto et al., 1996a) supernovae have been extensively studied (see Taubenberger, 2017, for a recent overview of the various Type Ia subtypes). High-cadence all sky surveys (e.g. Kulkarni, 2012; Shanks et al., 2015; Chambers et al., 2016; Kochanek et al., 2017) have discovered that members of the class exhibit a broad spectrum of disorders. However, the Branch-normal Type Ias (Branch et al., 2006) remain the dominant detected class and one of the best distance indicators at the disposal of astronomers. Following calibration procedures, for example the one by Phillips (1993), that correlate the width of the light curve with the peak brightness, SNe Ia exhibit a very

small dispersion in their absolute magnitudes. As such, their use in cosmology is extensive and understanding them is of general interest (Leibundgut & Sullivan, 2018).

Colgate & McKee (1969) proposed powering of the optical and infrared (IR) displays of SNe to originate in energy deposition from the decay of radioactive ^{56}Ni to ^{56}Co and subsequently to ^{Fe}Co. Depending on the temperature and density, burning to nuclear statistical equilibrium converts much of the progenitor white dwarf to iron group elements (Hoyle & Fowler, 1960; see Seitenzahl et al., 2013 for a recent calculation of yields). Many studies have provided both direct and indirect evidence for this scenario. Direct evidence can be found in Churazov et al. (2014) who detected γ-ray lines from the decay of ^{56}Co at 847 and 1238 keV. Indirect evidence was shown by Kuchner et al. (1994) who, in Type Ia late-time optical spectra $\approx$200 days, observed that the doubly ionised emission lines of Co and Fe evolved according to the expected ratio that would result from the production of Fe as the daughter product of the radioactive decay of ^{56}Co. The total energy of the explosion maps onto the mass of nucleosynthesised ^{56}Ni and the luminosity at maximum light is directly linked to the mass of ^{56}Ni (Arnett, 1982). The determination of the mass of ^{56}Ni based on optical and IR photometry and spectroscopy has been the subject of many papers and almost as many models. In general, of order 0.4 $M_\odot$ to 0.8 $M_\odot$ of ^{56}Ni is found to be produced in Branch-normal SNe Ia (Arnett, 1982; for a more recent study see Childress et al., 2015).

The post maximum optical and near-infrared (NIR) spectra of SNe Ia exhibit a plethora of iron group emission lines, predominantly in the singly and doubly ionised states (Axelrod, 1980; Fransson & Chevalier, 1989; Kozma et al., 2005; Fransson & Jerkstrand, 2015). Many authors have provided an extensive analysis of the physical conditions in the ejecta and the processes that generate the spectrum. Post-maximum spectra have been published by many authors and show remarkable similarity in features and evolution (Mazzali et al., 1998). Maeda et al. (2010b) made the startling discovery that often the singly ionised emission lines of the iron group elements exhibit a different systemic velocity when compared to their doubly ionised counterparts and proposed that there exists a region within the core of the ejecta where electron capture processes dominate the nucleosynthetic yield.

In this paper, we fit late-time NIR observations with emission lines from NLTE level populations to derive the evolution of the mass ratio of Co II to Fe II. We aim to place limits on the stable Fe and ^{57}Ni in the ejecta by observing the evolution in the mass ratio of Co to Fe. In Section *Observations*, we briefly describe the observations and in Section *Fitting the Spectra*, we present our NLTE emission line fit code. In Section *Fit Results*, we present the results of our spectral fits and derive the mass ratio $M_{\mathrm{Co\,II}} / M_{\mathrm{Fe\,II}}$. In Section *Comparison of $M_{\mathrm{Co\,II}} / M_{\mathrm{Fe\,II}}$ with explosion model yields*, we compare the mass ratio results of our SN sample with explosion model predictions within the Bayesian framework. The results are discussed in Section *Discussion*.

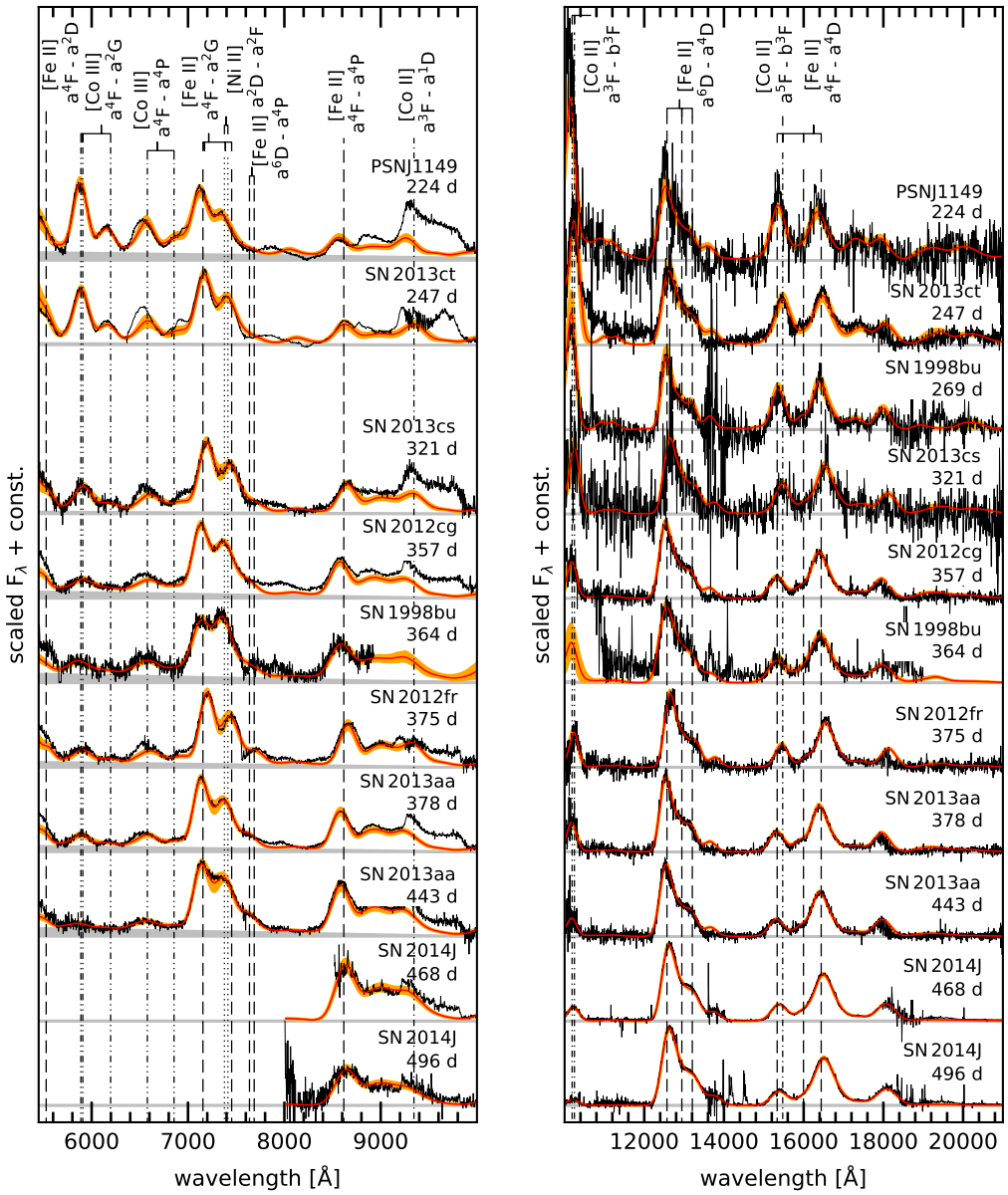

Figure B.1.: Optical (left) and NIR (right) spectra of SNe Ia obtained with X-Shooter, FORS1, and ISAAC at the VLT, SOFI at the NTT, and GNIRS at Gemini-North. The spectra are arranged in epoch starting with the youngest at the top and corrected for redshift and extinction. Fluxes are normalised to the 7 300 Å [Fe II] + [Ni II] feature (optical) and 12 600 Å [Fe II] feature (NIR). The red line indicates the mean flux of all fit models at each wavelength, the orange shaded area marks the 68 % uncertainty of the fit. Dashed vertical lines indicate the strongest lines as given in Table B.2. The subtracted background is shown as a grey band. Fits were performed for the optical and NIR spectra at the same time. The lines/ions composing the features below 5 500 Å are not included in our fits.

Observations

Four sets of data are included in this work (see Table B.1). One set from the GNIRS instrument on Gemini-North, two from the X-Shooter instrument at ESO's Paranal observatory and the fourth from SOFI at the New Technology Telescope (NTT) and ISAAC+FORS1 at the Very Large Telescope (VLT). GNIRS, SOFI, and ISAAC cover the NIR bands, FORS1 covers the optical while X-Shooter covers both the optical and NIR bands. As we are mainly interested in the abundances of various radioactive isotopes all epochs in this work are given in days after the explosion, assuming a rise time of ~ 18 days (Ganeshalingam et al., 2011).

We use two NIR spectra of SN2014J obtained with GNIRS at Gemini-North (see Dhawan et al., 2018, accepted). Optical+NIR spectra of SN 2013cg, SN 2012fr, SN 2013aa, SN 2013cs and SN 2013ct were obtained by Maguire et al. (2016) at the VLT. Maguire et al. (2018a) also obtained a spectrum of PSNJ11492548-0507138 (hereafter PSNJ1149) and a second spectrum of SN 2013aa. We also use two spectra of SN 1998bu (Spyromilio et al., 2004). For details of the reduction see the publication papers.

A number of broad ($\approx$ 7 000 to 9 000 $\mathrm{km\,s^{-1}}$) emission lines at 1.55 μm and 1.65 μm are evident in the data. We identify these as emission by the 1.644 μm [Fe II] line arising from the a^4F–a^4D multiplet and the 1.547 μm [Co II] line from the a^5F–b^3F multiplet. The a^4F-a^4D [Fe II] multiplet includes the 1.533 μm [Fe II] line. The identification of the various features has been extensively covered in the literature. The detection of the 1.257 μm $a^6D_{9/2}$–$a^4D_{7/2}$ confirms the identification and strength of the $a^4F_{9/2}$–$a^4D_{7/2}$ 1.644 μm line as they arise from the same upper level. Similarly the detection in many of our spectra of the 1.090 μm (a^3F_4–b^3F_4) line of [Co II] which shares an upper level with the 1.547 μm (a^5F_4–b^3F_4) line also secures the identification.

Fitting the spectra

Emission line model

We use a one zone model with Fe II, Ni II, and Co II; it also includes Co III if the spectrum covers the 6 000 Å region. For this set of ions, we solve the NLTE rate equations treating only collisional excitation and de-excitation by collisional and radiative processes to compute energy level populations and derive forbidden line emissivities. For the collisional processes we use a thermal electron gas characterised by a Boltzmann distribution and an electron density. We ignore radiative transfer effects as the optical depths of the lines under consideration are very low at the observed epochs. We also do not consider non-thermal excitations as the energy going into this channel at the relatively high electron densities we determine is also very low (Fransson & Chevalier, 1989). We do not include charge exchange and time-dependent terms in the NLTE rate equations. Even though we do not treat continuum processes directly, we include a parametrised smooth continuum in the model (see Section *Parameter Estimation*). We use such a smooth continuum to include uncertainties due to true continuum processes in the early

Table B.1.: Overview of spectra in our sample.

Supernova	$E(B-V)^a$ (mag)	z^b	Date of max.	Epoch[c]	Telescope	Instrument	Resolution $\lambda/\Delta\lambda$	Source
SN 1998bu	0.30[d]	0.002992	1998 May 21	269 d	NTT	SOFI	500	1[e]
				364 d	VLT	ISAAC, FORS1	1500, 440	1[e]
SN 2012cg	0.20[f]	0.001458	2012 June 03	357 d	VLT	X-Shooter	6200/8800/5300[g]	2
SN 2012fr	0.018	0.005457	2012 Nov 12	375 d	VLT	X-Shooter	6200/8800/5300[g]	2
SN 2013aa	0.169	0.003999	2013 Feb 21	378 d	VLT	X-Shooter	6200/8800/5300[g]	2
				443 d	VLT	X-Shooter	6200/8800/5300[g]	3
SN 2013cs	0.082	0.009243	2013 May 26	321 d	VLT	X-Shooter	6200/8800/5300[g]	2
SN 2013ct	0.025	0.003843	2013 May 04	247 d	VLT	X-Shooter	6200/8800/5300[g]	2
SN 2014J	1.37[h]	0.000677	2014 Feb 01	468 d	Gemini-North	GNIRS	1800	4
				496 d	Gemini-North	GNIRS	1800	4
PSN J1149	0.025	0.005589	2015 July 12	224 d	VLT	X-Shooter	6200/8800/5300[e]	3

References:
(1) Spyromilio et al. (2004); (2) Maguire et al. (2016); (3) Maguire et al. (2018a); (4) Dhawan et al. (2018).
Notes:
[a]MW $E(B-V)$ in magnitudes from Schlafly & Finkbeiner (2011). If additional host galaxy extinction is present we quote the combined Galactic and host galaxy $E(B-V)$ in magnitudes.
[b]Heliocentric redshifts are taken from the Nasa Extragalactic Database (NED).
[c]Days after the explosion, assuming a rise time of ~ 18 days (Ganeshalingam et al., 2011). The spectra were scaled to match the photometry at this phase.
[d]Jha et al. (1999) report the extinction towards the SN as $A_V = 0.94$ mag.
[e]We subtracted a light echo as found by Cappellaro et al. (2001) scaled up by a factor of two (see Spyromilio et al., 2004).
[f]Silverman et al. (2012b) found host galaxy extinction of $E(B-V) = 0.18$ mag.
[g]Resolution of the three X-Shooter arms UVB/VIS/NIR,
[h]Amanullah et al. (2014) determine $E(B-V) = 1.37$ mag with low total-to-selective extinction $R_V = 1.4$.

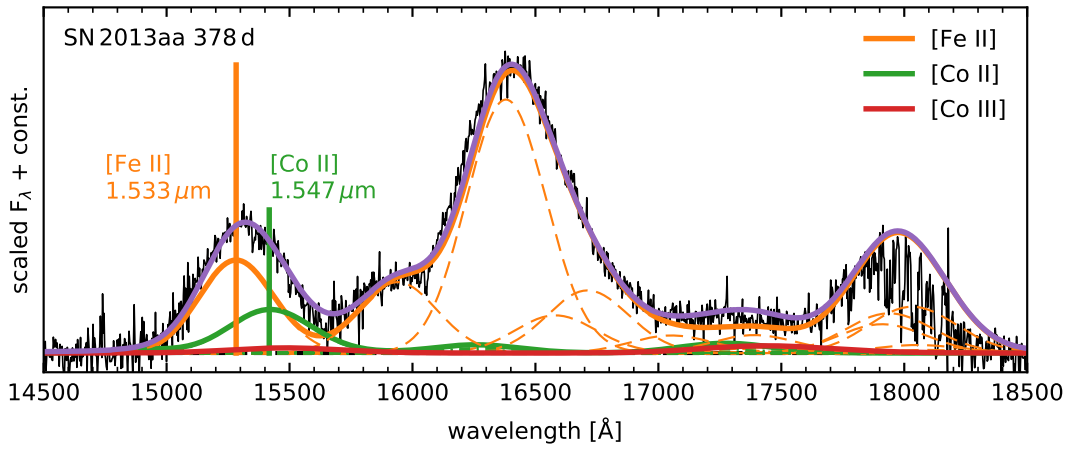

Figure B.2.: Best fit model of SN 2013aa at 378 d in the H-band. Shown is the extinction and redshift corrected spectrum (black line) and individual contributions from the ions Fe II (orange), Co II (green) and Co III (red) as solid curves. The purple line is the combined emission of the three ions. The two solid vertical lines are used to compute $M_{Co\,II} / M_{Fe\,II}$. Dashed curves indicate the contribution of the individual lines in the blended region. We do not show Ni II as it does not have any lines in this region.

spectra and potentially low-level light echoes. We do not treat energy deposition in the ejecta, and as a result our model does not match the emitted radiation over all wavelengths, but only for certain lines. We do not solve the ionisation balance but treat the number of emitting ions as a fit parameter. Effectively, we solve a simplified and parametrised NLTE problem.

A one-zone model, by default spherically symmetric, convolved with a Gaussian line profile serves to fit the spectra and extract the salient properties of the lines (flux, rest velocity, and Doppler broadening). One evident limitation of the one-zone model is that different ionisation stages, not necessarily co-located in the ejecta (see Section *Shifts and Widths of Singly and Doubly Ionised Material*), are likely to have different excitation conditions in some fraction of the emitting regions. This work, which concentrates on the singly ionised species, is not significantly affected by this limitation.

The features at 4700 and 5200 Å are a blend of singly and doubly ionised iron, with possibly asymmetric line profiles. Changes of the velocity offset and width of the 4 700 Å feature with time suggest that this wavelength region is not optically thin until 400 days after the explosion (Black et al., 2016). A detailed analysis of this feature would require a more sophisticated model process. As [Fe III] only slightly influences the rest of the Optical+NIR spectrum we do not attempt to fit spectral features below 5 500 Å.

We fit the 5 900 Å region with [Co III] and the double-peaked feature between 7 000 and 7 800 Å with [Fe II]+[Ni II]. All spectra exhibit a strong emission feature between 8 500 Å and 9 900 Å. We can reproduce the feature at 8 600 Å with lines from the Fe II a^4F–a^4P and Co II a^3F–b^3F

Table B.2.: Strongest lines of the included ions in the optical and NIR.

$\lambda_{\rm rest}(\mu{\rm m})$	Ion	Transition
0.5528	[Fe II]	$a^4F_{7/2} - a^2D_{5/2}$
0.5888	[Co III]	$a^4F_{9/2} - a^2G_{9/2}$
0.5908	[Co III]	$a^4F_{7/2} - a^2G_{7/2}$
0.6197	[Co III]	$a^4F_{7/2} - a^2G_{9/2}$
0.6578	[Co III]	$a^4F_{9/2} - a^4P_{5/2}$
0.6855	[Co III]	$a^4F_{7/2} - a^4P_{3/2}$
0.7155	[Fe II]	$a^4F_{9/2} - a^2G_{9/2}$
0.7172	[Fe II]	$a^4F_{7/2} - a^2G_{7/2}$
0.7378	[Ni II]	$z^2D_{5/2} - a^2F_{7/2}$
0.7388	[Fe II]	$a^4F_{5/2} - a^2G_{7/2}$
0.7414	[Ni II]	$z^2D_{3/2} - a^2F_{5/2}$
0.7453	[Fe II]	$a^4F_{7/2} - a^2G_{9/2}$
0.7638	[Fe II]	$a^6D_{7/2} - a^4P_{5/2}$

$\lambda_{\rm rest}$(Å)	Ion	Transition
0.7687	[Fe II]	$a^6D_{5/2} - a^4P_{3/2}$
0.8617	[Fe II]	$a^4F_{9/2} - a^4P_{5/2}$
0.9345	[Co II]	$a^3F_3 - a^1D_2$
1.0190	[Co II]	$a^3F_4 - b^3F_4$
1.0248	[Co II]	$a^3F_3 - b^3F_3$
1.2570	[Fe II]	$a^6D_{9/2} - a^4D_{7/2}$
1.2943	[Fe II]	$a^6D_{5/2} - a^4D_{5/2}$
1.3206	[Fe II]	$a^6D_{7/2} - a^4D_{7/2}$
1.5335	[Fe II]	$a^4F_{9/2} - a^4D_{5/2}$
1.5474	[Co II]	$a^5F_5 - b^3F_4$
1.5488	[Co III]	$a^2G_{9/2} - a^2H_{9/2}$
1.5995	[Fe II]	$a^4F_{7/2} - a^4D_{3/2}$
1.6440	[Fe II]	$a^4F_{9/2} - a^4D_{7/2}$

multiplets, but in spectra which are less than one year old the red part of the feature between 8 800 Å and 9 900 Å cannot be well explained by emission from only ions in our sample. Models by Botyánszki & Kasen (2017), among other authors, suggest the presence of S III in this region. We only use the 8 600 Å feature for spectra of SN 2014J, but we do not use the 8 800 to 9 900 Å region.

The strongest lines of the considered ions are given in Table B.2. An overview of the model ions with their respective atomic data is given in Table B.3. For Fe II we use the atomic data from Bautista et al. (2015) as they provide collision strengths for the higher levels responsible for optical transitions. The spectra are displayed in Fig. B.1 in chronological order. The data are corrected for the redshift of the host, as well as Galactic, and, if applicable, host galaxy extinction according to Table B.1. The simple model of Fe II, Co II, Co III and Ni II fits the data well above 5 500 Å.

Parameter estimation

We explore the parameter space using the nested-sampling algorithm Nestle[1] (see also Shaw et al., 2007). The algorithm allows us to sample from our flat priors over a large range by optimising the selection of variables based on the quality of the earlier fits. To compare the model with the data we assume a χ^2 likelihood. Our set of four ions shares the same temperature and electron density. Each ion is allowed to have its own line width, velocity offset, and strength. Uniform priors are used for all parameters except the electron density, for which we use a log-uniform distribution. There exists a significant body of work in the literature starting with Axelrod (1980), and

[1] https://github.com/kbarbary/nestle

Table B.3.: Ions included in the fits and their atomic data sets.

Ion	Levels[a]	Ref. A_{ij}[b]	Ref. Υ_{ij}[c]
Fe II	52	1	1
Co II	15	2	2
Co III	15	3	3
Ni II	18	4	5

References:
(1) Bautista et al. (2015); (2) Storey et al. (2016); (3) Storey & Sochi (2016); (4) Cassidy et al. (2016b); (5) Cassidy et al. (2010a)
Notes: [a]Energy levels and statistical weights are taken from NIST (Kramida et al., 2018).
[b]Einstein A coefficient between levels i and j.
[c]Maxwellian averaged collisional strength between levels i and j.

a plethora of other authors (see e.g. Kuchner et al., 1994; Kozma et al., 2005; Fransson & Jerkstrand, 2015; Botyánszki & Kasen, 2017) that have shown that temperatures for the ejecta of a SNe Ia during the first year after explosion lie in the range of $2\,000 - 15\,000$ K. For our modelling we adopt the following boundaries for the priors: temperature range (2 000 to 15 000 K), electron densities between 10^4 to $10^7\,\mathrm{cm}^{-3}$, Doppler widths between 2 and $15 \times 10^3\,\mathrm{km\,s}^{-1}$, and shifts between -3 and $3 \times 10^3\,\mathrm{km\,s}^{-1}$. The very large allowed range for the temperature prior does not affect the resulting fit. We note the presence of a weak continuum in some spectra bluewards of 9500 Å; in those cases, we subtract a linear background (grey bands in Fig. B.1) in the optical. Widths and shifts of individual ions are determined using a global fit where the individual species are allowed to vary within the prior space.

Besides the fit parameters noted above, the fits provide us with the individual emission line emissivities. The ratios of the transitions arising from within the a^4F–a^4D Fe II multiplet show little variation with temperature as the difference in the energy levels within a^4D is less than $1\,000\,\mathrm{cm}^{-1}$ and for the strongest lines at 1.644 μm and 1.533 μm less than $500\,\mathrm{cm}^{-1}$. The higher-lying states responsible for lines in the optical vary significantly in strength over the considered temperature range and thus allow us to estimate the electron temperature. However, there is a degeneracy between electron density and temperature. Good fits can be achieved with high temperature and low densities, and vice versa. Some of these high temperatures and low densities would not be compatible with a prior of $\sim 0.4 - 0.8\,\mathrm{M}_\odot$ of iron group elements. We have not adopted such a prior for the fitting as absolute mass estimates suffer considerably from systematics (e.g. distance). We want to emphasise that the uncertainties from this degeneracy are much smaller than the priors (see Table B.4).

Fit results

Fit parameters and $M_{Co\,II}$ / $M_{Fe\,II}$

The ratio of the H-band [Co II] to [Fe II] lines places limits on the temperature of the ejecta of above 1 500 K. Below this temperature, the blue wing of the 1.55 μm spectral feature is underproduced and the blend of the 1.634 [Co II] and 1.644 [Fe II] lines which accounts for the 1.65-μm feature is unable to reproduce the spectra. The presence of the shoulder from the $a^4F_{7/2}-a^4D_{3/2}$ [Fe II] line at 1.599 μm in spectra at all epochs indicates that the emission originates from a high-density region ($n_e > 10^5\,\mathrm{cm}^{-3}$).

The absolute mass of the emitting material strongly depends on the assumed temperature in the ejecta and the distance to the object. We do not consider that our model is sophisticated enough to provide detailed constraints on these parameters (see for example Fransson & Jerkstrand (2015) or Diamond et al. (2018) for such work). On the other hand, mass ratios are only weakly dependent on the temperature. In particular, from the line ratio of 1.547 μm [Co II] to 1.533 μm [Fe II] (see Fig. B.2) we can determine the mass fraction of Co II to Fe II (Varani et al., 1990):

$$\frac{M_{Co\,II}}{M_{Fe\,II}}(t) = \frac{F_{1.547}}{F_{1.533}}(t) \times \frac{1.533\,A_{1.533}\,g_{Fe\,II}\,Z_{Co\,II}(t)\,m_{Co\,II}}{1.547\,A_{1.547}\,g_{Co\,II}\,Z_{Fe\,II}(t)\,m_{Fe\,II}} \times e^{\frac{k_B\,2\,040\,\mathrm{K}}{k_B\,T(t)}}, \tag{B.1}$$

where T is the temperature of the gas in degrees Kelvin reflecting the difference in the upper energy levels of the two transitions, A are the transition probabilities between the $a^4F_{9/2}-a^4D_{5/2}$ Fe II and $a^5F_5-b^3F_4$ Co II levels, g are the statistical weights of the upper levels, m are the atomic masses and

$$Z(t) = \sum_i \left(g_i\ \exp\left[-E_i/(k_B T(t))\right]\right) \tag{B.2}$$

are the atomic partition functions. The flux ratio, partition functions, temperature and the inferred mass ratio are functions of time after explosion. For the atomic data used in this work Eq. B.1 reduces to:

$$\frac{M_{Co\,II}}{M_{Fe\,II}}(t) = 0.0613 \times \frac{F_{1.547}}{F_{1.533}}(t) \times \frac{Z_{Co\,II}}{Z_{Fe\,II}}(t) \times e^{\frac{k_B\,2\,040\,\mathrm{K}}{k_B\,T(t)}}. \tag{B.3}$$

As the SN 1998bu 269 d spectrum covers only the NIR we cannot determine the temperature and electron density from the ratio of optical to NIR Fe II lines. To determine the line widths and velocity offsets we fit the spectrum for a fixed temperature $T = 7\,200$ K and electron density $\log(n_e / \mathrm{cm}^{-3}) = 6.2$. These numbers lie between the fit results of SN 2013ct at 247 d and SN 2013cs at 321 d. The mass ratio is then computed for $T = (7200 \pm 1500)$ K and $\log(n_e / \mathrm{cm}^{-3}) = (6.20 \pm 0.15)$. The uncertainties of the density and temperature are reflected in an increased uncertainty of the derived mass ratio $M_{Co\,II}$ / $M_{Fe\,II}$ for this spectrum.

The spectrum of SN1998bu at 364 d does not cover the 1.019 μm Co II line, which affects the uncertainty of the inferred mass ratio significantly as the Co II 1.547 μm line is rather weak

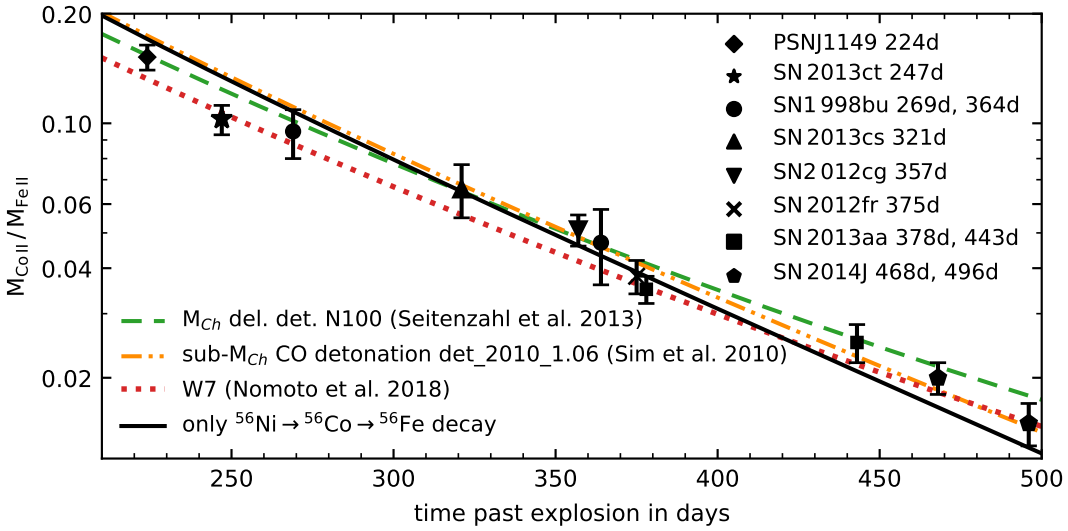

Figure B.3.: Evolution of the inferred $M_{Co\,II}/M_{Fe\,II}$ ratio with time. We assumed a rise time of 18 days (Ganeshalingam et al., 2011). The error bars reflect the 68% posterior interval of the mass ratio. The coloured lines show the expected mass ratio M_{Co}/M_{Fe} of the M_{Ch} delayed-detonation model 'N100' (Seitenzahl et al., 2013, green), the sub-M_{Ch} CO detonation model 'det_2010_1.06' (Sim et al., 2010, orange) and the M_{Ch} 'W7 $Z_{\odot}$' model (Nomoto & Leung, 2018, red). The black line is not a fit to the data and represents the M_{Co}/M_{Fe} ratio assuming only radioactive decay from ^{56}Ni to ^{56}Co to ^{Fe}Co. The same ionisation fractions of Co II and Fe II allow us to generalise $M_{Co\,II}/M_{Fe\,II}$ to M_{Co}/M_{Fe} and compare the two ratios (see Section *Comparison of $M_{Co\,II}/M_{Fe\,II}$ with explosion model yields*).

compared to the Fe II 1.533 μm line. Good fits can be achieved for a wide range of cobalt masses in this case.

The spectra of SN 2014J only cover the NIR wavelengths down to 8 500 Å. We therefore cannot use the 7 200 Å [Fe II] + [Ni II] complex to determine the density and temperature in the ejecta. We find that the 8 600 Å feature is well reproduced (best at late epochs > 350 d) by our emission model for other SNe in our sample with both optical and NIR wavelength coverage. We estimate the temperature and density of our SN 2014J spectra by fitting the 8 600 Å feature.

In Table B.4, we present the 68% credibility interval for the electron density, temperature, Co II / Fe II mass ratio, widths and shifts of [Fe II], [Co II] and [Co III]. The evolution of the mass ratio with the time since the supernova explosion is shown in Fig. B.3. The error bars in the plot reflect mainly the uncertainty of the degenerate density and temperature, and, for very late spectra (> 400 d), the Doppler width of singly ionised cobalt. Superimposed on the data points is the change of the mass ratio of cobalt to iron as expected from the radioactive decay of ^{56}Ni (black curve). The line is not a fit to the data but rather the evolution of the mass ratio assuming the established decay half-lives of 6.08 and 77.27 days for ^{56}Ni and ^{56}Co respectively:

$$^{56}_{28}\mathrm{Ni} \xrightarrow{T_{1/2}=6.08\,\mathrm{d}} {}^{56}_{27}\mathrm{Co} \xrightarrow{T_{1/2}=77.27\,\mathrm{d}} {}^{56}_{26}\mathrm{Fe}. \tag{B.4}$$

Shifts and widths of singly and doubly ionised material

We can use the velocity shifts of [Fe II], [Co II], and [Co III] to perform a similar study to Maguire et al. (2018a). We present our results in Figs. B.4 and B.5. Different velocity shifts between stable material ([Ni II]), singly ionised decay products ([Fe II], [Co II]) and doubly ionised decay products ([Fe III], [Co III]) would suggest their production in spatially separated regions of the ejecta (Maeda et al., 2010b). As we fit the forbidden Co II lines at 1.019 μm and 1.547 μm we can directly compare velocity offsets and widths of singly and doubly ionised cobalt. For Fe III and Fe II this cannot be done as the 4700 Å Fe III-dominated feature exhibits a shift of its central wavelength with time.

We find that the absolute velocity shifts of [Fe II], $(1.1 \pm 0.5) \times 10^3\,\mathrm{km\,s^{-1}}$, are very similar to the absolute velocity shifts of [Co II], $(0.9 \pm 0.7) \times 10^3\,\mathrm{km\,s^{-1}}$. Deviations of the velocity shift between the two ions are less than $500\,\mathrm{km\,s^{-1}}$ for most spectra and likely the result of noise near the 1.019 μm [Co II] feature. Velocity shifts of singly ionised ions can be either positive or negative for the observed sample.

Lines of Fe II and Co II exhibit comparable widths. Line widths of [Co II] usually have a higher uncertainty than line widths of [Fe II] as there is only one unblended Co II feature in our spectra, but multiple features of [Fe II] can be found at 7 200 Å, 8 600 Å, 12 600 Å and 16 400 Å. We find widths of $(7.9 \pm 1.0) \times 10^3\,\mathrm{km\,s^{-1}}$ for [Co II] and $(7.9 \pm 0.8) \times 10^3\,\mathrm{km\,s^{-1}}$ for [Fe II].

We find that [Co III] shows lower velocity offsets from its rest wavelength than singly ionised iron and cobalt. While there are spectra in which the [Co III] velocity shift is similar to [Fe II]

Table B.4.: 68% posterior probability intervals of the fit parameters.

SN	Age[a] [days]	Mass Ratio $M_{Co\,II}/M_{Fe\,II}$	log [n_e / cm^{-3}]	T [10^3 K]	Width [Fe II][b] [10^3 km s^{-1}]	Shift [Fe II][c] [10^3 km s^{-1}]	Width [Co II][b] [10^3 km s^{-1}]	Shift [Co II][c] [10^3 km s^{-1}]	Width [Co III][b] [10^3 km s^{-1}]	Shift [Co III][c] [10^3 km s^{-1}]
PSN J1149	224	$0.152^{+0.012}_{-0.012}$	$6.39^{+0.10}_{-0.08}$	$8.5^{+2.3}_{-1.3}$	$7.88^{+0.65}_{-0.55}$	$-1.74^{+0.26}_{-0.26}$	$7.21^{+0.99}_{-0.77}$	$-2.10^{+0.36}_{-0.37}$	$8.63^{+0.29}_{-0.28}$	$-0.71^{+0.17}_{-0.16}$
SN 2013ct	247	$0.103^{+0.010}_{-0.009}$	$6.42^{+0.28}_{-0.15}$	$7.6^{+1.6}_{-1.6}$	$8.19^{+0.53}_{-0.47}$	$0.28^{+0.20}_{-0.22}$	$7.78^{+0.76}_{-0.80}$	$0.78^{+0.43}_{-0.39}$	$9.31^{+0.34}_{-0.32}$	$-0.14^{+0.18}_{-0.18}$
SN 1998bu	269	$0.095^{+0.015}_{-0.014}$	$6.20^{+0.15}_{-0.15}$	$7.2^{+1.5}_{-1.5}$	$6.51^{+0.44}_{-0.44}$	$-0.94^{+0.32}_{-0.29}$	$7.34^{+0.54}_{-0.54}$	$-1.51^{+0.36}_{-0.36}$	–	–
SN 2013cs	321	$0.066^{+0.011}_{-0.011}$	$6.05^{+0.10}_{-0.10}$	$6.9^{+1.0}_{-0.9}$	$7.66^{+0.43}_{-0.39}$	$1.18^{+0.18}_{-0.19}$	$7.67^{+0.78}_{-0.85}$	$0.90^{+0.37}_{-0.40}$	$10.42^{+0.93}_{-0.82}$	$0.88^{+0.40}_{-0.37}$
SN 2012cg	357	$0.051^{+0.005}_{-0.005}$	$5.81^{+0.12}_{-0.10}$	$6.5^{+0.9}_{-0.9}$	$7.68^{+0.24}_{-0.22}$	$-1.48^{+0.10}_{-0.10}$	$7.36^{+0.89}_{-0.91}$	$-0.84^{+0.35}_{-0.39}$	$12.30^{+1.38}_{-1.21}$	$0.60^{+0.57}_{-0.58}$
SN 1998bu	364	$0.047^{+0.011}_{-0.011}$	$5.63^{+0.19}_{-0.12}$	$5.5^{+0.7}_{-0.8}$	$9.08^{+0.44}_{-0.40}$	$-1.08^{+0.16}_{-0.16}$	$8.52^{+0.54}_{-0.48}$	$-1.31^{+0.97}_{-0.88}$	$12.41^{+1.37}_{-1.21}$	$-1.03^{+0.68}_{-0.59}$
SN 2012fr	375	$0.038^{+0.004}_{-0.004}$	$5.77^{+0.16}_{-0.19}$	$5.7^{+1.5}_{-0.8}$	$7.17^{+0.19}_{-0.18}$	$1.42^{+0.10}_{-0.10}$	$6.97^{+0.97}_{-0.63}$	$0.65^{+0.28}_{-0.30}$	$10.16^{+1.12}_{-0.95}$	$0.58^{+0.55}_{-0.59}$
SN 2013aa	378	$0.035^{+0.003}_{-0.003}$	$5.67^{+0.14}_{-0.11}$	$6.6^{+1.1}_{-1.1}$	$7.32^{+0.24}_{-0.22}$	$-1.35^{+0.10}_{-0.09}$	$7.51^{+0.71}_{-0.65}$	$-0.91^{+028}_{-0.29}$	$10.29^{+1.57}_{-1.08}$	$-0.13^{+0.53}_{-0.55}$
SN 2013aa	443	$0.025^{+0.003}_{-0.003}$	$5.44^{+0.28}_{-0.16}$	$5.0^{+0.7}_{-0.9}$	$7.87^{+0.18}_{-0.17}$	$-1.18^{+0.07}_{-0.07}$	$8.19^{+0.46}_{-0.48}$	$-1.06^{+0.22}_{-0.22}$	$12.07^{+1.86}_{-1.88}$	$0.15^{+0.92}_{-0.86}$
SN 2014J	468	$0.020^{+0.002}_{-0.002}$	$5.24^{+0.28}_{-0.16}$	$4.3^{+0.7}_{-0.9}$	$8.59^{+0.14}_{-0.14}$	$0.45^{+0.06}_{-0.06}$	$9.13^{+0.31}_{-0.32}$	$0.36^{+0.13}_{-0.13}$	–	–
SN 2014J	496	$0.015^{+0.002}_{-0.002}$	$5.15^{+0.14}_{-0.15}$	$3.8^{+0.4}_{-0.3}$	$9.15^{+0.14}_{-0.14}$	$0.67^{+0.07}_{-0.07}$	$8.75^{+0.77}_{-0.66}$	$0.03^{+0.27}_{-0.29}$	–	–
Mean + Std[d]					7.9 ± 0.8	1.1 ± 0.5	7.9 ± 1.0	0.9 ± 0.7	10.7 ± 1.8	0.5 ± 0.6

For SN 1998bu at 269 days the temperature and density are not fitted (see text for details).
[a]Days after the explosion, assuming a rise time of ~ 18 days (Ganeshalingam et al., 2011).
[b]Doppler full width at half maximum.
[c]Shift velocity.
[d]Mean and standard deviation over all fit samples. For shift velocities we calculated the mean and standard deviation of the absolute values.

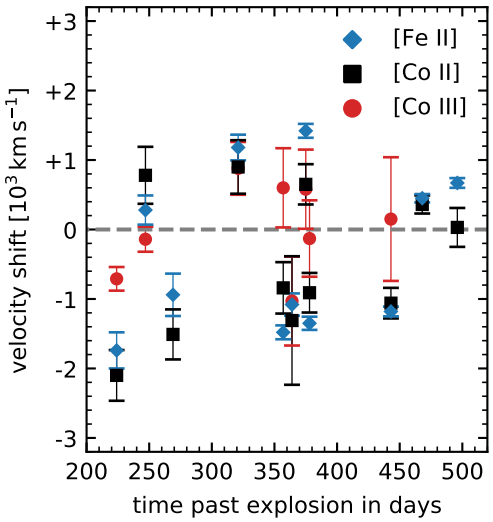

Figure B.4.: Velocity shifts of [Fe II], [Co II], and [Co III] as a function of time after explosion.

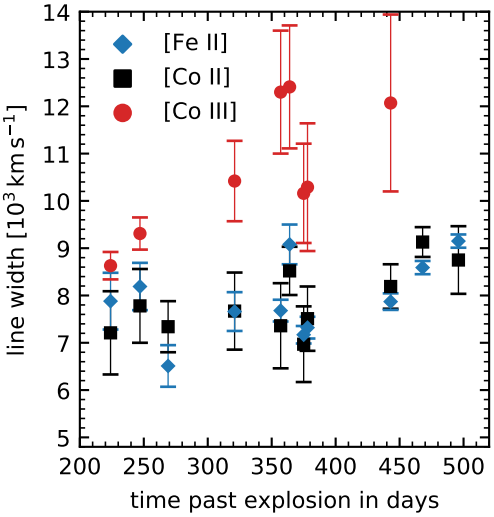

Figure B.5.: Line widths of [Fe II], [Co II], and [Co III] as a function of time after explosion.

and [Co II] (SN 2013cs, SN 1998bu), for the majority of spectra in our sample we get different velocity shifts between [Co III] and [Co II]. We find $(0.5 \pm 0.6) \times 10^3$ km s^{-1} for the mean absolute [Co III] velocity shift, compared to $(0.9 \pm 0.7) \times 10^3$ km s^{-1} for [Co II]. As noted in Maguire et al. (2018a), shifts of [Co III] seem to be consistent with zero offset from the rest wavelength.

On average, [Co III] lines also appear to be broader than [Co II] lines by about 3 000 km s^{-1} ($(10.7 \pm 1.8) \times 10^3$ km s^{-1} for [Co III] compared to $(7.9 \pm 1.0) \times 10^3$ km s^{-1} for [Co II]). We note that supernovae which exhibit a strong continuum in the 5 900 Å region (SN 2012cg, SN 1998bu at 364 d, SN 2013aa at 443 d) tend to have higher line widths than supernovae without continuum in this region. In these cases, the line widths appear to be strongly affected by the manual continuum subtraction. [Co III] widths determined in this work are compatible within their uncertainties with results from Maguire et al. (2018a). [Co III] lines in our fits are redshifted by $\sim$ 500 km s^{-1} compared to Maguire et al. (2018a). This systematic shift is mostly due to the presence of [Fe II] lines from the $a^4F - a^2D$ multiplet (5335, 5377, 5528 Å) on the blue side of the 5 900 Å feature which are not included in the work of Maguire et al. (2018a). We note that the choice of the continuum differs between this work and Maguire et al. (2018a).

Comparison of $M_{Co\,II}$ / $M_{Fe\,II}$ with explosion model yields

Besides ^{56}Ni, explosion models predict the presence of the isotopes ^{54,56}Fe, ^{57}Ni and ^{58}Ni. If the explosive burning in the white dwarf occurs at high densities (e.g. M_{Ch} models) stable ^{54,56}Fe and ^{58}Ni and rapidly decaying ^{57}Ni can be produced directly. Sub-M_{Ch} models lack a high enough central density to produce neutron-rich material. However, if the progenitor has a high metallicity (several times solar) there is an excess of neutrons, resulting in the synthesis of ^{54,56}Fe, ^{57}Ni, and stable ^{58}Ni with masses comparable to those of M_{Ch} explosions (Sim et al., 2010; Ruiter et al., 2013).

In Fig. B.3 the prediction of the $M_{Co\,II}$ / $M_{Fe\,II}$ ratio is shown in the case of pure ^{56}Ni to ^{56}Co to ^{Fe}Co decay and for nucleosynthetic yields of the M_{Ch} deflagration model 'W7 $Z_\odot$' (Nomoto & Leung, 2018), the M_{Ch} delayed-detonation model 'N100' (Seitenzahl et al., 2013), and the sub-M_{Ch} CO detonation model 'det_2010_1.06' (Sim et al., 2010). The 'W7 $Z_\odot$' model produces 2.8 % ^{57}Ni and 35 % ^{54,56}Fe, the M_{Ch} delayed detonation model 'N100' produces 3.1 % ^{57}Ni and 19.4 % ^{54,56}Fe, and the sub-M_{Ch} CO detonation model 'det_2010_1.06' produces 0.6 % ^{57}Ni and no stable iron, each given in fractions of the ^{56}Ni mass. As mentioned before, a high metallicity progenitor like in the 'det_2010_1.06_0.075Ne' model (Sim et al., 2010) produces similar masses of ^{54,56}Fe and ^{57}Ni as the 'N100' model.

Stable iron produced in the explosion has the strongest effect on M_{Co} / M_{Fe} while not all of the ^{56}Co has yet decayed to ^{Fe}Co (< 300 d). ^{57}Ni decays within a few days to ^{57}Co, which has a much longer half-life than ^{56}Co:

$$^{57}_{28}\mathrm{Ni} \xrightarrow{T_{1/2}=1.48\,\mathrm{d}} {}^{57}_{27}\mathrm{Co} \xrightarrow{T_{1/2}=271.74\,\mathrm{d}} {}^{57}_{26}\mathrm{Fe}. \tag{B.5}$$

Due to the longer half-life it can still be found late in the nebular phase (> 400 d) when almost no ^{56}Co remains.

Co II and Fe II have similar ionisation potentials and appear to be co-located within the ejecta (see Section *Fit Results*). We therefore assume that the relative ionisation fraction between Co II and Fe II does not change with time, allowing us to generalise $M_{Co\,II}$ / $M_{Fe\,II}$ to $M_{Co\,II}$ / $M_{Fe\,II}$. This ratio measures the total mass of cobalt to iron at a given time, with possible contributions from stable ^{54,56}Fe and decay products according to Eqs. B.4 and B.5. We compare the predicted $M_{Co\,II}$ / $M_{Fe\,II}$ ratio of different models with the results from our fits by determining their likelihood based on their Bayes factors. The Bayes factor quantifies the evidence of data D for model M_a compared to model M_b. In our analysis we consider the nested models M_0 to M_3 (see Table B.5). The possible parameters of these models are initial abundances of the isotopes ^{56}Ni, ^{54,56}Fe, and ^{57}Ni.

For nested models, the Bayes factor can be computed analytically if the priors are separable and the more complicated model M_b becomes the simpler model M_a for $\theta = \theta_0$:

$$B_{ab} = \frac{P(\theta = \theta_0 | D, M_b)}{P(\theta = \theta_0 | M_b)}. \tag{B.6}$$

Table B.5.: Models and their included isotopes produced in the explosion.

Model	^{56}Ni	^{54,56}Fe	^{57}Ni
M_0	✓	✗	✗
M_1	✓	✓	✗
M_2	✓	✗	✓
M_3	✓	✓	✓

Table B.6.: Bayes factors and their interpretation between the nested models and relative probabilities of the models.

Bayes F.[a]	ln(B)	Pref.[b]	Interpr.[c]	Model	Rel. Prob.[d]
B_{01}	+0.6	M_0	weak	M_0	0.022
B_{02}	+2.1	M_0	positive	M_1	0.013
B_{03}	−3.8	M_3	strong	M_2	0.002
B_{13}	−4.1	M_3	strong	M_3	0.963
B_{23}	−5.8	M_3	very strong		

[a]Bayes Factor B_{ab} between models M_a and M_b.
[b]Preferred model.
[c]Interpretation according to Kass & Raftery (1995).
[d]Relative probability $P(D|M_a) \,/\, \sum P(D|M_i)$.

We use the mass ratio results from our individual spectral fits to compute the Bayes factor between models M_0 and M_3. Prior odds are set to one as we do not have an initial preference for any model. For ^{54,56}Fe and ^{57}Ni we adopt flat priors $0 \leq \mathrm{M}_{^{54,56}\mathrm{Fe}} \,/\, \mathrm{M}_{^{56}textNi} \leq 0.5$ and $0 \leq \mathrm{M}_{^{57}textNi} \,/\, \mathrm{M}_{^{56}textNi} \leq 0.05$. The covariances and posterior densities of the models are shown in Fig. B.6 for M_3 and in Fig. B.7 for M_1 and M_2. Due to the introduction of additional degrees of freedom all models fit the data reasonably well.

To determine the best fitting model given the data we compute the Bayes factors between the models as shown in Table B.6. The $\mathrm{M}_{\mathrm{Co\,II}} \,/\, \mathrm{M}_{\mathrm{Fe\,II}}$ ratio of both M_{Ch} and sub-M_{Ch} explosion models follows closely the mass ratio from pure ^{56}Ni decay between 250 and 350 days after the explosion. Data points between these epochs cannot distinguish between either model.

Most M_{Ch} explosion models that predict between 0.4 and 0.8 $\mathrm{M}_\odot$ of ^{56}Ni (filled symbols in Fig. B.6) lie in the 3σ error ellipse of model M_3. The error ellipse also contains the aforementioned high-metallicity CO detonation model 'det_2010_1.06_0.075Ne' (Sim et al., 2010). Models, that yield less than 0.4 $\mathrm{M}_\odot$ or more than 0.8 $\mathrm{M}_\odot$ of ^{56}Ni are marked with empty symbols. The models with only ^{57}Ni or only ^{54,56}Fe in addition to the ^{56}Ni are not allowed as the gain in fit quality is small compared to the added parameter space (see Fig. B.7). A comparison between models ^{56}Ni only (M_0) and our more complex M_3 model favours the complex model.

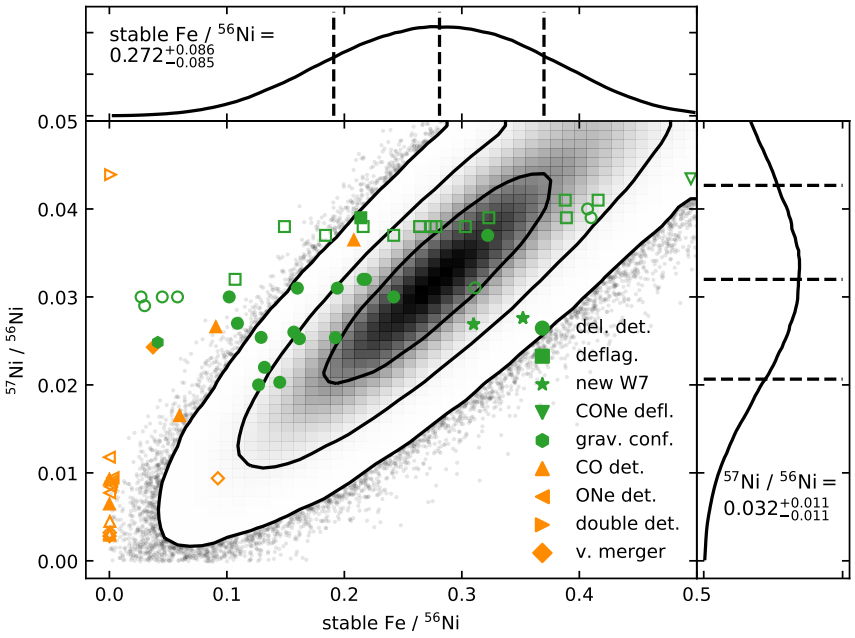

Figure B.6.: Covariances and normalised posterior densities of model M_3. Theoretical predictions of the initial ^{54,56}Fe and ^{57}Ni fraction of various explosion models are indicated by green (Near-Ch-mass) and orange (sub-Ch-mass) symbols. Theoretical predictions with too little ($< 0.4\,M_\odot$) or too much ($> 0.8\,M_\odot$) ^{56}Ni compared to Branch-normal SNe Ia are marked as empty symbols. Black lines show the 1, 2, and 3σ credibility regions. Numbers next to the 1D histograms indicate the 68 % credibility range of the individual parameters.
Models: Del. Det. (Seitenzahl et al., 2013; Ohlmann et al., 2014; Nomoto & Leung, 2018), Deflag. (Fink et al., 2014), new W7 (Nomoto & Leung, 2018), CONe Defl. (Kromer et al., 2015), Grav. Conf. (Seitenzahl et al., 2016), CO Det. (Sim et al., 2010; Nomoto & Leung, 2018), ONe Det. (Marquardt et al., 2015), Double Det. (Sim et al., 2012), V. Merger (Pakmor et al., 2010, 2012; Kromer et al., 2013b, 2016)

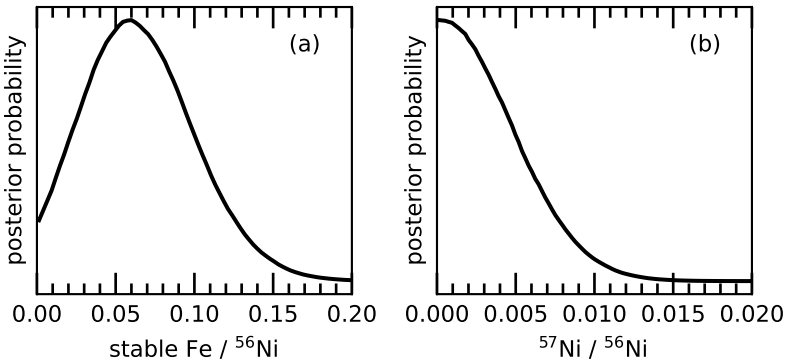

Figure B.7.: (a) Normalised posterior density of model M_1 with only stable iron ^{54,56}Fe and radioactive ^{56}Ni. (b) Normalised posterior density of model M_2 with only radioactive ^{57}Ni and ^{56}Ni.

Discussion

Emission line widths and velocity shifts

Maguire et al. (2018a) found that the velocity shifts and line widths of [Fe II] and [Ni II] of SNe in the sample are compatible within their uncertainties. We measure an average [Fe II] velocity shift of $(1.1 \pm 0.5) \times 10^3\,\mathrm{km\,s^{-1}}$, across the sample, compared to $(0.9 \pm 0.7) \times 10^3\,\mathrm{km\,s^{-1}}$ for [Co II]. Lines of [Fe II] and [Co II] are either both redshifted or both blueshifted. The average line widths are $(7.9 \pm 1.0) \times 10^3\,\mathrm{km\,s^{-1}}$ in the case of [Co II] and $(7.9 \pm 0.8) \times 10^3\,\mathrm{km\,s^{-1}}$ for [Fe II]. This indicates that the emission from all singly ionised iron-group ions originates from the same spatial region in the ejecta. The emitting region of singly ionised material appears to be located off-centre and is smaller than the emitting region of doubly ionised cobalt by about $3\,000\,\mathrm{km\,s^{-1}}$. We do not find significant velocity shift and line width offsets between [Fe II] emission in the optical and NIR. We confirm the results of Maguire et al. (2018a) that the absolute velocity shift of [Co III] is lower than that of the singly ionised species and for most spectra in our sample compatible with no offset from the rest wavelength.

Nucleosynthetic calculations for delayed detonations including multiple ignition points by Seitenzahl et al. (2013) show the stable iron group ^{54}Fe, ^{56}Fe, and ^{58}Ni to be distributed within the supernova in close association with ^{56}Ni. At the epochs of our observations ($\sim$ 200 to 500 days), the γ-rays still deposit energy into the ejecta and any stable iron, whether in the core or distributed within the ejecta, should be heated and contribute to the emission. If stable and radioactive materials are co-located in the same region, the stable material can also be heated by positrons. In fact, evidence for heating of stable elements is found in the late-time optical spectra where the line of [Ni II] is evident at 7 378 Å (e.g. Maeda et al., 2010b; Maguire et al.,

2018a). No significant amount of ^{56}Ni can be expected to be present in the ejecta 100 days after the explosion.

It is possible to hide a large amount of material if it is not heated and therefore not emitting. At epochs later than 350 days, when the mean free path for the γ-rays from the decay of ^{56}Co is larger than the radius of the supernova and the bulk of the γ-rays do not deposit their energy in the ejecta, the energy deposition within the ejecta is almost exclusively via the β^+ channel (e.g. Axelrod, 1980; Woosley et al., 1989; Leibundgut & Pinto, 1992; Woosley et al., 2007). It is assumed, due to trapping by magnetic fields, that the positron energy deposition is local to the emission region. It is, therefore, possible to have pockets of cold gas. In such a case those regions would not contribute to the spectra. Unlike the observations of SN 2003hv (Motohara et al., 2006; Maeda et al., 2010b; Mazzali et al., 2011), as discussed in Maguire et al. (2018a) our spectra do not exhibit flat-topped profiles of emission features and there is no evidence for an ashes bubble in the centre of, or off-centre, in the ejecta. A more sophisticated analysis of the line profiles of these species in the context of energy deposition scenarios and distributions can be found in Diamond et al. (2018).

The origin of iron and cobalt

Doubly ionised cobalt and iron lines have been used in the past by other authors (see Kuchner et al., 1994) to derive that the mass ratio $M_{Co\,II} / M_{Fe\,II}$ in SNe Ia is governed by the radioactive decay of ^{56}Co to ^{56}Fe. That work relied on iron and cobalt lines below 5 500 Å. Singly ionised lines above 7 000 Å become optically thin after about 150 days.

Our work determines that the singly ionised lines observed in the spectra arise from the daughter products of the radioactive ^{56}Ni. Even though we can only constrain the temperature weakly, it is evident that the mass ratio evolution is not a temperature effect. While it is plausible to assume variations in the temperature of the ejecta from one SN to another, these are unlikely to be extreme as the heating and cooling are fundamentally dictated by the same elements (the daughter products of the decay of ^{56}Ni). Furthermore, the production of ^{56}Ni is tightly linked to the density and temperature of the progenitor. Simply put, the inner ejecta of normal SNe Ia should be very similar in terms of their excitation within the boundaries of this analysis. This is borne out by the very strong similarity of the emission line spectra obtained during the first year after the explosion (Mazzali et al., 1998).

By fitting the spectra with forbidden emission lines of our set of NLTE atoms we find a decline of the temperature in the ejecta from $\sim 8\,000$ K at 200 days to $\sim 4\,000$ K at 500 days. Such a temperature evolution is consistent with predictions from simulations (Fransson & Jerkstrand, 2015). We also find that the density of the emitting material decreases from a few times 10^6 cm^{-3} to about 10^5 cm^{-3} between the youngest and oldest spectrum in our sample. These densities are consistent with a simple distribution of roughly half a solar mass of singly and doubly ionised iron group material in a volume expanding at $\sim 8\,000$ km s^{-1} for the age of the SN.

We ruled out models containing only stable iron or only ^{57}Ni in addition to ^{56}Ni. Theoretical predictions of the cobalt to iron mass ratio from M_{Ch} and sub-M_{Ch} explosion simulations differ only slightly from the pure ^{56}Ni decay chain. Within the Bayesian framework we find evidence ($B_{03} = -3.8$) for a model with ^{56}Ni, stable iron and ^{57}Ni produced during the explosion similar to most M_{Ch} models, compared to a purely ^{56}Ni origin of iron.

Due to largely unknown ejecta densities and temperatures, the uncertainties of the derived cobalt to iron mass ratio are quite large. Future observations of the relative strength of the [Co II] 10.52 μm, 14.74 μm and 15.46 μm lines (e.g. with *JWST*) would also allow for a direct measurement of the density and temperature of the emitting material in the range 10^4 – 10^6 cm^{-3} and 3 000 – 10 000 K (Storey et al., 2016). A more accurate Co II / Fe II mass ratio could be used to determine the amount of ^{57}Ni and ^{54,56}Fe for individual SNe rather than assuming similar progenitor scenarios for a sample of SNe.

The presence of ^{57}Ni was also discussed for the nearby SN 2011fe (Dimitriadis et al., 2017; Kerzendorf et al., 2017; Shappee et al., 2017) and SN 2012cg (Graur et al., 2016). For these two objects photometric measurements were obtained at extremely late phases (> 1 000 days after explosion) to construct a pseudo-bolometric light curve. Graur et al. (2016) claimed that ^{57}Ni is required to explain the late-time light curve of SN 2012cg. Both Dimitriadis et al. (2017) and Shappee et al. (2017) argued for a detection of ^{57}Ni in SN 2011fe, albeit with very different abundances, pointing to either near-M_{Ch} (Dimitriadis et al., 2017) or sub-M_{Ch} explosions (Shappee et al., 2017). Kerzendorf et al. (2017) tested the effect of various isotopic abundances and physical processes on the light curve and came to the conclusion that one cannot determine the ^{57}Ni abundance from the light curve without detecting the mid-IR cooling lines.

Conclusions

We fitted late time spectra of SNe Ia with broadened emission profiles from NLTE level populations using a Bayesian sampler. We computed good fits with similar widths and velocity offsets among the singly ionised atoms, indicating a common emission region. We find that doubly ionised cobalt is located in a broader and more centred region of the ejecta. We have shown that the singly ionised iron group elements in the late-time spectra of SNe Ia change their flux ratios in agreement with an evolution of their mass ratios that would be governed by the radioactive decay of ^{56}Co to ^{Fe}Co. This result disfavours the presence of only stable iron or only the decay products of ^{57}Ni in the ejecta in addition to ^{56}Ni, at least for the SNe observed here. For a model that produced both stable iron and ^{57}Ni in addition to ^{56}Ni during the explosion we find $^{54,56}\mathrm{Fe} / {}^{56}\mathrm{Ni} = 0.272 \pm 0.086$ and $^{57}\mathrm{Ni} / {}^{56}\mathrm{Ni} = 0.032 \pm 0.011$ with a ratio of stable iron to ^{57}Ni of $\sim 8.5 : 1$.

C. Paper III: Sub-Chandrasekhar progenitors favoured for type Ia supernovae: Evidence from late-time spectroscopy

A. Flörs, J. Spyromilio, S. Taubenberger, S. Blondin, R. Cartier, B. Leibundgut, L. Dessart, S. Dhawan and W. Hillebrandt

ABSTRACT
A non-local-thermodynamic-equilibrium (NLTE) level population model of the first and second ionisation stages of iron, nickel and cobalt is used to fit a sample of XShooter optical + near-infrared (NIR) spectra of Type Ia supernovae (SNe Ia). From the ratio of the NIR lines to the optical lines limits can be placed on the temperature and density of the emission region. We find a similar evolution of these parameters across our sample. Using the evolution of the Fe II 12 570 Å to 7 155 Å line as a prior in fits of spectra covering only the optical wavelengths we show that the 7200 Å feature is fully explained by [Fe II] and [Ni II] alone. This approach allows us to determine the abundance of Ni II/Fe II for a large sample of 130 optical spectra of 58 SNe Ia with uncertainties small enough to distinguish between Chandrasekhar mass (M_{Ch}) and sub-Chandrasekhar mass (sub-M_{Ch}) explosion models. We conclude that the majority (85%) of normal SNe Ia have a Ni/Fe abundance that is in agreement with predictions of sub-M_{Ch} explosion simulations of $\sim Z_{\odot}$ progenitors. Only a small fraction (11%) of objects in the sample have a Ni/Fe abundance in agreement with M_{Ch} explosion models.

Introduction

Type Ia supernovae (SNe Ia) are a remarkably homogeneous class of transients which are thought to originate from the explosion of a white dwarf (WD) star in a binary system. Radioactive ^{56}Ni produced in the thermonuclear explosion of the electron-degenerate matter (Hoyle & Fowler, 1960) powers the light curve (Colgate & McKee, 1969; Kuchner et al., 1994) for several years. Even though SNe Ia have been used as distance indicators for several decades and significantly contributed to our current understanding of cosmology (ΛCDM and the accelerated expansion

of the universe, Riess et al., 1998; Perlmutter et al., 1999), the precise mechanism that leads to the thermonuclear runaway reactions, as well as the progenitor system, remains elusive.

Two channels that can lead to the explosion of a WD as a SNe Ia have been extensively discussed in the literature. In Chandrasekhar-mass (M_{Ch}) explosions the burning front propagates either as a deflagration (e.g. Gamezo et al., 2003; Fink et al., 2014) or a delayed detonation (e.g. Blinnikov & Khokhlov, 1986, 1987; Khokhlov, 1991; Gamezo et al., 2005; Seitenzahl et al., 2013). The explosion is naturally triggered by an increase of the central density as the WD accretes material from its companion and comes close to the Chandrasekhar mass limit ($M \simeq M_{Ch}$). In the sub-M_{Ch} channel the central temperature of the primary white dwarf never reaches conditions that are sufficient to ignite carbon. However, an explosion significantly below the M_{Ch} may be triggered through dynamical processes such as mergers (e.g. Pakmor et al., 2010, 2013; Ruiter et al., 2013), double detonations (e.g. Fink et al., 2010; Woosley & Kasen, 2011; Moll & Woosley, 2013; Shen et al., 2018) or head-on collisions (e.g. Kushnir et al., 2013). For such systems the burning front propagates as a pure detonation (Sim et al., 2010).

The search for solutions to the SN Ia progenitor problem has been the focus of many studies. For historical supernova remnants one can search for a surviving companion star which was ejected at velocities of a few hundred $\mathrm{km\,s^{-1}}$, though no promising candidates have been found so far (Kerzendorf et al. 2018b for SN 1006, Kerzendorf et al. 2018a for SN 1572). Non-degenerate donor stars of SNe Ia in nearby galaxies should also be visible in deep images as their brightness increases by a factor of $\sim 10 - 10^3$, though again, no donor stars have been found for a sample of the closest SNe Ia in recent times (Li et al., 2011a; Bloom et al., 2012; Shappee et al., 2013).

The growth of a white dwarf star to the M_{Ch} limit requires a steady transfer of material from the companion (Nomoto et al., 1984). Material which was expelled from the companion but not accreted on the white dwarf enriches the circumstellar material (CSM). In few cases evidence for such a CSM has been detected (Hamuy et al. 2003, Deng et al. 2004 for SN 2002ic; Harris et al. 2018, Graham et al. 2019 for SN 2015cp; Vallely et al. 2019, Kollmeier et al. 2019 for SN 2018fhw). However, the bulk of Ias do not exhibit any evidence for CSM interaction. When the blast wave from the SN explosion runs through the CSM, electrons are accelerated to relativistic speeds and produce radio emission through synchrotron radiation (Chevalier, 1982b, 1998; Chevalier & Fransson, 2006). For a nearby SN Ia such as SN 2011fe radio emission should be observable if it exploded in the single degenerate channel. However, no radio emission was found by Horesh et al. (2012) for SN 2011fe (but see also Nugent et al. (2011b) for a counter argument)

One can also distinguish the two channels from direct observations of the aftermath of the explosion itself. Unfortunately, the uniformity of explosion model predictions of SNe Ia makes this a challenging task. A promising difference between M_{Ch} and sub-M_{Ch} models is the mass fraction of neutronised species produced in the explosion. While the progenitor metallicity affects how much neutron-rich material can be produced in both channels, additional neutrons are only available for explosions close to the M_{Ch} due to the high central densities ($\rho_{cen} \sim 2 \times 10^9\,\mathrm{g\,cm^{-3}}$)

which allow electron capture reactions to take place (Iwamoto et al., 1999; Seitenzahl et al., 2013).

X-ray spectroscopy of SN remnants in the Milky Way (MW) and the Large and Small Magellanic Clouds (LMC & SMC) allowed Park et al. (2013), Yamaguchi et al. (2014), Yamaguchi et al. (2015), Martínez-Rodríguez et al. (2017) and Seitenzahl et al. (2019) to estimate the fraction of the neutron-rich stable iron-peak isotopes ^{55}Mn and ^{58}Ni. They find considerable differences across their sample, but the number of objects for which such a study can be done is limited.

In this work we are interested in the composition of the iron-rich ejecta of SNe Ia. Theoretical explosion models contain the following isotopes in the central region:

a) ^{56}Ni, which is the most abundant radioactive isotope and responsible for the heating of the ejecta. It decays within a few days ($t_{1/2} = 6.075\,\mathrm{d}$) to ^{56}Co, which in turn decays ($t_{1/2} = 77.2\,\mathrm{d}$) to stable ^{56}Fe. ^{56}Ni can be produced in NSE (Nuclear Statistical Equilibrium) without an overabundance of neutrons ($Y_e = 0.5$) or high densities (Hoyle & Fowler, 1960). In our analysis, we treat ^{56}Ni as a reference point and give other abundances in fractions of the ^{56}Ni mass.

b) ^{57}Ni, which decays with $t_{1/2} = 1.48\,\mathrm{d}$ to ^{57}Co. The decay of ^{57}Co to stable ^{57}Fe is slower ($t_{1/2} = 271.74\,\mathrm{d}$) than the decay of ^{56}Co, so it can power the light curve at later epochs. Roughly 1 000 days after the explosion energy deposition from ^{57}Ni decay overtakes the energy deposition from ^{56}Ni (Seitenzahl et al., 2009). Most sub-M_{Ch} explosions models predict an abundance $M_{^{57}Ni}/M_{^{56}Ni} < 2\,\%$ (e.g. Sim et al., 2010; Pakmor et al., 2010; Yamaguchi et al., 2015; Nomoto & Leung, 2018; Shen et al., 2018), while M_{Ch} explosions predict $> 2\,\%$ (e.g. Seitenzahl et al., 2013; Yamaguchi et al., 2015; Nomoto & Leung, 2018).

c) stable ^{54,56}Fe which is directly synthesised in the explosion and not a daughter product of radioactive decay. M_{Ch} explosions produce $M_{^{54,56}Fe}/M_{^{56}Ni} > 10\,\%$, while most sub-$M_{Ch}$ models have $M_{^{54,56}Fe}/M_{^{56}Ni} < 10\,\%$ (see references in b).

d) stable ^{58}Ni which is synthesised in the explosion. Sub-M_{Ch} explosions contain $M_{^{58}Ni}/M_{^{56}Ni} < 6\,\%$ and M_{Ch} explosions have $M_{^{58}Ni}/M_{^{56}Ni}$ between 8 and 12 % (see references in b).

Contributions of slowly-decaying neutron-rich material (e.g. ^{57}Co - the daughter product of ^{57}Ni) to the quasi-bolometric light curve of the nearby SN 2011fe at > 1000 days after the explosion were investigated by Shappee et al. (2017), Dimitriadis et al. (2017) and Kerzendorf et al. (2017). This method was used for other nearby transients SN 2012cg (Graur et al., 2016), SN 2013aa (Jacobson-Galán et al., 2018), SN 2014J (Yang et al., 2018), SN 2014lp (Graur et al., 2018a) and SN 2015F (Graur et al., 2018b). However, the physical processes relevant at such late phases have long time constants and their onset is poorly constrained by the data (Fransson & Jerkstrand, 2015). In particular, it remains unclear what fraction of the radioactive decay energy is converted into optical photons as the majority of the energy is expected to come out in the mid-IR.

SNe Ia complete their transition into the nebular phase roughly half a year after the explosion when the ejecta become fully transparent and the bare iron core which gives insight into the explosion physics is visible. Nebular phase spectral models build on the early work of Axelrod (1980) and many authors over the years (Spyromilio et al., 1992; Kozma & Fransson, 1992; Kuchner et al., 1994; Kozma et al., 2005; Mazzali et al., 2007; Fransson & Jerkstrand, 2015; Botyánszki & Kasen, 2017; Maguire et al., 2018a; Diamond et al., 2018) with spectral synthesis codes of varying complexity.

The method presented herein enables the use Ni and Fe optical lines to constrain the fraction of neutron rich material in the ejecta. This approach increases the number of objects for which the analysis can be performed by about one order of magnitude compared to the number of optical+NIR spectra currently available. The analysis is made possible by using a small sample of optical+NIR spectra to determine the relative strength of the NIR 12 570 Å to the optical emission 7 155 Å lines of Fe II. With this relation we can model optical nebular spectra which do not have NIR observations. From the fits to observed late spectra we determine the stable Ni to Fe ratio. We estimate the systematic uncertainty of the method and show that emission lines from singly ionised iron and nickel are sufficient to model the 7 200 Å emission feature. Finally, we discuss the implications of the determined Ni to Fe ratio of the large sample of more than 100 spectra on the various explosion model predictions.

Observations

We extend the XShooter sample of nearby SNe Ia in the nebular phase from Maguire et al. (2018a) with SN 2015F (PI M. Sullivan, program ID 095.A-0316, PI R. Cartier, program IDs 096.D-0829, 097.D-0967 and 098.D-0692) and SN 2017bzc (PI L. Dessart, program ID 0100.D-0285). The epochs of the additional spectra range from $\sim$200 days to $\sim$420 days after the explosion. An overview of the observations for these two supernovae is given in Table C.1.

XShooter is an echelle spectrograph with three arms (UVB, VIS and NIR) covering the wavelength range of $\sim$3 000–25 000 Å located at the Very Large Telescope (VLT). The resolution of the individual arms depends on the slit widths. For the observations presented in this work slit widths of 1.0 (UVB), 0.9 (VIS) and 0.9 (NIR) arcseconds have been used. The corresponding resolution of the three arms is therefore 5400, 8900 and 5600, respectively. The spectra were reduced using the ESO pipeline with the XShooter module, producing flux-calibrated one-dimensional spectra in each of the three arms (Modigliani et al., 2010; Freudling et al., 2013). We also used a custom postprocessing pipeline to combine the rectified 2D-images, perform the sky-subtraction and extract the spectrum (`https://github.com/jselsing/xsh-postproc`).

Nebular phase spectra of SNe Ia exhibit a number of broad ($\approx$ 7 000 to 9 000 km s^{-1}) emission features (see Fig. C.1). In the NIR, we identify the strongest features as transitions of singly ionised [Fe II] and [Co II]. The 10 190 Å (a^3F_4–b^3F_4) transition of [Co II] decreases in strength according to the decay of ^{56}Co to ^{56}Fe (Spyromilio et al., 2004; Flörs et al., 2018). The emission

Table C.1.: Overview of the observations

SN name	Observation MJD	Observation date	Phase[a]	E($B-V$)[b] (mag)	Helio. z[c]	Host galaxy	Exposure time (s)
SN 2015F	57287.4	2015 Sept 22	+181d	0.260±0.021[d]	0.00489	NGC 2442	720
	57331.4	2015 Nov 05	+225d				1200
	57345.3	2015 Nov 19	+239d				3600
	57372.2	2015 Dec 16	+266d				7600
	57512.0	2016 May 04	+406d				3800
SN 2017bzc	58039.5	2017 Oct 12	+215d	0.0122±0.0002	0.00536	NGC 7552	10080

[a]Phase of late-time spectrum calculated with respect to maximum light.
[b]Galactic $E(B\text{-}V)$ values from Schlafly & Finkbeiner (2011).
[c]Heliocentric redshifts are from the Nasa Extragalactic Database (NED).
[d]Additional host galaxy extinction of $E(B\text{-}V)$=0.085 mag was found for SN 2015F by Cartier et al. (2017). The value given in the table is the combined MW and host galaxy $E(B\text{-}V)$.

feature at around 13 000 Å is identified as the 12 570 Å a^6D–a^4D multiplet of [Fe II]. The double peaked feature around 16 000 Å is composed of a blend of [Fe II] and [Co II] lines of the multiplets a^4F–a^4D and a^5F–b^3F, respectively. Redwards of the strong telluric absorption feature at $\sim$ 18 500 Å we also detect the $a^2F_{7/2}$–$a^4F_{9/2}$ line of [Ni II] in spectra with high SNR (Dhawan et al., 2018).

In the optical we see blends of singly and doubly ionised Fe, Co and Ni. The strong feature at 4 700 Å originates mainly from the $3d^6\,{}^5D$–^3F multiplet of [Fe III] (Axelrod, 1980; Kuchner et al., 1994). The broad emission centred around 5900 Å is primarily due to [Co III] in the a^4F–a^2G multiplet. The identification of the 5 900 Å [Co III] feature is secured by the fact that the relative strength of this feature with respect to e.g. the [Fe III] 4 700 Å feature decreases with time as predicted by radioactive decay of ^{56}Co (Kuchner et al., 1994; Childress et al., 2015; Dessart et al., 2014). Near the 7 200 Å region the spectra exhibit emission lines of the [Fe II] multiplets a^4F–a^2G and a^6D–a^4P and the [Ni II] multiplet z^2D–a^2F. The identification of the various emission lines in the optical and NIR of SNe Ia in the nebular phase has been extensively discussed in the literature and is considered secure. A detailed overview of the strongest emission lines is given in Table C.2.

Methods

Summary

We have determined that the line ratio of the 12 570 to 7 155 Å [Fe II] lines in the nebular spectra of type Ia supernovae evolves with supernova age in a predictable log-linear manner. We assume that evolution is valid for supernovae for which we only have optical coverage. The range of

Table C.2.: Selected forbidden lines of singly and doubly ionised Fe, Co and Ni in the optical and NIR.

$\lambda_{\rm rest}$(Å)	Ion	Transition
4 418	[Fe II]	$a^6D_{9/2} - b^4F_{9/2}$
4 659	[Fe III]	$^5D_4 - {}^3F_4$
4 891	[Fe II]	$a^6D_{7/2} - b^4P_{5/2}$
5 160	[Fe II]	$a^4F_{9/2} - a^4H_{13/2}$
5 272	[Fe III]	$^5D_3 - {}^3P_2$
5 528	[Fe II]	$a^4F_{7/2} - a^2D_{5/2}$
5 888	[Co III]	$a^4F_{9/2} - a^2G_{9/2}$
5 908	[Co III]	$a^4F_{7/2} - a^2G_{7/2}$
6 197	[Co III]	$a^4F_{7/2} - a^2G_{9/2}$
6 578	[Co III]	$a^4F_{9/2} - a^4P_{5/2}$
6 855	[Co III]	$a^4F_{7/2} - a^4P_{3/2}$
7 155	[Fe II]	$a^4F_{9/2} - a^2G_{9/2}$
7 172	[Fe II]	$a^4F_{7/2} - a^2G_{7/2}$
7 378	[Ni II]	$z^2D_{5/2} - a^2F_{7/2}$
7 388	[Fe II]	$a^4F_{5/2} - a^2G_{7/2}$
7 414	[Ni II]	$z^2D_{3/2} - a^2F_{5/2}$
7 453	[Fe II]	$a^4F_{7/2} - a^2G_{9/2}$
7 638	[Fe II]	$a^6D_{7/2} - a^4P_{5/2}$
7 687	[Fe II]	$a^6D_{5/2} - a^4P_{3/2}$
8 617	[Fe II]	$a^4F_{9/2} - a^4P_{5/2}$
9 345	[Co II]	$a^3F_3 - a^1D_2$
9 345	[Co II]	$a^3F_3 - a^1D_2$
9 704	[Fe III]	$^3H_6 - {}^1I_6$
10 190	[Co II]	$a^3F_4 - b^3F_4$
10 248	[Co II]	$a^3F_3 - b^3F_3$
10 611	[Fe III]	$^3F_4 - {}^1G_4$
12 570	[Fe II]	$a^6D_{9/2} - a^4D_{7/2}$
12 943	[Fe II]	$a^6D_{5/2} - a^4D_{5/2}$
13 206	[Fe II]	$a^6D_{7/2} - a^4D_{7/2}$
15 335	[Fe II]	$a^4F_{9/2} - a^4D_{5/2}$
15 474	[Co II]	$a^5F_5 - b^3F_4$
15 488	[Co III]	$a^2G_{9/2} - a^2H_{9/2}$
15 995	[Fe II]	$a^4F_{7/2} - a^4D_{3/2}$
16 440	[Fe II]	$a^4F_{9/2} - a^4D_{7/2}$
17 416	[Co III]	$a^2G_{9/2} - a^2H_{11/2}$
17 455	[Fe II]	$a^4F_{3/2} - a^4D_{1/2}$
18 098	[Fe II]	$a^4F_{7/2} - a^4D_{7/2}$
19 390	[Ni II]	$a^2F_{7/2} - a^4F_{9/2}$
20 028	[Co III]	$a^4P_{5/2} - a^2P_{3/2}$
20 157	[Fe II]	$a^2G_{9/2} - a^2H_{9/2}$
22 184	[Fe III]	$^3H_6 - {}^3G_5$

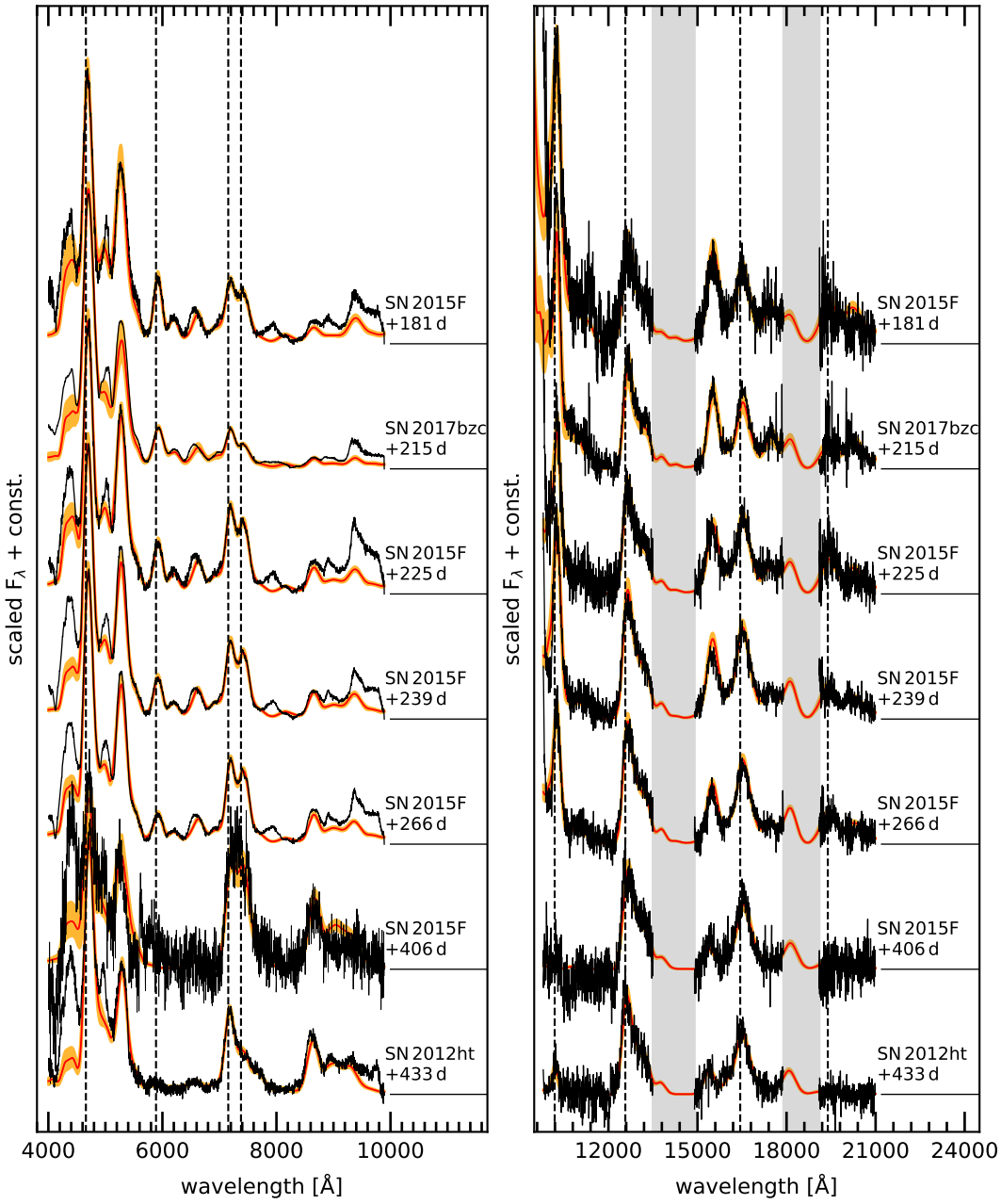

Figure C.1.: Optical (left) and NIR (right) spectra of SN 2015F and SN 2017bzc obtained with XShooter at the VLT. We also show the spectrum and the corresponding fit to SN 2012ht presented in Maguire et al. (2018a). The spectra are arranged in epoch starting with the youngest at the top. The spectra have been corrected for telluric absorption but not for extinction and host galaxy redshift. Instead, we redshift and extinguish the spectral models. Fluxes are normalised to the 4 700 Å [Fe III] feature (optical) and 12 600 Å [Fe II] feature (NIR). In the NIR the bands of heavy telluric absorption are masked in grey. In the optical the rest wavelengths of the 4 659 Å [Fe III], the 5 888 Å [Co III], the 7 155 Å [Fe II] and the 7 378 Å [Ni II] lines are indicated as dashed lines. In the NIR dashed lines indicate the 10 190 Å [Co II], the 12 570 Å [Fe II], the 16 440 Å [Fe II] and the 19 390 Å [Ni II] lines. The red line indicates the mean flux of all fit models at each wavelength, the orange shaded area marks the 68 % uncertainty of the fit.

Table C.3.: Ions included in the fits and their atomic data sets.

Ion	Levels[a]	Ref. A_{ij} [b]	Ref. Υ_{ij} [c]
Fe II	52	Bautista et al. (2015)	Bautista et al. (2015)
Fe III	39	Quinet (1996)	Zhang (1996)
Co II	15	Storey et al. (2016)	Storey et al. (2016)
Co III	15	Storey & Sochi (2016)	Storey & Sochi (2016)
Ni II	18	Cassidy et al. (2016a)	Cassidy et al. (2010a)
Ni III	9	Fivet et al. (2016)	Watts & Burke (1998)

[a]Energy levels and statistical weights are taken from NIST (Kramida et al., 2018).
[b]Einstein A coefficient between levels i and j.
[c]Maxwellian averaged collisional strength between levels i and j.

electron densities and temperatures that give rise to a given ratio is determined by the atomic data for these transitions. For each epoch we thus have prior knowledge of the range of n_e and T. This range is used to determine the ratio of the emissivity per atom for the 7 155 [Fe II] to 7 378 Å [Ni II] lines and thus determine the range of mass ratios of Nickel to Iron based on optical data alone at any given epoch.

The model

We use a one-zone model as described in Flörs et al. (2018). We extend the model to include all first and second ionisation stages of iron, nickel and cobalt (see Table C.3). For this set of ions we solve the NLTE rate equations and compute level populations. Throughout this work we do not correct the observed spectra for dust extinction and host galaxy redshift. In Table C.5 we show the redshift and reddening applied to our models. For the reddening correction in our models we adopt Cardelli et al. (1989). The strength of the reddening is strongly constrained by the presence of a number of lines arising from the same upper level in different ions (e.g. 12 570 and 16 440 Å of [Fe II]).

We compare our parameterised model M to the XShooter observations D described in Section *Observations* using the approach from Czekala et al. (2015). The likelihood function contains a correlation matrix C which has the uncertainties of the pixels as diagonal elements and the correlations of nearby pixels on the off-diagonals:

$$\ln p(D|M) = -\frac{1}{2}\left((D-M)^{\mathrm{T}} C^{-1} (D-M) + \ln\det C + N_{\mathrm{pix}} \ln 2\pi\right) \tag{C.1}$$

To account for systematic imperfections of the model (e.g. line profiles are not Gaussian far from the line centre), we use Gaussian processes with a Matérn kernel to add an additional noise term in the correlation matrix at the location of the feature edges (see Czekala et al., 2015). This prevents the sampling algorithm from only choosing a narrow set of parameter values, which yield a better fit in regions where the model is systematically unable to fit the observations. We

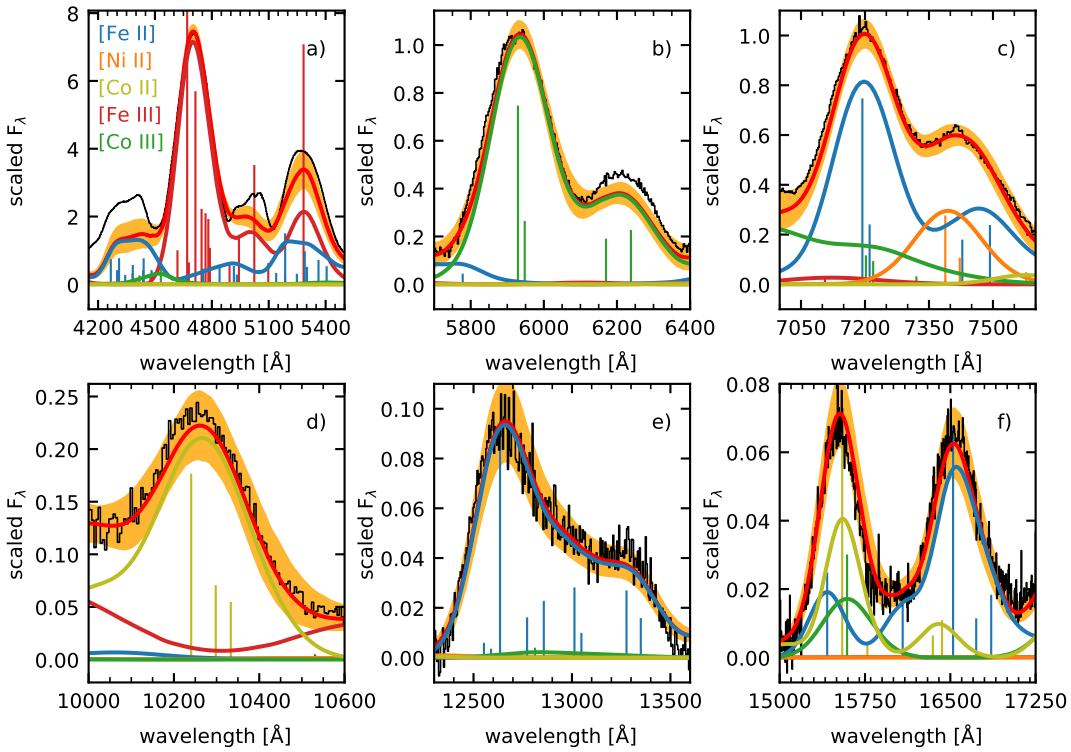

Figure C.2.: Example fit of SN 2017bzc at +215 days after B-band maximum. The individual panels highlight the ionic emission contributions to six features from the near-UV to the NIR. The strongest lines of each ion are indicated as vertical lines. The height of these lines shows their relative strengths. The flux of the spectrum was scaled to the 7 155 Å peak. The observed spectrum is not corrected for extinction and redshift of the host. Instead, all model lines are extinguished and redshifted.

employ flat priors for all parameters of the model. The upper and lower bounds of the flat priors are chosen in such a way that the posterior parameter distributions are not truncated.

We use nested sampling to find the posterior distributions of the parameters of the model that yield good fits with the observed spectrum. Fig. C.1 presents the fits results for the spectra given in Table C.1. The red line indicates the mean flux of all fit models at each wavelength while the orange shaded area marks the 68% uncertainty of the fit. Fit results for the previously published spectra of the XShooter sample are shown in Flörs et al. (2018). An exemplary zoom into the fit of SN 2017bzc at +215 days is shown in Fig. C.2.

For each spectrum we can use the posterior distribution of the model parameters to compute line emissivities of all lines of singly and doubly ionised Fe, Ni and Co. In this work we use line ratios of [Ni II] and [Fe II]. Ni II emission in the nebular phase can only be the result of the stable isotope ^{58}Ni, as the radioactive material has long since decayed. Fe can be produced directly during the explosion as ^{54,56}Fe or it can be the decay product of radioactive ^{55}Co, ^{56}Ni and ^{57}Ni. The line ratio of [Ni II] and [Fe II] allows us to determine the mass fraction of neutron

rich (leading to ^{58}Ni) to radioactive material, which in turn can be compared to predictions of explosion models. A similar study was performed for the NIR line ratio of the 15 470 Å [Co II] to the 15 330 AA [Fe II] line in Flörs et al. (2018). While the NIR nebular spectra are easier to model than the optical spectra, the mass ratio of Co II to Fe II changes with time and the number of spectra with NIR coverage is quite limited. In this work we want to make use of several decades of optical nebular phase spectroscopy to determine the distribution of the Ni/Fe abundance and compare our findings with predictions from explosion models.

Calibration of optical spectra of SNe Ia

To determine the Ni II / Fe II mass ratio we compute the ratio of the 7 378 Å [Ni II] and the 7 155 Å [Fe II] lines (see Fig. C.2 panel c). The conversion of line emissivities to emitting masses requires knowledge of the temperature and density of the emitting material. The one-zone-model employed in this study does not allow us to disentangle these two parameters. However, we find that the evolution of the ratio of the strongest Fe II line in the NIR (12 570 Å) and optical (7 155 Å) is very similar across our sample of optical+NIR spectra (see Fig. C.2 panel c and e for these lines). This seems to be a natural evolution from high temperatures and high densities towards lower values. Due to the decreasing temperature it becomes more difficult at late epochs to excite the levels giving rise to optical transitions, thus increasing the ratio of the NIR to optical lines. We fit a simple linear relation through our inferred data points (see Fig. C.3). The uncertainties of the individual data points are uncorrelated, thus justifying the use of a simple Chi-Square likelihood

$$\ln p(y|t, \Delta y, m, b, \sigma) = -\frac{1}{2} \sum_n \left(\frac{(y_n - m x_n - b)^2}{s_n^2} + \ln(2\pi s_n^2) \right) \tag{C.2}$$

where

$$s_n^2 = \sigma_n^2 + \sigma^2 (m x_n + b)^2. \tag{C.3}$$

In this equation y and Δy indicate the inferred values and uncertainties of the Fe II 12 570Å to 7 155 Å ratio for our sample, m is the slope of the fit curve, b is its intersect, and σ is the intrinsic scatter of the population. We add an intrinsic scatter term to the likelihood function that takes into consideration that our sample consists of many different objects. The uncertainty of the fit is then a combination of the uncertainty of slope and intersect and the intrinsic scatter term. We find for the ratio of Fe II 12 570Å to 7 155 Å

$$\log \frac{F_{12\,570}}{F_{7\,155}} = -(1.65 \pm 0.07) + (0.0043 \pm 0.0002)\, d^{-1} \times t_{\rm exp}[\rm days] \tag{C.4}$$

with an intrinsic scatter of 0.06 dex around the best fit curve. The choice of the atomic data has only very weak consequences on the inferred NIR/VIS ratio. Translating the NIR/VIS ratio to temperatures/densities does rely on the atomic data, however. The atomic data used throughout this work is given in Table C.3.

Alone, the optical spectra of SNe Ia do not allow us to constrain the temperature and density of the emitting material in any meaningful way - we can obtain good fits for a wide range of temperatures and densities. However, we notice that for a given Fe II 12 570Å to 7155 Å ratio

only specific tracks in the temperature/density space are possible. The inference uncertainty of the NIR/VIS ratio translates into a curve with non-zero width in the temperature/density space. The measurement of the NIR/VIS line ratio is considered robust - no other strong lines are present in the 12 500 Å feature, and in the 7 000 Å region only Co III of the iron group elements has a weak contribution. We exclude the extremes in the temperature/density space (see grey shaded areas in Fig. C.4) by fitting the many lines of singly and doubly ionised material at optical and NIR wavelengths. Each of the curves in Fig. C.4 corresponds to one value of the NIR/VIS ratio. We can thus determine a range of temperatures and densities of SNe Ia in the nebular phase assuming that the Fe II 12 570Å to 7 155 Å ratio evolves as the red curve in Fig. C.3 with a 1-sigma uncertainty of 0.06 dex. We add this constraint as a Gaussian prior into the likelihood function of our Bayesian fit model.

Determination of the Ni to Fe ratio

The temperature range is significant and thus the uncertainty in the absolute masses is large. A temperature difference of only a few hundred Kelvin can lead to an emitting mass that is different by a factor of a few. However, a more robust quantity is the mass ratio of ions of the same ionisation stage. Under the assumption that the same emitting region gives rise to these lines (Maguire et al., 2018a; Flörs et al., 2018) the physical conditions of the ions (temperature and electron density) are similar. Using a mass ratio also negates the effect of the rather unknown distance to the SN host galaxy and significantly reduces the effect of the emitting temperature.

For a given temperature and density we can directly infer the ratio of the number of emitting Fe II and Ni II ions required to match the observed flux ratio of the 7 155 Å and 7 378 Å lines (see Fig. C.2 panel c). Temperatures and densities that yield a good fit can be found if a NIR spectrum is available. For spectra that lack this additional information we have to use the relation obtained in Section *Calibration of Optical Spectra of SNe Ia*. We discuss the additional uncertainties from using the fit relation instead of the full optical + NIR spectrum in Section *Robustness of the Ni/Fe ratio*.

Discussion

The Fe II NIR/VIS ratio

In Section *Calibration of Optical Spectra of SNe Ia* we derived a relation between two of the strongest Fe II lines that are observed in nebular spectra of SNe Ia. Our extended XShooter sample now contains 14 spectra of 9 different SNe. The ratio of the NIR 12 570 Å and the 7 155 Å lines evolves similarly for all objects in our sample. In physical terms, the ratio of these lines is a direct measure of the cooling and expanding Fe-rich ejecta. The relation does not depend on the collision strengths but only on the transition rates of Fe II. These are well known, as can be seen from the match of the fit models and the observed spectra in regions where only

Table C.4.: Results of the ratio of the 12 570 Å and 7 155 Å lines of Fe II, the M_{Co} / M_{Fe} ratio and the M_{Ni} / M_{Fe} ratio for the extended XShooter sample.

SN	Ref[a]	Epoch	$R_{12570/7155}$	M_{Co}/M_{Fe}	M_{Ni}/M_{Fe}
SN 2015F	TW	+181 d	0.173 ± 0.16	0.231±0.02	0.061±0.010
PSNJ1149	M18	+206 d	0.199 ± 0.022	0.152±0.012[b]	0.044±0.011
SN 2017bzc	TW	+215 d	0.211 ± 0.044	0.154±0.01	0.035±0.009
SN 2015F	TW	+225 d	0.241 ± 0.018	0.142±0.02	0.055±0.008
SN 2013ct	M16	+229 d	0.279 ± 0.021	0.103±0.010[b]	0.037±0.006
SN 2015F	TW	+239 d	0.325 ± 0.022	0.127±0.02	0.052±0.008
SN 2015F	TW	+266 d	0.314 ± 0.020	0.097±0.01	0.055±0.009
SN 2013cs	M16	+303 d	0.486 ± 0.029	0.066±0.011[b]	0.031±0.006
SN 2012cg	M16	+339 d	0.726 ± 0.021	0.051±0.005[b]	0.038±0.006
SN 2012fr	M16	+357 d	0.947 ± 0.048	0.038±0.004[b]	0.025±0.005
SN 2013aa	M16	+360 d	1.00 ± 0.068	0.035±0.003[b]	0.033±0.006
SN 2015F	TW	+406 d	1.36 ± 0.06	–	0.049±0.009
SN 2013aa	M18	+425 d	2.07 ± 0.14	0.025±0.003[b]	0.035±0.007
SN 2012ht	M16	+433 d	1.87 ± 0.11	0.020±0.005	0.009±0.004

[a]Source of the nebular spectrum:
TW (This Work); M16 (Maguire et al., 2016); M18 (Maguire et al., 2018a)
[b]Result taken from Flörs et al. (2018)

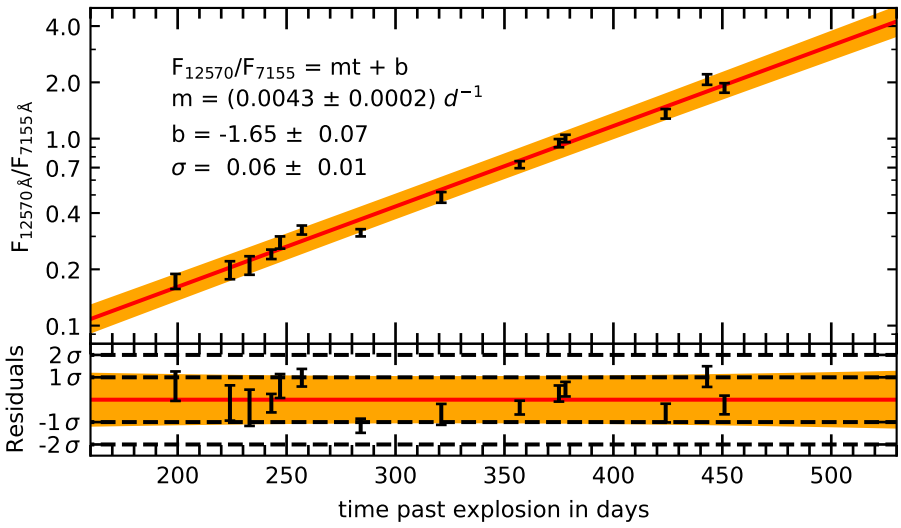

Figure C.3.: Inferred ratio of the Fe II 12 570 Å to 7 155 Å lines as a function of time after explosion. The red line marks a linear fit to data of the form y = mt + b with intrinsic scatter σ. The orange shaded band indicates the 68% confidence interval of the regression curve.

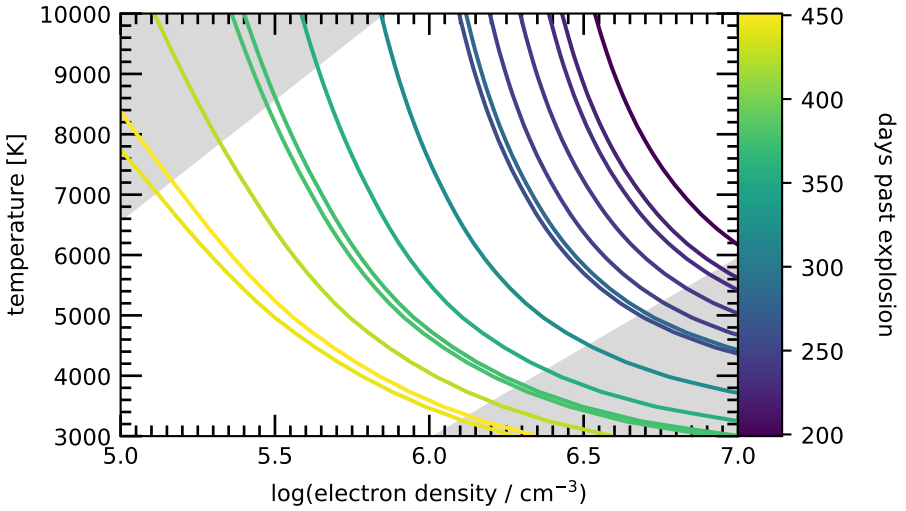

Figure C.4.: Allowed regions of the electron density and temperature for the SN Ia in our sample. Every curve corresponds to one value of the 12 570 Å to 7 155 Å Fe II line ratio. The allowed region is evolving with time to lower temperatures and densities. The density evolves as t^{-3} in accordance with homologous expansion of the ejecta. Colours indicate the epochs of the spectra. The grey shaded regions (high density + low temperature; low density + high temperature) are excluded by the fits to [Ni II] and [Co II].

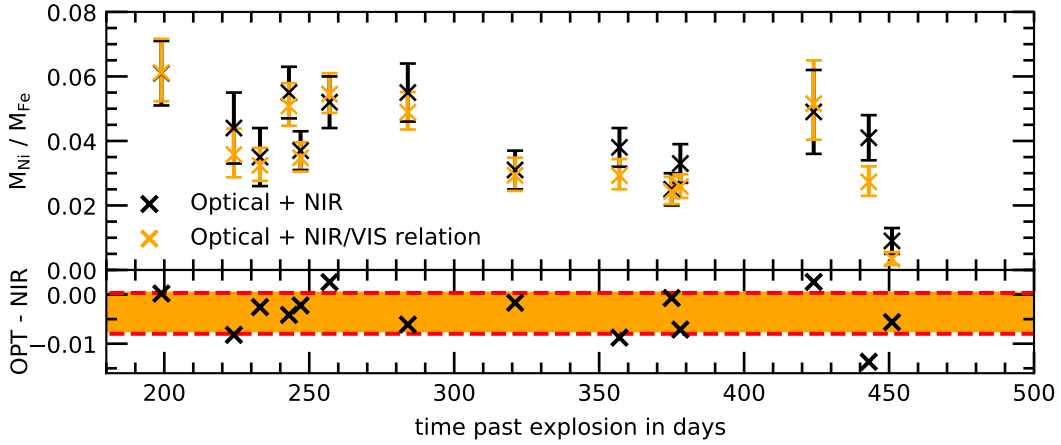

Figure C.5.: Inferred mass ratio of Ni II and Fe II from optical and NIR spectroscopy. Black data points indicate that the Fe II NIR/VIS ratio was directly inferred from a spectrum covering 4,000–20,000 Å. Orange data points indicate that only the optical part of the spectrum was used in conjunction with the relation from Fig. C.3 as a prior. We assume a rise time of $\sim$ 18 days (Ganeshalingam et al., 2011) to compute the time after explosion. The bottom panel shows the systematic differences between the two methods – optical spectra + the NIR/VIS relation (OPT) and fitting the full spectrum (NIR). The orange shaded band in the bottom panel marks the 68% confidence interval of the systematic uncertainty $\sigma_{\rm sys} = -0.0033^{+0.0037}_{-0.0041}$.

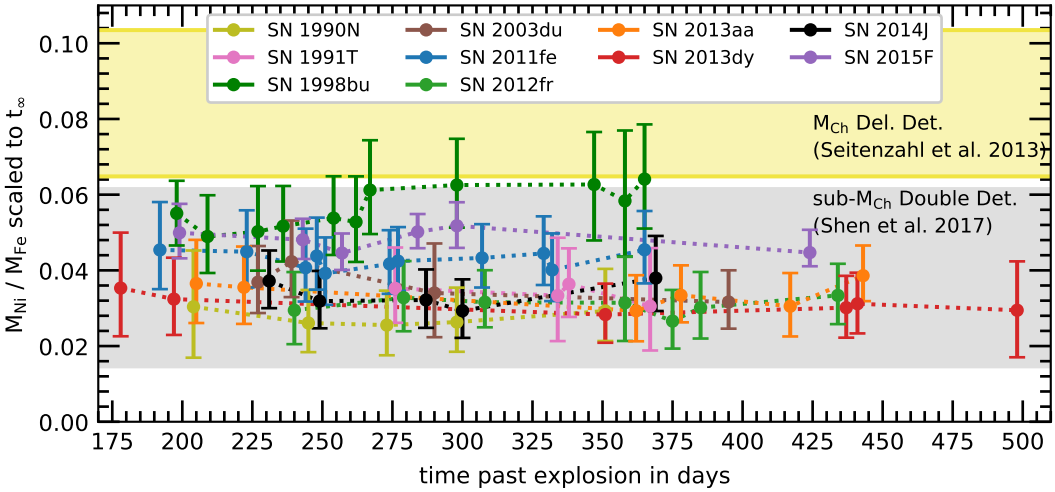

Figure C.6.: Inferred mass ratio of Ni and Fe for supernovae with multiple observations between $\sim$200 and 500 days after the explosion. Explosion model predictions and inferred data points were scaled to the Ni/Fe abundance at $t \to \infty$ to remove the time dependence of $M_{Fe}(t)$ in order to better illustrate the consistency of the method. We assume a rise time of $\sim$ 18 days (Ganeshalingam et al., 2011) to compute the time after explosion. Same colors indicate multiple observations of a supernova. Error bars represent the combined statistical fitting uncertainty and the systematic uncertainty from using the NIR/VIS relation if the spectrum only covers the optical wavelength region up to 10 000 Å.

Fe II emission is present. Additionally, the Fe II NIR/VIS relation as presented in this work is not just the result of a possible oversimplification of our one-zone model. It is obtained by effectively de-blending the lines of singly and doubly ionised iron, nickel and cobalt. It only depends on the total emission through the two lines. The assumed Gaussian line profile used in this work only has a marginal effect on the inferred values. More sophisticated explosion multi-zone models should be able to reproduce the relation by integrating the flux of the 12 570 Å and the 7 155 Å lines over all emitting regions.

Robustness of the Ni/Fe ratio

Fitting optical XShooter spectra with the Fe II NIR/VIS fit relation

We test for the presence of systematic effects arising from our method by applying it to the optical component of the Xshooter sample. The results of this comparison study (full spectrum vs optical only) in Fig. C.5. The use of the NIR/VIS relation as a prior does not imply that the posterior of the 12 570 Å to 7 155 Å line ratio for a given epoch t_i has the same width as the fit curve in Fig. C.3. In general, fitting the optical spectrum with the use of the NIR/VIS relation does not necessarily prefer the same ratio as fitting the full optical and NIR spectrum. As a result, we obtain different posteriors for the density and temperature for the two fitting methods. It seems that the optical is more sensitive to different regimes of the electron density and temperature than

the combined optical and NIR spectrum. On average, the use of the Fe II 12 570 Å to 7 155 Å fit relation instead of the NIR spectrum leads to a systematic difference of $\sigma_{\mathrm{sys}} = -0.0033^{+0.0037}_{-0.0041}$. The use of the NIR/VIS relation therefore results in mostly smaller $\mathrm{M_{Ni}} / \mathrm{M_{Fe}}$ ratios by about 0.0033 within the 68% confidence interval. We consider this a systematic uncertainty that adds to the statistical uncertainty linearly.

Time evolution of the Ni/Fe ratio

Even though the amount of ^{58}Ni produced in the explosion is fixed for a single object, the ratio of Ni/Fe changes with time (Fe being the daughter product of ^{56}Co decay, which at early times has not completely decayed yet). Only after $\sim$ 300 days ($4 \times \mathrm{t}_{1/2,^{56}\mathrm{Co}\rightarrow^{56}\mathrm{Fe}}$) the Ni/Fe ratio remains almost constant.

For supernovae that have several observations during the nebular phase we can test whether our modelling yields consistent Ni to Fe ratios (i.e. that the slope of the data points follows a single theoretical explosion model prediction). In Fig. C.6 we normalise the Ni to Fe to the value at $t = t_\infty$ to make it easier for the reader to see the slope of the measured data points. A flat series of data points indicates that the evolution with time behaves according to the expected yields from the radioactive decay of ^{56}Ni. For objects with both optical and near-infrared data the full spectrum is fit while for objects with optical data only the method described herein is used to provide the range and evolution of n_e and T.

The evolution of the Ni to Fe mass ratio for objects with multiple observations during the nebular phase is consistent with pure radioactive decay within the statistical uncertainties. A much shallower or steeper slope of the NIR/VIS ratio would lead to non-flat evolutionary curves of the Ni/Fe ratio. The only object that shows an evolution of the scaled Ni/Fe mass ratio is SN 1998bu. Roughly 270 days past its B-band maximum the inferred Ni/Fe mass ratio increases by about 15% and settles on this new value for the remaining observations. Such a behaviour could be the result of a light-echo contribution to the nebular spectrum, as was found for SN 1998bu by Cappellaro et al. (2001).

A possible contribution of Calcium at 7200 Å?

The method presented in Section *Methods* relies on the assumption that only [Fe II] and [Ni II] contribute to the 7 200 Å feature. If emission from another ion (e.g. Ca II]) contributes substantially to this feature, our measurement will be systematically wrong as the true contribution of Ni to the feature is lower than estimated from our model. Some NLTE radiative transfer calculations of SNe Ia in the nebular phase predict a non-negligible flux of Ca II] emission at $\lambda\lambda$ 7 291.5, 7 323.9 (Botyánszki & Kasen, 2017; Wilk et al., 2019). If the emitting region is a spherical shell at high velocities outside the iron core, the profile would be flat-topped. Such a plateau of Ca II] emission would raise the overall flux level in the 7 200 Å region without changing the characteristic double peaked shape of the feature.

We can test whether there is a contribution from other ions by fixing the strength of the Ni II 7 378 Å through the 19 390 Å line. The relative strength of the two lines only depends on the extinction and the ratio of the transition rates, as they originate from the same upper level:

$$\frac{F_{19\,390\,\text{Å}}}{F_{7\,378\,\text{Å}}} = \frac{A_{^2F_{7/2}-{}^4F_{9/2}}(E_{^2F_{7/2}} - E_{^4F_{9/2}})}{A_{^2F_{7/2}-{}^2D_{5/2}}(E_{^2F_{7/2}} - E_{^2D_{5/2}})} = 0.202 \tag{C.5}$$

The observed strength will depend on the extinction. Unfortunately, there is a strong telluric absorption band just bluewards of the 19 390 Å line of [Ni II]. The SNR in this region is only sufficiently high for a small number of objects in our XShooter sample. Dhawan et al. (2018) investigated the [Ni II] 19 390 Å line for the nearby SN 2014J.

The observations of SN 2015F, one of the closest SNe in the last decade, can be used to further verify this method. We obtained 5 nebular phase XShooter spectra between +181 and +406 days after B-band maximum. The first four epochs (+181, +225, +239, +266 days after maximum) are of exceptional quality and clearly show the 19 390 Å line. The observation at +406 days has a SNR that is insufficient to detect such a weak line, especially as it lies close to a telluric feature. SN 2017bzc was farther away than SN 2015F, but with an integration time of 10 080 s the [Ni II] 19 390 Å line can be seen in the +215 d spectrum.

An overview of the model fits for each of these spectra is shown in Fig. C.7. The 19 000 Å feature has not been used to compute the fits. A significant contribution of Ca II in the optical would lead to a much weaker 19 390Å line, which is in contradiction to our observations. A weak Ca II contribution cannot be ruled out but its effect on the Ni/Fe mass ratio would be very limited. None of the objects with sufficiently high SNR in the 19 000 Å region require any Ca II]. While it is not impossible that some SNe Ia – transitional objects such as the 86G-like or the faint 91bg-like – exhibit Calcium emission in the 7 200 Å region, the feature can be explained by only [Fe II] and [Ni II] for the normal and luminous population of SNe Ia (see also Graham et al., 2017).

$M_{Co/Fe}$ from the extended XShooter sample

The additional observations can be used to further the work described in Flörs et al. (2018). As has been noted by several authors (Maguire et al., 2018a; Flörs et al., 2018), the singly ionised lines of Fe, Ni and Co exhibit the same line shift and width. The same holds true for the two additional SNe with nebular phase XShooter observations presented in this work. It is therefore reasonable to assume that the singly ionised species are co-located in the ejecta and share the physical excitation conditions – temperature and density. Our updated model allows us to directly compute the Co to Fe mass ratio without having to use LTE approximations. The effect, however, is quite limited for the NIR lines in question ($< 5\%$).

Fig. C.8 displays a comparison of the new observations with the ones from Maguire et al. (2018a). We find that the three new objects (SN 2012ht, which was not included in the sample of Flörs et al. 2018, SN 2015F, SN 2017bzc) have a M_{Co} / M_{Fe} ratio that is consistent with sub-M_{Ch}

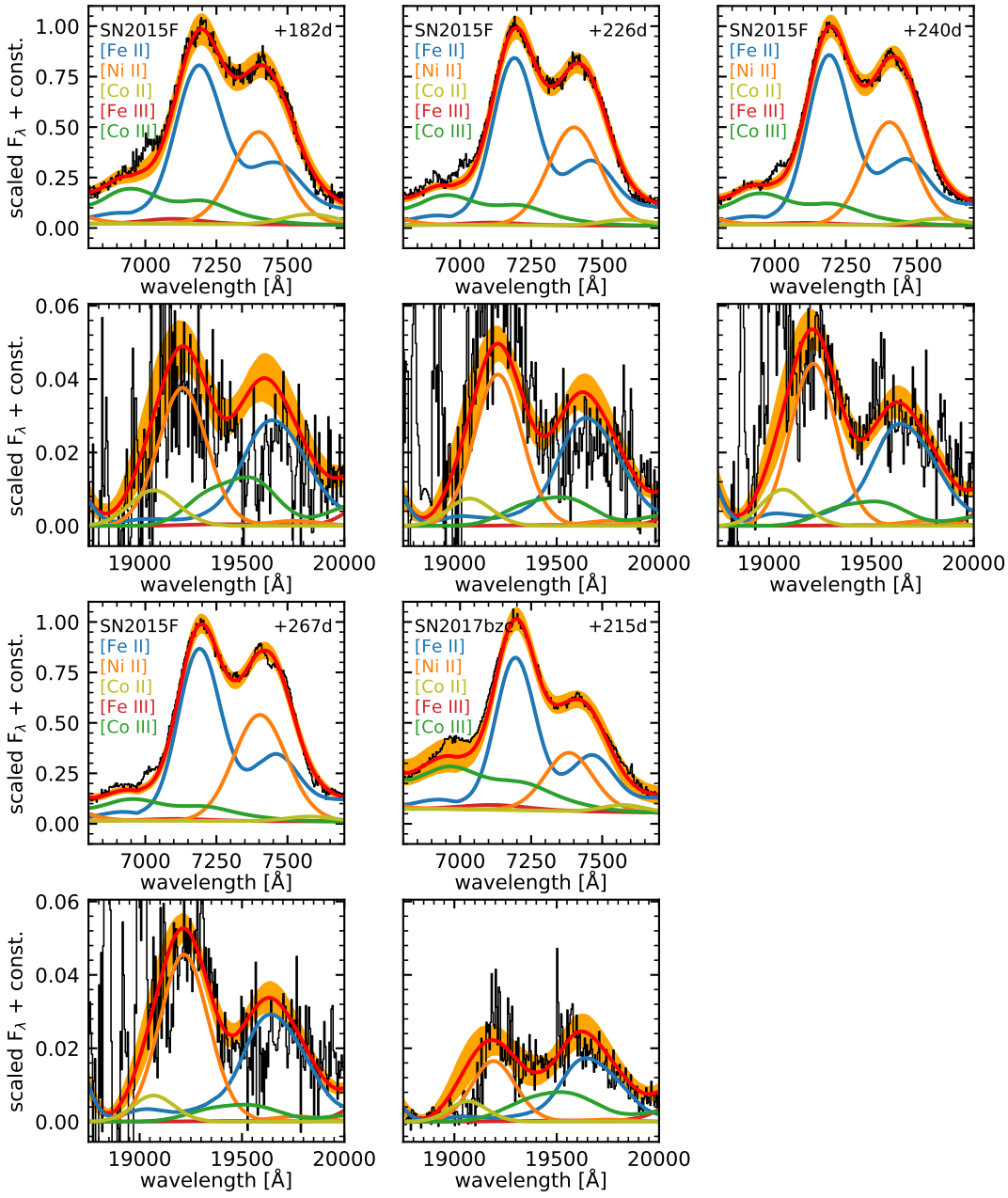

Figure C.7.: Comparison between the Fe II and Ni II dominated regions in the optical at 7 200 Å (top panel) and the NIR at 20 000 Å (bottom panel) for four observations of SN 2015F and one spectrum of SN 2017bzc. The Ni II lines at 7 378 Å and 19 390 Å originate in the same upper level $a^2F_{7/2}$ and have therefore a fixed line strength ratio that only depends on the ratio of their transition rates. For the atomic data adopted in this work the ratio of the 19 390 Å to the 7 378 Å line is 0.202. In the plots the ratio of the two Ni II emission features is different because of three effects: The optical Ni II feature is a blend of several lines, the flux density is lower at longer wavelengths and the ratio depends on galactic as well as host galaxy reddening. Regions of extremely low atmospheric transmission are shaded in grey.

explosions. Only the spectrum of SN 2012ht allows us to probe the ^{57}Ni content in the ejecta as all other spectra are significantly younger than 300 days. For them, the ratio instead is a measure of the fraction of stable iron (^{54,56}Fe) to radioactive iron (^{56}Ni decay products).

$M_{Ni/Fe}$ from archival optical spectra

The evolution of the NIR/VIS lines of Fe II allows us to model nebular spectra that cover only the optical wavelength range. We collected 130 spectra of 58 SNe Ia at epochs > 170 days after B-band maximum that have adequate SNR. A full list of all observations used for this study is given in Table C.5.

The spectra are modelled as described in Section *Methods*. For SNe which have multiple observations in the nebular phase we combine the inferred mass ratios. We report the inferred scaled Ni/Fe mass ratio in Table C.5. No corrections (e.g. fitting optical + NIR spectra vs only optical spectra; Section *Fitting optical XShooter spectra with the Fe* II *NIR/VIS fit relation*) have been applied to the inferred values. An overview of all objects (XShooter + archival) in our sample is given in Fig. C.9. We find that the majority of SNe exhibit Ni/Fe mass ratios below 0.05.

A similar study was conducted by Maguire et al. (2018a) for 8 objects in their XShooter sample. The same objects are also included in this work, however, a different method for the determination of the abundance ratio is used. Instead of modelling the full spectrum, Maguire et al. (2018a) restrict themselves to the 7 200 Å [Fe II] and [Ni II] dominated region. To convert the ratio of the LTE line fluxes to an abundance ratio of nickel and iron, they use average departure coefficients of a W7 model (Nomoto et al., 1984; Nomoto & Leung, 2018) at 330 days from Fransson & Jerkstrand (2015). As this model does not allow a determination of the temperature of the emitting material, Maguire et al. (2018a) assume temperatures similar to those of Fransson & Jerkstrand (2015) between 3 000 and 8 000 K.

The inferred abundance ratio of Ni and Fe from Maguire et al. (2018a) and this work deviate by about 1.5 σ for the same objects. The differences are mainly due to the placement of the (pseudo-)continuum across the 7 200 Å region, leading to a different line ratio of Fe II 7 155 Å and Ni II 7 378 Å. In this work we opted for a conservative continuum placement as most of it can be explained by a blend of weak lines of other singly and doubly ionised iron group ions (e.g. [Co III], [Fe III]). The departure coefficients corresponding to the allowed range of temperatures and densities (see Fig. C.4) of the emitting material are in good agreement with the ones used by Maguire et al. (2018a). The use of the Fe II NIR/VIS relation allows us to better constrain the allowed range of the physical parameters of the singly ionised ejecta, leading to reduced uncertainties compared to Maguire et al. (2018a). We want to emphasise that both works make use of the same atomic data for the ions in question.

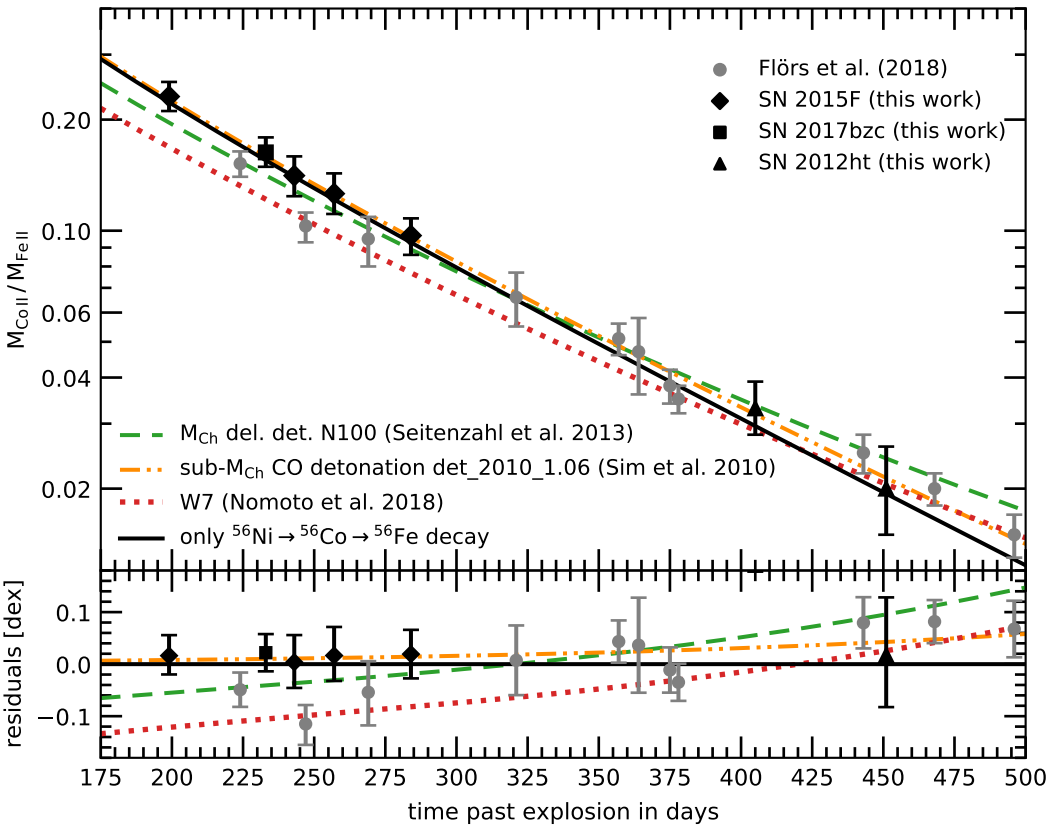

Figure C.8.: Evolution of the inferred $M_{Co\,II} / M_{Fe\,II}$ ratio with time for the extended XShooter sample. We assumed a rise time of 18 days (Ganeshalingam et al., 2011). The error bars reflect the 68% posterior interval of the mass ratio. The coloured lines show the expected mass ratio M_{Co} / M_{Fe} of the M_{Ch} delayed-detonation model 'N100' (Seitenzahl et al., 2013, green), the sub-M_{Ch} CO detonation model 'det_2010_1.06' (Sim et al., 2010, orange) and the M_{Ch} 'W7 $Z_{\odot}$' model (Nomoto & Leung, 2018, red). The black line is not a fit to the data and represents the M_{Co} / M_{Fe} ratio assuming only radioactive decay from ^{56}Ni to ^{56}Co to ^{56}Fe. Grey data points are from Flörs et al. (2018). Black data points are from the newly published objects in this work (SN 2015F and SN 2017bzc). The bottom panel shows the residuals normalised to the pure ^{56}Ni to ^{56}Co to ^{56}Fe decay.

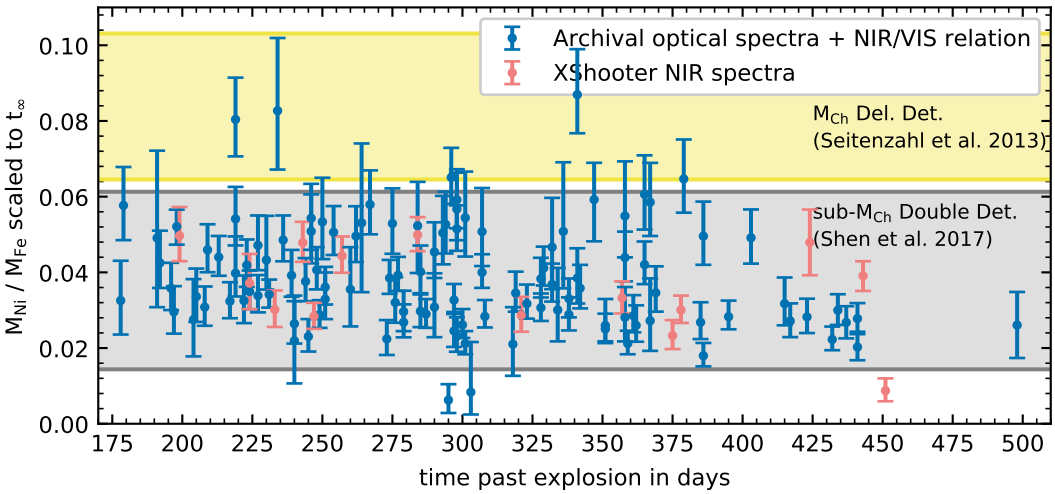

Figure C.9.: Inferred mass ratio of Ni and Fe from archival optical spectra and XShooter observations. Orange datapoints indicate that the Fe II NIR/VIS ratio was directly inferred from a spectrum covering 4,000–20,000 Å. Blue data points indicate optical nebular phase spectra that have been modelled using the relation from Fig. C.3 as a prior. Error bars only indicate the statistical uncertainty from the fit. We assume a rise time of $\sim$ 18 days (Ganeshalingam et al., 2011) to compute the time after explosion. The shaded bands display predictions of the Ni to Fe mass ratio from explosion model simulations (Seitenzahl et al., 2013; Shen et al., 2018). Inferred and predicted mass ratios were scaled to $t \to \infty$.

Implications on the explosion mechanism

The various theoretical explosion models of SNe Ia predict different amounts of neutron rich material. In M_{Ch} explosions the amount of synthesised neutron-rich material is determined by two processes: *Carbon simmering* and *neutron-rich burning*:

Carbon simmering occurs when a white dwarf accretes slowly towards the M_{Ch}. Densities and temperatures in the centre become high enough to ignite carbon, but no thermonuclear runaway happens due to a large convective core that allows for cooling through escaping neutrinos (Woosley et al., 2004; Wunsch & Woosley, 2004; Piro & Chang, 2008). The burning of carbon leads to mostly ^{13}N and ^{23}Na, which can subsequently capture electrons which further increases the neutron excess (Chamulak et al., 2008; Martínez-Rodríguez et al., 2016).

Neutron-rich burning to NSE can shift the equilibrium away from ^{56}Ni to more neutron-rich isotopes (^{54,56}Fe, ^{57,58}Ni, ^{55}Mn) (Iwamoto et al., 1999; Brachwitz et al., 2000). Just before the explosion, the high central density of the progenitor white dwarf leads to neutronisation through electron capture in the densest region. Neutron-rich NSE burning is only possible if there is a neutron excess in the NSE burning central region.

In sub-M_{Ch} models such processes are not possible as their progenitors cannot reach the required central density. However, an overabundance of neutrons in a high metallicity progenitor can still lead to the production of neutron-rich IGE (Timmes et al., 2003). The fraction of neutron rich to normal material can cover a wide range of values - from close to zero for $Z = Z_{\odot}$

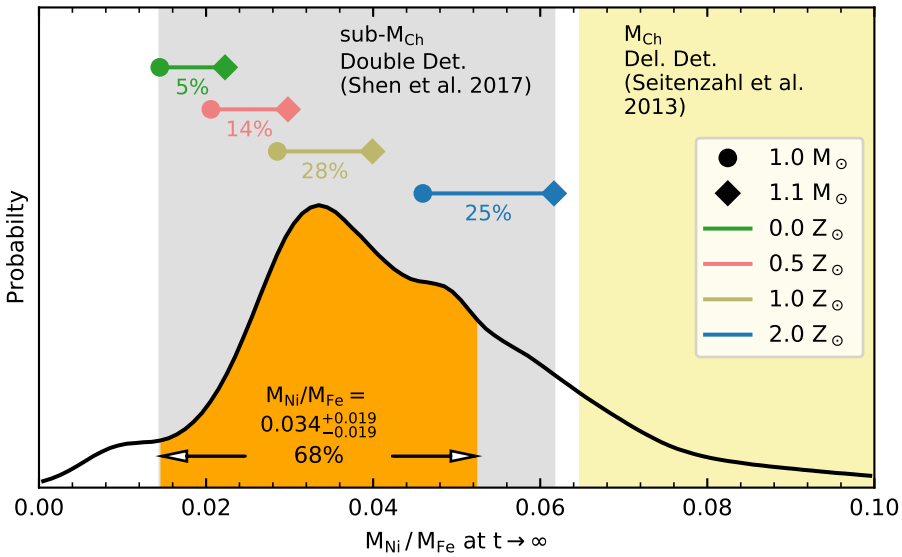

Figure C.10.: The distribution of the Ni/Fe ratio at $t \to \infty$ from all available nebular phase spectra (see Table C.5). The Ni/Fe ratio from only optical spectra was corrected according to Section *Fitting optical XShooter spectra with the Fe* II *NIR/VIS fit relation* by $\sigma_{\rm sys} = -0.0033^{+0.0037}_{-0.0041}$. The results for SNe with multiple observations were combined so that every supernova in the sample contributes equally to the shown distribution - irrespective of the number of spectra. For each unique SN we drew 100 000 samples from the posterior distribution of the Ni/Fe mass ratio. The orange shaded region indicates the region containing 68% of the posterior probability density. The shaded bands display predictions of the Ni to Fe mass ratio from sub-M_{Ch} (Shen et al., 2018, left) and M_{Ch} (Seitenzahl et al., 2013, right) explosion model simulations. For sub-M_{Ch} explosions we also show the range of models for 4 progenitor metallicities and their enclosed fraction of the posterior distribution of our sample.

to that of M_{Ch} explosions at several times solar metallicity (Shen et al., 2018). It remains to be seen whether such extremely-high metallicity progenitors really exist.

We focus on the neutron-rich, stable ^{58}Ni. The presence of a signature line close to 7 378 Å reveals that at least some amount of ^{58}Ni can be found in all normal SNe Ia observed so far. As shown in Fig. C.7 the 7 200 Å feature can be explained by a blend of mainly [Fe II] and [Ni II]. In principle there will also be varying amounts of stable iron produced during the explosion, but this contribution to the total iron mass is hard to disentangle from the overwhelming fraction of daughter products of radioactive ^{56}Co.

In contrast to the artificial W7 model (Nomoto et al., 1984), state-of-the-art explosion simulations from both the sub-M_{Ch} and M_{Ch} channels show that ^{58}Ni and ^{56}Ni are co-located in the ejecta and no spatial separation between ^{56}Ni and neutron-rich material is expected. Forbidden emission lines of Fe II and Ni II in nebular spectra of normal SNe Ia exhibit similar widths and shifts, pointing towards a shared emission region. If indeed no spatial separation between ^{58}Ni and ^{56}Ni occurs then the derived mass ratio of Fe II and Ni II should be representative for Fe/Ni.

The observed spectra are fit well with our emission model. By using the relation from Section *Calibration of Optical Spectra of SNe Ia* we can compute the Ni/Fe ratio. At early times the ratio is still evolving with time as not all the ^{56}Co has decayed to ^{56}Fe yet. At late times (¿250 days) the ratio remains constant. We find a large spread of Ni/Fe ratios, ranging from 0.02 to 0.08 within the 95% confidence interval. We do not find any objects for which we can exclude the contribution of Ni to the nebular phase spectrum.

Our results are in good agreement with sub-M_{Ch} explosions of solar- to super-solar metallicity progenitors. Only few objects have a Ni to Fe ratio that is consistent with explosion predictions from zero-metallicity sub-M_{Ch} white dwarfs. There are only few calculations of non-zero metallicity sub-M_{Ch} explosions (Sim et al., 2010; Shen et al., 2018). Our data are consistent with both sub-M_{Ch} detonations and double detonations, but they do not allow us to distinguish between these two scenarios.

We find a few objects which have Ni/Fe abundances consistent with nucleosynthetic predictions of exploding M_{Ch} white dwarfs. However, we do not find separate populations but instead the distribution displays a tail of objects which have high Ni/Fe abundances. The abundance distribution of objects which have nebular phase observations peaks at $M_{Ni} / M_{Fe} = 0.034$ with an 68% confidence region between 0.015 and 0.053. 85 % of the total probability density falls within the shaded band of sub-M_{Ch} explosion predictions. Our resulting distribution of the Ni/Fe abundance agrees well with the results of Kirby et al. (2019), who determined the Ni/Fe abundance from stellar populations of dwarf galaxies. Only 11 % of the total probability lies in the range of M_{Ch} delayed-detonation predictions. The presence of both channels is in agreement with findings from nearby SN remnants (Seitenzahl et al., 2019).

For sub-M_{Ch} we can compare our resulting distribution to explosion yields of progenitors with different masses and metallicities. Progenitors with masses of $0.9\,M_\odot$ or less do not produce enough ^{56}Ni ($< 0.3\,M_\odot$) to explain the brightness of normal SN Ia and are thus discarded for

this comparison. The overlap between the range of yields from 1.0 $M_\odot$ to 1.1 $M_\odot$ progenitors with our inferred Ni/Fe distribution is shown in Fig. C.10. We find good agreement with progenitors between 0.5 and 2 $Z_\odot$.

Conclusions

The 7 200 Å feature in nebular spectra of SNe Ia is composed of emission from Fe II and Ni II and is present in all objects for which this wavelength region has been observed. The relative contributions of the two ions to the feature vary between different SNe. We have presented a method that allows us to place prior constraints on the N_e and T and applied it to more than 100 optical archival spectra allowing us to determine the distribution of the Ni/Fe ratio for all objects in our sample. Our main results are:

i) The Fe II emission in the nebular phase can be described by purely thermal forbidden line emission, and it is in agreement with an expanding and cooling nebula.

ii) The strongest [Fe II] lines in the NIR and at optical wavelengths evolve with time, and the evolution seems to be very homogeneous across our sample. We obtained a relation that describes the evolution of this line ratio. The ratio does not depend on the atomic data. The evolution of the Fe II lines can be used to test more sophisticated spectral synthesis calculations of explosion model predictions – spectra that have been computed from explosion models need to be able to reproduce this relation.

iii) The 7 200 Å feature only contains Fe II and Ni II in normal SNe Ia. A contribution of Ca II] to this feature would have to be very limited in strength. We used the 19 390 Å line to constrain the 7 378 Å line for SN 2015F and SN 2017bzc as these two lines originate from the same upper level. We find no evidence that Ca II] emission is required to reproduce the 7 200 Å feature.

iv) For all objects in the extended sample of more than 100 nebular phase spectra we find that the lines of singly ionised Fe II and Ni II have similar widths and shifts and thus come from the same emitting region and share the same physical conditions. For objects for which NIR spectra are available we can extend this claim to Co II as well.

v) The display of 130 nebular phase spectra shows a large variety in the relative strengths of the Fe II and Ni II lines in the 7 200 Å feature. Translating the relative line strengths into a mass ratio of the singly ionised species results in a distribution which is expected from mainly sub-M_{Ch} explosions.

vi) We do not find separate populations of sub-M_{Ch} and M_{Ch} explosions. However, the high abundance tail of the distribution extends into the M_{Ch} regime. 11% of the total probability distribution lies within the M_{Ch} predictions of the Ni/Fe abundance.

VLT nebular spectra

Fig. C.11 presents previously unpublished spectra obtained at the VLT with the FORS2 spectrograph (PI: S. Taubenberger, programme ids: 086.D-0747, 087.D-0161, 088.D-0184, 090.D-0045). The spectra have been corrected for redshift and galactic extinction to better illustrate the position of the strongest Iron, Nickel and Cobalt lines (dashed vertical lines). Additional information on these observations can be found in Table C.5.

Overview of nebular spectra

In Table C.5, we provide the SN name, subtype, combined galactic and host galaxy colour excess, redshift and the date of B-band maximum for each SN Ia that is used in the analysis. Multiple observations of the same SN Ia are sorted by increasing epoch. We also show the telescope and instrument that was used to obtain the spectrum. The measured Ni/Fe mass ratio in the limit $t \to \infty$ is also given in Table C.5 for each spectrum.

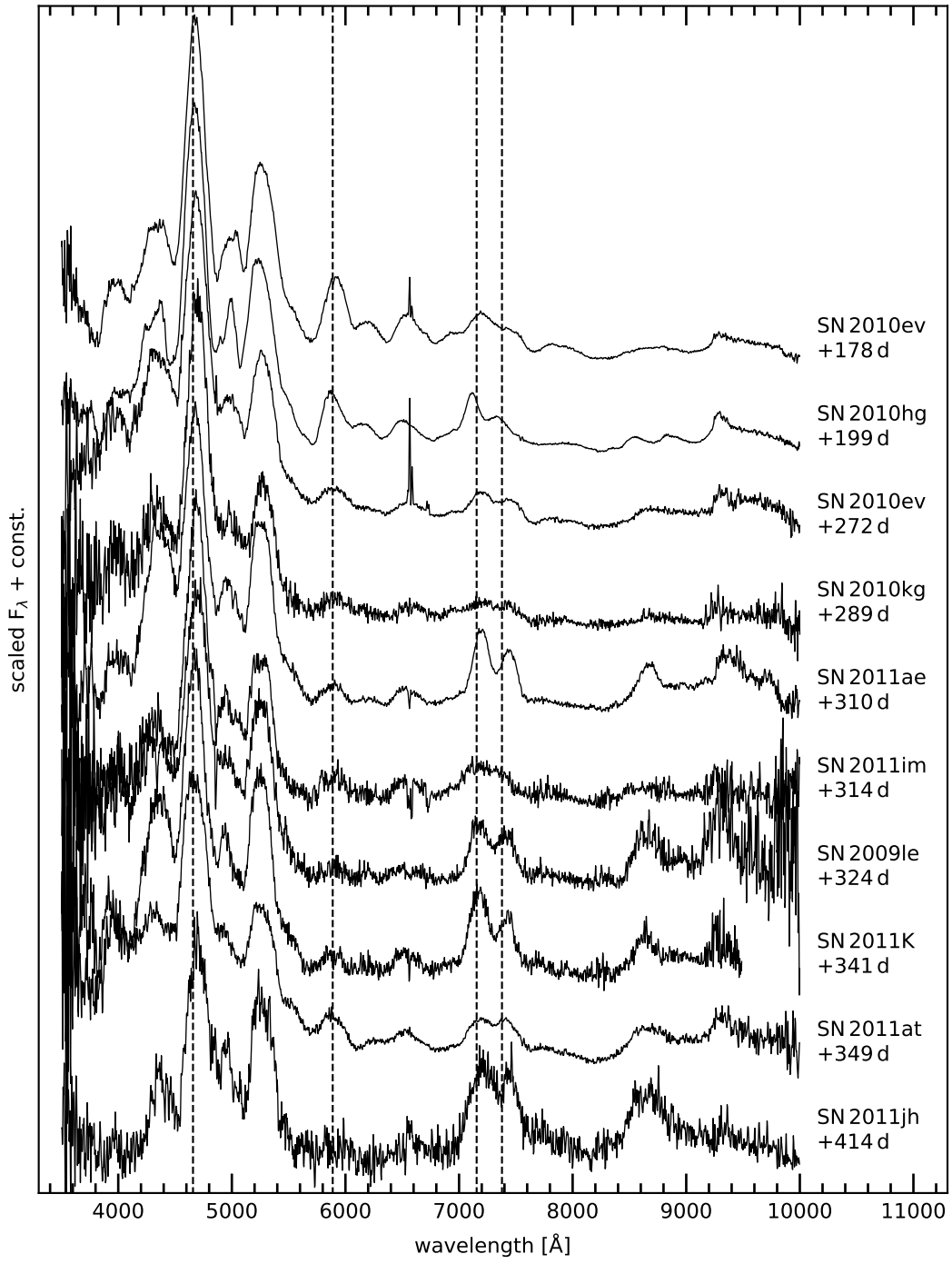

Figure C.11.: Spectra obtained at the VLT with FORS2 (PI: S. Taubenberger, programme ids: 086.D-0747, 087.D-0161, 088.D-0184, 090.D-0045). The rest wavelengths of the 4 659 Å [Fe III], the 5 888 Å [Co III], the 7 155 Å [Fe II] and the 7 378 Å [Ni II] lines are indicated as dashed lines.

Table C.5.: Overview of spectra observations.

Supernova	Subtype	E($B-V$) (mag)	z	Date of max.	Epoch	Telescope	Instrument	Ref Spec	Ref Ext	M_{Ni} / M_{Fe} ($t \to \infty$)
SN 1990N	Ia-norm	0.0223	0.003395	10 July 1990	+186	WHT-4.2m	FOS-2	1	-	$0.027^{+0.011}_{-0.010}$
					+227	WHT-4.2m	FOS-2	1		$0.023^{+0.006}_{-0.004}$
					+255	WHT-4.2m	FOS-2	1		$0.023^{+0.005}_{-0.004}$
					+280	WHT-4.2m	FOS-2	1		$0.023^{+0.005}_{-0.004}$
					+333	WHT-4.2m	FOS-2	1		$0.026^{+0.007}_{-0.004}$
SN 1991T	91T-like	0.16	0.005777	28 Apr 1991	+258	WHT-4.2m	ISIS	1	2	$0.032^{+0.007}_{-0.005}$
					+316	INT-2.5m	FOS	1		$0.031^{+0.011}_{-0.009}$
					+320.4	Lick-3m	KAST	3		$0.033^{+0.006}_{-0.006}$
					+349.4	Lick-3m	KAST	3		$0.027^{+0.011}_{-0.008}$
SN 1993Z	Ia-norm	0.0370	0.004503	28 Aug 1993	+201	Lick-3m	KAST	3	-	$0.040^{+0.010}_{-0.007}$
					+233	Lick-3m	KAST	3		$0.033^{+0.007}_{-0.006}$
SN 1994ae	Ia-norm	0.096	0.004266	29 Nov 1994	+368	MMT	MMT-Blue	4	5	$0.050^{+0.009}_{-0.008}$
SN 1995D	Ia-norm	0.0484	0.006561	20 Feb 1995	+276.8	MMT	MMT-Blue	4	-	$0.006^{+0.004}_{-0.004}$
					+284.7	MMT	MMT-Blue	4		$0.008^{+0.006}_{-0.006}$
SN 1996X	Ia-norm	0.0596	0.008876	18 Apr 1996	+246	ESO-1.5m	BC-ESO	6	-	$0.053^{+0.020}_{-0.018}$
SN 1998aq	Ia-norm	0.0122	0.003699	27 Apr 1998	+211.5	FLWO-1.5m	FAST	7	-	$0.043^{+0.012}_{-0.010}$
					+231.5	FLWO-1.5m	FAST	7		$0.052^{+0.012}_{-0.008}$
					+241.5	FLWO-1.5m	FAST	7		$0.037^{+0.011}_{-0.010}$
SN 1998bu	Ia-norm	0.34	0.002992	19 May 1998	+179.5	FLWO-1.5m	FAST	8	9	$0.052^{+0.005}_{-0.005}$
					+190.5	FLWO-1.5m	FAST	8		$0.046^{+0.007}_{-0.006}$
					+208.5	FLWO-1.5m	FAST	8		$0.047^{+0.008}_{-0.007}$
					+217.5	FLWO-1.5m	FAST	8		$0.049^{+0.007}_{-0.006}$
					+236.4	Lick-3m	KAST	3		$0.051^{+0.007}_{-0.006}$
					+243.5	FLWO-1.5m	FAST	8		$0.050^{+0.008}_{-0.007}$
					+249	Danish-1.54m	DFOSC	10		$0.058^{+0.009}_{-0.008}$
					+280.4	Lick-3m	KAST	3		$0.059^{+0.008}_{-0.008}$
					+329	ESO-3.6m	EFOSC2-3.6	10		$0.058^{+0.010}_{-0.011}$
					+340.3	Lick-3m	KAST	3		$0.055^{+0.015}_{-0.011}$
					+347.3	VLT	FORS1	11		$0.061^{+0.010}_{-0.009}$
SN 1999aa	91T-like	0.0342	0.014907	26 Feb 1999	+256.6	Keck1	LRIS	3	-	$0.053^{+0.009}_{-0.008}$
					+282.6	Keck1	LRIS	3		$0.055^{+0.012}_{-0.010}$
SN 2002bo	Ia-norm	0.53	0.0043	24 Mar 2002	+227.7	Keck2	ESI	3	12	$0.051^{+0.010}_{-0.009}$
SN 2002cs	Ia-norm	0.088	0.015771	16 May 2002	+174.2	Keck2	ESI	3	-	$0.059^{+0.018}_{-0.017}$
SN 2002dj	Ia-norm	0.096	0.009393	24 Jun 2002	+222	ESO-NTT	EFOSC2-NTT	13	13	$0.046^{+0.012}_{-0.011}$
					+275	VLT-UT1	FORS1	13		$0.051^{+0.010}_{-0.008}$
SN 2002er	Ia-norm	0.36	0.009063	06 Sept 2002	+216	TNG	DOLORES	14	15	$0.083^{+0.019}_{-0.016}$
SN 2003cg	Ia-norm	1.33	0.004113	31 Mar 2003	+385	VLT-UT1	FORS2	16	16	$0.049^{+0.008}_{-0.007}$
SN 2003du	Ia-norm	0.0081	0.006408	06 May 2003	+209	CA-3.5m	MOSCA	17	-	$0.034^{+0.005}_{-0.005}$
					+221	CA-2.2m	CAFOS	17		$0.039^{+0.007}_{-0.006}$
					+272	CA-3.5m	MOSCA	17		$0.031^{+0.009}_{-0.008}$
					+377	TNG	DOLORES	17		$0.028^{+0.004}_{-0.004}$
SN 2003gs	Ia-norm	0.066	0.004770	28 July 2003	+201	Keck2	ESI	3	18	$0.054^{+0.008}_{-0.007}$
SN 2003hv	Ia-norm	0.0133	0.005624	06 Sept 2003	+323	VLT-UT1	FORS2	19	-	$0.087^{+0.012}_{-0.010}$
SN 2003kf	Ia-norm	0.269	0.007388	11 Dez 2003	+397.3	Magellan-Clay	LDSS-2	4	-	$0.032^{+0.007}_{-0.006}$
SN 2004bv	91T-like	0.0546	0.010614	17 May 2004	+161	Keck1	LRIS	3	-	$0.058^{+0.010}_{-0.009}$
SN 2004eo	Ia-norm	0.093	0.015718	30 Sept 2004	+228	VLT-UT1	FORS2	20	-	$0.055^{+0.009}_{-0.008}$
SN 2005cf	Ia-norm	0.20	0.006461	12 Jun 2005	+267	Gemini-N	GMOS	21	22	$0.030^{+0.005}_{-0.005}$
					+319.6	Keck1	LRIS	22		$0.029^{+0.006}_{-0.005}$
SN 2006dd	Ia-norm	0.083	0.005871	03 July 2006	+195	LCO-duPont	WFCCD	23	23	$0.044^{+0.006}_{-0.005}$
SN 2006X	Ia-norm	1.46	0.005294	19 Feb 2006	+277.6	Keck1	LRIS	24	12	$0.065^{+0.008}_{-0.007}$
					+360.5	Keck1	LRIS	3		$0.063^{+0.010}_{-0.009}$
SN 2007af	Ia-norm	0.181	0.005464	16 Mar 2007	+301	MMT	MMT-Blue	4	12	$0.035^{+0.006}_{-0.005}$
SN 2007le	Ia-norm	0.40	0.006721	27 Oct 2007	+304.7	Keck1	LRIS	3	12	$0.032^{+0.005}_{-0.005}$
SN 2007sr	Ia-norm	0.17	0.005477	16 Dez 2007	+190	Magellan-Clay	LDSS-3	4	-	$0.031^{+0.006}_{-0.005}$
SN 2008Q	Ia-norm	0.0716	0.008016	09 Feb 2008	+201.1	Keck1	LRIS	3	-	$0.081^{+0.011}_{-0.010}$
SN 2009ig	Ia-norm	0.049	0.008770	06 Sept 2009	+405	VLT-UT1	FORS2	25	12	$0.028^{+0.005}_{-0.005}$
SN 2009le	Ia-norm	0.111	0.017786	26 Nov 2009	+324	VLT-UT1	FORS2	TW	12	$0.036^{+0.006}_{-0.005}$
SN 2010ev	Ia-norm	0.41	0.009211	05 July 2010	+178	VLT-UT1	FORS2	TW	12	$0.038^{+0.008}_{-0.007}$
					+272	VLT-UT1	FORS2	TW		$0.044^{+0.007}_{-0.006}$
SN 2010gp	Ia-norm	0.21	0.024480	25 July 2010	+279	VLT-UT1	FORS2	25	26	$0.033^{+0.005}_{-0.005}$
SN 2010hg	Ia-norm	0.101	0.008219	15 Sept 2010	+199	VLT-UT1	FORS2	TW	-	$0.033^{+0.005}_{-0.006}$
SN 2010kg	Ia-norm	0.130	0.016642	11 Dec 2010	+289	VLT-UT1	FORS2	TW	-	$0.051^{+0.012}_{-0.009}$

Table C.5.: Overview of spectra observations.

Supernova	Subtype	E($B-V$) (mag)	z	Date of max.	Epoch	Telescope	Instrument	Ref Spec	Ref Ext	M_{Ni} / M_{Fe} ($t \to \infty$)
SN 2011ae	Ia-norm	0.0483	0.006046	24 Feb 2011	+310	VLT-UT1	FORS2	TW	-	$0.031^{+0.005}_{-0.005}$
SN 2011at	Ia-norm	0.0585	0.006758	14 Mar 2011	+349	VLT-UT1	FORS2	TW	-	$0.059^{+0.010}_{-0.009}$
SN 2011by	Ia-norm	0.0119	0.002843	10 May 2011	+206	Keck1	LRIS	27	-	$0.035^{+0.006}_{-0.005}$
					+310	Keck1	LRIS	27		$0.039^{+0.006}_{-0.006}$
SN 2011ek	Ia-norm	0.306	0.005027	14 Aug 2011	+423	VLT-UT1	FORS2	25	-	$0.020^{+0.005}_{-0.006}$
SN 2011fe	Ia-norm	0.10	0.000804	10 Sept 2011	+174	WHT-4.2m	ISIS	28	12	$0.043^{+0.009}_{-0.007}$
					+205	Lick-3m	KAST	28		$0.042^{+0.006}_{-0.006}$
					+226	Lick-3m	KAST	28		$0.038^{+0.006}_{-0.005}$
					+230	LBT	MODS1	28		$0.041^{+0.006}_{-0.005}$
					+233	Lijiang-2.4m	YFOSC	29		$0.036^{+0.005}_{-0.005}$
					+256	WHT-4.2m	ISIS	30		$0.039^{+0.005}_{-0.005}$
					+259	WHT-4.2m	ISIS	28		$0.039^{+0.005}_{-0.005}$
					+289	WHT-4.2m	ISIS	28		$0.040^{+0.005}_{-0.005}$
					+311	Lick-3m	KAST	28		$0.041^{+0.006}_{-0.005}$
					+314	GTC	OSIRIS	31		$0.047^{+0.006}_{-0.006}$
					+347	WHT-4.2m	ISIS	28		$0.042^{+0.006}_{-0.006}$
SN 2011im	Ia-norm	0.0556	0.016228	06 Dec 2011	+314	VLT-UT1	FORS2	TW	-	$0.047^{+0.013}_{-0.011}$
SN 2011iv	Ia-norm	0.0098	0.006494	10 Dec 2011	+318	VLT-UT1	FORS2	25	-	$0.051^{+0.018}_{-0.015}$
SN 2011jh	Ia-norm	0.0322	0.007789	03 Jan 2012	+414	VLT-UT1	FORS2	TW	-	$0.022^{+0.005}_{-0.006}$
SN 2011K	Ia-norm	0.0852	0.014891	20 Jan 2012	+341	VLT-UT1	FORS2	TW	-	$0.021^{+0.006}_{-0.005}$
SN 2012cg	Ia-norm	0.20	0.001458	03 Jun 2012	+279	Keck1	LRIS	30	32	$0.025^{+0.005}_{-0.005}$
					+339	VLT-UT2	XShooter	33		$0.033^{+0.006}_{-0.006}$
					+343	VLT-UT1	FORS2	25		$0.029^{+0.006}_{-0.005}$
SN 2012cu	Ia-norm	1.02	0.003469	27 Jun 2012	+340	VLT-UT1	FORS2	25	30	$0.044^{+0.007}_{-0.006}$
SN 2012fr	Ia-norm	0.0177	0.005457	12 Nov 2012	+222	ANU-2.3m	WiFeS	34	-	$0.027^{+0.006}_{-0.005}$
					+261	ANU-2.3m	WiFeS	34		$0.030^{+0.006}_{-0.005}$
					+290	Gemini-S	GMOS-S	35		$0.028^{+0.005}_{-0.005}$
					+340	SALT	RSS	34		$0.028^{+0.008}_{-0.007}$
					+357	VLT-UT2	XShooter	33		$0.023^{+0.005}_{-0.005}$
					+367	ANU-2.3m	WiFeS	34		$0.027^{+0.005}_{-0.006}$
					+416	Gemini-S	GMOS-S	35		$0.030^{+0.007}_{-0.006}$
SN 2012hr	Ia-norm	0.0389	0.007562	27 Dec 2012	+283	Gemini-S	GMOS-S	34	-	$0.021^{+0.006}_{-0.006}$
					+368	ANU-2.3m	WiFeS	34		$0.018^{+0.007}_{-0.006}$
SN 2012ht	Ia-norm	0.0252	0.003556	03 Jan 2013	+433	VLT-UT2	XShooter	33	-	$0.009^{+0.004}_{-0.004}$
SN 2013aa	Ia-norm	0.1458	0.003999	21 Feb 2013	+187	SALT	RSS	34	-	$0.034^{+0.007}_{-0.007}$
					+204	ANU-2.3m	WiFeS	34		$0.033^{+0.007}_{-0.006}$
					+344	ANU-2.3m	WiFeS	34		$0.026^{+0.005}_{-0.005}$
					+360	VLT-UT2	XShooter	33		$0.030^{+0.006}_{-0.006}$
					+399	Gemini-S	GMOS-S	35		$0.027^{+0.005}_{-0.006}$
					+425	VLT-UT2	XShooter	33		$0.039^{+0.006}_{-0.006}$
SN 2013cs	Ia-norm	0.0788	0.009243	26 May 2013	+261	Gemini-S	GMOS-S	35	-	$0.027^{+0.005}_{-0.006}$
					+300	ANU-2.3m	WiFeS	34		$0.022^{+0.010}_{-0.008}$
					+303	VLT-UT2	XShooter	33		$0.029^{+0.006}_{-0.005}$
SN 2013ct	Ia-norm	0.0244	0.003843	04 Apr 2013	+229	VLT-UT2	XShooter	33	-	$0.029^{+0.006}_{-0.006}$
SN 2013dy	Ia-norm	0.338	0.003889	28 July 2013	+160	Lijiang-2.4m	YFOSC	29	36	$0.033^{+0.011}_{-0.009}$
					+179	Lijiang-2.4m	YFOSC	29		$0.030^{+0.007}_{-0.006}$
					+333	Keck2	DEIMOS	36		$0.025^{+0.005}_{-0.005}$
					+419	Keck2	DEIMOS	34		$0.027^{+0.004}_{-0.005}$
					+423	Keck1	LRIS	36		$0.028^{+0.005}_{-0.006}$
					+480	Keck1	LRIS	36		$0.026^{+0.009}_{-0.009}$
SN 2013gy	Ia-norm	0.155	0.014023	18 Dec 2013	+276	Keck2	DEIMOS	34	37	$0.053^{+0.009}_{-0.008}$
					+280	Keck1	LRIS	35		$0.057^{+0.010}_{-0.008}$
SN 2014J	Ia-norm	1.43	0.000677	01 Feb 2014	+212.5	WHT-4.2m	ACAM	38	39	$0.034^{+0.004}_{-0.005}$
					+231	Keck2	DEIMOS	34		$0.029^{+0.005}_{-0.005}$
					+269	HCT-2m	HFOSC	40		$0.029^{+0.005}_{-0.004}$
					+282	ARC 3.5m	DIS	30		$0.026^{+0.005}_{-0.006}$
					+351	HCT-2m	HFOSC	40		$0.033^{+0.007}_{-0.006}$
ASASSN-14jg	Ia-norm	0.0128	0.0148	31 Oct 2014	+267	Gemini-S	GMOS-S	35	-	$0.041^{+0.007}_{-0.006}$
					+323	VLT-UT2	XShooter	33		$0.039^{+.008}_{-0.007}$
ASASSN-15be	Ia-norm	0.17	0.0219	29 Jan 2015	+266	VLT-UT2	XShooter	33	-	$0.053^{+0.012}_{-0.013}$

Table C.5.: Overview of spectra observations.

Supernova	Subtype	E($B-V$) (mag)	z	Date of max.	Epoch	Telescope	Instrument	Ref Spec	Ref Ext	M_{Ni} / M_{Fe} ($t \to \infty$)
SN 2015F	Ia-norm	0.26	0.00489	25 Mar 2015	+181	VLT-UT2	XShooter	TW	41	$0.050^{+0.008}_{-0.007}$
					+225	VLT-UT2	XShooter	TW		$0.048^{+0.006}_{-0.005}$
					+239	VLT-UT2	XShooter	TW		$0.045^{+0.005}_{-0.005}$
					+266	VLT-UT2	XShooter	TW		$0.050^{+0.005}_{-0.004}$
					+280	Gemini-S	GMOS-S	35		$0.052^{+0.006}_{-0.006}$
					+406	VLT-UT2	XShooter	TW		$0.049^{+0.009}_{-0.009}$
PSNJ1149	Ia-norm	0.0247	0.005589	11 July 2015	+206	VLT-UT2	XShooter	33	-	$0.037^{+0.008}_{-0.007}$
SN 2017bzc	Ia-norm	0.0122	0.00536	14 Mar 2015	+215	VLT-UT2	XShooter	TW	-	$0.030^{+0.005}_{-0.005}$

References:
(1) Gómez & López (1998); (2) Phillips et al. (1999); (3) Silverman et al. (2012a);
(4) Blondin et al. (2012); (5) Wang et al. (1996); (6) Salvo et al. (2001);
(7) Branch et al. (2003); (8) Matheson et al. (2008); (9) Jha et al. (1999);
(10) Cappellaro et al. (2001); (11) Spyromilio et al. (2004); (12) Phillips et al. (2013);
(13) Pignata et al. (2008); (14) Kotak et al. (2005); (15) Pignata et al. (2004);
(16) Elias-Rosa et al. (2006); (17) Stanishev et al. (2007); (18) Krisciunas et al. (2009);
(19) Leloudas et al. (2009); (20) Pastorello et al. (2007); (21) Leonard (2007);
(22) Wang et al. (2009); (23) Stritzinger et al. (2010); (24) Wang et al. (2008);
(25) Maguire et al. (2016); (26) Miluzio et al. (2013); (27) Graham et al. (2015);
(28) Mazzali et al. (2015); (29) Zhang et al. (2016); (30) Amanullah et al. (2015);
(31) Taubenberger et al. (2015); (32) Silverman et al. (2012b); (33) Maguire et al. (2018a);
(34) Childress et al. (2015); (35) Graham et al. (2017); (36) Pan et al. (2015);
(37) Holmbo et al. (2019); (38) Galbany et al. (2016); (39) Amanullah et al. (2014);
(40) Srivastav et al. (2016); (41) Cartier et al. (2017); TW: This Work

Bibliography

Abbott, B. P., Abbott, R., Abbott, T. D., et al. 2017, Phys. Rev. Lett., 119, 161101, [1710.05832], [ADS], [DOI]

Althaus, L. G., García-Berro, E., Renedo, I., et al. 2010, ApJ, 719, 612, [1006.4170], [ADS], [DOI]

Amanullah, R., Goobar, A., Johansson, J., et al. 2014, ApJ, 788, L21, [1404.2595], [ADS], [DOI]

Amanullah, R., Johansson, J., Goobar, A., et al. 2015, MNRAS, 453, 3300, [1504.02101], [ADS], [DOI]

Ambwani, K. & Sutherland, P. 1988, ApJ, 325, 820, [ADS], [DOI]

Antonini, F. & Perets, H. B. 2012, ApJ, 757, 27, [1203.2938], [ADS], [DOI]

Arcones, A., Martínez-Pinedo, G., Roberts, L. F., & Woosley, S. E. 2010, A&A, 522, A25, [1002.3854], [ADS], [DOI]

Arnett, W. D. 1969, Ap&SS, 5, 180, [ADS], [DOI]

Arnett, W. D. 1982, ApJ, 253, 785, [ADS], [DOI]

Arnett, W. D., Bahcall, J. N., Kirshner, R. P., & Woosley, S. E. 1989, ARA&A, 27, 629, [ADS], [DOI]

Ashall, C., Mazzali, P., Bersier, D., et al. 2014, MNRAS, 445, 4427, [1409.7066], [ADS], [DOI]

Axelrod, T. S. 1980, PhD thesis, California Univ., Santa Cruz., [ADS]

Baade, W. 1938, ApJ, 88, 285, [ADS], [DOI]

Baade, W. 1943, ApJ, 97, 119, [ADS], [DOI]

Baade, W. & Zwicky, F. 1934, Proceedings of the National Academy of Science, 20, 254, [ADS], [DOI]

Badenes, C., Bravo, E., & Hughes, J. P. 2008, ApJ, 680, L33, [0805.3344], [ADS], [DOI]

Baron, E., Hauschildt, P. H., Nugent, P., & Branch, D. 1996, MNRAS, 283, 297, [ADS], [DOI]

Bautista, M. A., Fivet, V., Ballance, C., et al. 2015, ApJ, 808, 174, [ADS], [DOI]

Bé, M.-M., Chisté, V., Dulieu, C., et al. 2006, Monographie BIPM-5, Vol. 3, Table of Radionuclides (Pavillon de Breteuil, F-92310 Sèvres, France: Bureau International des Poids et Mesures)

Bé, M.-M., Chisté, V., Dulieu, C., et al. 2004, Monographie BIPM-5, Vol. 1, Table of Radionuclides (Pavillon de Breteuil, F-92310 Sèvres, France: Bureau International des Poids et Mesures)

Benz, W., Hills, J. G., & Thielemann, F. K. 1989, ApJ, 342, 986, [ADS], [DOI]

Bildsten, L., Shen, K. J., Weinberg, N. N., & Nelemans, G. 2007, ApJ, 662, L95, [astro-ph/0703578], [ADS], [DOI]

Black, C. S., Fesen, R. A., & Parrent, J. T. 2016, MNRAS, 462, 649, [1604.01044], [ADS], [DOI]
Blinnikov, S. I. & Khokhlov, A. M. 1986, Soviet Astronomy Letters, 12, 131, [ADS]
Blinnikov, S. I. & Khokhlov, A. M. 1987, Soviet Astronomy Letters, 13, 364, [ADS]
Blondin, S., Dessart, L., & Hillier, D. J. 2018, MNRAS, 474, 3931, [1711.09107], [ADS], [DOI]
Blondin, S., Dessart, L., Hillier, D. J., & Khokhlov, A. M. 2013, MNRAS, 429, 2127, [1211.5892], [ADS], [DOI]
Blondin, S., Dessart, L., Hillier, D. J., & Khokhlov, A. M. 2017, MNRAS, 470, 157, [1706.01901], [ADS], [DOI]
Blondin, S., Matheson, T., Kirshner, R. P., et al. 2012, AJ, 143, 126, [1203.4832], [ADS], [DOI]
Bloom, J. S., Kasen, D., Shen, K. J., et al. 2012, ApJ, 744, L17, [1111.0966], [ADS], [DOI]
Borkowski, K. J., Reynolds, S. P., & Roberts, M. S. E. 2016, ApJ, 819, 160, [1602.03531], [ADS], [DOI]
Botyánszki, J. & Kasen, D. 2017, ApJ, 845, 176, [1704.06275], [ADS], [DOI]
Bowers, E. J. C., Meikle, W. P. S., Geballe, T. R., et al. 1997, MNRAS, 290, 663, [astro-ph/9707119], [ADS], [DOI]
Brachwitz, F., Dean, D. J., Hix, W. R., et al. 2000, ApJ, 536, 934, [astro-ph/0001464], [ADS], [DOI]
Branch, D., Dang, L. C., Hall, N., et al. 2006, PASP, 118, 560, [astro-ph/0601048], [ADS], [DOI]
Branch, D., Fisher, A., & Nugent, P. 1993, AJ, 106, 2383, [ADS], [DOI]
Branch, D., Garnavich, P., Matheson, T., et al. 2003, AJ, 126, 1489, [astro-ph/0305321], [ADS], [DOI]
Branch, D., Romanishin, W., & Baron, E. 1996, ApJ, 467, 473, [ADS], [DOI]
Branch, D. & Tammann, G. A. 1992, ARA&A, 30, 359, [ADS], [DOI]
Brandt, T. D., Tojeiro, R., Aubourg, É., et al. 2010, AJ, 140, 804, [1002.0848], [ADS], [DOI]
Brecher, K., Lieber, E., & Lieber, A. E. 1978, Archaeoastronomy, 1, 4, [ADS]
Brown, P. J., Smitka, M. T., Wang, L., et al. 2015, ApJ, 805, 74, [1408.2381], [ADS], [DOI]
Bulla, M., Goobar, A., Amanullah, R., Feindt, U., & Ferretti, R. 2018, MNRAS, 473, 1918, [1707.00696], [ADS], [DOI]
Bulla, M., Sim, S. A., Kromer, M., et al. 2016a, MNRAS, 462, 1039, [1607.04081], [ADS], [DOI]
Bulla, M., Sim, S. A., Pakmor, R., et al. 2016b, MNRAS, 455, 1060, [1510.04128], [ADS], [DOI]
Burns, C. R., Stritzinger, M., Phillips, M. M., et al. 2014, ApJ, 789, 32, [1405.3934], [ADS], [DOI]
Camilo, F., Stairs, I. H., Lorimer, D. R., et al. 2002, ApJ, 571, L41, [astro-ph/0204219], [ADS], [DOI]
Cappellaro, E., Patat, F., Mazzali, P. A., et al. 2001, ApJ, 549, L215, [astro-ph/0101342], [ADS], [DOI]
Cardelli, J. A., Clayton, G. C., & Mathis, J. S. 1989, ApJ, 345, 245, [ADS], [DOI]
Cartier, R., Sullivan, M., Firth, R. E., et al. 2017, MNRAS, 464, 4476, [1609.04465], [ADS], [DOI]
Cassidy, C. M., Hibbert, A., & Ramsbottom, C. A. 2016a, A&A, 587, A107, [ADS], [DOI]
Cassidy, C. M., Hibbert, A., & Ramsbottom, C. A. 2016b, A&A, 587, A107, [ADS], [DOI]
Cassidy, C. M., Ramsbottom, C. A., Scott, M. P., & Burke, P. G. 2010a, A&A, 513, A55, [ADS], [DOI]

Cassidy, C. M., Ramsbottom, C. A., Scott, M. P., & Burke, P. G. 2010b, A&A, 513, A55, [ADS], [DOI]

Caughlan, G. R. & Fowler, W. A. 1988, Atomic Data and Nuclear Data Tables, 40, 283, [ADS], [DOI]

Chakradhari, N. K., Sahu, D. K., Srivastav, S., & Anupama, G. C. 2014, MNRAS, 443, 1663, [1406.6139], [ADS], [DOI]

Chambers, K. C., Magnier, E. A., Metcalfe, N., et al. 2016, arXiv e-prints, arXiv:1612.05560, [1612.05560], [ADS]

Chamulak, D. A., Brown, E. F., Timmes, F. X., & Dupczak, K. 2008, ApJ, 677, 160, [0801.1643], [ADS], [DOI]

Chandrasekhar, S. 1931, ApJ, 74, 81, [ADS], [DOI]

Chandrasekhar, S. 1935, MNRAS, 95, 207, [ADS], [DOI]

Chen, X., Han, Z., & Tout, C. A. 2011, ApJ, 735, L31, [1106.1252], [ADS], [DOI]

Chevalier, R. A. 1982a, ApJ, 259, L85, [ADS], [DOI]

Chevalier, R. A. 1982b, ApJ, 259, 302, [ADS], [DOI]

Chevalier, R. A. 1998, ApJ, 499, 810, [ADS], [DOI]

Chevalier, R. A. & Fransson, C. 2006, ApJ, 651, 381, [astro-ph/0607196], [ADS], [DOI]

Childress, M. J., Hillier, D. J., Seitenzahl, I., et al. 2015, MNRAS, 454, 3816, [1507.02501], [ADS], [DOI]

Churazov, E., Sunyaev, R., Isern, J., et al. 2015, ApJ, 812, 62, [1502.00255], [ADS], [DOI]

Churazov, E., Sunyaev, R., Isern, J., et al. 2014, Nature, 512, 406, [1405.3332], [ADS], [DOI]

Clark, D. H. & Stephenson, F. R. 1975, The Observatory, 95, 190, [ADS]

Clifford, F. E. & Tayler, R. J. 1965, MmRAS, 69, 21, [ADS]

Colgate, S. A. & McKee, C. 1969, ApJ, 157, 623, [ADS], [DOI]

Colgate, S. A., Petschek, A. G., & Kriese, J. T. 1980, ApJ, 237, L81, [ADS], [DOI]

Conley, A., Sullivan, M., Hsiao, E. Y., et al. 2008, ApJ, 681, 482, [0803.3441], [ADS], [DOI]

Cormier, D. & Davis, T. M. 2011, MNRAS, 410, 2137, [ADS], [DOI]

Cox, A. 2000, Allen's astrophysical quantities; 4th ed. (New York, NY: AIP), [DOI]

Cristiani, S., Cappellaro, E., Turatto, M., et al. 1992, A&A, 259, 63, [ADS]

Czekala, I., Andrews, S. M., Mandel, K. S., Hogg, D. W., & Green, G. M. 2015, ApJ, 812, 128, [1412.5177], [ADS], [DOI]

Dan, M., Guillochon, J., Brüggen, M., Ramirez-Ruiz, E., & Rosswog, S. 2015, MNRAS, 454, 4411, [1508.02402], [ADS], [DOI]

Dan, M., Rosswog, S., Guillochon, J., & Ramirez-Ruiz, E. 2011, ApJ, 737, 89, [1101.5132], [ADS], [DOI]

Darnley, M. J., Henze, M., Steele, I. A., et al. 2015, A&A, 580, A45, [1506.04202], [ADS], [DOI]

De, S., Timmes, F. X., Brown, E. F., et al. 2014, ApJ, 787, 149, [1304.4942], [ADS], [DOI]

de Vaucouleurs, G. & Corwin, H. G., J. 1985, ApJ, 295, 287, [ADS], [DOI]

Deloye, C. J. & Bildsten, L. 2002, ApJ, 580, 1077, [astro-ph/0207623], [ADS], [DOI]

Deng, J., Kawabata, K. S., Ohyama, Y., et al. 2004, ApJ, 605, L37, [astro-ph/0311590], [ADS], [DOI]
Dessart, L., Hillier, D. J., Blondin, S., & Khokhlov, A. 2014, MNRAS, 439, 3114, [1310.7750], [ADS], [DOI]
Dhawan, S., Flörs, A., Leibundgut, B., et al. 2018, A&A, 619, A102, [1805.02420], [ADS], [DOI]
Dhawan, S., Leibundgut, B., Spyromilio, J., & Blondin, S. 2016, A&A, 588, A84, [1601.04874], [ADS], [DOI]
Diamond, T. R., Hoeflich, P., & Gerardy, C. L. 2015, ApJ, 806, 107, [ADS], [DOI]
Diamond, T. R., Hoeflich, P., Hsiao, E. Y., et al. 2018, ApJ, 861, 119, [1805.03556], [ADS], [DOI]
Dickel, J. R., Strom, R. G., & Milne, D. K. 2001, ApJ, 546, 447, [astro-ph/0008042], [ADS], [DOI]
Diehl, R., Siegert, T., Hillebrandt, W., et al. 2014, Science, 345, 1162, [1407.3061], [ADS], [DOI]
Dilday, B., Howell, D. A., Cenko, S. B., et al. 2012, Science, 337, 942, [1207.1306], [ADS], [DOI]
Dimitriadis, G., Foley, R. J., Rest, A., et al. 2019, ApJ, 870, L1, [1811.10061], [ADS], [DOI]
Dimitriadis, G., Sullivan, M., Kerzendorf, W., et al. 2017, MNRAS, 468, 3798, [1701.07267], [ADS], [DOI]
Dong, S., Katz, B., Kushnir, D., & Prieto, J. L. 2015, MNRAS, 454, L61, [1401.3347], [ADS], [DOI]
Edwards, Z. I., Pagnotta, A., & Schaefer, B. E. 2012, ApJ, 747, L19, [1201.6377], [ADS], [DOI]
Einstein, A. 1918, Sitzungsberichte der Königlich Preußischen Akademie der Wissenschaften (Berlin, 154, [ADS]
Elias, J. H., Frogel, J. A., Hackwell, J. A., & Persson, S. E. 1981, ApJ, 251, L13, [ADS], [DOI]
Elias-Rosa, N., Benetti, S., Cappellaro, E., et al. 2006, MNRAS, 369, 1880, [astro-ph/0603316], [ADS], [DOI]
Fesen, R. A., Hamilton, A. J. S., & Saken, J. M. 1989, ApJ, 341, L55, [ADS], [DOI]
Filippenko, A. V., Richmond, M. W., Branch, D., et al. 1992a, AJ, 104, 1543, [ADS], [DOI]
Filippenko, A. V., Richmond, M. W., Matheson, T., et al. 1992b, ApJ, 384, L15, [ADS], [DOI]
Fink, M., Hillebrandt, W., & Röpke, F. K. 2007, A&A, 476, 1133, [0710.5486], [ADS], [DOI]
Fink, M., Kromer, M., Seitenzahl, I. R., et al. 2014, MNRAS, 438, 1762, [1308.3257], [ADS], [DOI]
Fink, M., Röpke, F. K., Hillebrandt, W., et al. 2011, Astronomical Society of the Pacific Conference Series, Vol. 444, Modeling Sub-Chandrasekhar Type Ia Supernovae, ed. N. V. Pogorelov, E. Audit, & G. P. Zank, 15, [ADS]
Fink, M., Röpke, F. K., Hillebrandt, W., et al. 2010, A&A, 514, A53, [1002.2173], [ADS], [DOI]
Fisher, R. & Jumper, K. 2015, ApJ, 805, 150, [1504.00014], [ADS], [DOI]
Fivet, V., Quinet, P., & Bautista, M. A. 2016, A&A, 585, A121, [ADS], [DOI]
Flörs, A., Spyromilio, J., Maguire, K., et al. 2018, A&A, 620, A200, [1810.10781], [ADS], [DOI]
Flörs, A., Spyromilio, J., Taubenberger, S., et al. 2020, MNRAS, 491, 2902, [1909.11055], [ADS], [DOI]
Foley, R. J., Challis, P. J., Chornock, R., et al. 2013, ApJ, 767, 57, [1212.2209], [ADS], [DOI]
Foley, R. J., Chornock, R., Filippenko, A. V., et al. 2009, AJ, 138, 376, [0902.2794], [ADS], [DOI]
Foley, R. J., Fox, O. D., McCully, C., et al. 2014, MNRAS, 443, 2887, [1405.3677], [ADS], [DOI]

Fossey, S. J., Cooke, B., Pollack, G., Wilde, M., & Wright, T. 2014, Central Bureau Electronic Telegrams, 3792, [ADS]

Fransson, C. & Chevalier, R. A. 1989, ApJ, 343, 323, [ADS], [DOI]

Fransson, C. & Jerkstrand, A. 2015, ApJ, 814, L2, [1511.00245], [ADS], [DOI]

Freudling, W., Romaniello, M., Bramich, D. M., et al. 2013, A&A, 559, A96, [1311.5411], [ADS], [DOI]

Friesen, B., Baron, E., Wisniewski, J. P., et al. 2014, ApJ, 792, 120, [1407.7732], [ADS], [DOI]

Gal-Yam, A. 2017, Observational and Physical Classification of Supernovae, ed. A. W. Alsabti & P. Murdin, 195, [ADS], [DOI]

Galbany, L., Moreno-Raya, M. E., Ruiz-Lapuente, P., et al. 2016, MNRAS, 457, 525, [1510.06596], [ADS], [DOI]

Gallagher, J. S., Garnavich, P. M., Berlind, P., et al. 2005, ApJ, 634, 210, [astro-ph/0508180], [ADS], [DOI]

Gamezo, V. N., Khokhlov, A. M., & Oran, E. S. 2005, ApJ, 623, 337, [astro-ph/0409598], [ADS], [DOI]

Gamezo, V. N., Khokhlov, A. M., Oran, E. S., Chtchelkanova, A. Y., & Rosenberg, R. O. 2003, Science, 299, 77, [astro-ph/0212054], [ADS], [DOI]

Ganeshalingam, M., Li, W., & Filippenko, A. V. 2011, MNRAS, 416, 2607, [1107.2404], [ADS], [DOI]

Garavini, G., Folatelli, G., Goobar, A., et al. 2004, AJ, 128, 387, [astro-ph/0404393], [ADS], [DOI]

García-Berro, E., Althaus, L. G., Córsico, A. H., & Isern, J. 2008, ApJ, 677, 473, [0712.1212], [ADS], [DOI]

García-Senz, D. & Bravo, E. 2005, A&A, 430, 585, [astro-ph/0409480], [ADS], [DOI]

Gardner, F. F. & Milne, D. K. 1965, AJ, 70, 754, [ADS], [DOI]

Garnavich, P. M., Bonanos, A. Z., Krisciunas, K., et al. 2004, ApJ, 613, 1120, [astro-ph/0105490], [ADS], [DOI]

Gerardy, C. L., Höflich, P., Fesen, R. A., et al. 2004, ApJ, 607, 391, [astro-ph/0309639], [ADS], [DOI]

Gerardy, C. L., Meikle, W. P. S., Kotak, R., et al. 2007, ApJ, 661, 995, [astro-ph/0702117], [ADS], [DOI]

Gilfanov, M. & Bogdán, Á. 2010, Nature, 463, 924, [1002.3359], [ADS], [DOI]

Gómez, G. & López, R. 1998, AJ, 115, 1096, [ADS], [DOI]

González Hernández, J. I., Ruiz-Lapuente, P., Filippenko, A. V., et al. 2009, ApJ, 691, 1, [0809.0601], [ADS], [DOI]

Goobar, A., Johansson, J., Amanullah, R., et al. 2014, ApJ, 784, L12, [1402.0849], [ADS], [DOI]

Graham, J. R., Wright, G. S., & Longmore, A. J. 1987, ApJ, 313, 847, [ADS], [DOI]

Graham, M. L., Foley, R. J., Zheng, W., et al. 2015, MNRAS, 446, 2073, [1408.2651], [ADS], [DOI]

Graham, M. L., Harris, C. E., Nugent, P. E., et al. 2019, ApJ, 871, 62, [1812.02757], [ADS], [DOI]

Graham, M. L., Kumar, S., Hosseinzadeh, G., et al. 2017, MNRAS, 472, 3437, [1708.07799], [ADS], [DOI]

Graur, O., Bianco, F. B., Modjaz, M., et al. 2017, ApJ, 837, 121, [1609.02923], [ADS], [DOI]
Graur, O., Zurek, D., Shara, M. M., et al. 2016, ApJ, 819, 31, [1505.00777], [ADS], [DOI]
Graur, O., Zurek, D. R., Cara, M., et al. 2018a, ApJ, 866, 10, [1808.00972], [ADS], [DOI]
Graur, O., Zurek, D. R., Rest, A., et al. 2018b, ApJ, 859, 79, [1711.01275], [ADS], [DOI]
Green, D. A. & Gull, S. F. 1984, Nature, 312, 527, [ADS], [DOI]
Guillochon, J., Dan, M., Ramirez-Ruiz, E., & Rosswog, S. 2010, ApJ, 709, L64, [0911.0416], [ADS], [DOI]
Gutierrez, J., Garcia-Berro, E., Iben, Icko, J., et al. 1996, ApJ, 459, 701, [ADS], [DOI]
Guy, J., Astier, P., Nobili, S., Regnault, N., & Pain, R. 2005, A&A, 443, 781, [astro-ph/0506583], [ADS], [DOI]
Hallakoun, N. & Maoz, D. 2019, MNRAS, 490, 657, [1905.00032], [ADS], [DOI]
Hamuy, M., Phillips, M. M., Suntzeff, N. B., et al. 2003, Nature, 424, 651, [astro-ph/0306270], [ADS], [DOI]
Hamuy, M., Phillips, M. M., Suntzeff, N. B., et al. 1996, AJ, 112, 2391, [astro-ph/9609059], [ADS], [DOI]
Hamuy, M., Trager, S. C., Pinto, P. A., et al. 2000, AJ, 120, 1479, [astro-ph/0005213], [ADS], [DOI]
Hanbury Brown, R. & Hazard, C. 1952, Nature, 170, 364, [ADS], [DOI]
Harkness, R. P. & Wheeler, J. C. 1990, in Supernovae, 1–29, [ADS]
Harris, C. E., Nugent, P. E., Horesh, A., et al. 2018, ApJ, 868, 21, [1812.02756], [ADS], [DOI]
Hartmann, D., Woosley, S. E., & El Eid, M. F. 1985, ApJ, 297, 837, [ADS], [DOI]
Hatano, K., Branch, D., Nomoto, K., et al. 2001, in American Astronomical Society Meeting Abstracts, Vol. 198, American Astronomical Society Meeting Abstracts #198, 39.02, [ADS]
Heitler, W. 1954, Quantum theory of radiation, [ADS]
Hillebrandt, W., Kromer, M., Röpke, F. K., & Ruiter, A. J. 2013, Frontiers of Physics, 8, 116, [1302.6420], [ADS], [DOI]
Hillebrandt, W. & Niemeyer, J. C. 2000, ARA&A, 38, 191, [astro-ph/0006305], [ADS], [DOI]
Hillman, Y., Prialnik, D., Kovetz, A., & Shara, M. M. 2016, ApJ, 819, 168, [1508.03141], [ADS], [DOI]
Höflich, P., Gerardy, C. L., Nomoto, K., et al. 2004, ApJ, 617, 1258, [astro-ph/0409185], [ADS], [DOI]
Höflich, P. & Stein, J. 2002, ApJ, 568, 779, [astro-ph/0104226], [ADS], [DOI]
Holmbo, S., Stritzinger, M. D., Shappee, B. J., et al. 2019, A&A, 627, A174, [1809.01359], [ADS], [DOI]
Horesh, A., Kulkarni, S. R., Fox, D. B., et al. 2012, ApJ, 746, 21, [1109.2912], [ADS], [DOI]
Hoyle, F. & Fowler, W. A. 1960, ApJ, 132, 565, [ADS], [DOI]
Hubbell, J. H. 1969, Photon cross sections, attenuation coefficients, and energy absorption coefficients from 10 keV to 100 GeV (Washington, DC: NSRDS)
Hubble, E. P. 1928, Leaflet of the Astronomical Society of the Pacific, 1, 55, [ADS]
Hut, P. & Inagaki, S. 1985, ApJ, 298, 502, [ADS], [DOI]
Iben, I., J. & Tutukov, A. V. 1984, ApJS, 54, 335, [ADS], [DOI]

Iliadis, C. 2015, Nuclear physics of stars (Hoboken, NJ: Wiley)

Ilkov, M. & Soker, N. 2012, MNRAS, 419, 1695, [1106.2027], [ADS], [DOI]

Iwamoto, K., Brachwitz, F., Nomoto, K., et al. 1999, ApJS, 125, 439, [astro-ph/0002337], [ADS], [DOI]

Jacobson-Galán, W. V., Dimitriadis, G., Foley, R. J., & Kilpatrick, C. D. 2018, ApJ, 857, 88, [1802.02252], [ADS], [DOI]

Jefferies, J. T. 1968, Spectral line formation, [ADS]

Jeffery, D. J., Leibundgut, B., Kirshner, R. P., et al. 1992, ApJ, 397, 304, [ADS], [DOI]

Jerkstrand, A. 2011, PhD thesis, -, [ADS]

Jha, S., Garnavich, P. M., Kirshner, R. P., et al. 1999, ApJS, 125, 73, [astro-ph/9906220], [ADS], [DOI]

Jha, S., Riess, A. G., & Kirshner, R. P. 2007, ApJ, 659, 122, [astro-ph/0612666], [ADS], [DOI]

Jordan, George C., I., Perets, H. B., Fisher, R. T., & van Rossum, D. R. 2012, ApJ, 761, L23, [1208.5069], [ADS], [DOI]

Kahabka, P. & van den Heuvel, E. P. J. 1997, ARA&A, 35, 69, [ADS], [DOI]

Karachentsev, I. D. & Kashibadze, O. G. 2006, Astrophysics, 49, 3, [ADS], [DOI]

Kasen, D. 2006, ApJ, 649, 939, [astro-ph/0606449], [ADS], [DOI]

Kashi, A. & Soker, N. 2011, MNRAS, 417, 1466, [1105.5698], [ADS], [DOI]

Kass, R. E. & Raftery, A. E. 1995, Journal of the American Statistical Association, 90, 773, [https://www.tandfonline.com/doi/pdf/10.1080/01621459.1995.10476572], [DOI]

Kattner, S., Leonard, D. C., Burns, C. R., et al. 2012, PASP, 124, 114, [1201.2913], [ADS], [DOI]

Katz, B. & Dong, S. 2012, arXiv e-prints, arXiv:1211.4584, [1211.4584], [ADS]

Kawabata, K. S., Akitaya, H., Yamanaka, M., et al. 2014, ApJ, 795, L4, [1407.0452], [ADS], [DOI]

Kelly, P. L., Fox, O. D., Filippenko, A. V., et al. 2014, ApJ, 790, 3, [1403.4250], [ADS], [DOI]

Kerzendorf, W. E., Childress, M., Scharwächter, J., Do, T., & Schmidt, B. P. 2014, ApJ, 782, 27, [1309.5964], [ADS], [DOI]

Kerzendorf, W. E., Long, K. S., Winkler, P. F., & Do, T. 2018a, MNRAS, 479, 5696, [1803.07562], [ADS], [DOI]

Kerzendorf, W. E., McCully, C., Taubenberger, S., et al. 2017, MNRAS, 472, 2534, [1706.01460], [ADS], [DOI]

Kerzendorf, W. E., Schmidt, B. P., Asplund, M., et al. 2009, ApJ, 701, 1665, [0906.0982], [ADS], [DOI]

Kerzendorf, W. E., Schmidt, B. P., Laird, J. B., Podsiadlowski, P., & Bessell, M. S. 2012, ApJ, 759, 7, [1207.4481], [ADS], [DOI]

Kerzendorf, W. E., Strampelli, G., Shen, K. J., et al. 2018b, MNRAS, 479, 192, [1709.06566], [ADS], [DOI]

Kerzendorf, W. E., Yong, D., Schmidt, B. P., et al. 2013, ApJ, 774, 99, [1210.2713], [ADS], [DOI]

Khokhlov, A., Mueller, E., & Hoeflich, P. 1992, A&A, 253, L9, [ADS]

Khokhlov, A. M. 1989, MNRAS, 239, 785, [ADS], [DOI]

Khokhlov, A. M. 1991, A&A, 245, 114, [ADS]

Kirby, E. N., Xie, J. L., Guo, R., et al. 2019, arXiv e-prints, arXiv:1906.10126, [1906.10126], [ADS]

Kochanek, C. S., Shappee, B. J., Stanek, K. Z., et al. 2017, PASP, 129, 104502, [1706.07060], [ADS], [DOI]

Kollmeier, J. A., Chen, P., Dong, S., et al. 2019, MNRAS, 486, 3041, [1902.02251], [ADS], [DOI]

Kotak, R., Meikle, W. P. S., Pignata, G., et al. 2005, A&A, 436, 1021, [astro-ph/0503339], [ADS], [DOI]

Kozai, Y. 1962, AJ, 67, 591, [ADS], [DOI]

Kozma, C. & Fransson, C. 1992, ApJ, 390, 602, [ADS], [DOI]

Kozma, C., Fransson, C., Hillebrandt, W., et al. 2005, A&A, 437, 983, [astro-ph/0504317], [ADS], [DOI]

Kramida, A., Yu. Ralchenko, Reader, J., & and NIST ASD Team. 2018, NIST Atomic Spectra Database (ver. 5.5.6), [Online]. Available: `https://physics.nist.gov/asd` [2017, September 15]. National Institute of Standards and Technology, Gaithersburg, MD.

Krause, O., Tanaka, M., Usuda, T., et al. 2008, Nature, 456, 617, [0810.5106], [ADS], [DOI]

Krisciunas, K., Marion, G. H., Suntzeff, N. B., et al. 2009, AJ, 138, 1584, [0908.1918], [ADS], [DOI]

Krisciunas, K., Phillips, M. M., & Suntzeff, N. B. 2004, ApJ, 602, L81, [astro-ph/0312626], [ADS], [DOI]

Kromer, M., Fink, M., Stanishev, V., et al. 2013a, MNRAS, 429, 2287, [1210.5243], [ADS], [DOI]

Kromer, M., Fremling, C., Pakmor, R., et al. 2016, MNRAS, 459, 4428, [1604.05730], [ADS], [DOI]

Kromer, M., Ohlmann, S. T., Pakmor, R., et al. 2015, MNRAS, 450, 3045, [1503.04292], [ADS], [DOI]

Kromer, M., Pakmor, R., Taubenberger, S., et al. 2013b, ApJ, 778, L18, [1311.0310], [ADS], [DOI]

Kuchner, M. J., Kirshner, R. P., Pinto, P. A., & Leibundgut, B. 1994, ApJ, 426, L89, [ADS], [DOI]

Kuhlen, M., Woosley, S. E., & Glatzmaier, G. A. 2006, ApJ, 640, 407, [astro-ph/0509367], [ADS], [DOI]

Kulkarni, S. R. 2012, ArXiv e-prints, [1202.2381], [ADS]

Kulkarni, S. R. 2018, The Astronomer's Telegram, 11266, 1, [ADS]

Kunkel, W., Madore, B., Shelton, I., et al. 1987, IAU Circ., 4316, 1, [ADS]

Kushnir, D., Katz, B., Dong, S., Livne, E., & Fernández, R. 2013, ApJ, 778, L37, [1303.1180], [ADS], [DOI]

Leibundgut, B. 2001, ARA&A, 39, 67, [ADS], [DOI]

Leibundgut, B., Kirshner, R. P., Phillips, M. M., et al. 1993, AJ, 105, 301, [ADS], [DOI]

Leibundgut, B. & Pinto, P. A. 1992, ApJ, 401, 49, [ADS], [DOI]

Leibundgut, B. & Sullivan, M. 2018, Space Sci. Rev., 214, A57, [ADS], [DOI]

Leloudas, G., Stritzinger, M. D., Sollerman, J., et al. 2009, A&A, 505, 265, [0908.0537], [ADS], [DOI]

Leonard, D. C. 2007, in American Institute of Physics Conference Series, Vol. 937, Supernova 1987A: 20 Years After: Supernovae and Gamma-Ray Bursters, ed. S. Immler, K. Weiler, &

R. McCray, 311–315, [ADS], [DOI]
Leonard, D. C., Li, W., Filippenko, A. V., Foley, R. J., & Chornock, R. 2005, ApJ, 632, 450, [astro-ph/0506470], [ADS], [DOI]
Li, W., Bloom, J. S., Podsiadlowski, P., et al. 2011a, Nature, 480, 348, [1109.1593], [ADS], [DOI]
Li, W., Leaman, J., Chornock, R., et al. 2011b, MNRAS, 412, 1441, [1006.4612], [ADS], [DOI]
Lidov, M. L. 1962, Planet. Space Sci., 9, 719, [ADS], [DOI]
Livio, M. & Mazzali, P. 2018, Phys. Rep., 736, 1, [ADS], [DOI]
Livio, M. & Riess, A. G. 2003, ApJ, 594, L93, [astro-ph/0308018], [ADS], [DOI]
Livio, M. & Truran, J. W. 1992, ApJ, 389, 695, [ADS], [DOI]
Livne, E. 1990, ApJ, 354, L53, [ADS], [DOI]
Livne, E. & Arnett, D. 1995, ApJ, 452, 62, [ADS], [DOI]
Long, M., Jordan, George C., I., van Rossum, D. R., et al. 2014, ApJ, 789, 103, [1307.8221], [ADS], [DOI]
Lundmark, K. 1921, PASP, 33, 225, [ADS], [DOI]
Ma, H., Woosley, S. E., Malone, C. M., Almgren, A., & Bell, J. 2013, ApJ, 771, 58, [1305.2433], [ADS], [DOI]
Maeda, K., Benetti, S., Stritzinger, M., et al. 2010a, Nature, 466, 82, [1006.5888], [ADS], [DOI]
Maeda, K., Taubenberger, S., Sollerman, J., et al. 2010b, ApJ, 708, 1703, [0911.5484], [ADS], [DOI]
Magee, M. R., Kotak, R., Sim, S. A., et al. 2016, A&A, 589, A89, [1603.04728], [ADS], [DOI]
Maguire, K. 2017, Type Ia Supernovae, ed. A. W. Alsabti & P. Murdin, 293, [ADS], [DOI]
Maguire, K., Sim, S. A., Shingles, L., et al. 2018a, MNRAS, 477, 3567, [1803.10252], [ADS], [DOI]
Maguire, K., Sim, S. A., Shingles, L., et al. 2018b, MNRAS, [1803.10252], [ADS], [DOI]
Maguire, K., Sullivan, M., Pan, Y. C., et al. 2014, MNRAS, 444, 3258, [1408.1430], [ADS], [DOI]
Maguire, K., Taubenberger, S., Sullivan, M., & Mazzali, P. A. 2016, MNRAS, 457, 3254, [1512.07107], [ADS], [DOI]
Mannucci, F., Della Valle, M., Panagia, N., et al. 2005, A&A, 433, 807, [astro-ph/0411450], [ADS], [DOI]
Maoz, D., Mannucci, F., Li, W., et al. 2011, MNRAS, 412, 1508, [1002.3056], [ADS], [DOI]
Maoz, D., Mannucci, F., & Nelemans, G. 2014, ARA&A, 52, 107, [1312.0628], [ADS], [DOI]
Margutti, R., Parrent, J., Kamble, A., et al. 2014, ApJ, 790, 52, [1405.1488], [ADS], [DOI]
Marquardt, K. S., Sim, S. A., Ruiter, A. J., et al. 2015, A&A, 580, A118, [1506.05809], [ADS], [DOI]
Martínez-Rodríguez, H., Badenes, C., Yamaguchi, H., et al. 2017, ApJ, 843, 35, [1701.07073], [ADS], [DOI]
Martínez-Rodríguez, H., Piro, A. L., Schwab, J., & Badenes, C. 2016, ApJ, 825, 57, [1602.00673], [ADS], [DOI]
Mason, R. E., Côté, S., Kissler-Patig, M., et al. 2014, in Proc. SPIE, Vol. 9149, Observatory Operations: Strategies, Processes, and Systems V, 914910, [1408.5916], [ADS], [DOI]
Matheson, T., Kirshner, R. P., Challis, P., et al. 2008, AJ, 135, 1598, [0803.1705], [ADS], [DOI]
Mazzali, P. A., Benetti, S., Altavilla, G., et al. 2005, ApJ, 623, L37, [astro-ph/0502531], [ADS], [DOI]

Mazzali, P. A., Cappellaro, E., Danziger, I. J., Turatto, M., & Benetti, S. 1998, ApJ, 499, L49, [astro-ph/9803229], [ADS], [DOI]

Mazzali, P. A., Chugai, N., Turatto, M., et al. 1997, MNRAS, 284, 151, [ADS], [DOI]

Mazzali, P. A., Danziger, I. J., & Turatto, M. 1995, A&A, 297, 509, [ADS]

Mazzali, P. A. & Hachinger, S. 2012, MNRAS, 424, 2926, [ADS], [DOI]

Mazzali, P. A., Maurer, I., Stritzinger, M., et al. 2011, MNRAS, 416, 881, [1105.1298], [ADS], [DOI]

Mazzali, P. A., Maurer, I., Valenti, S., Kotak, R., & Hunter, D. 2010, MNRAS, 408, 87, [1006.4259], [ADS], [DOI]

Mazzali, P. A., Röpke, F. K., Benetti, S., & Hillebrandt, W. 2007, Science, 315, 825, [astro-ph/0702351], [ADS], [DOI]

Mazzali, P. A., Sullivan, M., Filippenko, A. V., et al. 2015, MNRAS, 450, 2631, [1504.04857], [ADS], [DOI]

Mazzali, P. A., Sullivan, M., Hachinger, S., et al. 2014, MNRAS, 439, 1959, [1305.2356], [ADS], [DOI]

McCully, C., Jha, S. W., Foley, R. J., et al. 2014, Nature, 512, 54, [1408.1089], [ADS], [DOI]

Meikle, W. P. S., Cumming, R. J., Geballe, T. R., et al. 1996, MNRAS, 281, 263, [ADS], [DOI]

Meng, X. C., Li, Z. M., & Yang, W. M. 2011, PASJ, 63, 31, [1105.5265], [ADS], [DOI]

Messier, C. 1781, Catalogue des Nébuleuses et des Amas d'Étoiles (Catalog of Nebulae and Star Clusters), Connoissance des Temps ou des Mouvements Célestes, [ADS]

Mihalas, D. 1978, Stellar atmospheres, [ADS]

Miller, W. C. 1955, Leaflet of the Astronomical Society of the Pacific, 7, 105, [ADS]

Mills, B. Y., Slee, O. B., & Hill, E. R. 1961, Australian Journal of Physics, 14, 497, [ADS], [DOI]

Miluzio, M., Cappellaro, E., Botticella, M. T., et al. 2013, A&A, 554, A127, [1303.3803], [ADS], [DOI]

Minkowski, R. 1940, PASP, 52, 206, [ADS], [DOI]

Minkowski, R. 1941, PASP, 53, 224, [ADS], [DOI]

Modigliani, A., Goldoni, P., Royer, F., et al. 2010, in Society of Photo-Optical Instrumentation Engineers (SPIE) Conference Series, Vol. 7737, Observatory Operations: Strategies, Processes, and Systems III, 773728, [ADS], [DOI]

Mohr, P. J., Taylor, B. N., & Newell, D. B. 2012, Reviews of Modern Physics, 84, 1527, [1203.5425], [ADS], [DOI]

Moll, R. & Woosley, S. E. 2013, ApJ, 774, 137, [1303.0324], [ADS], [DOI]

Motohara, K., Maeda, K., Gerardy, C. L., et al. 2006, ApJ, 652, L101, [astro-ph/0610303], [ADS], [DOI]

Müller, B. 2019, Annual Review of Nuclear and Particle Science, 69, annurev, [1904.11067], [ADS], [DOI]

Nadyozhin, D. K. 1994, ApJS, 92, 527, [ADS], [DOI]

Nadyozhin, D. K. & Yudin, A. V. 2004, Astronomy Letters, 30, 634, [ADS], [DOI]

Nielsen, M. T. B., Voss, R., & Nelemans, G. 2012, MNRAS, 426, 2668, [1109.6605], [ADS], [DOI]

Nobili, S., Amanullah, R., Garavini, G., et al. 2005, A&A, 437, 789, [astro-ph/0504139], [ADS], [DOI]
Nobili, S. & Goobar, A. 2008, A&A, 487, 19, [0712.1155], [ADS], [DOI]
Nomoto, K. 1980, Space Sci. Rev., 27, 563, [ADS], [DOI]
Nomoto, K. 1982a, ApJ, 253, 798, [ADS], [DOI]
Nomoto, K. 1982b, ApJ, 257, 780, [ADS], [DOI]
Nomoto, K. & Kondo, Y. 1991, ApJ, 367, L19, [ADS], [DOI]
Nomoto, K. & Leung, S.-C. 2018, Space Sci. Rev., 214, 67, [1805.10811], [ADS], [DOI]
Nomoto, K., Saio, H., Kato, M., & Hachisu, I. 2007, ApJ, 663, 1269, [astro-ph/0603351], [ADS], [DOI]
Nomoto, K. & Sugimoto, D. 1977, PASJ, 29, 765, [ADS]
Nomoto, K., Thielemann, F.-K., & Yokoi, K. 1984, ApJ, 286, 644, [ADS], [DOI]
Nonaka, A., Aspden, A. J., Zingale, M., et al. 2012, ApJ, 745, 73, [1111.3086], [ADS], [DOI]
Nugent, P., Phillips, M., Baron, E., Branch, D., & Hauschildt, P. 1995, ApJ, 455, L147, [astro-ph/9510004], [ADS], [DOI]
Nugent, P., Sullivan, M., Bersier, D., et al. 2011a, The Astronomer's Telegram, 3581, 1, [ADS]
Nugent, P. E., Sullivan, M., Cenko, S. B., et al. 2011b, Nature, 480, 344, [1110.6201], [ADS], [DOI]
Nussbaumer, H. & Storey, P. J. 1980, A&A, 89, 308, [ADS]
Nussbaumer, H. & Storey, P. J. 1988, A&A, 193, 327, [ADS]
Ohlmann, S. T., Kromer, M., Fink, M., et al. 2014, A&A, 572, A57, [1409.2866], [ADS], [DOI]
Paczynski, B. & Zytkow, A. N. 1978, ApJ, 222, 604, [ADS], [DOI]
Pakmor, R. 2017, Violent Mergers, ed. A. W. Alsabti & P. Murdin, 1257, [ADS], [DOI]
Pakmor, R., Kromer, M., Röpke, F. K., et al. 2010, Nature, 463, 61, [0911.0926], [ADS], [DOI]
Pakmor, R., Kromer, M., Taubenberger, S., et al. 2012, ApJ, 747, L10, [1201.5123], [ADS], [DOI]
Pakmor, R., Kromer, M., Taubenberger, S., & Springel, V. 2013, ApJ, 770, L8, [1302.2913], [ADS], [DOI]
Pan, Y.-C., Foley, R. J., Kromer, M., et al. 2015, MNRAS, 452, 4307, [1504.02396], [ADS], [DOI]
Panagia, N., Van Dyk, S. D., Weiler, K. W., et al. 2006, ApJ, 646, 369, [astro-ph/0603808], [ADS], [DOI]
Pankey, Titus, J. 1962, PhD thesis, Howard University., [ADS]
Park, S., Badenes, C., Mori, K., et al. 2013, ApJ, 767, L10, [1302.5435], [ADS], [DOI]
Pastorello, A., Mazzali, P. A., Pignata, G., et al. 2007, MNRAS, 377, 1531, [astro-ph/0702565], [ADS], [DOI]
Patat, F., Taubenberger, S., Cox, N. L. J., et al. 2015, A&A, 577, A53, [1407.0136], [ADS], [DOI]
Penney, R. & Hoeflich, P. 2014, ApJ, 795, 84, [ADS], [DOI]
Perets, H. B., Gal-Yam, A., Mazzali, P. A., et al. 2010, Nature, 465, 322, [0906.2003], [ADS], [DOI]
Pérez-Torres, M. A., Lundqvist, P., Beswick, R. J., et al. 2014, ApJ, 792, 38, [1405.4702], [ADS], [DOI]
Perlmutter, S., Aldering, G., Goldhaber, G., et al. 1999, ApJ, 517, 565, [astro-ph/9812133], [ADS], [DOI]
Phillips, M. M. 1993, ApJ, 413, L105, [ADS], [DOI]

Phillips, M. M., Lira, P., Suntzeff, N. B., et al. 1999, AJ, 118, 1766, [astro-ph/9907052], [ADS], [DOI]
Phillips, M. M., Simon, J. D., Morrell, N., et al. 2013, ApJ, 779, 38, [1311.0147], [ADS], [DOI]
Phillips, M. M., Wells, L. A., Suntzeff, N. B., et al. 1992, AJ, 103, 1632, [ADS], [DOI]
Pignata, G., Benetti, S., Mazzali, P. A., et al. 2008, MNRAS, 388, 971, [0805.1089], [ADS], [DOI]
Pignata, G., Patat, F., Benetti, S., et al. 2004, MNRAS, 355, 178, [astro-ph/0408234], [ADS], [DOI]
Pinto, P. A. & Eastman, R. G. 2000, ApJ, 530, 757, [ADS], [DOI]
Piro, A. L. & Chang, P. 2008, ApJ, 678, 1158, [0801.1321], [ADS], [DOI]
Plewa, T., Calder, A. C., & Lamb, D. Q. 2004, ApJ, 612, L37, [astro-ph/0405163], [ADS], [DOI]
Pskovskii, I. P. 1977, Soviet Ast., 21, 675, [ADS]
Quimby, R., Höflich, P., Kannappan, S. J., et al. 2006, ApJ, 636, 400, [astro-ph/0509304], [ADS], [DOI]
Quinet, P. 1996, A&AS, 116, 573, [ADS]
Raskin, C., Scannapieco, E., Fryer, C., Rockefeller, G., & Timmes, F. X. 2012, ApJ, 746, 62, [1112.1420], [ADS], [DOI]
Reifenstein, E. C., Brundage, W. D., & Staelin, D. H. 1969, Phys. Rev. Lett., 22, 311, [ADS], [DOI]
Reinecke, M., Hillebrandt, W., & Niemeyer, J. C. 2002, A&A, 391, 1167, [astro-ph/0206459], [ADS], [DOI]
Reynolds, S. P. 2017, Dynamical Evolution and Radiative Processes of Supernova Remnants, ed. A. W. Alsabti & P. Murdin, 1981, [ADS], [DOI]
Reynolds, S. P., Borkowski, K. J., Green, D. A., et al. 2008, ApJ, 680, L41, [0803.1487], [ADS], [DOI]
Reynoso, E. M., Hughes, J. P., & Moffett, D. A. 2013, AJ, 145, 104, [1302.4678], [ADS], [DOI]
Richmond, M., Treffers, R. R., & Filippenko, A. V. 1993, PASP, 105, 1164, [ADS], [DOI]
Riess, A. G. 1996, PhD thesis, Harvard University., [ADS]
Riess, A. G., Filippenko, A. V., Challis, P., et al. 1998, AJ, 116, 1009, [astro-ph/9805201], [ADS], [DOI]
Röpke, F. K. 2005, A&A, 432, 969, [astro-ph/0408296], [ADS], [DOI]
Röpke, F. K., Gieseler, M., Reinecke, M., Travaglio, C., & Hillebrandt, W. 2006a, A&A, 453, 203, [astro-ph/0506107], [ADS], [DOI]
Röpke, F. K. & Hillebrandt, W. 2005, A&A, 431, 635, [astro-ph/0409286], [ADS], [DOI]
Röpke, F. K., Hillebrandt, W., Niemeyer, J. C., & Woosley, S. E. 2006b, A&A, 448, 1, [astro-ph/0510474], [ADS], [DOI]
Röpke, F. K., Hillebrandt, W., Schmidt, W., et al. 2007a, ApJ, 668, 1132, [0707.1024], [ADS], [DOI]
Röpke, F. K., Woosley, S. E., & Hillebrandt, W. 2007b, ApJ, 660, 1344, [astro-ph/0609088], [ADS], [DOI]
Rosswog, S., Kasen, D., Guillochon, J., & Ramirez-Ruiz, E. 2009, ApJ, 705, L128, [0907.3196], [ADS], [DOI]
Ruiter, A. J., Sim, S. A., Pakmor, R., et al. 2013, MNRAS, 429, 1425, [1209.0645], [ADS], [DOI]

Ruiz-Lapuente, P. 2004, ApJ, 612, 357, [astro-ph/0309009], [ADS], [DOI]

Ruiz-Lapuente, P., Cappellaro, E., Turatto, M., et al. 1992, ApJ, 387, L33, [ADS], [DOI]

Ruiz-Lapuente, P. & Lucy, L. B. 1992, ApJ, 400, 127, [ADS], [DOI]

Ryder, S., Staveley-Smith, L., Dopita, M., et al. 1993, ApJ, 416, 167, [ADS], [DOI]

Salvo, M. E., Cappellaro, E., Mazzali, P. A., et al. 2001, MNRAS, 321, 254, [astro-ph/0009065], [ADS], [DOI]

Sasdelli, M., Mazzali, P. A., Pian, E., et al. 2014, MNRAS, 445, 711, [1409.0116], [ADS], [DOI]

Sato, Y., Nakasato, N., Tanikawa, A., et al. 2015, ApJ, 807, 105, [1505.01646], [ADS], [DOI]

Scalzo, R., Aldering, G., Antilogus, P., et al. 2014, MNRAS, 440, 1498, [1402.6842], [ADS], [DOI]

Scalzo, R. A., Aldering, G., Antilogus, P., et al. 2010, ApJ, 713, 1073, [1003.2217], [ADS], [DOI]

Schaefer, B. E. & Pagnotta, A. 2012, Nature, 481, 164, [ADS], [DOI]

Schlafly, E. F. & Finkbeiner, D. P. 2011, ApJ, 737, 103, [1012.4804], [ADS], [DOI]

Schunk, R. W. & Hays, P. B. 1971, Planet. Space Sci., 19, 113, [ADS], [DOI]

Seitenzahl, I. R., Ciaraldi-Schoolmann, F., Röpke, F. K., et al. 2013, MNRAS, 429, 1156, [1211.3015], [ADS], [DOI]

Seitenzahl, I. R., Ghavamian, P., Laming, J. M., & Vogt, F. P. A. 2019, Phys. Rev. Lett., 123, 041101, [1906.05972], [ADS], [DOI]

Seitenzahl, I. R., Kromer, M., Ohlmann, S. T., et al. 2016, A&A, 592, A57, [1606.00089], [ADS], [DOI]

Seitenzahl, I. R., Taubenberger, S., & Sim, S. A. 2009, MNRAS, 400, 531, [0908.0247], [ADS], [DOI]

Seitenzahl, I. R. & Townsley, D. M. 2017, Nucleosynthesis in Thermonuclear Supernovae, ed. A. W. Alsabti & P. Murdin, 1955, [ADS], [DOI]

Shanks, T., Metcalfe, N., Chehade, B., et al. 2015, MNRAS, 451, 4238, [1502.05432], [ADS], [DOI]

Shappee, B. J., Kochanek, C. S., & Stanek, K. Z. 2013, ApJ, 765, 150, [1205.5028], [ADS], [DOI]

Shappee, B. J., Stanek, K. Z., Kochanek, C. S., & Garnavich, P. M. 2017, ApJ, 841, 48, [1608.01155], [ADS], [DOI]

Shaw, J. R., Bridges, M., & Hobson, M. P. 2007, MNRAS, 378, 1365, [astro-ph/0701867], [ADS], [DOI]

Shea, W. 2005, in Astronomical Society of the Pacific Conference Series, Vol. 342, 1604-2004: Supernovae as Cosmological Lighthouses, ed. M. Turatto, S. Benetti, L. Zampieri, & W. Shea, 13, [ADS]

Shen, K. J. & Bildsten, L. 2007, ApJ, 660, 1444, [astro-ph/0702049], [ADS], [DOI]

Shen, K. J. & Bildsten, L. 2009, ApJ, 699, 1365, [0903.0654], [ADS], [DOI]

Shen, K. J. & Bildsten, L. 2014, ApJ, 785, 61, [1305.6925], [ADS], [DOI]

Shen, K. J., Kasen, D., Miles, B. J., & Townsley, D. M. 2018, ApJ, 854, 52, [1706.01898], [ADS], [DOI]

Shingles, L. J., Sim, S. A., Kromer, M., et al. 2020, MNRAS, 492, 2029, [1912.02214], [ADS], [DOI]

Silverman, J. M., Foley, R. J., Filippenko, A. V., et al. 2012a, MNRAS, 425, 1789, [1202.2128], [ADS], [DOI]

Silverman, J. M., Ganeshalingam, M., Cenko, S. B., et al. 2012b, ApJ, 756, L7, [1206.1328], [ADS], [DOI]

Silverman, J. M., Ganeshalingam, M., & Filippenko, A. V. 2013a, MNRAS, 430, 1030, [1211.0279], [ADS], [DOI]

Silverman, J. M., Ganeshalingam, M., Li, W., et al. 2011, MNRAS, 410, 585, [1003.2417], [ADS], [DOI]

Silverman, J. M., Nugent, P. E., Gal-Yam, A., et al. 2013b, ApJS, 207, 3, [1304.0763], [ADS], [DOI]

Sim, S. A., Fink, M., Kromer, M., et al. 2012, MNRAS, 420, 3003, [1111.2117], [ADS], [DOI]

Sim, S. A., Röpke, F. K., Hillebrandt, W., et al. 2010, ApJ, 714, L52, [1003.2917], [ADS], [DOI]

Smith, R. C. 1997, AJ, 114, 2664, [ADS], [DOI]

Sobolev, V. V. 1957, Soviet Ast., 1, 678, [ADS]

Sollerman, J., Ghavamian, P., Lundqvist, P., & Smith, R. C. 2003, A&A, 407, 249, [astro-ph/0306196], [ADS], [DOI]

Spencer, L. V. & Fano, U. 1954, Physical Review, 93, 1172, [ADS], [DOI]

Spyromilio, J., Gilmozzi, R., Sollerman, J., et al. 2004, A&A, 426, 547, [astro-ph/0407177], [ADS], [DOI]

Spyromilio, J., Meikle, W. P. S., Allen, D. A., & Graham, J. R. 1992, MNRAS, 258, 53P, [ADS], [DOI]

Srivastav, S., Ninan, J. P., Kumar, B., et al. 2016, MNRAS, 457, 1000, [1601.00805], [ADS], [DOI]

Stanishev, V., Goobar, A., Benetti, S., et al. 2007, A&A, 469, 645, [0704.1244], [ADS], [DOI]

Stephenson, F. R. 1971, QJRAS, 12, 10, [ADS]

Stephenson, F. R. & Green, D. A. 2002, Historical supernovae and their remnants, 5, [ADS]

Stoner, E. 1930, The London, 9, 944, [ADS]

Storey, P. J. & Sochi, T. 2016, MNRAS, 459, 2558, [1602.00712], [ADS], [DOI]

Storey, P. J., Zeippen, C. J., & Sochi, T. 2016, MNRAS, 456, 1974, [1509.03164], [ADS], [DOI]

Stritzinger, M., Burns, C. R., Phillips, M. M., et al. 2010, AJ, 140, 2036, [1009.4390], [ADS], [DOI]

Stritzinger, M., Leibundgut, B., Walch, S., & Contardo, G. 2006, A&A, 450, 241, [astro-ph/0506415], [ADS], [DOI]

Sullivan, M., Kasliwal, M. M., Nugent, P. E., et al. 2011, ApJ, 732, 118, [1103.1797], [ADS], [DOI]

Sullivan, M., Le Borgne, D., Pritchet, C. J., et al. 2006, ApJ, 648, 868, [astro-ph/0605455], [ADS], [DOI]

Swartz, D. A., Sutherland, P. G., & Harkness, R. P. 1995, ApJ, 446, 766, [astro-ph/9501005], [ADS], [DOI]

Taam, R. E. 1980a, ApJ, 237, 142, [ADS], [DOI]

Taam, R. E. 1980b, ApJ, 242, 749, [ADS], [DOI]

Tanaka, M., Mazzali, P. A., Maeda, K., & Nomoto, K. 2006, ApJ, 645, 470, [astro-ph/0603184], [ADS], [DOI]

Tang, S., Bildsten, L., Wolf, W. M., et al. 2014, ApJ, 786, 61, [1401.2426], [ADS], [DOI]

Taubenberger, S. 2017, The Extremes of Thermonuclear Supernovae, ed. A. W. Alsabti & P. Murdin, 317, [ADS], [DOI]

Taubenberger, S., Benetti, S., Childress, M., et al. 2011, MNRAS, 412, 2735, [1011.5665], [ADS], [DOI]

Taubenberger, S., Elias-Rosa, N., Kerzendorf, W. E., et al. 2015, MNRAS, 448, L48, [1411.7599], [ADS], [DOI]

Taubenberger, S., Kromer, M., Hachinger, S., et al. 2013, MNRAS, 432, 3117, [1304.4952], [ADS], [DOI]

Thielemann, F. K., Nomoto, K., & Yokoi, K. 1986, A&A, 158, 17, [ADS]

Thomas, R. C., Branch, D., Baron, E., et al. 2004, ApJ, 601, 1019, [astro-ph/0302260], [ADS], [DOI]

Thompson, T. A. 2011, ApJ, 741, 82, [1011.4322], [ADS], [DOI]

Timmes, F. X., Brown, E. F., & Truran, J. W. 2003, ApJ, 590, L83, [astro-ph/0305114], [ADS], [DOI]

Tonry, J. L., Denneau, L., Heinze, A. N., et al. 2018, PASP, 130, 064505, [1802.00879], [ADS], [DOI]

Toonen, S., Perets, H. B., & Hamers, A. S. 2018, A&A, 610, A22, [1709.00422], [ADS], [DOI]

Torii, K., Tsunemi, H., Dotani, T., et al. 1999, ApJ, 523, L69, [ADS], [DOI]

Townsley, D. M., Calder, A. C., Asida, S. M., et al. 2007, ApJ, 668, 1118, [arXiv:0706.1094], [ADS], [DOI]

Townsley, D. M., Miles, B. J., Shen, K. J., & Kasen, D. 2019, ApJ, 878, L38, [1903.10960], [ADS], [DOI]

Turatto, M. 2003, Classification of Supernovae, ed. K. Weiler, Vol. 598, 21–36, [ADS], [DOI]

Turatto, M., Benetti, S., Cappellaro, E., et al. 1996a, MNRAS, 283, 1, [astro-ph/9605178], [ADS], [DOI]

Turatto, M., Benetti, S., Cappellaro, E., Danziger, I. J., & Mazzali, P. A. 1996b, The Messenger, 85, 34, [ADS]

Urtiew, P. A. & Oppenheim, A. K. 1966, Proceedings of the Royal Society of London Series A, 295, 13, [ADS], [DOI]

Vacca, W. D., Hamilton, R. T., Savage, M., et al. 2015, ApJ, 804, 66, [1503.01229], [ADS], [DOI]

Vallely, P., Moreno-Raya, M. E., Baron, E., et al. 2016, MNRAS, 460, 1614, [ADS], [DOI]

Vallely, P. J., Fausnaugh, M., Jha, S. W., et al. 2019, MNRAS, 487, 2372, [1903.08665], [ADS], [DOI]

van den Heuvel, E. P. J., Bhattacharya, D., Nomoto, K., & Rappaport, S. A. 1992, A&A, 262, 97, [ADS]

Van Dyk, S. D. 2017, Supernova Progenitors Observed with HST, ed. A. W. Alsabti & P. Murdin, 693, [ADS], [DOI]

Van Dyk, S. D., Peng, C. Y., Barth, A. J., & Filippenko, A. V. 1999, AJ, 118, 2331, [astro-ph/9907252], [ADS], [DOI]

van Kerkwijk, M. H., Chang, P., & Justham, S. 2010, ApJ, 722, L157, [1006.4391], [ADS], [DOI]

van Regemorter, H. 1962, ApJ, 136, 906, [ADS], [DOI]

Varani, G. F., Meikle, W. P. S., Spyromilio, J., & Allen, D. A. 1990, MNRAS, 245, 570, [ADS]

Veigele, W. J. 1973, Atomic Data, 5, 51, [ADS], [DOI]

Vink, J., Bleeker, J., van der Heyden, K., et al. 2006, ApJ, 648, L33, [astro-ph/0607307], [ADS], [DOI]

Wang, L., Wheeler, J. C., Li, Z., & Clocchiatti, A. 1996, ApJ, 467, 435, [astro-ph/9602155], [ADS], [DOI]

Wang, X., Li, W., Filippenko, A. V., et al. 2009, ApJ, 697, 380, [0811.1205], [ADS], [DOI]

Wang, X., Li, W., Filippenko, A. V., et al. 2008, ApJ, 675, 626, [0708.0140], [ADS], [DOI]

Watts, M. S. T. & Burke, V. M. 1998, Journal of Physics B Atomic Molecular Physics, 31, 145, [ADS], [DOI]

Webbink, R. F. 1984, ApJ, 277, 355, [ADS], [DOI]

Weisberg, J. M., Taylor, J. H., & Fowler, L. A. 1981, Scientific American, 245, 74, [ADS], [DOI]

Whelan, J. & Iben, Icko, J. 1973, ApJ, 186, 1007, [ADS], [DOI]

Wilk, K. D., Hillier, D. J., & Dessart, L. 2018, MNRAS, 474, 3187, [1711.00105], [ADS], [DOI]

Wilk, K. D., Hillier, D. J., & Dessart, L. 2019, MNRAS, 487, 1218, [1905.05798], [ADS], [DOI]

Wolf, W. M., Bildsten, L., Brooks, J., & Paxton, B. 2013, ApJ, 777, 136, [1309.3375], [ADS], [DOI]

Wood-Vasey, W. M., Friedman, A. S., Bloom, J. S., et al. 2008, ApJ, 689, 377, [0711.2068], [ADS], [DOI]

Woosley, S. E. & Kasen, D. 2011, ApJ, 734, 38, [1010.5292], [ADS], [DOI]

Woosley, S. E., Kasen, D., Blinnikov, S., & Sorokina, E. 2007, ApJ, 662, 487, [astro-ph/0609562], [ADS], [DOI]

Woosley, S. E., Pinto, P. A., & Hartmann, D. 1989, ApJ, 346, 395, [ADS], [DOI]

Woosley, S. E., Taam, R. E., & Weaver, T. A. 1986, ApJ, 301, 601, [ADS], [DOI]

Woosley, S. E. & Weaver, T. A. 1980, ApJ, 238, 1017, [ADS], [DOI]

Woosley, S. E. & Weaver, T. A. 1986, ARA&A, 24, 205, [ADS], [DOI]

Woosley, S. E. & Weaver, T. A. 1994, ApJ, 423, 371, [ADS], [DOI]

Woosley, S. E., Wunsch, S., & Kuhlen, M. 2004, ApJ, 607, 921, [astro-ph/0307565], [ADS], [DOI]

Wunsch, S. & Woosley, S. E. 2004, ApJ, 616, 1102, [ADS], [DOI]

Xu, Y. & McCray, R. 1991, ApJ, 375, 190, [ADS], [DOI]

Yamaguchi, H., Badenes, C., Foster, A. R., et al. 2015, ApJ, 801, L31, [1502.04255], [ADS], [DOI]

Yamaguchi, H., Eriksen, K. A., Badenes, C., et al. 2014, in AAS/High Energy Astrophysics Division #14, AAS/High Energy Astrophysics Division, 304.02, [ADS]

Yamanaka, M., Kawabata, K., Kinugasa, K., et al. 2010, in Progenitors and Environments of Stellar Explosions, 57, [ADS]

Yang, Y., Wang, L., Baade, D., et al. 2018, ApJ, 852, 89, [1704.01431], [ADS], [DOI]

Yang, Y., Wang, L., Baade, D., et al. 2017, ApJ, 834, 60, [1610.02458], [ADS], [DOI]

Yaron, O., Prialnik, D., Shara, M. M., & Kovetz, A. 2005, ApJ, 623, 398, [astro-ph/0503143], [ADS], [DOI]

Yoon, S. C. & Langer, N. 2005, A&A, 443, 643, [astro-ph/0508242], [ADS], [DOI]

Younger, S. M. 1981, J. Quant. Spec. Radiat. Transf., 26, 329, [ADS], [DOI]

Zhang, H. 1996, A&AS, 119, 523, [ADS]

Zhang, K., Wang, X., Zhang, J., et al. 2016, ApJ, 820, 67, [1602.02951], [ADS], [DOI]

Zingale, M., Almgren, A. S., Bell, J. B., Nonaka, A., & Woosley, S. E. 2009, ApJ, 704, 196, [0908.2668], [ADS], [DOI]

Zingale, M., Woosley, S. E., Rendleman, C. A., Day, M. S., & Bell, J. B. 2005, ApJ, 632, 1021, [astro-ph/0501655], [ADS], [DOI]

Zwicky, F. 1964, Annales d'Astrophysique, 27, 300, [ADS]

Acknowledgments

Over the last few years, many people have helped me to grow, both academically and personally. Without their support, this work would not have been possible.

First and foremost, I am deeply indebted to my Doktorvater Wolfgang Hillebrandt, who gave me the chance to work on this project. This work would not have been possible without the guidance and tutelage of my thesis supervisor and teacher at ESO, Jason Spyromilio, who has worked diligently with me over the years of my thesis research. Jason gave me the freedom and provided the time necessary to develop my own ideas. This balance between guidance and freedom that I found in his supervision was essential to my research and to putting my ideas in shape. The time he invested in our fruitful discussions is highly appreciated and often revealed treacherous pitfalls along the way. This thesis would not be the same without the invaluable help of Stefan Taubenberger on the art of supernova observations and data reduction. Stefan has always been very helpful when asked about 'this one peculiar supernova' – truly being a living supernova almanac – and I thank him for his patience. Thanks to Stefan I was able to enjoy several observing trips to Italy and Chile, and I fondly remember our hikes in the Dolomites and the Atacama desert. I have to thank Christian Vogl for the countless discussions on supernovae, statistics and the problem of spectral fitting during our daily coffee breaks. I also want to thank Wolfgang Kerzendorf, who introduced me to open-source software development and whose enthusiasm for Python is contagious. I thank Bruno Leibundgut, Stuart Sim, Luke Shingles and Kate Maguire for many stimulating discussions. A big thank you goes out to the Garching supernova group for the pleasant working environment. Thank you to all of you for three wonderful years in Garching and to many more, in academia or otherwise.

I am grateful to Tania Johnston and Wolfgang Vieser for letting me present the celestial wonders in the ESO Supernova planetarium. There are only few things which are more fulfilling than the astonishment of an audience upon seeing the magnificent night sky.

I thank all the students and fellows, both at ESO and MPA, for their friendship and support during the last three years. I want to thank the members of the GarGaming group for introducing me to innumerable board games and for instigating an environment that welcomes experienced and new players alike. Especially I'd like to thank Anne-Laure Cheffot, Josh Hopgood, Matthias Seidel, Ivana Kurečić and Caroline Reid for the many hours of fun exploring the dungeons of Gloomhaven.

This PhD would not have been possible without support from ESO, in the form of a studentship, and from MPA – thank you.

Last but not least I would like to express my deepest gratitude to my family, first and foremost my parents. They supported me on this journey and their encouragement accompanied me through this PhD project.